A unified state equation for neutron stars and core-collapse supernovae

Thi Hoa Dinh

Normandie Université

UNIVERSITÉ CAEN NORMANDIE

THÈSE

Pour obtenir le diplôme de doctorat

Spécialité **PHYSIQUE**

Préparée au sein de l'**Université de Caen Normandie**

A unified state equation for neutron stars and core-collapse supernovae

Présentée et soutenue par

THI HOA DINH

Thèse soutenue le 18/09/2023

devant le jury composé de :

M. CONSTANCA PROVIDENCIA	Professeur - Université de Coïmbra	Rapporteur du jury
M. MICHAEL URBAN	Directeur de recherche - Labo. de Physique des 2 Infinis Irène Joliot-Curie	Rapporteur du jury
M. NICOLAS CHAMEL	Professeur - BRUXELLES - UNIVERSITE DE	Membre du jury
MME ANTHEA FANTINA	Chargé de recherche au CNRS - 14 GANIL de CAEN	Membre du jury Co-encadrante
MME MICAELA OERTEL	Directeur de recherche au CNRS - LUTH, CNRS/Observatoire de Paris	Président du jury
MME FRANCESCA GULMINELLI	Professeur des universités - Université de Caen Normandie	Directeur de thèse

Thèse dirigée par **FRANCESCA GULMINELLI** (Laboratoire de physique corpusculaire (Caen))

ED 591 PSIME

lpc caen
laboratoire de physique corpusculaire

Acknowledgement

I would like to express my sincere gratitude to all the individuals who have been supporting me throughout my three-year Ph.D. thesis journey.

First and foremost, I extend my heartfelt thanks to Gilles Ban, the former director of LPC Caen, for welcoming me into the lab and providing me with support during my Ph.D. His care and encouragement, especially during the challenging period of the COVID-19 pandemic, had a positive impact not only to me but also to all the students in the lab. In addition, I would like to extend my appreciation to Etienne Lienard, the current director of LPC Caen, for his invaluable support during the final year of my Ph.D. study.

Moreover, I am profoundly thankful to Véronique Devaux, whose assistance in all my missions has been indispensable. My gratitude also extends to Aurélie Gontier for her invaluable assistance in different administrative procedures. Her support allowed me to quickly integrate into the lab upon my arrival and participate in French classes. Furthermore, I would like to express my appreciation to Marie Legay Meleux for her kind assistance in the administrative procedures with the doctoral school.

I would like to express my deep appreciation to the members of my thesis jury, Constança Providência, Michael Urban, Micaela Oertel, and Nicolas Chamel, for dedicating their time reading my thesis and providing insightful feedback and comments on my research. Special recognition goes to Michael Urban for pointing out a sign mistake in the curvature energy of the bubble phases. Moreover, his detailed corrections and suggestions for the manuscript have been immensely helpful, for which I am deeply grateful.

I extend my deepest gratitude to my esteemed supervisors, Francesca Gulminelli and Anthea F. Fantina. I feel incredibly fortunate to have had them as my supervisors in my Ph.D. study (as well as a significant part of my Master's study). I have learnt so much from every discussion and interaction with them. Their enthusiasm and dedication to research are a source of inspiration for me to pursue a career in research. Moreover, I am sincerely grateful for the numerous opportunities they provided for me to attend various workshops, conference, schools, and seminars. Thanks to their guidance, I have grown substantially from a scientific perspective, and my Ph.D. journey has been full of positivity and excitement. For these reasons, I am deeply indebted to them.

I send my special thanks to Thomas Carreau, my predecessor, for his help with the NSEoS

code during the inception of my thesis. Thanks to his instruction, I was able to grasp the intricacies of the code quickly. The foundation that he laid during his thesis was the kick-starter for launching my project, for which I am truly thankful.

Throughout my Ph.D. journey, I had the privilege of participating in numerous enlightening meetings with esteemed researchers. I thank them very much for insightful discussions. Additionally, I had the honor of collaborating closely with Helena Pais, to whom I extend my appreciation for her encouragement and support.

I had a pleasant working environment, thanks to the kindness of everyone at LPC. Moreover, I highly appreciate the cafe docs, where I had the chance to learn about the works of other Ph.D. students and to share my work with them. I wish them all the best with their defenses in the future.

I am proud to be in the Theory group at LPC Caen with not only competent and hard-working colleagues but also interesting ones. First, I thank Chiranjib Mondal, with whom I shared the office for more than two years. I have learnt a lot from him, and I appreciate that he traveled to Caen from Brussels to support me in my defense. I also learnt a lot from Marco Antonelli, especially during lunch breaks. Special thanks to Philip Davis for the training he provided on developing and maintaining code with GitHub and Git. I found his lessons to be very useful. I will always remember the delicious Sicilian sweets that Luigi Scurto brought and his kindness in giving me a ride several times. I appreciate the moments I shared with Antoine Pfaff and Mateus Pelicer during the time they spent at LPC.

I thank José Pablo Linares Fernández, my partner and also my friend, for his care and support during these years. I cannot imagine going through this marvelous journey without him. I also thank my close friends, Hien, Hanh, Ly, Men, Linh, and Hang, for believing in me more than I ever do. I wish Men, Ly, and Hien the best with their upcoming defenses.

I would like to take this opportunity to express my gratitude to my parents for being my examples of hard work and for their sacrifices. Their immeasurable love has given me motivation to overcome life's obstacles. I am also thankful for the love and support I receive from my brother and my sister-in-law. Lastly, I want to tell my niece and nephew that I love them very much.

Contents

CHAPTER 1

Introduction

1.1 Neutron stars

The most extreme stars known in the Universe are believed to be neutron stars (NS), and therefore, they serve as extraordinary laboratories for testing theories of many different branches of physics, one of which is nuclear physics [1]. With the recent development of multi-messenger observations, the theoretical modeling of NS has entered a new era where it becomes a topic of incredible interest and importance in the physics community.

The first hypothesis on the connection between supernovae (SN) and neutron stars dates back to 1934 by Baade & Zwicky [2]. About more than thirty years later, in 1967, the first radio pulsar was discovered by Bell (Burnell) & Hewish at the Mullard Radio Astronomy Observatory [3]. This "rapidly pulsating radio source", which is now named as PSR B1919+21, was speculated to be associated with either oscillations of white dwarfs (WD) or neutron stars. Later on, the discovery of the Crab pulsar (PSR B0531+21) and the measurement of its spin period, $P = 33.09$ milliseconds, by Comella *et al.* in 1969 [4] confirmed the idea of Gold [5], who suggested: "The constancy of frequency in the recently discovered pulsed radio sources can be accounted for by the rotation of a neutron star". Indeed, with such rapid rotation, a WD would not sustain the centrifugal forces. Up to now, there are around 3400 pulsars that have been identified [6], with a spin period spanning from a few milliseconds to several seconds. See Ref. [1] for a detailed overview.

Theoretically, the formation of a NS can be described as in Fig. 1.1. When a massive star, whose typical mass is of the order $M \gtrsim 8.0\ M_\odot$ (with $M_\odot = 1.9891 \times 10^{30}$ kg being the solar mass), runs out of energy from nuclear fusion, it starts to collapse due to its gravity. The core collapse halts as the density approaches the nuclear saturation point, leading to the formation of a shock wave. Because of the energy loss from the neutrino emission and nuclear dissociation, the shock wave stalls at the distance $\sim 100 - 200$ km from the center (stage (I)). The shock wave is then revived and propagates outwards, leading to a supernova explosion, and leaving behind a newly born proto-neutron star (PNS), which contracts rapidly due to neutrino loss (stage (II)). This shrinkage of the PNS heats up the core up to ~ 50 MeV

(stage(III)). Then, the PNS cools down by emitting neutrinos until their energy becomes small enough that the neutrino mean free path overcomes the star radius, and the PNS becomes neutrino transparent, and beta equilibrium without neutrino is established [7] (stage (IV)). The achievement of neutrino transparency significantly enhances the PNS cooling process. At stage (V), due to the inward heat conduction by electrons and the outward radiation of neutrinos, the PNS becomes isothermal. The neutrino cooling continues to dominate until the NS is around 3×10^5 years old (stage (V)), and the cooling by photon emission takes place. See Ref. [8] for details.

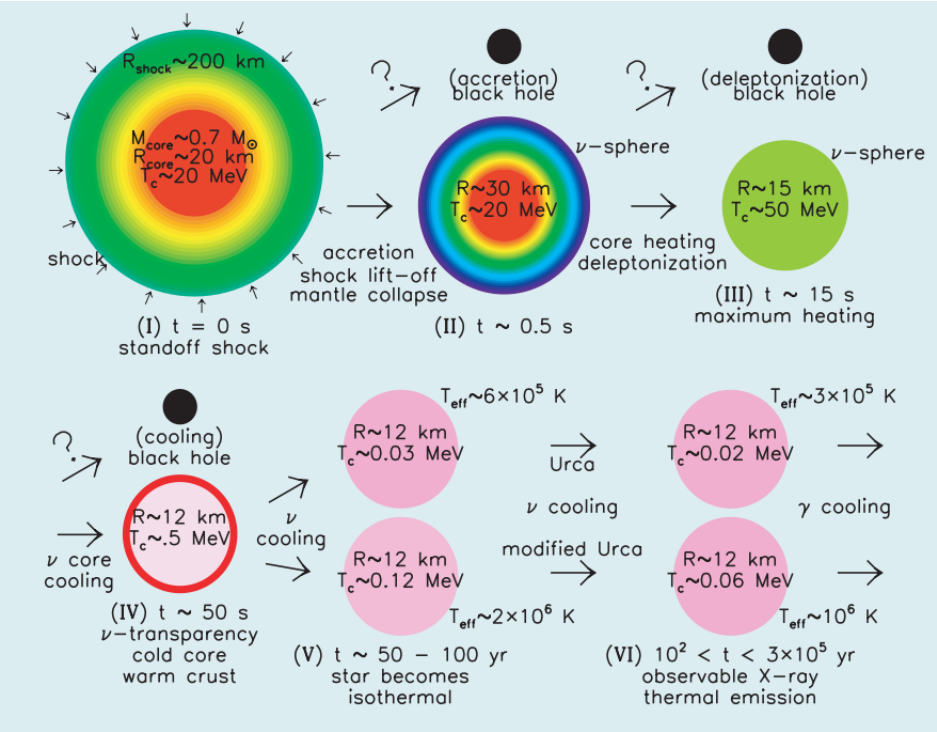

Figure 1.1: Different stages in the evolution of a NS. Figure taken from Ref. [8].

Static properties of a NS, such as mass and radius, are determined under the condition of hydrostatic equilibrium, that is, the state in which the pressure balance between the self-gravity and the internal pressure is achieved. As a result, the key ingredient of a NS model, at beta equilibrium, is the relation between the pressure and density, as well as temperature, of matter, $P(\rho, T)$, which is commonly called the equation of state (EOS). For NS that are sufficiently old, the characteristic thermal energy, $k_B T$, is negligible with respect to the characteristic microscopic excitation energy. Therefore, matter in these NS can be considered as "cold". Furthermore, if nuclear equilibrium rates are fast compared to cooling rates, we can consider that matter is in its absolute ground state, i.e., cold–catalyzed matter [9]. Under this cold–catalyzed matter hypothesis, the pressure can be calculated at $T = 0$, and the EOS depends on the density only, $P = P(\rho)$. The NS EOS, $P(\rho)$, is directly connected to the composition of matter and the underlying microphysical model.

1.2 The interior structure of a neutron star

Typically, it is assumed that the interior of a cold NS is composed of different matter phases, from a solid crust to a liquid core [1]. A sketch for the structure of a NS is presented in Fig. 1.2. Particularly, the *outer crust* is widely believed to consist of fully-ionized ions arranged in a lattice, surrounded by a background of an electron gas. Since the electron Thomas-Fermi screening lengths are considerably larger than the distances between nuclei [10], variations in electron density can be disregarded, and the electron gas can be treated as uniform [10,11]. Due to the presence of the electron background, the electrostatic energy of the system includes not only the Coulomb self-energy of the nuclei, but also the lattice energy (with a correction on the finite size of nuclei), which represents the attractive Coulomb interaction between nuclei in the lattice [9], see Sect. 2.1.2.1 and Appendix A for details. As the density increases, the matter becomes more and more neutron-rich, and at density around $\rho_{\rm ND} \approx 4 \times 10^{11}$g cm^{-3}, all the bound states of neutrons are filled up, and neutrons start to drip out of the nuclei. As a result, the NS crust is composed not only of nuclei and electrons but also of a neutron gas. This region is called the *inner crust*. The crust has a thickness of about one kilometer, and it contributes only a small proportion to the NS total mass (see Chapter 2), but it is important for different astrophysical phenomena. At low densities, nuclei are sufficiently far apart from each other that their structure is not influenced by neighboring nuclei. As a result, nuclear self-energies, i.e., surface and Coulomb self-energy, dominate, and nuclei are expected to be more or less spherical [12]. At the bottom of the crust, the density is very high, and nuclei are very close to each other. In this case, the lattice term prevails over the nuclear self-energies, and therefore, it is energetically possible for non-spherical structures to appear [12,13]. This region with non-spherical nuclei is called the "pasta" mantle (see Chapter 3).

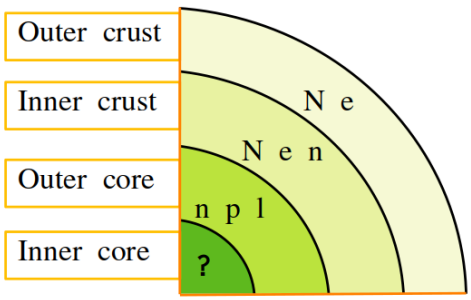

Figure 1.2: A sketch of the structure of a NS (not to scale).

At $\rho \approx \rho_{\rm sat}/2$, with $\rho_{\rm sat} \approx 2.8 \times 10^{14}$ g cm^{-3} being the nuclear saturation mass density, nuclei dissolve into homogeneous nuclear matter. This region is called the *outer core*, and it spans a wide density range, $0.5\rho_{\rm sat} \lesssim \rho \lesssim 2\rho_{\rm sat}$, where neutrons and protons are in beta equilibrium with electrons and muons. Finally, in the innermost region of a NS, called the *inner core*, the density is very high, up to $\sim 10\rho_{\rm sat}$. Such high densities are currently not accessible in the laboratories on Earth, making NS excellent laboratories to explore matter under extreme density conditions. The core of a NS is around several kilometers thick and it

contains most of the mass of the star; the properties of the core are discussed in Chapter 2.

Due to the ultradense condition in the interior of NS, different exotic degrees of freedom, such as hyperons, pions, free quarks, etc., are speculated to appear. Particularly, the possible presence of hyperons, a group of baryons with at least one strange quark, in NS cores was first predicted in 1959 by Cameron [14]. To be more specific, the author argued that at high densities, $10^{15} - 10^{17}$ g cm^{-3}, protons and neutrons can be transformed into various kinds of hyperons. Furthermore, he qualitatively discussed that the creation of these new baryons depresses the Fermi level, and therefore, reduces the dependence on the density of the nuclear potential. In 1960, the first quantitative study on hyperons in NS was conducted by Ambartsumyan and Saakyan [15]. Interestingly, the authors of Ref. [15] found that the first hyperons to appear are Σ^-, even though the rest mass of Σ^- is larger than those of Λ and $\Sigma^{+,0}$. As the density increases, Λ, and other heavier hyperons are predicted to subsequently appear. The densities at which these transitions happen were also evaluated in Ref. [15]. Up to now, there have been many works devoted to this topic, see e.g., Refs. [16–24] (see also Refs. [7, 25–29] for a review). In general, hyperons are expected to appear at $\sim 2-3\rho_{\rm sat}$, and the onset densities of different hyperon species are model-dependent. Due to the conversion of neutrons and protons into heavier baryons, the Fermi pressure exerted by nucleons is depleted, leading to the softening of the EOS. Consequently, the maximum mass predicted by many hyperons models (see e.g., Refs. [18, 19, 30]) fails to reach the current observational NS masses [31]. This problem is also known as the "hyperon puzzle". To solve this puzzle, different mechanisms providing additional repulsion to stiffen the EOS were proposed. They include: more repulsive hyperon-hyperon interactions, repulsive hyperonic three-body forces, a phase transition to deconfined matter, and the possible presence of other hadronic species, such as the Δ isobar and meson condensates (see Ref. [27–29] and references therein for details).

Recently, the signatures of hyperons inside neutron stars were investigated in a Bayesian analysis by Malik & Providência [24], where the hadronic matter is described within a relativistic mean field (RMF) framework. Particularly, the authors showed that if hyperons are included and the maximum NS mass obtained for each EOS is required to be larger than 2 $M_\odot$, then the radius and tidal deformability obtained are larger than those determined from a nucleonic EOS. Furthermore, they also found that the presence of hyperons in NS could be ruled out if: a 1.4 $M_\odot$ NS has a radius $R < 12.5$ km, a 2.0 $M_\odot$ NS has a radius below 11.5 km, or a mass measurement with $M > 2.2$ $M_\odot$.

One can also expect hadrons in NS inner cores to disintegrate into quark matter, as depicted in Fig. 1.3. Specifically, at baryonic number density[1] $n_B \lesssim 2n_{\rm sat}$ (with $n_{\rm sat}$ being the number density at saturation), three quarks are confined together to form a color singlet object, the interaction between hadrons occurs via a few meson or quark exchanges, and matter can be described with nucleon degrees of freedom. As the density increases, the interactions between baryons are dominated by the exchanges of many quarks, and the system gradually transforms from hadronic to quark matter. At $n_B \gtrsim 4-7n_{\rm sat}$, matter is percolated, and the effective degrees of freedom can be replaced by quarks and gluons. If the density is very high, $n_B \gtrsim 10n_{\rm sat}$, the strong coupling constant is expected to be small enough that

[1] I use ρ, n, and ρ_B for denoting mass density, number density, and total mass-energy density, respectively.

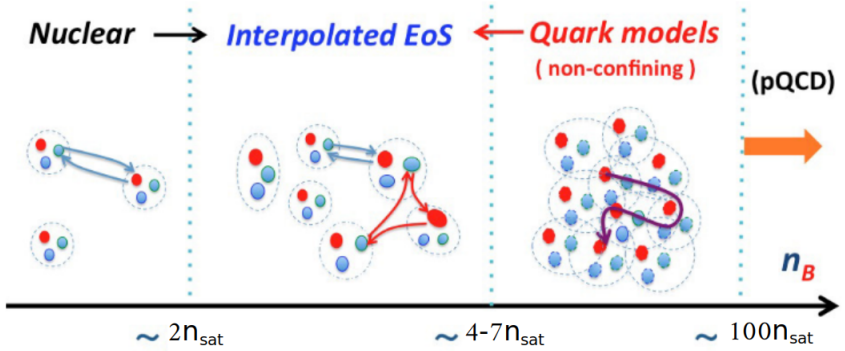

Figure 1.3: Illustration of the transition from nuclear to deconfined matter with increasing density. Figure adapted from Ref. [32].

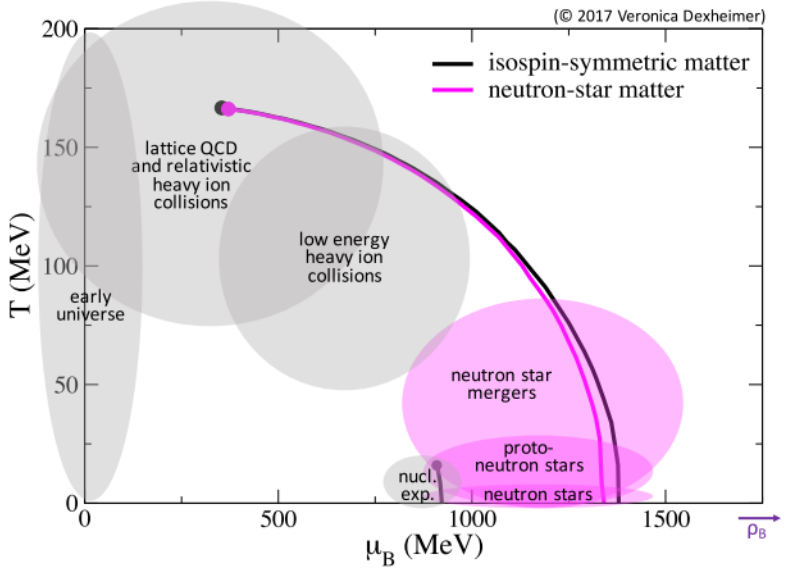

Figure 1.4: QCD phase diagram for isospin-symmetric matter and neutron-star matter obtained with the chiral mean field model. Figure taken from Ref. [33].

perturbation theory can be applied, i.e., quark matter can be treated in perturbative quantum chromodynamics (pQCD). However, such a high-density range is unlikely to happen in NS, see Ref. [32] and references therein for detailed descriptions. The density domain explored in the NS core is particularly challenging for nuclear theory.

On the one hand, the density range in NS is too low for the pQCD to be valid. On the other hand, NS matter is too dense and cold with respect to the conditions accessible in lattice QCD simulations and heavy-ion collision (Fig. 1.4). Due to these difficulties, phenomenological approaches of QCD are typically proposed to describe quark matter in NS. For example, A. Pfaff *et al.* [34] performed a Bayesian analysis to study the hybrid stars, i.e., NS with a quark core inside a hadronic outer shell, where the quark phase is described using the SU(3) Nambu-Jona-Lasinio model. They found that the quark cores tend to be relatively small and only appear in very heavy stars. Moreover, they showed that with the present observations on the mass [31], radii [35–38], and tidal deformability [39–42], it is not possible to distinguish

between the purely nucleonic scenario and the transition towards quark matter. As another example, instead of having a first-order phase transition, another approach to describe the deconfinement of matter called *quarkyonic matter* model was proposed by McLerran & Reddy in 2019 [43], and it was applied by many works, see e.g., Refs. [44,45] and references therein. In particular, the quarkyonic model suggests a crossover between the nucleonic and the quark phases, and therefore, the transition from nuclear matter to quarkyonic matter is a second-order phase transition, where the sound speed is smooth but its derivative is not.

So far, the presence of additional degrees of freedom in the cores of NS, e.g., hyperons and free quarks, is still under debate. In this thesis, it is assumed that the only baryonic constituents in NS cores are nucleons, and this hypothesis is confronted with current astrophysical observations within a Bayesian inference, see Sect. 2.3 for more details.

1.3 Neutron-star observations

The observations of NS provide us with insights not only into global properties, such as mass, radius, and tidal deformability of the star, but also different properties related to the cooling and transport processes. These measurements can be transformed into valuable information on the EOS as well as the composition of matter in different regions of NS.

Most of the NS mass measurements are performed with radio timing in compact binary systems. In particular, the inference of the component masses is based on our understanding of relativistic orbital dynamics [48]. There are different types of binaries, and their mass measurements are displayed in Fig. 1.5. We can see that NS masses are most reliably determined in double NS binaries (yellow area). However, the masses of NS in this group are relatively low, i.e., typically below 1.5 $M_\odot$. The most massive and precisely measured NS are those with a WD companion, as shown in the grey area. Specifically, in 2010, the mass of the millisecond radio pulsar PSR J1614-2230 was measured by Demorest *et al.* [49] thanks to its strong Shapiro delay signature. This measurement was then improved by Fonseca *et al.* [50] in 2016 and Arzoumanian *et al.* [51] in 2018. PSR J1614-2230 has a spin period of 3.15 milliseconds, and its most updated mass is $M_{\rm J16} = 1.908 \pm 0.016\ M_\odot$. In 2013, Antoniadis *et al.* [31] used pulsar timing in combination with phase-resolved optical spectroscopy of the WD companion to provide data on another heavy pulsar, PSR J0348+0432. Particularly, they found that this pulsar has a spin period of 39 milliseconds and a mass of $M_{\rm J03} = 2.01 \pm 0.04\ M_\odot$. Up to now, the heaviest pulsar known is PSR J0740+6620, which is also in the binary with a WD and has a spin period of 2.8 milliseconds. Its mass measurement was recently reported in Ref. [52] (not shown in Fig. 1.5), $M_{\rm J07} = 2.08 \pm 0.07\ M_\odot$. The discoveries of these pulsars with masses in the order of around 2 $M_\odot$ has a strong implication on the properties of dense matter. Indeed, these mass constraints indicate that the NS EOS should be sufficiently stiff, i.e., the pressure of matter should increase rapidly with density, to support such high mass, hence eliminating models that are too soft to reach these criteria.

The observations based on radio timing have not yet been able to provide us with information on NS radii. Fortunately, this information has become available with NASA's soft X-ray telescope, Neutron Star Interior Composition Explorer (NICER) [35–38]. In particular, in 2019, the mass and radius of the millisecond pulsar PSR J0030+0451 were determined [35,36],

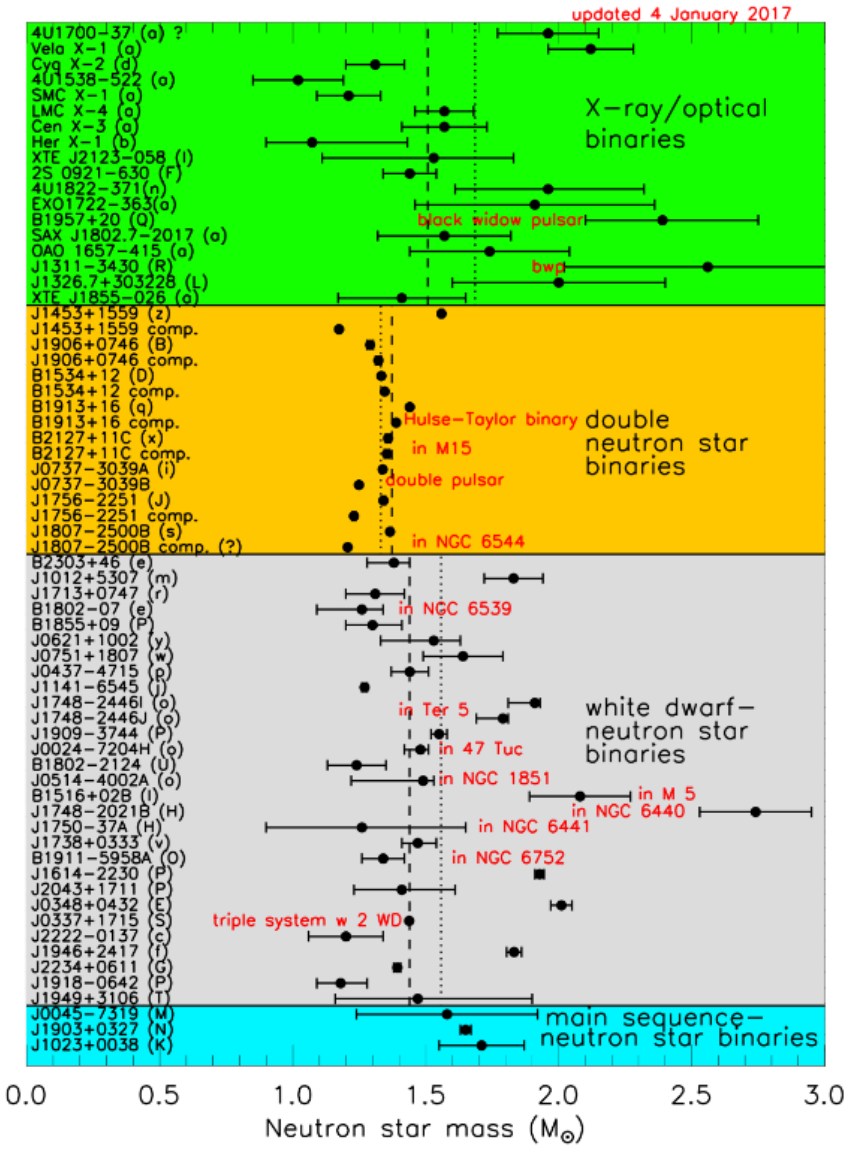

Figure 1.5: NS mass measurements with pulsar timing, updated in 2017. Vertical dashed (dotted) line correspond to the error-weighted (unweighted) averages for each category of binary. Figure taken from Ref. [46] (see also Ref. [47] for a more recent compilation).

while similar measurements were performed for PSR J0740+6620 in 2021 [37,38]. While PSR J0030+0451 is an isolated NS, PSR J0740+6620 belongs to a binary system, as mentioned above. As a result, measurements of the mass and orbital inclination were performed independently, leading to better precision. Nevertheless, the count rate of PSR J0740+6620 is very low compared to PSR J0030+0451, leading to some uncertainty. Consequently, the information about the hot regions on the surface of the star is less precise, and therefore, the radius is measured with higher uncertainty, see Refs. [37, 38] for details. Although NICER has achieved remarkable progresses in determining NS radii, the present uncertainties are sufficiently substantial that many EOS are still compatible with these measurements, as will be shown later on in Fig. 2.28.

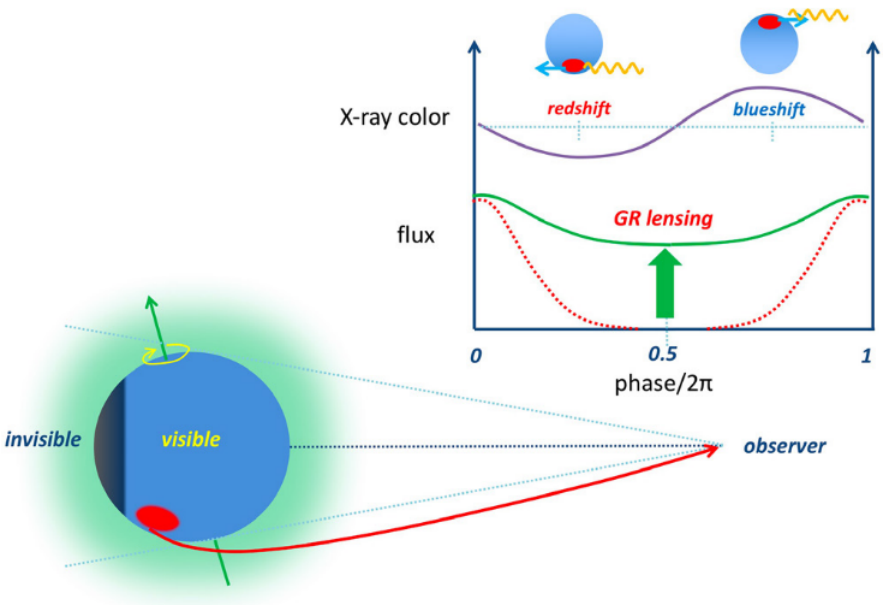

Figure 1.6: X-ray flux from a single (red) hot spot on the surface of a rotating NS with (solid green line) and without (dotted red line) gravitational lensing. Figure taken from Ref. [32].

The mass-radius distribution by the NICER collaboration was obtained via pulse-profile modeling, see e.g., Ref. [53] for a review of different techniques. Particularly, pulse-profile modeling is a technique probing general relativity effects on thermal emission from hot spots, caused by the energy deposit of magnetospheric currents on the star's surface, of rotation-powered millisecond pulsars [35]. The basic mechanism of a single hot spot is displayed in Fig. 1.6. The main idea is that the strong NS gravitational field causes the bending of light and therefore allows the visibility of the NS back side, as illustrated by the red arrow originating from the hot spot (red oval area) and reaching the observer. In the inset (upper right), the lower section depicts the flux from the X-ray emission of the hot spot as a function of the rotational phase, considering the presence (solid green line) or absence (dotted red line) of gravitational lensing, while the upper section demonstrates the color shifts exhibited by the spot due to the Doppler effect. As we can see, the gravitational lensing effect reduces the size of the invisible area and, therefore, decreases the contrast between the flux emitted by the brightest, corresponding to phase $= 0$ and 2π, and darkest, corresponding to phase $= \pi$, regions. Clearly, this bending effect is related to the NS mass M and radius R. Thus, combining information from the gravitational lensing effect, the velocity deduced from Doppler shifts, and rotational frequency, one can constrain the mass and radius of a NS within a Bayesian analysis, see Refs. [32, 35–38] for details.

Properties of NS matter can also be probed with gravitational wave (GW) signals emitted from NS binary coalescence. Figure 1.7 demonstrates the GW signal expected from a binary NS merger (red curve) and a binary black hole merger (grey curve) for the same chirp mass $\mathcal{M}_c$, defined as:

$$\mathcal{M}_c = \frac{(m_1 m_2)^{3/5}}{(m_1 + m_2)^{1/5}}, \tag{1.1}$$

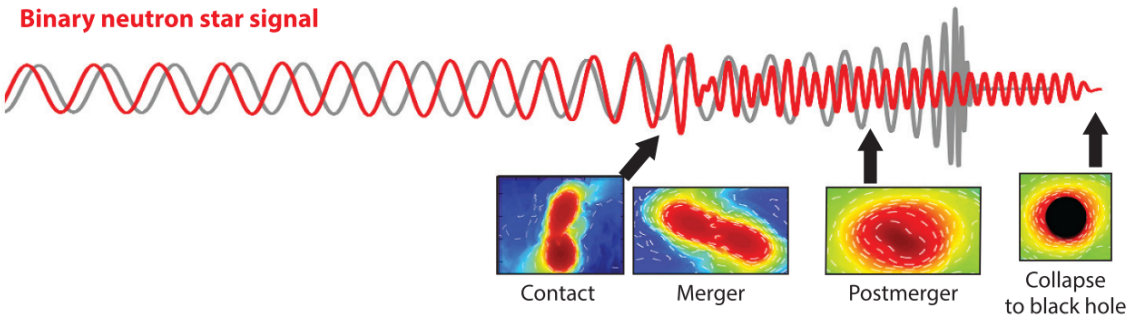

Figure 1.7: Comparison of the GW signal expected from the merger of a binary NS (red) and black hole (grey) system with the same chirp mass. See text for details. Figure taken from Ref. [54].

with m_1 and m_2 being the component masses. For a system of NS, the tidal field of the companion induces a mass-quadrupole moment, and the tidal deformation speeds up the coalescence and results in an advance in the binary NS gravitational wave phase, see Ref. [54]. The images in the lower right of Fig. 1.7 indicate different stages: contact, merger, postmerger, and the collapse into a black hole.

On August 17, 2017, the first GW signals, GW170817, from a merger of a binary NS system were detected by the LIGO-Virgo Collaboration (LVC) [39–42]. Then, a gamma-ray burst, GRB 170817A, was observed 1.7 seconds after the merger time. The GW signals allow one to extract the chirp mass $\mathcal{M}_c$ and the so-called *tidal deformability*, which measures how much an object is deformed when subjected to a tidal field. For the binary associated with GW170817, the chirp mass is very precisely determined, $\mathcal{M} = 1.188^{+0.004}_{-0.002}\ M_\odot$ at 90% confidence interval[2]. On the other hand, the individual masses are not well controlled, $m_{1,2} \in [1.17, 1.60]\ M_\odot$ for low-spin priors, because different combinations of m_1 can m_2 can result in the same chirp mass. The low upper limit in the masses and the emissions of gamma-ray burst as well as subsequent electromagnetic radiation implies that the source of GW170817 must be a NS-NS binary, see Refs. [39–42] for detailed discussions.

Besides the measurements of NS global properties, such as mass, radius, and tidal deformability, as presented above, there are other astrophysical observations, specifically those associated to spin-down and cooling, that could also shed light on the interior structure and transport properties of NS matter. Particularly, the properties of the inner crust are expected to have a strong impact on these phenomena. Indeed, this was shown, for example, in Refs. [55, 56]. To illustrate this point, in Figs. 1.8-1.9, I show the results from Viganò *et al.* [55] in comparison with the observational data for the thermal and timing evolution of different NS classes. In this calculation, one of the microscopical inputs is the electrical and thermal conductivity, which depends on the crust composition, particularly the so-called *impurity parameter* $Q_{\rm imp}$ that accounts for the presence of multiple species in the medium and represents the variance of the atomic number. In Figs. 1.8-1.9, the results are obtained by setting $Q_{\rm imp} = 100$ at $\rho > 6 \times 10^{13}$ g cm^{-3} and $Q_{\rm imp} = 0.1$ elsewhere in the crust, see Ref. [55] for details. However, $Q_{\rm imp}$ can be calculated consistently throughout the whole crust, and this is one of the main goals of the thesis (See Chapter 4).

[2]If it is not mentioned otherwise, the properties of the NS binary system associated to GW170817 are reported at 90% confidence interval, while the other data are cited at 68%.

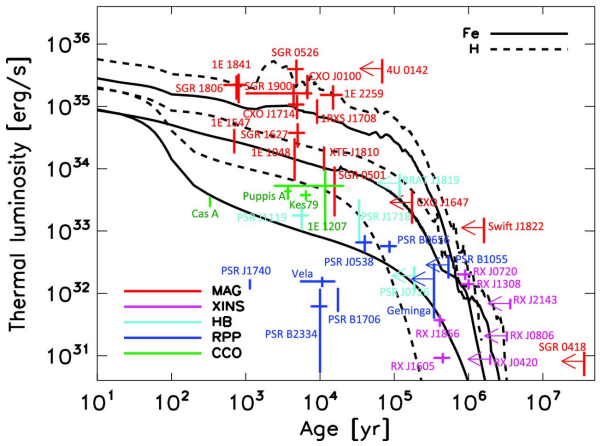

Figure 1.8: Comparison between the theoretical calculation for the cooling curves by Viganò *et al.* [55] with observational data for two different values of the initial magnetic field, 0.3×10^{14} G and 3×10^{15} G, for Fe envelopes (solid lines) and light-element envelopes (dashed lines). The color data points show data from observations for different NS classes: magnetars (MAG, red), X-ray isolated neutron stars (XINS, magenta), high-B radio pulsars (HB, cyan), rotation powered pulsars (RPP, dark blue), and Central Compact Objects (CCOs, green). Figure taken from Ref. [55].

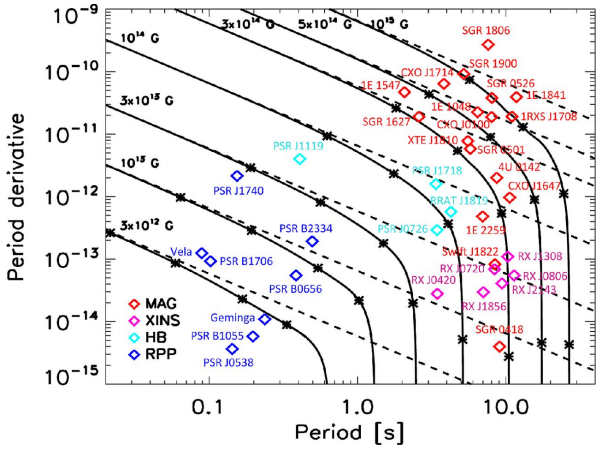

Figure 1.9: Theoretical calculations for the evolutionary tracks in the P-$\dot{P}$ diagram with (solid lines) and without magnetic field decay (dashed lines) at different values of initial magnetic fields B in comparision with observational data (color diamonds). The black asterisks, from left to right, mark the real ages: 10^3, 10^4, 10^5, and 5×10^5 years. Figure taken from Ref. [55].

Last but not least, there are also transient NS phenomena that could further constrain the NS EOS and structure, such as glitches (see e.g., Refs. [57–59]), quasi-periodic oscillation in accreating NS (see e.g., Refs. [60, 61]), and giant flares (see e.g., Refs. [62, 63]).

1.4 Neutron-star modeling

As mentioned before, one of the fundamental ingredients of a NS model is the EOS, which is needed to solve the Tolman-Oppenheimer-Volkov equations of hydrostatic equilibrium and thus to calculate different NS observables (see Sect. 2.2.1). Therefore, it is crucial to have the most realistic prediction possible for nuclear EOS. For this reason, an immense amount

of effort is presently devoted to this topic.

Theoretical approaches for describing the nuclear system can be broadly categorized into two main groups: *ab-initio* and phenomenological methods, see e.g., Refs. [25, 29] and references therein for a review. In the absence of an exact solution of QCD from quark and gluon degrees of freedom, *ab-initio* calculations in nuclear theory start with effective bare nucleon-nucleon interactions that are adjusted to reproduce experimental scattering data and the properties of bound few-nucleon systems [7]. These interactions encompass various classes, including phenomenological interactions, renormalization group methods, the resonating-group method, and chiral effective field theory (EFT). Upon establishing an interaction, different approaches can be employed to solve the many-body problem in nuclear matter, such as (Dirac)–Brueckner–Hartree–Fock, self-consistent Green's function, and Quantum Monte Carlo methods. The primary limitation of *ab-initio* methods is their applicability solely to homogeneous matter in the core of NS while being unable to describe the inhomogeneities of the NS crust. In phenomenological approaches, bare interactions are replaced by effective interactions, converting the complex many-body problem of interacting particles into an effective one of independent particles. Within this framework, the wave function is expressed in terms of Slater determinants. Notably, these approaches are based on the energy density functional theory, which describes the energy of the system as a functional that depends only on one-body densities. Phenomenological methods include both non-relativistic approaches, such as those derived from effective forces of Skyrme or Gogny type, and relativistic ones, derived from an effective Lagrangian incorporating baryon and meson fields. One advantage of phenomenological approaches is that they can accurately reproduce the properties of symmetric matter because coupling constants in the density functional are directly determined from many-body observables. Additionally, these methods can be used to describe both clustered and homogeneous matter [25, 29]. In this work, we employ the *meta-modeling* technique, inspired by a Taylor expansion around the saturation density of symmetric nuclear matter, as proposed by Refs. [64,65], to construct the nuclear matter EOS. The metamodel is a parametrization of the nuclear matter energy, calculated from either an *ab-initio* or phenomenological approach, in terms of the so-called *empirical parameters*, without relying on specific nucleon-nucleon interactions and many-body methods. The formalism and advantages of the meta-modeling approach are discussed in Sect. 2.1.1.1.

Due to the cluster extreme isospin asymmetry, the condition present in the NS crust beyond the neutron drip is not accessible in terrestrial laboratories. Consequently, the description of the ground state of the inner crust relies solely on theoretical modelings. As mentioned earlier, the applicability of current *ab-initio* approaches with realistic interactions to describe inhomogeneous matter is limited. Therefore, when it comes to the crust, one must depend on phenomenological models. Furthermore, in most cases, the crust is studied under the Wigner-Seitz (WS) approximation, which divides matter into identical electrically neutral cells, see also Ref. [58] for a review on the physics of NS crusts. The pioneering work on quantum mechanical Hartree-Fock (HF) calculation of the inner crust was carried out by Negele and Vautherin [66]. In order to incorporate pairing effects, the HF scheme has been expanded to the Hartree-Fock-Bogoliubov (HFB) framework (see e.g., Refs. [67–69]) and Hartree-Fock-Bardeen-Cooper-Schrieffer (HFBCS) framework (see e.g.,

Refs. [70–72]). However, these fully quantum methods have certain drawbacks, as they can be computationally expensive and may introduce numerical inaccuracies due to the chosen boundary conditions during the calculation. To overcome these problems, semiclassical methods based on the (extended) Thomas–Fermi (ETF) approximation have been employed, see e.g., Refs. [73,74]. Moreover, important shell effects can be recovered in the ETF plus Strutinski Integral (ETFSI) approach, and pairing corrections can also be taken into account, as in the works by Refs. [75–77]. In this thesis, we model the inhomogeneities in the NS crust within a compressible liquid drop model (CLDM), which is less sophisticated compared to HF- and (E)TF-type models. In CLDM, clusters are assumed to have well-defined surfaces, while the nucleons inside and outside the clusters are treated as having uniform distributions. Furthermore, quantum effects, which could play a crucial role in determining the equilibrium composition of the crust, are neglected. However, despite these simplifications, results obtained in CLDM exhibit a qualitatively good agreement with more microscopic approaches [78,79]. In addition, given the considerable uncertainties associated with the nuclear interaction, the predictive power of CLDM can be considered sufficient. Notably, CLDM offers distinct advantages over HF and (E)TF calculations, making it well-suited for the objectives of this thesis. Specifically, CLDM allows one to study the physical contributions and effects of different terms of the total energy separately. This decomposition becomes particularly relevant for studying the pasta phases (Chapter 3) and liquid crust (Chapter 4). Moreover, CLDM is numerically more affordable, and therefore, is powerful in Bayesian studies and multi-component calculations. Another important aspect is that CLDM allows for a unified treatment of crust and core, as we will discuss in Sect. 2.1.

The crust described in Sect. 1.2 corresponds to the case of a cold–catalyzed NS, where the crust is supposed to have a pure crystalline structure at zero temperature. In the finite-temperature phenomena, such as those related to the early stages of NS cooling (see Fig. 1.1), the crust is expected to be made of a liquid multi-component plasma (MCP) composed of different nuclear species [80–89]. Due to the complexity of the MCP calculation, many calculations for the crust at finite temperatures are performed in the one-component plasma (OCP) approximation, where the nuclear distribution is represented by one single nucleus. The comparison between the OCP and MCP predictions was previously investigated in several works, see e.g., Refs. [82,84,85], in which the OCP and MCP approaches are referred to as the single nucleus approximation and nuclear statistical equilibrium, respectively. Specifically, the calculations by Refs. [84,85] considered core-collapse supernovae matter, while the calculation by Ref. [82] was performed for general stellar matter, which can be applied for any temperature, density, and proton fraction. Interestingly, these works all highlight that the thermodynamic properties of matter, such as pressure and entropy, can be described relatively well with the single-nucleus approach. On the contrary, if the quantity of interest is the composition, the mean mass number of the clusters is systematically overestimated by the OCP. Moreover, the MCP calculation also predicts a considerable contribution of light clusters, which prevails over heavy ones as the density increases. Even though the presence of complex light particles as independent degrees of freedom was taken into account in several OCP calculations by including α particles, see e.g., Refs. [90,91], and also deuterons, tritons, and helions, see e.g., Refs. [92–94], the average isotopic content of these very light ions is

expected to be neutron rich in stellar matter, at high densities, especially in the case of beta equilibrium [82]. As a consequence, all possible species in the nuclear distribution should be considered with a statistical approach. This point is investigated in Chapter 4.

Among the pulsars that have been discovered, about 30 of them are magnetars [95], which are young NS with very strong magnetic fields, $B \gtrsim 10^{14}$ Gauss. These highly magnetized objects are relevant for various X-ray observations, such as short bursts, large outbursts, giant flares, and quasi-periodic oscillations. Moreover, they are also associated with interesting timing properties like enhanced spin-down, glitches, and anti-glitches (see Ref. [96] for a review). Such strong magnetic field could affect different properties of NS, see e.g, Refs. [97–100], for some recent studies on different topics related to magnetars. However, in this thesis, we limit ourselves to the case of non-magnetized NS.

1.5 Structure of the thesis

The thesis is organized as follows: In Chapter 2, I present the formalism for constructing a unified EOS for cold–catalyzed NS under the nucleonic hypothesis (Sect. 2.1). The EOS is then used as input in the hydrostatic equilibrium equations to calculate different NS observables, such as mass, radius, tidal deformability, and moment of inertia in Sect. 2.2. Employing Bayesian inference, in Sect. 2.3, the nucleonic hypothesis is confronted with different astrophysical data. Chapter 3 focuses on the properties of a particular structures that can appear at the bottom layers of the inner crust in the inner crust, called the "pasta" phases, in cold–catalyzed NS. In particular, the model dependence of the pasta-phase properties is investigated in Sect. 3.3, while the uncertainties of these properties are quantified in Sect. 3.4. In Sect. 4, the equilibrium composition of the PNS crust in the liquid phase is investigated, both in the one-component plasma approximation (Sect. 4.1) and multi-component plasma approach (Sect. 4.2). Finally, general conclusions and outlooks of the thesis can be found in Chapter 5.

CHAPTER 2

Cold–catalyzed neutron stars under the nucleonic hypothesis

In this chapter, I discuss the equation of state for matter in cold, isolated, non-accreting, and non-rotating neutron stars as well as the connection to their observables.

With their central density reaching several $\rho_{\rm sat}$, NS are the most compact stars known in the Universe [1]. The EOS of matter at sub-saturation densities is relatively well-constrained thanks to the information from nuclear physics theory and experiments. On the other hand, understanding the EOS behavior at supra-saturation densities is still a challenging task. Indeed, knowledge of the EOS in these regions is not yet accessible in terrestrial laboratories, even though future experiments such as those in heavy-ion collision [101, 102] could open a new window in understanding properties of extremely dense matter [103]. Fortunately, over the last few years, together with the growth of multi-messenger astronomy we have witnessed several breakthroughs in NS observations, which in turn provide us with valuable hints on the high-density EOS. To be more specific, masses of heavy pulsars were measured with high precision via radio timing, e.g., PSR J0348+0432 ($M_{\rm J03} = 2.01 \pm 0.04\ M_\odot$) [31] and PSR J0740+6620 ($M_{\rm J07} = 2.08 \pm 0.07\ M_\odot$) [52]. In addition, GW signals (GW170817) from the merger of a binary NS system detected by the LVC delivers the very first information about the NS tidal deformability [39–41]. Moreover, with the development of X-ray timing telescopes, the joint mass-radius distributions of the millisecond pulsars PSR J0030+0451 (NICER data) [35, 36] and PSR J0740+6620 (NICER+XMM-Newton data) [37, 38] became available [104, 105]. Due to the one-to-one correspondence between the EOS and cold NS static observables [106], these measurements together with the upcoming data [42] can be transformed into valuable information on matter at extreme conditions that cannot be reproduced on Earth. Thus, they are expected to be very promising tools to uncover the open questions about dense matter, such as whether or not exotic degrees of freedom exist in the cores of NS [7].

This chapter is organized as follows. In Sect. 2.1, I briefly describe the structure of a NS and show the formalism for obtaining the NS EOS, from the core (Sect. 2.1.1) to the crust (Sect. 2.1.2). The transition from the crust to the core is presented in Sect. 2.1.3, and a unified EOS for NS is discussed in Sect. 2.1.4. In Sect. 2.2, the relation between the EOS

with NS observables is explained in great detail. Particularly, the equations of hydrostatic equilibrium in general relativity will be presented in Sect. 2.2.1, from which the mass-radius relation can be obtained. In Sects. 2.2.2 and 2.2.3, I respectively recall the expressions of NS tidal deformability and moment of inertia. With some given energy functionals, these properties of NS are illustrated in Sect. 2.2.4. Finally, to incorporate the uncertainty in the nucleonic EOS into NS predictions, as well as to study the impact of NS observations on the nucleonic EOS, a Bayesian analysis is performed in Sect. 2.3.

2.1 Neutron star equation of state

As it was shown in Ref. [107], to determine the composition as well as the EOS, in principle, one should minimize the Gibbs free energy per nucleon at a constant pressure P (see also Ref. [81]). However, such calculations could become computationally expensive at high densities. An alternative approach is to minimize the Helmholtz free-energy density of the system at a constant density. It was shown in Ref. [107] that the error introduced by using the latter approach is negligible.

In the following, I present in detail the formalism for getting the composition and the EOS of a NS core (Sect. 2.1.1) and crust (Sect. 2.1.2).

2.1.1 Homogeneous matter in NS core

As described above, the core of a NS has a mass density from around $\rho_{\rm sat}/2$ to several $\rho_{\rm sat}$. We assume that the only baryonic species in the entire core are nucleons, which are in beta equilibrium with the lepton components, specifically, electrons and muons. At each given total baryon number density n_B, to find the equilibrium composition in the core, one needs to minimize the free-energy density of the system. At zero temperature, the free-energy density is equal to the energy density, and can be written as:

$$\varepsilon_{npe\mu}(n_B,\delta,n_e,n_\mu)=\varepsilon_B(n_B,\delta)+\varepsilon_e(n_e)+\varepsilon_\mu(n_\mu)+n_B\frac{1-\delta}{2}(m_p-m_n)c^2+n_Bm_nc^2, \quad (2.1)$$

where c denotes the speed of light, m_n (m_p) are the neutron (proton) mass, $\varepsilon_{\rm B}(n_B,\delta)$, $\varepsilon_e(n_e)$, $\varepsilon_\mu(n_\mu)$[1] are respectively the energy densities of nuclear matter, electrons, and muons, with n_e (n_μ) being the electron (muon) number density, δ denotes the isospin asymmetry in the core. Let n_p be the total proton density in the core, from the charge neutrality condition, we have:

$$n_p=n_e+n_\mu. \quad (2.2)$$

Then, δ can be written as:

$$\delta=\frac{n_B-2n_p}{n_B}. \quad (2.3)$$

This leads to the following equation:

$$n_B\frac{1-\delta}{2}=n_e+n_\mu. \quad (2.4)$$

Details of the nuclear matter and lepton energy terms will be elaborated as follows.

[1] I use respectively ε and e (with a subscript) to indicate the energy density and energy per particle. We have, $e=\varepsilon/n$.

2.1.1.1 Nuclear matter properties in the meta-modeling approach

Let us consider an infinite nuclear matter system composed of neutrons and protons of respective number densities[2] n_n and n_p, which are related to the Fermi wave number $k_{F_{n,p}}$ through:

$$n_{n,p} = \frac{1}{3\pi^2} k_{F_{n,p}}^3. \tag{2.5}$$

The energy of the system is calculated employing the so-called *meta-modeling* technique proposed by Refs. [64,65], which was inspired by the Taylor expansion around the saturation density of symmetric nuclear matter. Within this approach, the energy density at a total baryon density $n_B = n_n + n_p$ and isospin asymmetry $\delta = (n_n - n_p)/n_B$ can be decomposed into a potential and kinetic part as:

$$\varepsilon_B(n_B, \delta) = \mathcal{V}(n_B, \delta) + \varepsilon_{\rm kin}(n_B, \delta). \tag{2.6}$$

Two boundaries of the isospin asymmetry, which are $\delta = 0$ and $\delta = 1$, respectively correspond to symmetric nuclear matter (SNM) and pure neutron matter (PNM):

$$\varepsilon_{\rm SNM} = \varepsilon_B(n_B, \delta = 0), \tag{2.7}$$

$$\varepsilon_{\rm PNM} = \varepsilon_B(n_B, \delta = 1). \tag{2.8}$$

For a non-relativistic free Fermi gas, the kinetic energy density can be expressed as:

$$\varepsilon^{\rm FG}(n_B, \delta) = n_B \frac{t_{\rm sat}^{\rm FG}}{2} \left(\frac{n_B}{n_{\rm sat}}\right)^{2/3} \left[(1+\delta)^{5/3} + (1-\delta)^{5/3}\right], \tag{2.9}$$

where $t_{\rm sat}^{\rm FG} = 3\hbar^2/(10m)(3\pi^2/2)^{2/3} n_{sat}^{2/3}$ is the kinetic energy per nucleon of SNM at $n_B = n_{\rm sat}$, and $m = (m_n + m_p)/2$ is the mean nucleon mass[3]. Taking into account the contribution from the non-locality and energy dependence of the nucleon self-energy, the nucleon bare mass is replaced by its effective mass [108], and the kinetic energy density, $\varepsilon_{\rm kin}$, can be written as:

$$\varepsilon_{\rm kin}(n_B, \delta) = n_B \frac{t_{\rm sat}^{\rm FG}}{2} \left(\frac{n_B}{n_{\rm sat}}\right)^{2/3} \left[(1+\delta)^{5/3} \frac{m}{m_n^*} + (1-\delta)^{5/3} \frac{m}{m_p^*}\right], \tag{2.10}$$

The parameterization of the Landau effective mass, m_q^*, with $q = n, p$ labeling neutrons and protons, reads

$$\frac{m}{m_q^*(n_B, \delta)} = 1 + (\kappa_{\rm sat} + \tau_3 \kappa_{\rm sym}\delta)(1 + 3x), \tag{2.11}$$

where $\tau_3 = 1$ ($\tau_3 = -1$) for neutrons (protons). In Eq. (2.11), we have introduced a new variable x, defined as:

$$x = \frac{n_B - n_{\rm sat}}{3n_{\rm sat}}, \tag{2.12}$$

and we can easily see that the value $x = 0$ corresponds to the saturation density, $n_B = n_{\rm sat}$. The difference in the neutron and proton effective masses is quantified by $\Delta m^* = m_n^* - m_p^*$. The two parameters, $\kappa_{\rm sat}$ and $\kappa_{\rm sym}$, can be expressed in terms of the effective mass and isospin

[2] In this section, n_p refers to the proton density in homogeneous matter, while in Sect. 2.1.2, $n_p = Z/V_{\rm WS}$.
[3] In the numerical code, m takes the value of neutron mass, $m \approx m_n$

splitting at saturation density, $m^*_{\rm sat} = m^*(n_B = n_{\rm sat}, \delta = 0)$, $\Delta m^*_{\rm sat} = \Delta m^*(n_B = n_{\rm sat}, \delta = 1)$, as:

$$\kappa_{\rm sat} = \frac{m}{m^*_{\rm sat}} - 1, \tag{2.13}$$

$$\kappa_{\rm sym} = \frac{1}{2}\left(\frac{m}{m^*_n} - \frac{m}{m^*_p}\right). \tag{2.14}$$

The potential term, $\mathcal{V} = \mathcal{V}^{\mathscr{N}}_{\rm MM}$, can be expressed as a Taylor expansion in x around $x = 0$, with x being defined in Eq. (2.12), truncated at order $\mathscr{N}$. As mentioned in Sect. 1.4, this expression is not a nuclear model, but it is a flexible parametrization that can be adjusted to microscopic nuclear models of both *ab-initio* and phenomenological families. In Ref. [64], it was shown that different nucleonic energy functionals at zero temperature can be well reproduced by truncating the expansion at order $\mathscr{N} = 4$. Therefore, we can write the potential term as:

$$\mathcal{V}(n_B, \delta) \approx \mathcal{V}^{\mathscr{N}=4}_{\rm MM}(n_B, \delta) = \sum_{k=0}^{4} \frac{n_B}{k!}(v^{\rm is}_k + v^{\rm iv}_k \delta^2) x^k u^{\mathscr{N}=4}_k(x), \tag{2.15}$$

where

$$u^{\mathscr{N}}_k(x) = 1 - (-3x)^{\mathscr{N}+1-k} \exp(-b(1+3x)). \tag{2.16}$$

This term was introduced to ensure convergence at the zero-density limit. The coefficient b is a parameter governing the function at low densities, and we usually take the value $b = 10\ln(2)$. An improved version of this correction was considered recently by Ref. [109], in which two parameters, $b_{\rm sat}$ and $b_{\rm PNM}$, were introduced in order to control separately the low-density behaviors of SNM and PNM. Particularly, to fix $b_{\rm sat}$ and $b_{\rm PNM}$, the authors performed a fit to the many-body perturbation theory (MBPT) calculations from Ref. [110] using different scaling methods. A significant difference in $b_{\rm sat}$ and $b_{\rm PNM}$ was found when the fit was conducted with equidistant grids in Fermi momentum k_F. On the other hand, the discrepancy between the two parameters is reduced if the fit was done with density grids. For the latter case, the value $b = 10\ln(2)$ is consistent with the 1σ levels of the parameter posterior distributions, $b_{\rm sat} = 9 \pm 5$ and $b_{\rm PNM} = 15 \pm 9$. In this work, we still keep the original version of meta-modeling, that is, with only one parameter b. Nevertheless, the improvement proposed by Ref. [109] could be taken into consideration for future works.

In Eq. (2.15), the parameters $v^{\rm is}_k$ and $v^{\rm iv}_k$ are linear combinations of the so-called nuclear matter empirical parameters, which are the successive derivatives with respect to x at $x = 0$ (equivalently, at the saturation density) of the nuclear matter energy per nucleon of SNM, ($E_{\rm sat}$, $K_{\rm sat}$, $Q_{\rm sat}$, $Z_{\rm sat}$), and symmetry energy, defined as the difference between the PNM and SNM energy per nucleon, ($E_{\rm sym}$, $L_{\rm sym}$, $K_{\rm sym}$, $Q_{\rm sym}$, $Z_{\rm sym}$):

$$X_{{\rm sat},k} = \left.\frac{d^k e_{\rm SNM}}{dx^k}\right|_{x=0}, \tag{2.17}$$

$$X_{{\rm sym},k} = \left.\frac{d^k (e_{\rm PNM} - e_{\rm SNM})}{dx^k}\right|_{x=0}. \tag{2.18}$$

The relations between the isoscalar parameters $v_k^{\rm is}$ with the corresponding empirical parameters are given by:

$$v_0^{\rm is} = E_{\rm sat} - t_{\rm sat}^{\rm FG}(1+\kappa_{\rm sat}), \tag{2.19}$$
$$v_1^{\rm is} = -t_{\rm sat}^{\rm FG}(2+5\kappa_{\rm sat}), \tag{2.20}$$
$$v_2^{\rm is} = K_{\rm sat} - 2t_{\rm sat}^{\rm FG}(-1+5\kappa_{\rm sat}), \tag{2.21}$$
$$v_3^{\rm is} = Q_{\rm sat} - 2t_{\rm sat}^{\rm FG}(4-5\kappa_{\rm sat}), \tag{2.22}$$
$$v_4^{\rm is} = Z_{\rm sat} - 8t_{\rm sat}^{\rm FG}(-7+5\kappa_{\rm sat}). \tag{2.23}$$

Similarly, for the isovector parameters, we have:

$$v_0^{\rm iv} = E_{\rm sym} - \frac{5}{9}t_{\rm sat}^{\rm FG}[1+(\kappa_{\rm sat}+3\kappa_{\rm sym})], \tag{2.24}$$
$$v_1^{\rm iv} = L_{\rm sym} - \frac{5}{9}t_{\rm sat}^{\rm FG}[2+5(\kappa_{\rm sat}+3\kappa_{\rm sym})], \tag{2.25}$$
$$v_2^{\rm iv} = K_{\rm sym} - \frac{10}{9}t_{\rm sat}^{\rm FG}[-1+5(\kappa_{\rm sat}+3\kappa_{\rm sym})], \tag{2.26}$$
$$v_3^{\rm iv} = Q_{\rm sym} - \frac{10}{9}t_{\rm sat}^{\rm FG}[4-5(\kappa_{\rm sat}+3\kappa_{\rm sym})], \tag{2.27}$$
$$v_4^{\rm iv} = Z_{\rm sym} - \frac{40}{9}t_{\rm sat}^{\rm FG}[-7+5(\kappa_{\rm sat}+3\kappa_{\rm sym})]. \tag{2.28}$$

For the detailed derivation, see Sect. III in Ref. [64]. Values of the empirical parameters for some nuclear functionals are listed in Table 2.1.

The δ-dependence of the nuclear matter energy density is usually expressed in the parabolic approximation, $\varepsilon_B(n_B,\delta) \approx \varepsilon_B(n_B,\delta=0) + \frac{1}{2}\frac{\partial^2\varepsilon_B}{\partial\delta^2}\Big|_{\delta=0}\delta^2$. However, one can notice that $\varepsilon_B(n_B,\delta)$ in the meta-modeling approach, Eq. (2.6), is not purely quadratic in the isospin-asymmetry expansion due to the non-parabolic behaviors in the kinetic term, see Eq. (2.10). Generally, extra non-quadratic terms can also come from nuclear interactions. In Ref. [109], which performed a fit to the MBPT results by Ref. [110] as mentioned above, it was shown that the non-quadratic contributions in the nuclear matter energy originate mainly from the kinetic energy, and they represent a correction of about $3-5\%$ to the symmetry energy. Moreover, the authors also found a correction of around 5% in the crust-core transition density when the non-quadratic terms are included. Even though the correction is relatively small, these contributions are necessary for a precise determination of the crust-core boundary (see Ref. [109] for detailed discussions). In addition, the high-order terms of the δ expansion were recently extracted by Ref. [111] using chiral EFT nuclear interactions including two-body and three-body forces. They found that fourth-order terms could impact the proton fraction of beta-equilibrated nuclear matter at $n_B \approx 2n_{\rm sat}$, thus highlighting the importance of going beyond the parabolic approximation in the isospin asymmetry in studying the NS cores.

The expression in Eq. (2.15) together with the empirical parameters given in Table 2.1 correspond to the *empirical local density functional (ELF)–version c* (ELFc) of Ref. [64] (see Eq. (40) and Tables X-XI of the referred paper). If the metamodel is used in order to reproduce a give reference model, then the technique ELFc reproduces well the reference model up to $2-3n_{\rm sat}$, while the convergence is not sufficient at higher densities (see Fig. 5 of Ref. [64]). In principle, the performance at densities far from the saturation point can be

improved by increasing the expansion order $\mathscr{N}$. However, it was remarked by Ref. [64] that the absolute values of the empirical parameters increase with the expansion order and that the third- and fourth-order parameters have opposite signs. Consequently, one would need plenty of higher-order derivatives, and the convergence would be lengthy. In order to have a better convergence of the metamodel at high densities without adding new terms into the Taylor series, the higher-order parameters $Q_{\rm sat,sym}$ and $Z_{\rm sat,sym}$ are readjusted by fitting them to the reference EOS at a high-density point. This version of the metamodel is referred to as ELFd (see Sect. III.E and Table XIII in Ref. [64]). The latter modification is necessary whenever the high-density part of the EOS is involved, such as in computing the NS mass-radius relation. At variance with that, if only the crust is studied, the metamodel leads to a better reproduction of the reference models if the ELFc technique is employed (that is, the model parameters are fixed only by the derivatives at saturation). Unless it is explicitly stated, ELFc is our default model.

Table 2.1: Bulk parameters used in the Taylor expansion of ELFc metamodel [64] to reproduce the low-density behavior of symmetric matter and pure neutron matter of the effective models BSk24 and BSk25 [112], SLy4 [113], RATP [114], NRAPR [115], DD-ME2 [116], DD-MEδ [117], FSU [118], NL3 [119], PKDD [120], and TM1 [91]. Table adapted from Ref. [121].

	$n_{\rm sat}$ ($\rm fm^{-3}$)	$E_{\rm sat}$ (MeV)	$E_{\rm sym}$ (MeV)	$L_{\rm sym}$ (MeV)	$K_{\rm sat}$ (MeV)	$K_{\rm sym}$ (MeV)	$Q_{\rm sat}$ (MeV)	$Q_{\rm sym}$ (MeV)	$Z_{\rm sat}$ (MeV)	$Z_{\rm sym}$ (MeV)
BSk24	0.1578	-16.05	30.00	46.4	245.5	-37.6	-274.5	710.9	1184.2	-4031.3
BSk25	0.1587	-16.03	29.00	36.9	236.0	-28.5	-316.5	885.9	1355.0	-4919.9
SLy4	0.1595	-15.97	32.01	46.0	230.0	-120.0	-363.0	521.0	1587.0	-3197.0
RATP	0.1598	-16.05	29.26	32.4	240.0	-191.0	-350.0	440.0	1452.0	-2477.0
NRAPR	0.1606	-15.85	32.78	59.7	226.0	-123.0	-363.0	312.0	1611.0	-1838.0
DD-ME2	0.1520	-16.14	32.31	51.3	251.0	-87.0	479.0	777.0	4448.0	-7048.0
DD-MEδ	0.1520	-16.12	32.35	52.8	219.0	-118.0	-748.0	846.0	3950.0	-3545.0
FSU	0.1480	-16.30	32.50	60.5	230.0	-51.3	-526.6	434.2	2839.9	-6408.0
NL3	0.1480	-16.24	37.35	118.3	271.0	101.0	198.0	182.0	9302.0	-3961.0
PKDD	0.1495	-16.27	31.19	79.5	261.0	-50.0	-119.0	-28.0	4213.0	-1315.0
TM1	0.1450	-16.26	36.94	111.0	281.0	34.0	-285.0	-67.0	2014.0	-1546.0

Once we have the energy density, other quantities, such as the nucleon chemical potential and pressure, can be obtained directly from thermodynamic relations. For the former, we have:

$$\mu_{{\rm HM},q}(n_B,\delta) = \left(\frac{\partial \varepsilon_B}{\partial n_q}\right)_{n_{q'}} + m_q c^2, \tag{2.29}$$

where the partial derivatives with respect to the density n_q of particles of type q are computed keeping the density of the other species $n_{q'}$ constant. Additionally, it is worth noting that $\mu_{{\rm HM},q}$ includes the nucleon rest mass. We can easily show that Eq. (2.29) is equivalent to:

$$\mu_{{\rm HM},q}(n_B,\delta) = e_B + n_B \left(\frac{\partial e_B}{\partial n_q}\right)_{n_{q'}} + m_q c^2. \tag{2.30}$$

Likewise, in terms of x and δ:

$$\mu_{\mathrm{HM},q}(n_B,\delta) = e_B + \frac{1+3x}{3}\left(\frac{\partial e_B}{\partial x}\right)_\delta + (\tau_3-\delta)\left(\frac{\partial e_B}{\partial \delta}\right)_x + m_q c^2. \tag{2.31}$$

Finally, the nuclear pressure can be calculated from

$$P_B(n_B,\delta) = \sum_{q=n,p} n_q(\mu_{\mathrm{HM},q}(n_B,\delta) - m_q c^2) - \varepsilon_B(n_B,\delta). \tag{2.32}$$

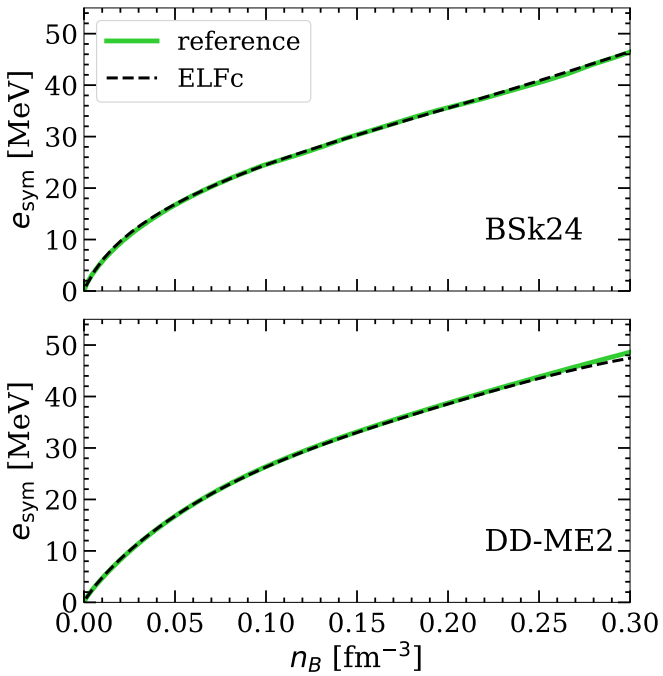

Figure 2.1: Symmetry energy, $e_{\mathrm{sym}}(n_B)$, as a function of the total nuclear matter density n_B obtained for the BSk24 (top panel) and DD-ME2 (bottom panel) functionals within the meta-modeling ELFc approach (dashed black lines). The solid green line shows the reference values from the original BSk24 [75, 112] and DD-ME2 [116] models.

To demonstrate the performance of the meta-modeling technique, in Fig. 2.1, I show the symmetry energy, $e_{\mathrm{sym}}(n_B) = e_{\mathrm{PNM}}(n_B) - e_{\mathrm{SNM}}(n_B)$, as a function of the total nuclear matter density n_B for the original (solid green lines) BSk24 [112] (top panel) and DD-ME2 [116] (bottom panel) in comparison with those obtained in meta-modeling ELFc approach (dashed black lines) for the same functionals. We can see that the metamodels overlap very well with the result of the original functionals, even in the region close to zero density. Furthermore, not only the meta-modeling approach can mimic the behaviors of original models with high precision, but it also has several interesting advantages: (i) no *a priori* correlations between the empirical parameters are imposed, hence allowing all arbitrary density dependence to be explored; (ii) the effects of different parameters can be studied independently of each other; (iii) the mapping between the uncertainties on the empirical parameters and EOS can be done with the Bayesian analysis, which will be shown in the last section of this chapter.

The SNM and PNM energy per nucleon, e_{SNM} and e_{PNM}, as a function of density for

some functionals[4] listed in Table 2.1 are depicted in Fig. 2.2. The orange bands are the corresponding results produced by the MBPT calculations from Ref. [110], based on two- and three-nucleon chiral EFT interactions at the next-to-next-to-next-to-leading order. In the mentioned work, the authors considered seven different Hamiltonians and the bands were obtained by extracting the maximal spread of the results.

For SNM (left panel), we can see that the models agree quite well at low densities up to the saturation, and the difference among them is narrower than the uncertainty of the *ab initio* calculation. Moreover, their predictions of the saturation density and energy, i.e., the position and value of $\min(e_{\rm SNM})$, are almost the same. This is because this information on SNM is relatively well-known from various nuclear physics experiments, such as mass measurements and electron scattering in finite nuclei. At higher densities, the discrepancies in the predictions of these models become more pronounced, especially for non-linear couplings models such as NL3 and TM1 which result in much higher $e_{\rm SNM}$ mainly because of their high values of $K_{\rm sat}$.

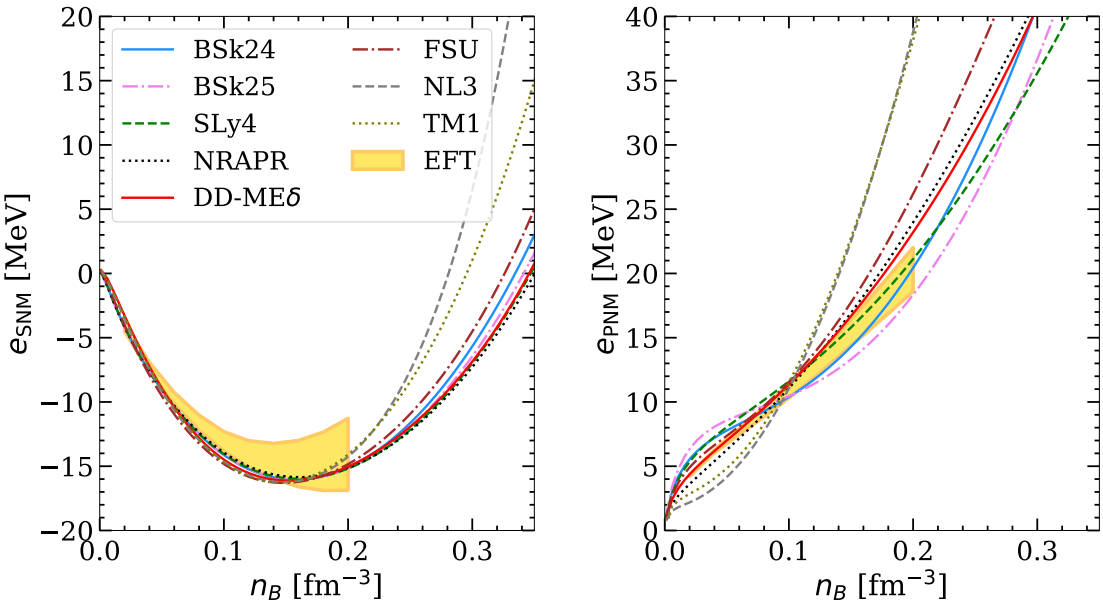

Figure 2.2: Energy per nucleon of symmetric nuclear matter (left panel) and pure neutron matter (right panel) for some nuclear functionals. The orange bands represent the MBPT calculation with chiral interactions by Drischler *et al.* 2016 [110].

On the other hand, due to the lack of information in the isovector channel, the uncertainty in $e_{\rm PNM}$ is very large compared to the EFT band (see the right panel). Among the models considered, BSk24 and SLy4 are compatible with the uncertainty band at high densities, while at low densities the band is very thin and it is DD-MEδ that has the best agreement. Similar to the case of symmetric matter, the behaviors of NL3 and TM1 are noticeably stiffer with respect to the rest. This can be expected because these models not only have very large $L_{\rm sym}$, but they have positive $K_{\rm sym}$ while others have negative $K_{\rm sym}$.

Similar behavior is observed with the nuclear matter pressure as shown in Fig. 2.3. The

[4]If it is not mentioned otherwise, whenever I refer to a functional in the results, I indicate the corresponding meta-modeling version, not the original one.

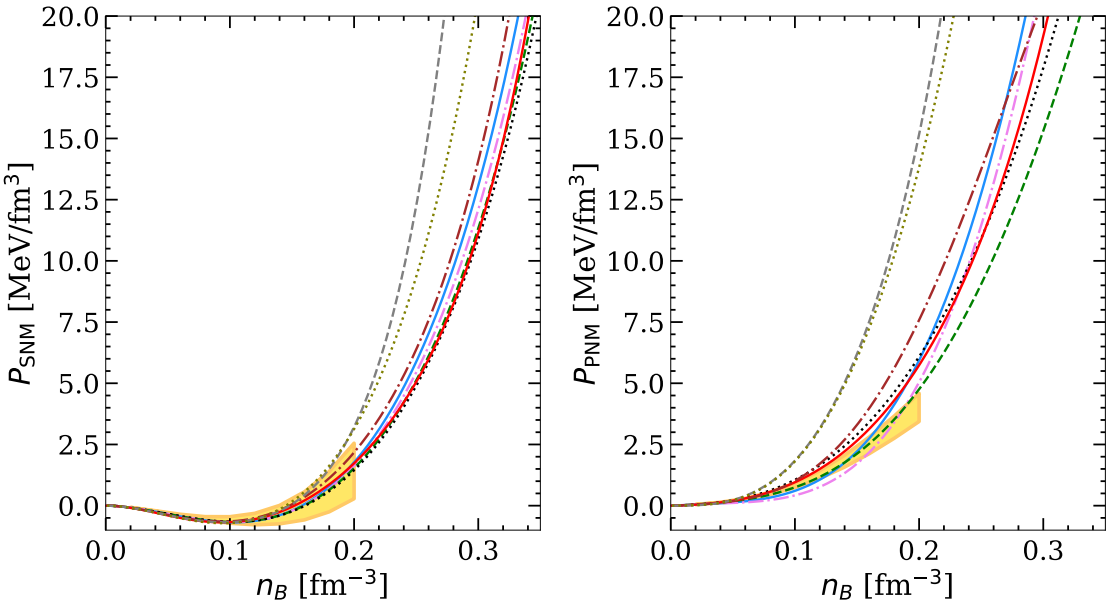

Figure 2.3: Same as Fig. 2.2 but for the pressure.

different behaviors of the models concerning the nuclear-matter energy and pressure will reflect in the different results on the NS properties, as it will be discussed in the following sections.

2.1.1.2 Leptonic matter

In this section, I present the expressions of leptonic matter in a NS core, i.e., electrons and muons. At zero temperature, the relativistic lepton energy density is given by

$$\varepsilon_l = \frac{c}{\pi^2}\int_{k=0}^{k_{F_l}} dk k^2 \sqrt{\hbar^2 k^2 + m_l^2 c^2}, \tag{2.33}$$

where $l = e, \mu$, $\hbar$ is the reduced Planck constant, m_l is the lepton mass, and $k_{F,l}$ is the lepton Fermi wave number. Let $x = \hbar k/(m_e c)$, Eq. (2.33) can be rewritten as

$$\varepsilon_l = \frac{m_l^4 c^5}{\pi^2 \hbar^3}\int_{x=0}^{x_r} dx x^2 \sqrt{x^2+1}, \tag{2.34}$$

where $x_r = \hbar k_{F_l}/(m_l c)$. Integrating Eq. (2.34) by part leads to

$$\varepsilon_l(n_l) = \frac{P_r}{8\pi^2}\left[x_r(2x_r^2+1)\gamma_r - \ln(x_r+\gamma_r)\right], \tag{2.35}$$

in which $\gamma_r = \sqrt{x_r^2+1}$ and $P_r = \frac{m_l^4 c^5}{\hbar^3}$.

Then, the lepton pressure can be calculated using

$$\begin{aligned} P_l &= n_l \frac{\partial \varepsilon_l}{\partial n_l} - \varepsilon_l \\ &= \frac{P_r}{8\pi^2}\left[x_r\left(\frac{2}{3}x_r^2 - 1\right)\gamma_r + \ln(x_r+\gamma_r)\right]. \end{aligned} \tag{2.36}$$

Eqs. (2.35) and (2.36) are respectively equivalent to Eqs. (2.65) and (2.67) in Ref. [1] at the zero-temperature limit.

Finally, the lepton chemical potential can be found with

$$\mu_l = \frac{P_l + \varepsilon_l}{n_l}. \tag{2.37}$$

2.1.1.3 Core composition

In order to determine the composition and EOS of the core, as I have mentioned before, the total energy density of the system, defined in Eq. (2.1), has to be minimized at each given n_B, given that the charge neutrality holds (Eq. (2.4)). To this aim, we introduce a Lagrange multiplier λ_c, and the function to be minimized can be written as

$$\Omega_c = \varepsilon_B(n_B,\delta)+\varepsilon_e(n_e)+\varepsilon_\mu(n_\mu)+n_B\frac{1-\delta}{2}(m_p-m_n)c^2+n_Bm_nc^2+\lambda_c\left(n_B\frac{1-\delta}{2}-n_e-n_\mu\right). \tag{2.38}$$

Taking the derivative of Ω_c with respect to n_e we get:

$$\lambda_c = \frac{\partial\varepsilon_e}{\partial n_e} = \mu_e. \tag{2.39}$$

As we go deeper to the center of a NS, the electron density, hence chemical potential, increases. If the electron chemical potential μ_e exceeds the muon rest-mass energy $m_\mu c^2$, i.e., $\mu_e \geq m_\mu c^2$, then muons appear. In that case, Ω_c needs to be minimized with respect to the muon density n_μ also, and we obtain:

$$\lambda_c = \frac{\partial\varepsilon_\mu}{\partial n_\mu} = \mu_\mu. \tag{2.40}$$

Therefore, from Eqs. (2.39) and (2.40), we have the chemical potential equality:

$$\mu_e = \mu_\mu. \tag{2.41}$$

Finally, the minimization of Ω_c with respect to the core isospin asymmetry δ gives:

$$\left.\frac{\partial\Omega_c}{\partial\delta}\right|_{n_e,n_\mu} = 0, \tag{2.42}$$

$$2\frac{\partial\varepsilon_B}{\partial\delta} - n_B(m_p-m_n)c^2 - n_B\mu_e = 0. \tag{2.43}$$

Using

$$\frac{\partial\varepsilon_B}{\partial\delta} = \frac{\partial\varepsilon_B}{\partial n_p}\frac{\partial n_p}{\partial\delta} + \frac{\partial\varepsilon_B}{\partial n_n}\frac{\partial n_n}{\partial\delta}, \tag{2.44}$$

$$= \frac{n_B}{2}(-\mu_{\mathrm{HM},p} + m_pc^2 + \mu_{\mathrm{HM},n} - m_nc^2). \tag{2.45}$$

Equations (2.43) and (2.45) lead to the equation of beta equilibrium:

$$\mu_{\mathrm{HM},n} = \mu_e + \mu_{\mathrm{HM},p}. \tag{2.46}$$

Note that the nucleon chemical potentials include the nucleon rest masses (see Eq. (2.29)). Finally, it is easy to see that the total pressure of a homogeneous system equals to the sum of all components:

$$P = P_B(n_B, \delta) + P_e(n_e) + P_\mu(n_\mu), \tag{2.47}$$

where P_B and $P_{e,\mu}$ are given respectively by Eqs. (2.32) and (2.36).

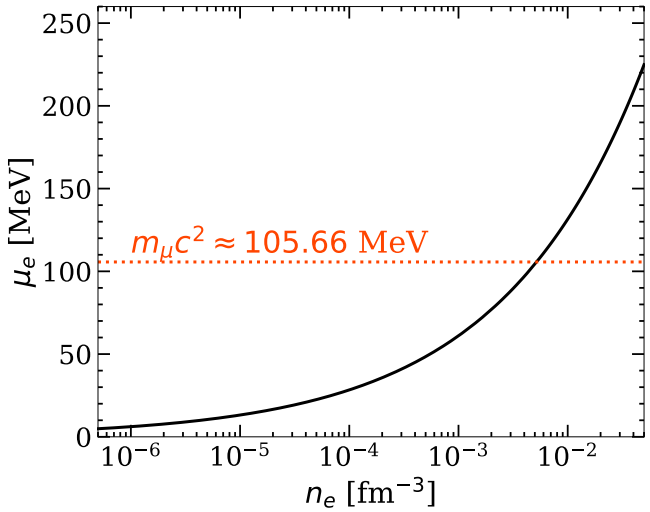

Figure 2.4: Evolution of the electron chemical potential μ_e as a function of the electron density n_e at zero temperature (solid black line). The horizontal dotted orange line indicates the value of the muon rest-mass energy $m_\mu c^2$.

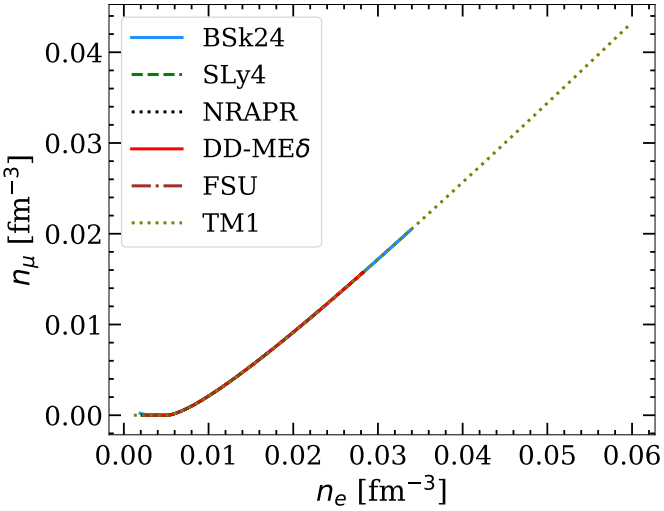

Figure 2.5: Muon density n_μ versus electron density n_e found in the NS core for different models.

Numerically, first, Eqs. (2.4) and (2.46) are solved without muons, i.e., $n_\mu = 0$, and the outputs are n_e and δ. Then, the corresponding electron chemical potential μ_e is calculated and compared with the muon rest-mass energy $m_\mu c^2$. If $\mu_e \geq m_\mu c^2$, Eq. (2.41) is added into the system of equations to be solved. This process is continued until the causality condition in the core is violated.

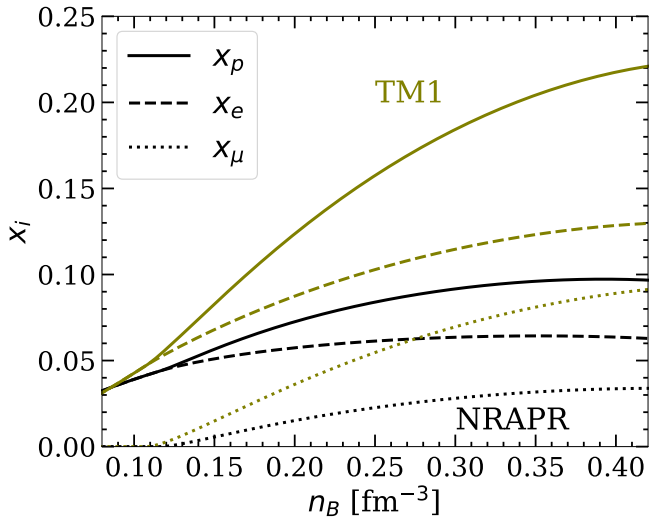

Figure 2.6: The proton fraction x_p (solid lines), electron fraction x_e (dashed lines), and muon fraction x_μ (dotted lines) as a function of the total baryon number density n_B in the NS core. Two models are considered: TM1 (olive) and NRAPR (black).

The comparison between the electron chemical potential and the muon rest-mass energy is plotted in Fig. 2.4. We can see that muons appear when the electron density exceeds approximately 5×10^{-3} fm^{-3}. Indeed, this can be observed in the equilibrium compositions obtained for different models as shown in Fig. 2.5. The relation between n_e and n_μ is governed solely by the chemical equilibrium in Eq. (2.41). Thus, it is not surprising that the result in Fig. 2.5 is not model dependent.

The model dependence is exhibited clearly when the compositions are plotted against the total baryon number density n_B, as in Fig. 2.6. Particularly, the proton fraction x_p (solid lines), electron fraction x_e (dashed lines), and muon fraction x_μ (dotted lines) are shown as a function of n_B for models TM1 (olive) and NRAPR (black). These quantities are defined as follows:

$$x_p = \frac{n_p}{n_B} = \frac{1-\delta}{2}, \tag{2.48}$$

$$x_e = \frac{n_e}{n_B}, \tag{2.49}$$

$$x_\mu = \frac{n_\mu}{n_B}. \tag{2.50}$$

The figures suggest that muons appear at $n_B \approx 0.12$ fm^{-3}, and this result does not differ significantly between the two models. On the other hand, the fractions x_i, where $i = p, e, \mu$, in TM1 is noticeably higher than those in NRAPR. It was pointed out by Ref. [122] that the proton fraction x_p is correlated with the symmetry energy $e_{\rm sym}$. Indeed, this statement is intuitively understandable because more energy is required for matter to be asymmetric in models with higher symmetry energy. As we can infer from Fig. 2.2, at $n_B \gtrsim 0.1$ fm^{-3}, the symmetry energy in TM1 is larger than that in NRAPR. As a result, x_p, hence x_e and x_μ (as $x_p = x_e + x_\mu$), found for TM1 are greater than those for NRAPR.

2.1.2 Inhomogeneous matter in NS crust

In the NS crust ground state, nuclei are arranged in a body-centered cubic (bcc) lattice structure [1, 123], surrounded by a uniform background of free electrons and neutrons of densities n_e and n_{gn}. In the outer crust, there are no free neutrons, therefore, $n_{gn} = 0$. The lattice can be divided into identical unit cells, called Wigner-Seitz (WS) cells [124], with one nucleus of mass number A, proton number Z, radius r_N, and density n_i located in the center. The volume of each WS cell, $V_{\rm WS}$, is determined such that the cell is neutral:

$$V_{\rm WS} = \frac{Z}{n_p}, \tag{2.51}$$

where $n_p = n_e$ is the overall proton density in each cell. Due to the charge neutrality in each cell, the Coulomb interaction between different cells, originated from quadrupole and higher moments, can be neglected in the first approximation [9].

As mentioned in Sect. 1.2, at the bottom of the crust, the so-called "pasta" phases can appear. A thorough study on the pasta phase will be discussed in Chapter 3. However, the pasta mantle is expected to constitute a very thin layer in the inner crust and thus to have a negligible impact on static NS global properties, which is the main focus of this chapter. Thus, for all the results presented in the present chapter, we assume that nuclei in the NS crust are always spherical and denser than the surrounding neutron background.

In this work, we employ an effective macroscopic approach, which is the CLDM to describe the cluster energy, as in the seminal work by Ref. [9]. Within this approach, the cluster binding energy can be decomposed into bulk, Coulomb, surface and curvature terms, and the total cluster energy[5] E_i is written as follows:

$$E_i = (A - Z)m_n c^2 + Z m_p c^2 + E_{\rm bulk} + E_{\rm Coul+surf+curv}, \tag{2.52}$$

where $E_{\rm bulk} = \frac{A}{n_i}\varepsilon_B(n_i, I)$, with $\varepsilon_B(n_i, I)$ being energy density of nuclear matter inside the cluster at density n_i and isospin asymmetry $I = (A - 2Z)/A$ (see Sect. 2.1.1.1), and $E_{\rm Coul+surf+curv} = V_{\rm WS}(\varepsilon_{\rm Coul}+\varepsilon_{\rm surf}+\varepsilon_{\rm curv})$ is the total finite-size contribution (see Sect. 2.1.2.1). At each given total baryonic density n_B, the total energy density in each WS cell can be written as:

$$\varepsilon_{\rm WS} = \varepsilon_e + \varepsilon_{\rm g}(1 - u) + \frac{E_i}{V_{\rm WS}}, \tag{2.53}$$

where ε_e is given in Eq. (2.35), u is the ratio of the cluster volume V_N to the WS cell volume $V_{\rm WS}$, $u = \frac{V_N}{V_{\rm WS}}$, $\varepsilon_{\rm g} = \varepsilon_B(n_{gn}, 1) + n_{gn}m_n c^2$ is the energy density of the neutron background including the neutron rest mass.

The CLDM has been widely used to describe the NS crust in several works [125–127] (see also [1, 7, 58] for a review). Even though this approach is not microscopic as a full density functional treatment and it treats clusters as classical degrees of freedom, CLDM has recently proved to provide results in good agreement with those obtained with the still (semi) classical, but microscopic ETF calculations both at zero (see Ref. [78]) and finite temperature (see Ref. [79]). Particularly, in the former case, it was shown that the thermodynamic quantities such as pressure, energy, and chemical potential, as well as the electron fraction found in

[5] I use captial letter E to indicate the energy per cell.

CLDM overlap very well with the fourth-order ETF and even ETFSI, where quantum shell corrections are accounted for. Moreover, as it was mentioned in Ref. [122], the CLDM is numerically inexpensive. As a result, it can be implemented in a statistical study with low numerical cost (see Sect. 2.3). Additional, the CLDM allows a decomposition of the cluster energy in different terms (such as bulk and finite-size terms) which simplifies the assessment of the impact of each contribution to the total energy. Finally, it will be a great asset to perform complex multi-component calculations, as I will discuss in Chapter 4.

I detail the interface energy, namely, the Coulomb, surface, and curvature energy in Sect. 2.1.2.1. Then, I review the derivation of the equilibrium equations of the crust in Sect. 2.1.2.2.

2.1.2.1 Interface energy

The Coulomb term gives the electrostatic proton-proton, proton-electron, and electron-electron interaction energy. In the WS approximation, the Coulomb energy density reads:

$$\varepsilon_{\rm Coul} = 2\pi \left(e y_p n_i r_N\right)^2 u \eta_{\rm Coul}(u), \tag{2.54}$$

where e is the elementary charge, $y_p = \frac{Z}{A}$ is the cluster proton fraction. Assuming a spherical geometry for the WS cell, the function $\eta_{\rm Coul}(u)$ accounting for the electron screening can be written as [12, 128]:

$$\eta_{\rm Coul}(u) = \frac{1}{5}\left[u + 2\left(1 - \frac{3}{2}u^{1/3}\right)\right]. \tag{2.55}$$

The detailed derivation of the Coulomb energy is presented in Appendix A. Regarding the surface and curvature energies, we employ the expression of Refs. [90, 129–132]:

$$\varepsilon_{\rm surf} + \varepsilon_{\rm curv} = \frac{3u}{r_N}\left(\sigma_{\rm s}(I, T=0) + \frac{2\sigma_{\rm c}(I, T=0)}{r_N}\right), \tag{2.56}$$

where $\sigma_{\rm s}$ ($\sigma_{\rm c}$) are the surface (curvature) tension, and $I = 1 - 2y_p$ is the cluster isospin asymmetry. At zero temperature, we adopt the expressions of $\sigma_{\rm s}(I, T=0)$ and $\sigma_{\rm c}(I, T=0)$ from Refs. [131–134], based on Thomas-Fermi calculations at extreme isospin asymmetries:

$$\sigma_{\rm s}(I, T=0) = \sigma_0 \frac{2^{p+1} + b_s}{y_p^{-p} + b_s + (1-y_p)^{-p}}\ , \tag{2.57}$$

$$\sigma_{\rm c}(I, T=0) = 5.5\,\sigma_s(I, T=0)\frac{\sigma_{0,\rm c}}{\sigma_0}(\beta - y_p)\ , \tag{2.58}$$

where the parameters $(\sigma_0, \sigma_{0,c}, b_s, \beta, p)$ can be optimized for each given density functional of energy to reproduce the experimental nuclear masses in the Atomic Mass Evaluation (AME) 2016 [135].

In vacuum, the nuclear mass of a spherical fully ionized atom of charge Z and mass number A can be deduced using Eqs. (2.6), (2.54), and (2.56) as:

$$\begin{aligned} M(A,Z)c^2 = {} & m_p c^2 Z + m_n c^2 (A-Z) \\ & + \frac{A}{n_0}\varepsilon_B(n_0, I) + 4\pi r_N^2\left(\sigma_s + \frac{2\sigma_c}{r_N}\right) \\ & + \frac{3}{5}\frac{e^2 Z^2}{r_N}, \end{aligned} \tag{2.59}$$

where bulk density n_0 is given by the equilibrium density of nuclear matter at isospin asymmetry I, defined by $\partial e_B/\partial n|_{I,n=n_0} = 0$, and is given by Ref. [136]:

$$n_0 \approx n_{\rm sat}\left(1 - \frac{3L_{\rm sym}I^2}{K_{\rm sat} + K_{\rm sym}I^2}\right). \tag{2.60}$$

The theoretical binding energy per nucleon can be inferred from Eq. (2.59), that is,

$$B_{\rm theo}(A,Z) = e_B(n_0,I) + \frac{1}{A}\left[4\pi r_N^2\left(\sigma_s + \frac{2\sigma_c}{r_N}\right) + \frac{3}{5}\frac{e^2Z^2}{r_N}\right]. \tag{2.61}$$

In previous applications of Eq. (2.56) on the NS crust and supernova modeling within the compressible liquid drop approximation [90, 131, 134, 137–139], the surface parameters were fixed on Thomas-Fermi or Hartree-Fock calculations, independently of the bulk functional. However, both bulk and surface terms must be specified to variationally obtain the matter composition, and they are clearly correlated notably by the constraint of reproducing the nuclear mass, which is experimentally known for a large panel of nuclei in the vacuum. For this reason, in this work, we include the uncertainty on the surface energy by adding $(\sigma_0, \sigma_{0,c}, b_s, \beta, p)$ to our parameter space. Following Ref. [122], for each given energy functional, the associated surface parameters are determined by a χ^2-fit of the binding energies per nucleon in Eq. (2.61) to the experimental values[6], $B_{\rm exp}$, in the atomic mass table AME2016 [135], as mentioned above. Here, the correction from the electron binding energy per nucleon $B_e(Z)/A$, with $B_e(Z)$ given Eq. (2) of Ref. [135], is not included in $B_{\rm exp}$. This is because the correction from the electron binding energy is negligible compared to the nuclear binding energy ($\sim 0.02\%$, on average), and therefore, it does not impact the outcomes of the fit. Among the surface parameters, a well-defined minimum could not be obtained for the parameter p. The reason is that p governs the behavior of the surface tension at extreme isospin values, while nuclei in the experimental mass table are quite symmetric, with $I \lesssim 0.3$. Therefore, if it is not specifically mentioned, p is fixed to $p = 3$. This value was chosen to reproduce the crust-core transition points for different functionals [59, 122, 127], as estimated from the spinodal method [140].

Table 2.2: Optimized surface and curvature parameters with their absolute uncertainties for different functionals: BSk24, SLy4, DD-MEδ, and FSU, fitted to the AME2016 mass table. Parameter p is fixed, $p = 3$. The last column is the value of penalty function per degree of freedom, χ^2.

	σ_0 (MeV/fm^2)	b_s	$\sigma_{0,c}$ (MeV/fm)	β	χ^2
BSk24	1.05021 ± 0.00113	30.32168 ± 0.36424	0.12147 ± 0.00370	0.6649 ± 0.00625	1.02857
SLy4	0.98911 ± 0.00133	19.02416 ± 0.26103	0.15141 ± 0.00434	0.75548 ± 0.00802	1.33741
DD-MEδ	1.08212 ± 0.00112	19.74375 ± 0.22250	0.11813 ± 0.00364	0.55971 ± 0.00432	0.81496
FSU	1.17734 ± 0.00110	21.18512 ± 0.22729	0.09335 ± 0.00357	0.28396 ± 0.00961	0.659508

In Fig. 2.7, I display the relative error in nuclear binding energy per nucleon between CLDM and the experimental value, $\frac{B_{\rm theo}-B_{\rm exp}}{B_{\rm exp}}$, as a function of neutron number N for four

[6]The binding energy per nucleon values in the AME2016 table [135] are given in positive values. However, in the numerical code, since $B_{\rm theo}$ defined in Eq. (2.61) is negative, one needs to make sure that $B_{\rm exp}$ also carries the negative sign.

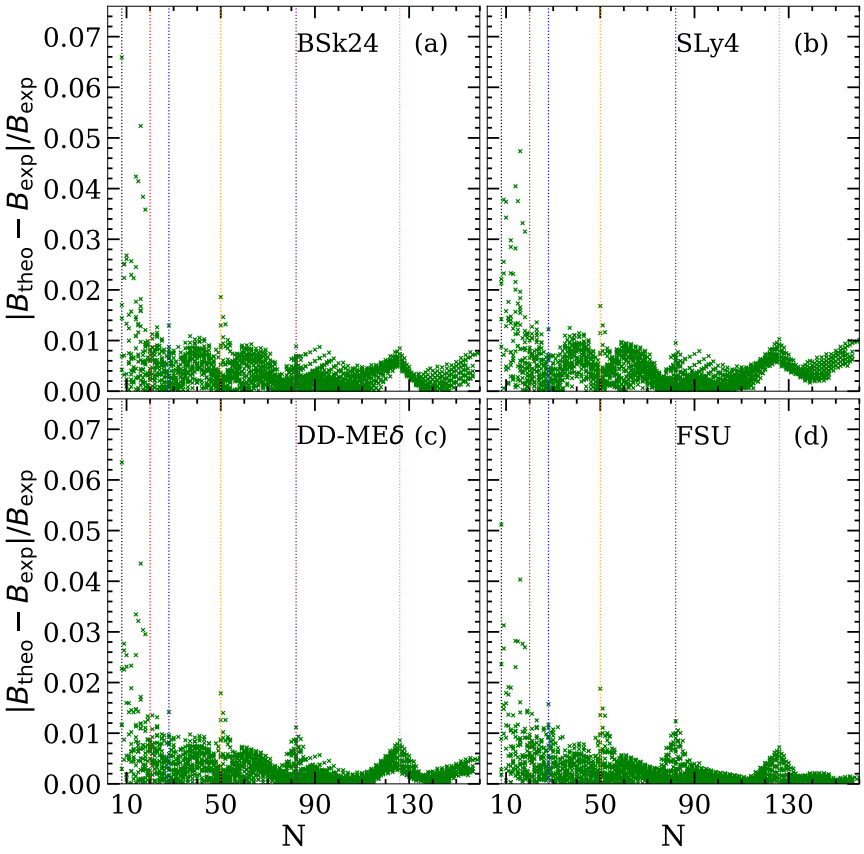

Figure 2.7: The relative error in the binding energy per nucleon in the theoretical calculation within the CLDM approach compared to the experimental values in the AME2016 table [135] as a function of neutron number N for four different functionals. The vertical dotted lines indicate the magic numbers, $N = 8, 20, 28, 50, 82, 126$, from left to right in each panel.

different models. The surface parameters for these models are listed in Table 2.2. The penalty function per degree of freedom[7] for the fit is defined as follows [141]:

$$\chi^2 = \frac{1}{N_{\rm dof}} \sum_{i=1}^{N_d} \frac{(B^{(i)}_{\rm theo} - B^{(i)}_{\rm exp})^2}{\Delta B_i^2}, \tag{2.62}$$

where N_d is the number of data points. In our case, the fit was performed for $N_d = 2408$ nuclei with $N, Z \geq 8$. Moreover, in Eq. (2.62), ΔB_i is the adopted error, and it accounts for theoretical, experimental, and numerical errors:

$$\Delta B_i^2 = \Delta B_{i,\rm theo}^2 + \Delta B_{i,\rm exp}^2 + \Delta B_{i,\rm num}^2. \tag{2.63}$$

In the AME2016 mass table, $\Delta B_{i,\rm exp} \approx 0.5$ eV, and therefore it can be neglected. Assuming that the numerical error is small, then $\Delta B_i^2 \approx \Delta B_{i,\rm theo}^2$. In principle, $\Delta B_{i,\rm theo}$ can vary with A and Z. However, in our model, this error is assumed to be the same for all nuclei. Additionally, in statistical analysis, it is required that the average χ^2 needs to be normalized

[7]The number of degrees of freedom is defined as, $N_{\rm dof} = N_d - N_p$, with N_d (N_p) being the number of data points (parameters in the fit). In our case, we are fitting 4 surface parameters to 2408 data points in the AME2016 mass table (we only fit for nuclei with $N, Z \geq 8$). As a result, $N_{\rm dof} = 2408 - 4 = 2404$.

to 1. Thus, we have chosen $|\Delta B_i| = |\Delta B_{i,\text{theo}}| = 0.04$ MeV as an average estimation of the systematic theoretical error.

As it is shown in Fig. 2.7, for all models considered, the experimental nuclear masses are reproduced very well, and the relative error is typically below 1%. At low N, we can see that the error becomes more significant, $\sim 7\%$, showing the limitation of CLDM in describing light nuclei. Furthermore, one can also observe some peaks whose positions coincide with the neutron magic numbers, $N = 8, 20, 28, 50, 82, 126$. This is not surprising because shell effects are not included in our formalism; nevertheless, the relative errors remains small, typically around 1%.

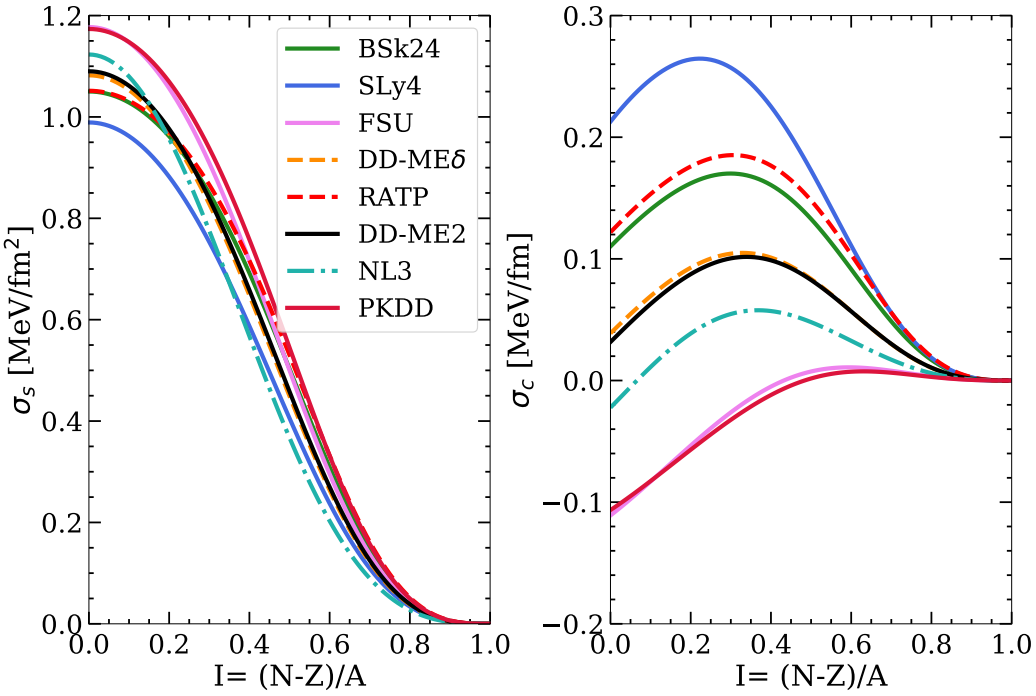

Figure 2.8: Surface (left panel) and curvature (right panel) tensions as a function of the cluster isospin asymmetry for different models. The surface parameters are obtained by fitting to the mass table AME2016 [135], and the parameter p is fixed, $p = 3$.

The surface and curvature tensions as a function of the cluster isospin are shown in Fig. 2.8 for various functionals. As the isospin increases, the surface tension decreases. Especially, at $I = 1$, that is, for PNM, both the surface and curvature tensions disappear, as one may expect. Interestingly, while the surface tension is always positive and decreases monotonically with I, the curvature tension first increases and then decreases and, depending on the model, can even take negative values below $I \lesssim 0.5$. This is due to the competition between the $(\beta - y_p)$ and the σ_s term in Eq. (2.58). Indeed, the curvature tension is proportional to σ_s, which decreases with I. On the other hand, the term $(\beta - y_p)$ increases with I. At low I, the surface tension decreases at a slower rate, hence, σ_c increases. On the contrary, σ_s decreases faster at high I, resulting in a decrease of the curvature tension. A negative curvature tension is observed for NL3 (dash-dotted teal line), FSU (solid violet line), and PKDD (solid red line); this is due to the fact that $(\beta - y_p) < 0$. Indeed, whereas β is larger than 0.5 for most of the considered models, such as BSk24, SLy4, and DD-MEδ (see Table 2.2), for FSU, NL3,

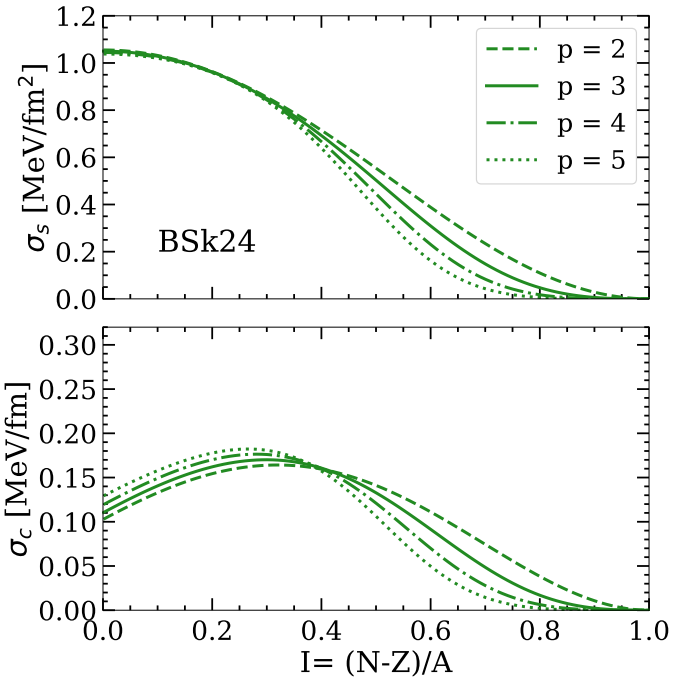

Figure 2.9: Surface (top panel) and curvature (bottom panel) tensions as a function of isospin I at four different p values: $p = 2$ (dashed line), $p = 3$ (solid line), $p = 4$ (dash-dotted line), and $p = 5$ (dotted line). For each p, the surface parameters $(\sigma_0, \sigma_{0,c}, b_s, \beta)$ are obtained by fitting the nuclear binding energy to the AME2016 mass table. The bulk energy is characterized by the BSk24 model.

and PKDD β is relatively small. As an example, for the FSU model, $\beta = 0.28$, thus the curvature tension is negative for $I \lesssim 0.44$, as shown in Fig. 2.8. Clearly, a negative curvature tension is unphysical for a convex shape, and an improvement of Eq. (2.58) is needed for the parametrization of the curvature tension. Nevertheless, from a statistical point of view, σ_c is always positive within one standard deviation of the mean, as will be shown afterward in Fig. 3.22.

It is important to stress that even though the p parameter does not constrain the χ^2 function and therefore cannot be determined from the fit, it plays an important role in controlling the surface tension at high isospin values, hence properties of matter in the inner crust. This point was discussed thoroughly in Ref. [127]. Particularly, the authors showed that different values of p can lead to very different crust compositions, as well as very different density and pressure at the crust-core interface. To illustrate the importance of the p parameter, in Fig. 2.9, I show the surface (top panel) and curvature (bottom panel) tensions corresponding to the BSk24 functional as a function of I at $p = 2$ (dashed lines), 3 (solid lines), 4 (dash-dotted lines), and 5 (dotted lines). At high values of isospin, we can see that higher p leads to smaller $\sigma_{s,c}$. Since the surface tension is correlated to the cluster size [9], one can expect that smaller clusters are obtained with larger p. The reduction in the size makes the inhomogeneous matter more energetically favorable, hence higher crust-core transition density at higher p.

Values of the surface parameters $(\sigma_0, \sigma_{0,c}, b_s, \beta)$ obtained for BSk24 from the fit to the AME2016 [135] mass table at different values of p are presented in Fig. 2.10. The fact that

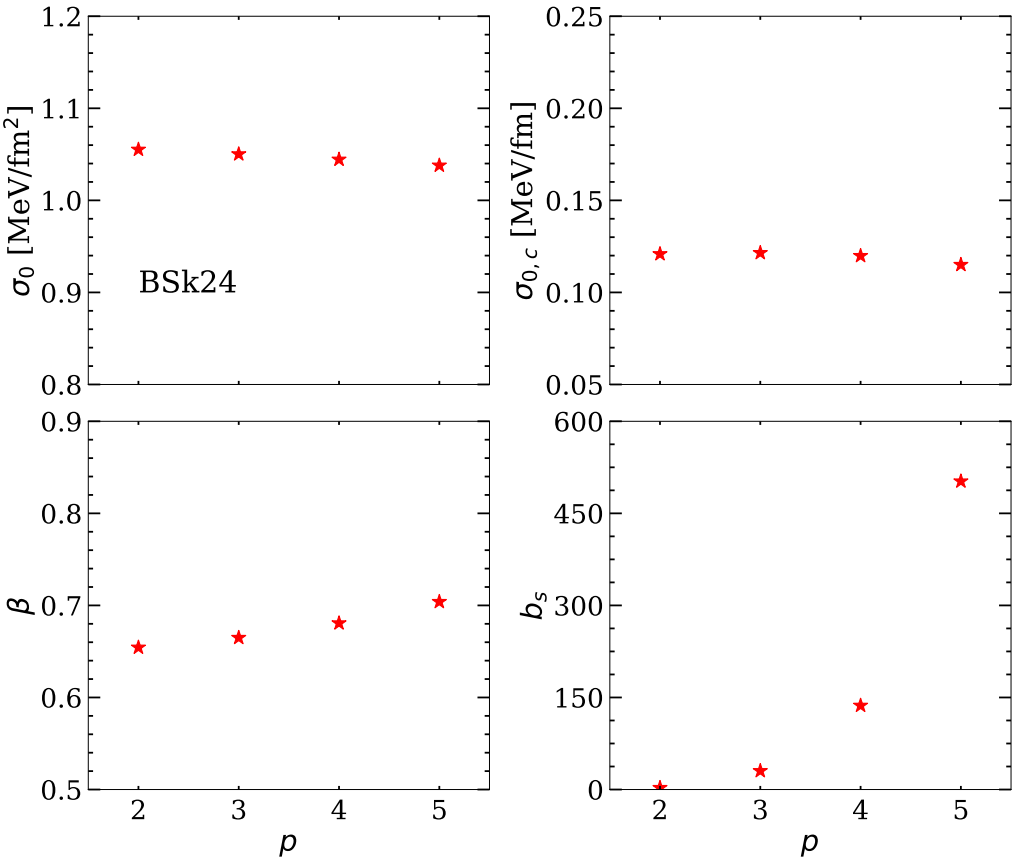

Figure 2.10: Surface parameters $(\sigma_0, \sigma_{0,c}, b_s, \beta)$ as a function of p, obtained from fitting BSk24 to the AME2016 mass table.

$\sigma_0, \sigma_{0,c}$, and β only vary slightly with p suggests that these three parameters are mostly related to the isoscalar properties of matter, hence, they are well defined by the nuclear masses. On the contrary, b_s changes dramatically against p indicating that these two parameters are strongly correlated with the isovector properties. Consequently, they cannot be constrained very well by experimental nuclear data.

2.1.2.2 Crust composition

The equilibrium composition of the crust in its ground state is calculated variationally within a CLDM approach, as first introduced in Ref. [9]. We use the same formalism as in Refs. [79, 80, 121, 122, 127, 142], where the meta-modeling technique is employed for the description of homogeneous nuclear matter.

In order to find the optimal composition in beta equilibrium at each given baryonic density n_B, the WS cell energy density in Eq. (2.53) needs to be minimized under the constraint of

the baryonic number conservation:

$$n_B = \frac{A + n_{gn}(1-u)V_{\rm WS}}{V_{\rm WS}} = \frac{2n_p}{1-I}\left(1 - \frac{n_{gn}}{n_i}\right) + n_{gn}. \tag{2.64}$$

Introducing a Lagrange multiplier λ_i, the function to be minimized can be expressed as:

$$\Omega = \varepsilon_{\rm WS} - \lambda_i \left[\frac{2n_p}{1-I}\left(1 - \frac{n_{gn}}{n_i}\right) + n_{gn}\right], \tag{2.65}$$

$$= \varepsilon_e + \varepsilon_{\rm g}(1-u) + \frac{E_i}{V_{\rm WS}} - \lambda_i \left[\frac{2n_p}{1-I}\left(1 - \frac{n_{gn}}{n_i}\right) + n_{gn}\right]. \tag{2.66}$$

In the variation, we chose the following five independent variables: n_{gn}, r_N, n_i, I, and n_p. Taking the derivative with respect to the neutron gas density n_{gn}, we have:

$$\lambda_i = \frac{\partial \varepsilon_{\rm g}}{\partial n_{gn}} = \mu_{gn}, \tag{2.67}$$

which identifies with the chemical potential of the neutron background, $\mu_{gn} = \mu_{{\rm HM},n}(n_{gn}, 1)$, see Eq. (2.30). Note that Eq. (2.67) is valid only if there is no dependence of the cluster energy E_i on the neutron gas density n_{gn}. Similarly, minimizing Ω (Eq. (2.66)) with respect to r_N, n_i, I, and n_p, we obtain the following system of equations:

$$\frac{\partial}{\partial r_N}\left(\frac{E_i}{A}\right) = 0, \tag{2.68}$$

$$n_i^2 \frac{\partial}{\partial n_i}\left(\frac{E_i}{A}\right) = P_{gn}, \tag{2.69}$$

$$\frac{E_i}{A} + (1-I)\frac{\partial}{\partial I}\left(\frac{E_i}{A}\right) = \mu_{gn} - \frac{P_{gn}}{n_i}, \tag{2.70}$$

$$2\left[\frac{\partial}{\partial I}\left(\frac{E_i}{A}\right) - \frac{n_p}{1-I}\frac{\partial}{\partial n_p}\left(\frac{E_i}{A}\right)\right] = \mu_e, \tag{2.71}$$

where $P_{gn} = \mu_{gn} n_{gn} - \varepsilon_{\rm g} = P_B(n_{gn}, 1)$ is the pressure of the dripped neutrons. Details of the derivation are presented in Appendix B. One can easily show that Eq. (2.68) is equivalent to:

$$E_{\rm surf} + 2E_{\rm curv} = 2E_{\rm Coul}. \tag{2.72}$$

This equation corresponds to the well-known Baym virial theorem with an additional curvature term with respect to the equation originally found in Ref. [9]. Equation (2.72) coincides with the expression obtained in Ref. [143] where the curvature energy was taken into account. It is interesting to notice that only the surface, the curvature, and the Coulomb energy are involved in this first equilibrium condition. Furthermore, the combination of Eqs. (2.68)-(2.69) gives us the pressure equilibrium between the cluster and the surrounding gas:

$$P_{\rm cl} = P_{gn}, \tag{2.73}$$

with

$$P_{\rm cl} = n_i^2 \left.\frac{\partial}{\partial n_i}\left(\frac{E_i}{A}\right)\right|_{A,I,n_p,n_{\rm gn}}. \tag{2.74}$$

Note that the partial derivative in Eq. (2.74) is taken at fixed particle number A, while in Eq. (2.69) it is at fixed radius r_N.

Solving the system of Eqs. (2.68)-(2.71) together with the baryon number conservation in Eq. (2.64), we obtain the five variables r_N, n_i, I, n_p, and $n_{\rm gn}$ for the inner crust. From this, the total pressure of the system can also be calculated from the thermodynamics relation:

$$P = -\frac{\partial E_{\rm WS}}{\partial V_{\rm WS}} = -\frac{\partial (E_{\rm g} + E_e + E_i)}{\partial V_{\rm WS}} = P_{\rm gn} + P_e + P_{\rm int}, \tag{2.75}$$

where $P_{\rm int}$ is the pressure contribution from the ion arising from the (Coulomb) interaction, also referred to as *interaction* or *lattice* pressure. The latter can also be written as

$$P_{\rm int} = -\frac{\partial E_i}{\partial V_{\rm WS}} = -\frac{\partial E_i}{\partial n_p}\frac{\partial n_p}{\partial V_{\rm WS}} = \frac{n_p^2}{Z}\frac{\partial E_i}{\partial n_p} = \frac{n_p^2}{Z}\frac{\partial E_{\rm Coul}}{\partial n_p}. \tag{2.76}$$

For the outer crust, $n_{\rm gn} = 0$, thus, Eqs. (2.68)-(2.71) reduce to the following equations:

$$\frac{\partial}{\partial r_N}\left(\frac{E_i}{A}\right) = 0, \tag{2.77}$$

$$\frac{\partial}{\partial n_i}\left(\frac{E_i}{A}\right) = 0, \tag{2.78}$$

$$2\left[\frac{\partial}{\partial I}\left(\frac{E_i}{A}\right) - \frac{n_p}{1-I}\frac{\partial}{\partial n_p}\left(\frac{E_i}{A}\right)\right] = \mu_e. \tag{2.79}$$

Details of the derivation can also be found in Appendix. B.

The calculation of the crust starts at $n_B = 10^{-10}$ fm^{-3} with $n_{\rm gn} = 0$. This point has a mass density of $\rho \approx 2 \times 10^5$ g cm^{-3}, which is high enough that atoms are supposed to be fully ionized [1].

Table 2.3: Neutron-drip density and the element at the transition for different energy functionals.

	BSk24	SLy4	NRAPR	DD-MEδ	FSU	TM1
$n_{\rm ND}$[fm^{-3}]	2.66×10^{-4}	2.50×10^{-4}	2.50×10^{-4}	2.50×10^{-4}	2.55×10^{-4}	2.50×10^{-4}
X_Z^A	Sr_{38}^{125}	Br_{35}^{113}	Br_{35}^{111}	Kr_{36}^{116}	Rb_{37}^{120}	Br_{35}^{113}

At each n_B, the system of Eqs. (2.77)-(2.79) together with the baryon number conservation constraint are solved simultaneously. This process results in the optimal composition, r_N (or A), n_i, I, and n_p. With this composition, the neutron chemical potential is computed using $\mu_n = \frac{P+\varepsilon_{\rm WS}}{n_B}$. The condition $\mu_n \geq m_n c^2$ defines the onset of neutron drip and marks the beginning of the inner crust. At this point, we add $n_{\rm gn}$ as a variable, and solve the system of equations (2.68)-(2.71) together with Eq. (2.64). A more detailed description of the numerical code can be found in T. Carreau's thesis [122].

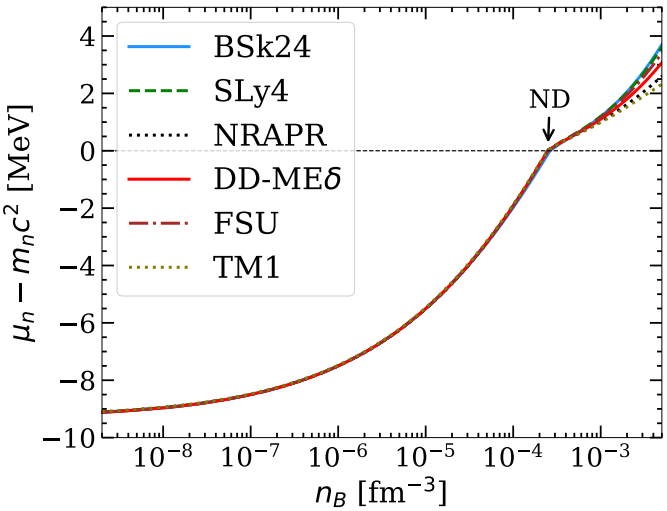

Figure 2.11: Neutron chemical potential in the crust without rest mass, $\mu_n - m_n c^2$, as a function of the total baryon density n_B for different functionals. The intersection with the thin black dashed line indicates the neutron drip (ND) point.

The evolution of μ_n with n_B is depicted in Fig. 2.11 for different energy functionals. The intersection between the result with the thin black dashed line indicates the neutron drip (ND) point. As one can see, the result in the outer crust is almost model-independent, and the transition density $n_{\rm ND}$ is almost the same for all models (see also Table 2.3). However, small model dependence can still be observed in the optimal element, as shown in Fig. 2.12. Even though both the neutron number $N = A - Z$ (top panel) and proton number Z (middle panel) increase with n_B, the former rises with a larger slope, yielding an increase in the isospin asymmetry I (bottom panel). In the outermost layer of the crust, there is a difference of $\Delta Z \approx 1$ among the functionals in our calculation, while the discrepancy is around 3 protons in the bottom layer of the outer crust. This behavior is consistent with our expectation. Indeed, at $n_B < 10^{-4}$ fm^{-3}, the cluster isospin asymmetry I is less than 0.3, and therefore, nuclei found at these densities exist in the terrestrial nuclear experiments. Since all the functionals are fitted to the same experimental nuclear mass table, AME2016, the difference in the cluster binding energy among different models is expected to be negligible thanks to the good quality of the fit. On the other hand, at higher densities, nuclei become so neutron-rich that they are no longer available in the mass table. Consequently, model dependence arises.

In Fig. 2.12, I also display the results obtained by Baym, Pethick, and Sutherland (BPS) [144] (dashed orange lines with thin crosses) as well as those obtained by Pearson *et al.* [75] (dashed green lines with thick crosses) for comparison. The former took the nuclear mass values from the mass table by Myers and Swiatecki [145], while the latter employed the AME2016 table supplemented with the state-of-the-art microscopic theoretical mass table HFB-24 [112]. At low densities, the results in our calculation are in good agreement with the referred works. However, at high densities, one can observe a noticeable discrepancy induced by the shell closures, which are neglected in our CLDM approach. Particularly, at $n_B \geq 10^{-6}$ fm^{-3}, the neutron number N obtained in our calculation increases continuously from $N \approx 40$

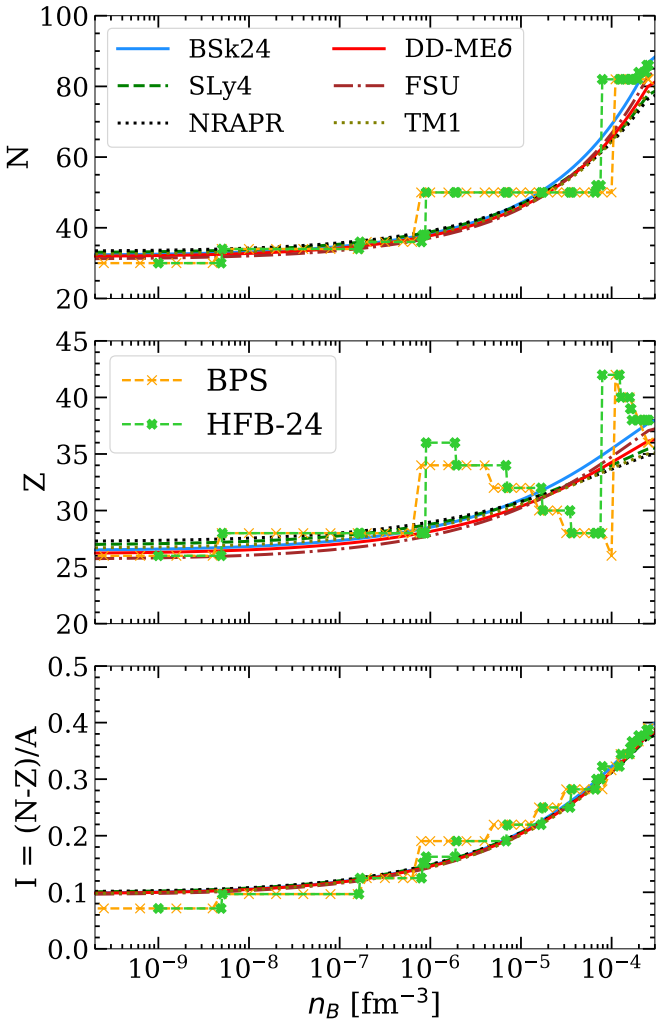

Figure 2.12: Neutron number (top panel), proton number (middle panel), and isospin asymmetry (bottom panel) of nuclei in the outer crust as a function of the total baryon density for different functionals as in Fig. 2.11. The dashed green (orange) line with thick (thin) crosses are the results obtained by Pearson *et al.* [75] using experimental mass data from the AME2016 table supplemented with the theoretical mass table HFB-24 [112] (Baym, Pethick, and Sutherland [144]).

to $N \approx 80$, while in BPS [144] and Pearson *et al.* [75], N remains constant, $N = 50$, up to $n_B \approx 10^{-4}$ fm^{-3} and then jumps to $N = 82$. Thus, in order to have precise predictions for the crust composition, one needs to use a microscopic model such as HFB or ETFSI to account for shell effects. Nevertheless, since the main interests of our work focus on NS EOS and global static properties, which are not very sensitive to the detailed composition of the crust, it is sufficient to use CLDM for the purposes of the present chapter.

At the neutron drip, Refs. [144] and [75] (with HFB-24) respectively found Kr_{36}^{118} and Sr_{38}^{124}. These results agree surprisingly well with our predictions using DD-MEδ and BSk24, as shown in Table 2.3.

In the NS inner crust, the model dependence becomes much more pronounced. This is demonstrated in Fig. 2.13. Due to the extreme isospin condition in the inner crust, which

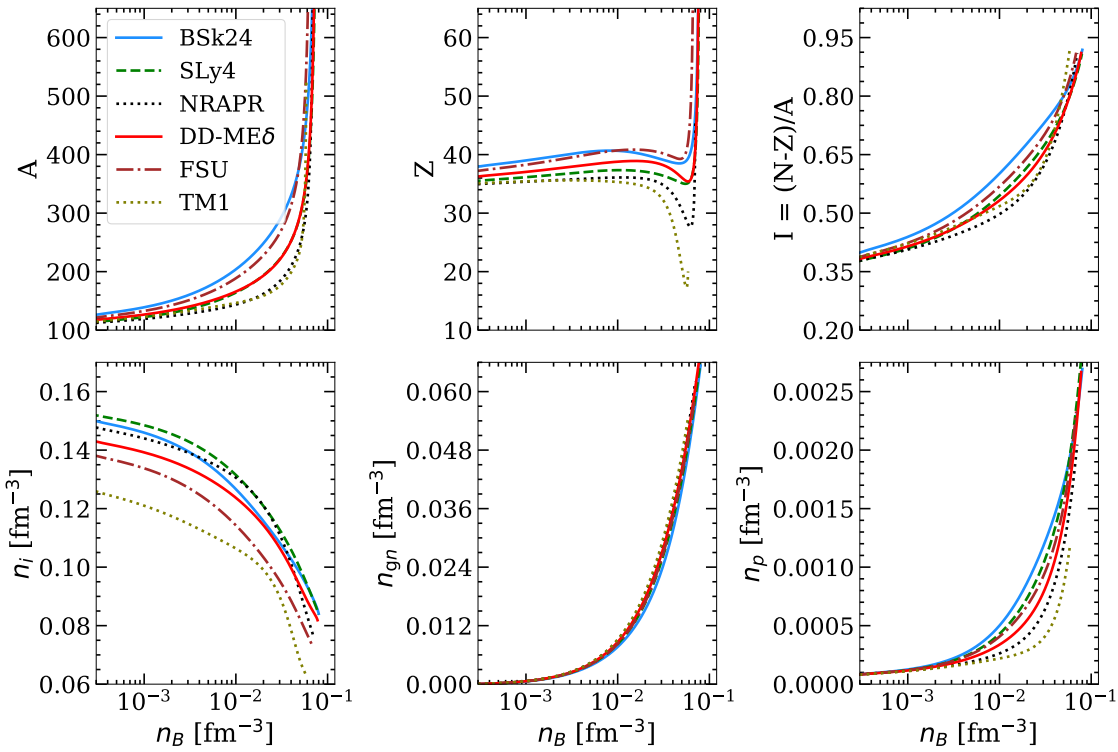

Figure 2.13: Evolution of cluster mass number A, proton number Z, isospin I, internal density n_i, free neutron gas density n_{gn}, and total proton (electron) density n_p in the inner crust as a function of n_B for different functionals. Figure inspired by Ref. [122].

reaches up to $I \sim 0.9$, there are very few protons in the cluster compared to neutrons. Indeed, even though the number of nucleons in the cluster increases monotonically with density up to $A \sim 1000$, the proton number Z remains almost constant, $Z \sim 40$. A similar value of Z has been found also in several other works [66,75,146,147] as already mentioned in Ref. [122]. As density increases, the difference between the cluster internal density n_i and that of free neutron gas n_{gn} reduces. At the crust-core transition, the two densities become comparable, $n_i \approx n_{gn} \approx 0.07$ fm^{-3}. Finally, the last panel in Fig. 2.13 shows the averaged proton density n_p, which equals electron density n_e, as a function of n_B. In the inner crust, although n_p increases, the global proton fraction, $Y_p^{\rm tot} = \frac{n_p}{n_B}$, decreases with n_B. At the interface with the core, $Y_p^{\rm tot}$ is very small, that is, $\approx 0.02 - 0.04$.

2.1.3 Crust-core transition

An accurate prediction of the crust-core transition point is crucial in estimating crustal observables, such as crustal mass, thickness, and moment of inertia [59,148]. These quantities are of particular relevance for the description of pulsar glitches [57] (see Ref. [58] for a review). In the literature, various works were devoted to the determination of the crust-core transition density $n_{\rm CC}$ using different many-body methods and nuclear functionals. The results span a large range of values, from $n_{\rm CC} \approx 0.05$ fm^{-3} to $n_{\rm CC} \approx 0.08$ fm^{-3}; for example, a value of $n_{\rm CC} = 0.055$ fm^{-3} was obtained in Ref. [149] using the TF approach with the NL3 functional

while the value $n_{\rm CC} = 0.081$ fm^{-3} was predicted in Ref. [76] within a full fourth-order ETF approach employing the BSk24 functional.

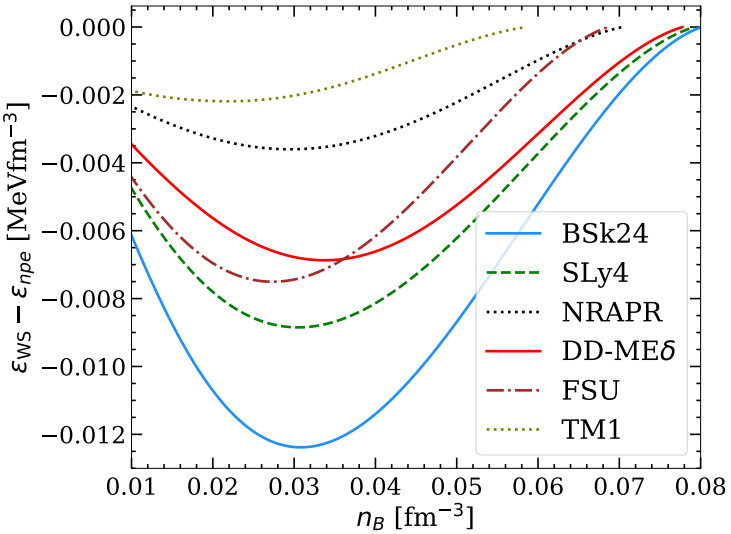

Figure 2.14: Difference in energy density between the inhomogeneous matter in crust and homogeneous matter at beta equilibrium for different energy density functionals as a function of n_B.

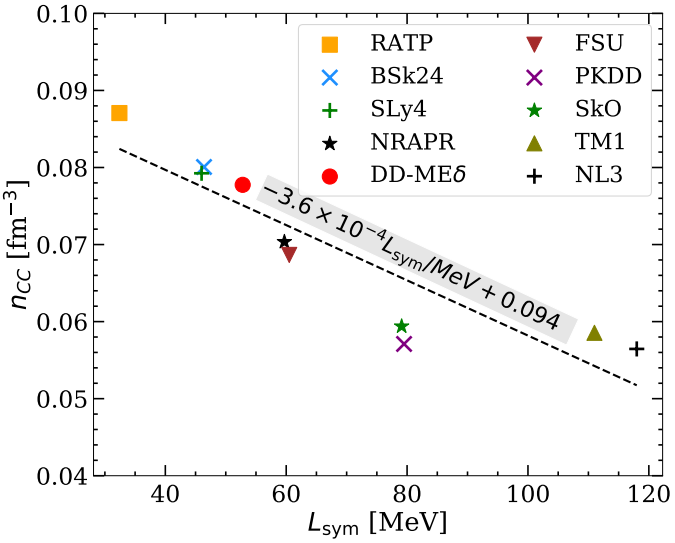

Figure 2.15: Crust-core transition density $n_{\rm CC}$ against the slope of symmetry energy $L_{\rm sym}$ for different functionals (scattered points). The thin black dashed line is the linear regression fitted from the points: $n_{\rm CC}/{\rm fm}^{-3} = -3.6 \times 10^{-4} L_{\rm sym}/{\rm MeV} + 0.094$.

The crust-core transition can be determined checking for the instability of the *npe* matter against density perturbation. Common approaches which have been broadly investigated are dynamical method [9, 128, 144, 150–152], thermodynamical method [153, 154], and random phase approximation [155, 156] (see Ref. [157] for detailed discussions). In our calculation, the transition from the solid crust to the liquid core is determined by comparing the corresponding energy density of the inhomogeneous matter $\varepsilon_{\rm WS}$, defined in Eq. (2.53), to that of

homogeneous matter in beta equilibrium ε_{npe}:

$$\varepsilon_{npe}(n_B) = \varepsilon_B + \varepsilon_e + n_e(m_p - m_n)c^2 + n_B m_n c^2, \tag{2.80}$$

where n_e in Eq. (2.80) is obtained from the beta equilibrium condition (Eq. (2.46)) for each given n_B. The transition density (and pressure) is thus defined at the point when homogeneous matter becomes energetically favored, i.e., $\varepsilon_{npe} \leq \varepsilon_{\rm WS}$. The difference between the energy density of homogeneous and inhomogeneous matter varies considerably with the model, as shown in Fig. 2.14, thus making the crust-core transition density and pressure strongly model-dependent.

Many works pointed out that $n_{\rm CC}$ is anti-correlated to the slope parameter of the symmetry energy $L_{\rm sym}$, for instance, see Refs. [122,126,151,157–159] and references therein. Figure 2.15 shows the crust-core transition density $n_{\rm CC}$ obtained with different models as a function of $L_{\rm sym}$. Indeed, one can see that generally models with higher $L_{\rm sym}$ have lower $n_{\rm CC}$. Using a simple linear regression, the dependence of $n_{\rm CC}$ on $L_{\rm sym}$ can be expressed by: $n_{\rm CC}/{\rm fm}^{-3} \approx -3.6\times10^{-4} L_{\rm sym}/{\rm MeV} + 0.094$. Although here we only consider ten functionals, the coefficient obtained is in good agreement with that reported in Refs. [122, 158], in which a larger set of models was studied, namely $\frac{\Delta n_{\rm CC}}{\Delta L_{\rm sym}} \approx -3.8 \times 10^{-4}/{\rm fm}^3/{\rm MeV}$. In Sect. 2.3, a statistical analysis for this correlation will be presented.

2.1.4 Unified EOS

Due to the complexity in modeling the inhomogeneity of the crust with respect to that of the homogeneous core, in many works on studying the NS properties, the EOS is constructed in a *non-unified* manner, that is, different nuclear models are used for the core and the crust. As an example, in Abbott *et al.* 2019 [40], the EOS at densities above half of the saturation density were sampled using spectral parameterization. Then, this parameterized high-density part was glued to the SLy EOS by Ref. [125]. Similarly, in Miller *et al.* 2021 [37], the EOS at high densities were sampled using different methods, such as piecewise polytrope, spectral parameterization, or Gaussian processes, while the low-density counterpart was fixed using the QHC19 EOS [160]. This manual stitching of the crust to the core EOS might be justified because the crust EOS is not expected to impact significantly the global properties of NS, such as mass and tidal deformability. Nonetheless, a non-unified EOS can lead to errors in NS macrophysical parameters, such as radius, tidal deformability, and moment of inertia [47,161,162]. Specifically, Fortin *et al.* 2016 [161] estimated that the use of "matched" EOS instead of unified ones (and the way the match is performed) could induce a discrepancy of $\sim 4\%$ in the prediction of the NS radius. Likewise, Suleiman *et al.* 2021 [47] stated that depending on the matching density, the difference could be as large as 5% for the radius, 20% for the tidal deformability, and 10% for the moment of inertia. Clearly, these uncertainties could be as large as those estimated in next-generation telescopes [163–165]. As a result, it is important to have a consistent treatment for the crust and core.

In this work, we always use the same nuclear interaction for all NS regions: outer crust, inner crust, and core. The unified EOS obtained using different functionals are illustrated in Fig. 2.16. The total pressure P of the crust (core) is calculated using Eq. (2.75)

(Eq. (2.47)), while the corresponding mass-energy density[8] $\rho_B = \varepsilon/c^2$ is estimated from Eq. (2.53) (Eq. (2.1)). In this Fig. 2.16, the grey dashed line at $\sim 4 \times 10^{11}$ g cm^{-3} marks the transition from the outer crust to the inner crust. As mentioned before, the neutron-drip density is almost model-independent. On the other hand, as shown in Figs. 2.14, the transition density to the liquid core depends on the nuclear parameters, particularly the symmetry energy (see Fig. 2.15). The sensitivity of the crust-core transition on the nuclear parameters in a statistical study will be discussed later. In Fig. 2.16, the left and right boundaries of the grey vertical band are respectively obtained from TM1 ($\rho_B^{\rm CC} \approx 1.0 \times 10^{14}$ g cm^{-3}) and BSk24 ($\rho_B^{\rm CC} \approx 1.3 \times 10^{14}$ g cm^{-3}). They are respectively the models with the lowest and highest crust-core transition density among the considered models.

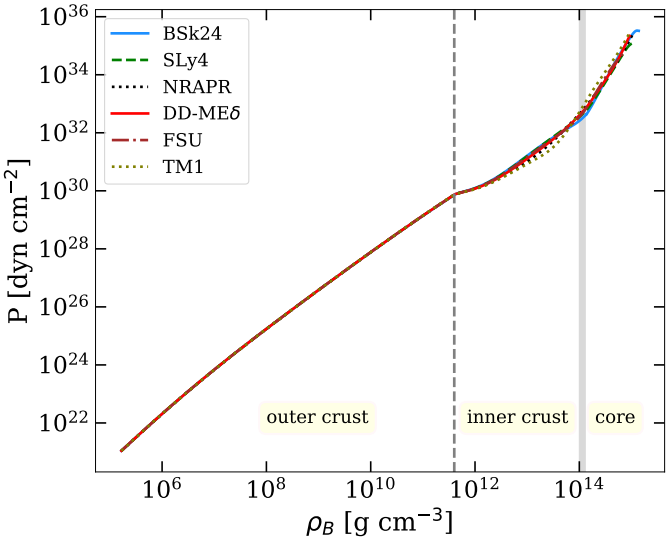

Figure 2.16: Pressure P as a function of mass-energy density ρ_B for different functionals[9]. The grey dashed line indicates the neutron-drip point, $\rho_{\rm ND} \approx 4 \times 10^{11}$ g cm^{-3}, while the grey band represents the uncertainty in determining the transition from the inner crust to the core. See text for more details.

Similar to the NS composition (see Sect. 2.1.2), the model dependence of the NS EOS mainly arises starting from the inner crust and becomes larger with increasing density. Indeed, the pressure varies by a factor of ~ 2 among the models shown in Fig. 2.16 at $\rho_B = 10^{14}$ g cm^{-3}. The limitation in our knowledge of the high-density EOS is also reflected by the large uncertainties of high-order parameters, such as $Q_{\rm sat,sym}$ and $Z_{\rm sat,sym}$. Later on, I discuss these uncertainties and their implication on the predictions of NS observables in a Bayesian analysis.

Finally, it is worth mentioning again that the EOS shown in Fig. 2.16 are obtained with the ELFc version of meta-modeling. Thus, the high-density region of these EOS may not be correctly reproduced with the parameter sets used to produce Fig. 2.16 and reported in Table 2.1. The parameter values leading to an optimized reproduction of the high-density EOS will be discussed in Table 2.4.

[8] I use $\rho_B = \varepsilon/c^2$ and $\rho = n_B m_u$, with $m_u = 931.5$ MeV/c^2 being the atomic mass unit, to denote mass-energy density and mass density, respectively.

[9] The conversion factor for pressure from MeV fm^{-3} to dyn cm^{-2} is 1.6021766×10^{33}, and the conversion factor from the energy density in unit of MeV fm^{-3} to the mass-energy density in unit of g cm^{-3} is $1.6/9 \times 10^{13}$.

2.2 Neutron star observables

2.2.1 Equations of hydrostatic equilibrium

Being relativistic objects, the structure and evolution of NS should be studied using the theory of general relativity. For slowly rotating spherically symmetric NS, the hydrostatic equilibrium is determined by solving the the so-called Tolman-Oppenheimer-Volkov (TOV) equations [166, 167]:

$$\frac{dP}{dr} = -\frac{G\rho_B \mathcal{M}}{r^2}\left(1+\frac{P}{\rho_B c^2}\right)\left(1+\frac{4\pi P r^3}{\mathcal{M}c^2}\right)\left(1-\frac{2G\mathcal{M}}{rc^2}\right)^{-1}, \tag{2.81}$$

$$\frac{d\mathcal{M}}{dr} = 4\pi r^2 \rho_B, \tag{2.82}$$

where G is the gravitational constant, and $\mathcal{M}$ is the mass contained in a sphere of radius r and density ρ_B with the boundary condition $\mathcal{M}(r=0)=0$. For each central density $\rho_{B,c} = \rho_B(r=0)$, Eqs. (2.81)-(2.82) are integrated from the center to the surface, defined by the condition of vanishing pressure, i.e., $P(r \geq R) = 0$, where R is the circumferential radius of the star. The mass is then defined by $M = \mathcal{M}(r=R) = \int_0^R 4\pi r^2 \rho_B(r) dr$.

Therefore, the mass-radius relation represents a family of NS that can exist at equilibrium, each one with a different central density (and pressure). The TOV equation was derived simultaneously by Tolman and Oppenheimer & Volkoff in 1939. By assuming the EOS of degenerate Fermi neutron gas, they found the maximum mass of NS to be only 0.71 $M_\odot$, which is definitely much lower than the maximum mass observed nowadays [31, 37, 38]. This underestimation is due to the neglect of the nuclear forces [1], and it gives an indirect but model-independent proof that nuclear matter exists in the core of compact objects.

The effects of general relativity in a NS can be characterized by the so-called *compactness parameter*, which is defined as:

$$x_{\rm GR} = \frac{r_g}{R}, \tag{2.83}$$

where r_g is the Schwarzschild radius:

$$r_g = \frac{2GM}{c^2} \approx 2.95 \frac{M}{M_\odot} \text{ km}. \tag{2.84}$$

In the non-relativistic limit, where $P \ll \rho_B c^2$, $Pr^3 \ll \mathcal{M}c^2$, and $r_g \ll R$, the TOV equation reduces to the Newtonian equation of stellar equilibrium (see Ref. [1] for detailed discussions).

In order to solve the TOV equations, Eqs. (2.81)-(2.82), the EOS, $P(\rho_B)$, is needed. Here, the core EOS is calculated as described in Sect. 2.1.1, using the ELFd meta-model. Indeed, the higher-order parameters $Q_{\rm sym,sat}$ and $Z_{\rm sym,sat}$ need to be adjusted for an improved behavior at the highest density encountered in the core. Values of $Q_{\rm sym,sat}$ and $Z_{\rm sym,sat}$ in the ELFd model for different energy density functionals, both relativistic and non-relativistic, are listed in Table XIII of Ref. [64]. The new (adjusted) values of $Q_{\rm sym,sat}$ and $Z_{\rm sym,sat}$ can be computed by performing a fit only at the high-density region while keeping the low-order parameters fixed. In Table 2.4, I list the values of the 3rd- and 4th-order parameters for four different models available in Table XIII of Ref. [64], which will be used to discuss the results in the following sections: RATP, SLy4, DD-MEδ, and NL3. These four models are chosen for

illustrating the results because they represent different groups in $L_{\rm sym}$ value, hence different stiffness in the EOS: low (RATP with $L_{\rm sym} = 32.4$ MeV), intermediate (SLy4 and DD-MEδ with $L_{\rm sym} = 46.0$ MeV and 52.8 MeV, respectively), and high (NL3 with $L_{\rm sym} = 118.3$ MeV) (see Table 2.1).

Table 2.4: Higher-order parameters, $Q_{\rm sat,sym}$ and $Z_{\rm sat,sym}$, used in the Taylor expansion of ELFd [64] to reproduce the high-density behavior of symmetric matter and pure neutron matter of the effective models SLy4 from [113], RATP from [114], DD-ME2 from [116], NL3 from [119].

	$Q_{\rm sat}$ (MeV)	$Q_{\rm sym}$ (MeV)	$Z_{\rm sat}$ (MeV)	$Z_{\rm sym}$ (MeV)
SLy4	-225.01	350.68	-443.11	- 690.35
RATP	-222.18	347.83	-414.59	-1126.54
DD-ME2	657.79	318.84	-2611.93	-1317.33
NL3	1307.33	-571.12	-4049.23	200.86

2.2.2 Tidal deformability

When a non-rotating and spherically symmetric star is exposed to a time-independent external quadrupolar tidal field $\mathcal{E}_{ij}$, the tidal field deforms the star, thus inducing a quadrupole moment $\mathcal{Q}_{ij}$ [168–171]. To the linear order in the tidal field, the induced quadrupole moment reads:

$$\mathcal{Q}_{ij} = -\lambda \mathcal{E}_{ij}, \tag{2.85}$$

where λ can be expressed in term of the $l = 2$ tidal Love number k_2:

$$k_2 = \frac{3}{2}\lambda \left(\frac{Rc^2}{G}\right)^{-5}. \tag{2.86}$$

For a binary system with masses m_1 and m_2, from the GW signal, it is possible to extract information on the combined tidal deformability of the system [39–42], defined as:

$$\tilde{\Lambda} = \frac{16}{13}\frac{(m_1 + 12m_2)m_1^4\Lambda_1 + (m_2 + 12m_1)m_2^4\Lambda_2}{(m_1 + m_2)^5}, \tag{2.87}$$

where $\Lambda_{1,2} = \Lambda(M = m_{1,2})$ is the dimensionless tidal deformability calculated at $M = m_{1,2}$, and it is related to the star compactness through:

$$\Lambda = \frac{\lambda}{M^5} = \frac{2}{3}k_2\beta^{-5}, \tag{2.88}$$

where $\beta = x_{\rm GR}/2$, with $x_{\rm GR}$ being the compactness parameter defined in Eq. (2.83). Following the calculation by Refs. [170,171], we used the following expression for the tidal Love number k_2:

$$k_2 = \frac{8}{5}\beta^5(1-2\beta)^2[2 - y + 2\beta(y-1)]/a, \tag{2.89}$$

where

$$\begin{aligned} a = {} & 6\beta[2 - y + \beta(5y - 8)] \\ & + 4\beta^3[13 - 11y + \beta(3y - 2) + 2\beta^2(1 + y)] \\ & + 3(1 - 2\beta)^2[2 - y + 2\beta(y - 1)]\ln(1 - 2\beta). \end{aligned} \tag{2.90}$$

The quantity y is the solution of the following differential equation:

$$\begin{aligned} \frac{dy}{dr} = {} & -\frac{y^2}{r} - \frac{y - 6}{r - 2G\mathcal{M}/c^2} \\ & - \frac{4\pi G}{c^2} r^2 \frac{(5 - y)\rho_B + (9 + y)P/c^2 + (P + \rho_B c^2)/c_s^2}{r - 2G\mathcal{M}/c^2} \\ & + \frac{1}{r}\left[\frac{2G}{c^2}\frac{(\mathcal{M} + 4\pi P r^3/c^2)}{r - 2G\mathcal{M}/c^2}\right]^2, \end{aligned} \tag{2.91}$$

where $c_s^2 = dP/d\rho_B$ is the squared sound speed.

2.2.3 Moment of inertia

The expression of the moment of inertia of a uniformly and slowly rotating star is given by Ref. [172]:

$$I_{\rm tot} = \frac{c^2}{G}\frac{w(R)R^3}{6 + 2w(R)}. \tag{2.92}$$

where the function $\omega(r)$ can be obtained from the following differential equation:

$$\frac{dw}{dr} = \frac{4\pi G}{c^2}\frac{(P + \rho_B c^2)(4 + w)r^2}{rc^2 - 2G\mathcal{M}} - \frac{w}{r}(3 + w), \tag{2.93}$$

with the boundary condition $\omega(r = 0) = 0$, implying $I(r = 0) = 0$. For the full calculations on the equilibrium configurations of slowly rotating[10] stars in the framework of General Relativity, see Hartle *et al.* (1967) [106].

The value of the crustal moment of inertia $I_{\rm crust}$ is of particular interest because it is believed to be related to the glitch phenomenon [57,58]. As was discussed in Refs. [173,174], the glitch may be related to the superfluid vortices formation in the inner crust of the rotating NS. In particular, when the pulsar is rotating fast, the vortices density is so high that the superfluid can be collectively considered as a "rigid" body. As the rotation slows down, some of the vortices, which were initially pinned to the ion lattice, begin to unpin, and the angular momentum from the vortices is transferred to the solid crust. As a result, the pulsar spins up (see also Ref. [148] for a more detailed description). The amount of angular momentum transfer is related to the ratio between the moment of inertia of the superfluid and the solid crust. This ratio can be approximate by $\frac{I_{\rm crust}}{I_{\rm tot}}$, which can be determined in our calculation (see Sect. 2.2.4).

[10] According to Ref. [106], slow rotation implies that the angular velocity of the star is small, and therefore, the fractional changes induced by the rotation in pressure, energy density, and gravitational field are much smaller than unity.

2.2.4 Numerical results

In order to obtain the NS observables, Eqs. (2.81), (2.82), (2.91), and (2.93) are solved simultaneously in the TOV solver [175].

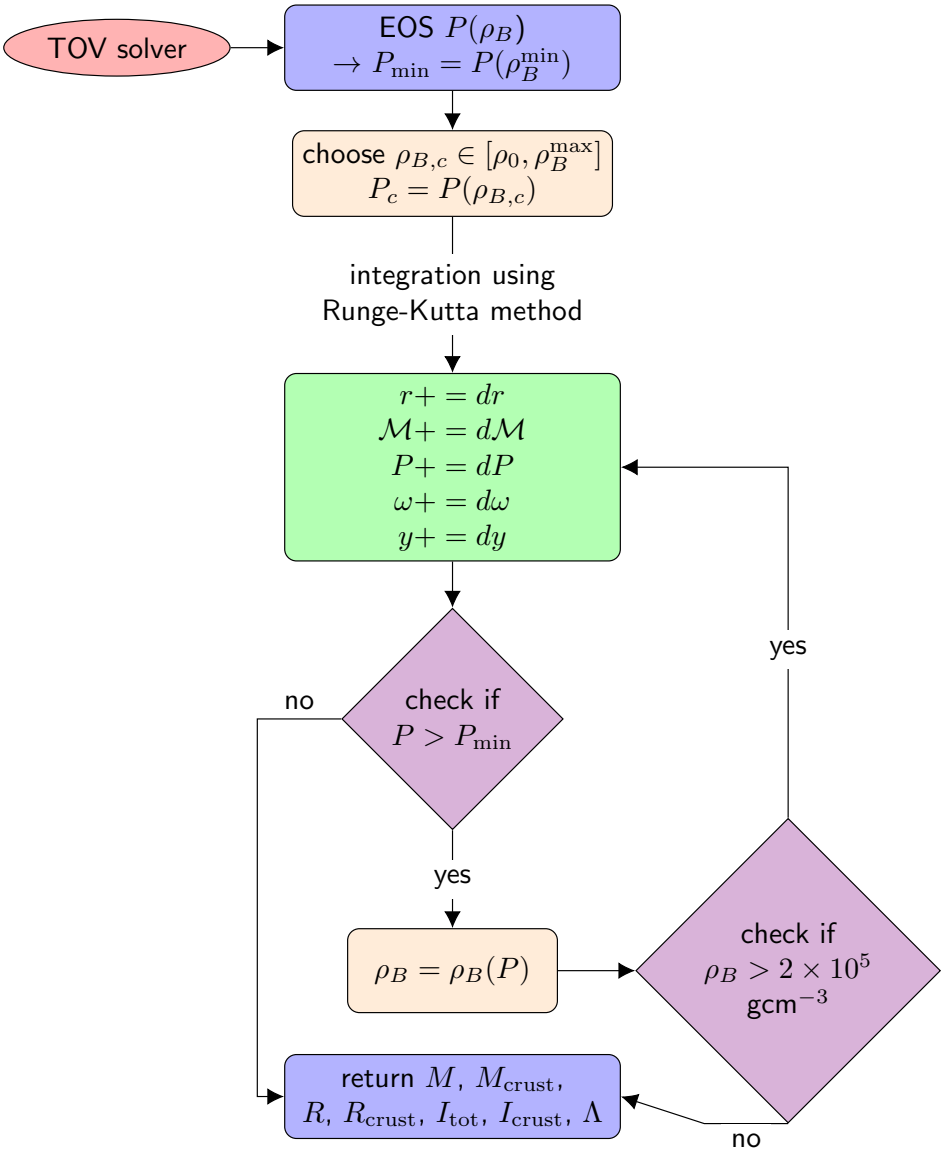

Figure 2.17: A flow chart describing the TOV solver [175].

For a given EOS, and for each value of the central density $\rho_{B,c}$, Eqs. (2.81), (2.82), (2.91), and (2.93) are integrated, thus determining the circumferential radius R, the gravitational mass M, the tidal deformability Λ, and the moment of inertia $I_{\rm tot}$ of the NS. In our TOV solver, whose flow chart is illustrated in Fig. 2.17, the NS observables are therefore obtained as follows. For each (metamodel) EOS, we choose the value of $\rho_{B,c}$ to be between $\rho_{B,c}^{\rm min} = \rho_0 = 2.3 \times 10^{14}$ g cm^{-3}, which is around the saturation density, and the maximum density of the EOS table. Then, the central pressure $P_c = P(\rho_{B,c}) = P(r = 0)$, is obtained from a linear

interpolation of the EOS table. With the step $dr = 100$ cm, using a Runge-Kutta method, we integrate Eqs. (2.81), (2.82), (2.91), and (2.93) up to the NS surface, that is, $r = R$. Theoretically, the surface of the NS is defined as the point where the pressure vanishes, that is, $P(r = R) = 0$. In the numerical code, the NS surface is determined from the condition $\rho_B \leq 2 \times 10^5$ g cm^{-3}, corresponding to the first point in the EOS table, $n_B \approx 10^{-10}$ fm^{-3}.

With the numerical tool described above, using the four energy density functionals SLy4, RATP, DD-MEδ, and NL3 within the ELFd meta-modeling (see Table 2.4), in the following, I show the numerical results obtained for different NS observables. The unified EOS for the

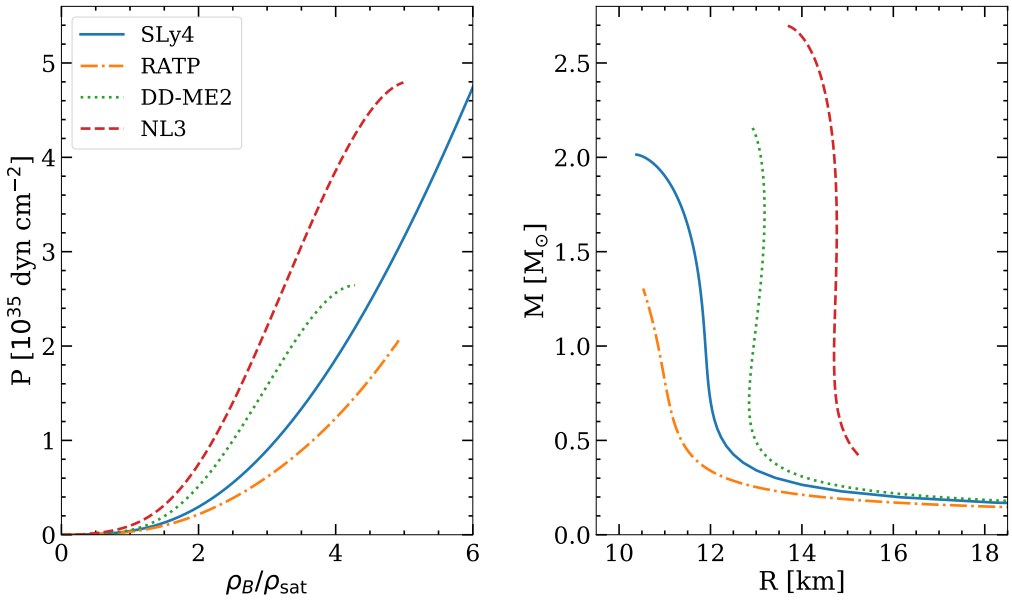

Figure 2.18: Left panel: Total pressure P as a function of the ratio between the total mass-energy density to the saturation density $\frac{\rho_B}{\rho_{sat}}$. Right panel: Corresponding mass-radius relations.

four functionals are shown in the left panel of Fig. 2.18, and the corresponding mass-radius relations are shown on the right panel of the same figure. As we can see, the uncertainty in the EOS is propagated to our prediction for the mass-radius relation. Particularly, stiffer EOS leads to a larger radius for a given mass, and also higher mass for a given radius. Since nowadays we have observables of NS with mass above $2M_\odot$, such as PSR J0348+0432 ($M = 2.01 \pm 0.04 M_\odot$) [31] and PSR J0740+6620 ($M = 2.08 \pm 0.07 M_\odot$) [52], any EOS should be able to reproduce this maximum mass limit. Among the considered models, RATP (dash-dotted orange line) is the only one that does not fulfill this constraint.

To get the thickness and mass of the crust, in the numerical solver, we integrate Eqs. (2.81)-(2.82) from $r = 0$ up to $r = R_{\rm core}$, where $R_{\rm core}$ is defined as the radius at which the crust-core transition occurs, i.e., $P(r = R_{\rm core}) = P_{\rm CC}$. The crustal thickness and mass then can be obtained from:

$$R_{\rm crust} = R - R_{\rm core}, \tag{2.94}$$

$$M_{\rm crust} = M - M_{\rm core}. \tag{2.95}$$

The absolute and fractional values of the crustal thickness and mass are illustrated in Fig.

2.19 as a function of the gravitational mass M. We can observe that stiffer EOS leads to larger $R_{\rm crust}$ and $M_{\rm crust}$. Since the determination of the crustal observables depends on the position of the crust-core transition that is very sensitive to the slope of the symmetry energy, as discussed in Sect. 2.1.3. Therefore, we expect $R_{\rm crust}$ and $M_{\rm crust}$ to have some correlation with the isovector parameters. This point will be discussed in Sect. 2.3. In addition, from Fig. 2.19, we can also observe that both the absolute and relative value of the crustal mass and thickness decrease with the NS total mass. Consequently, for heavy NS, the impact of the crust on global properties is expected to be small.

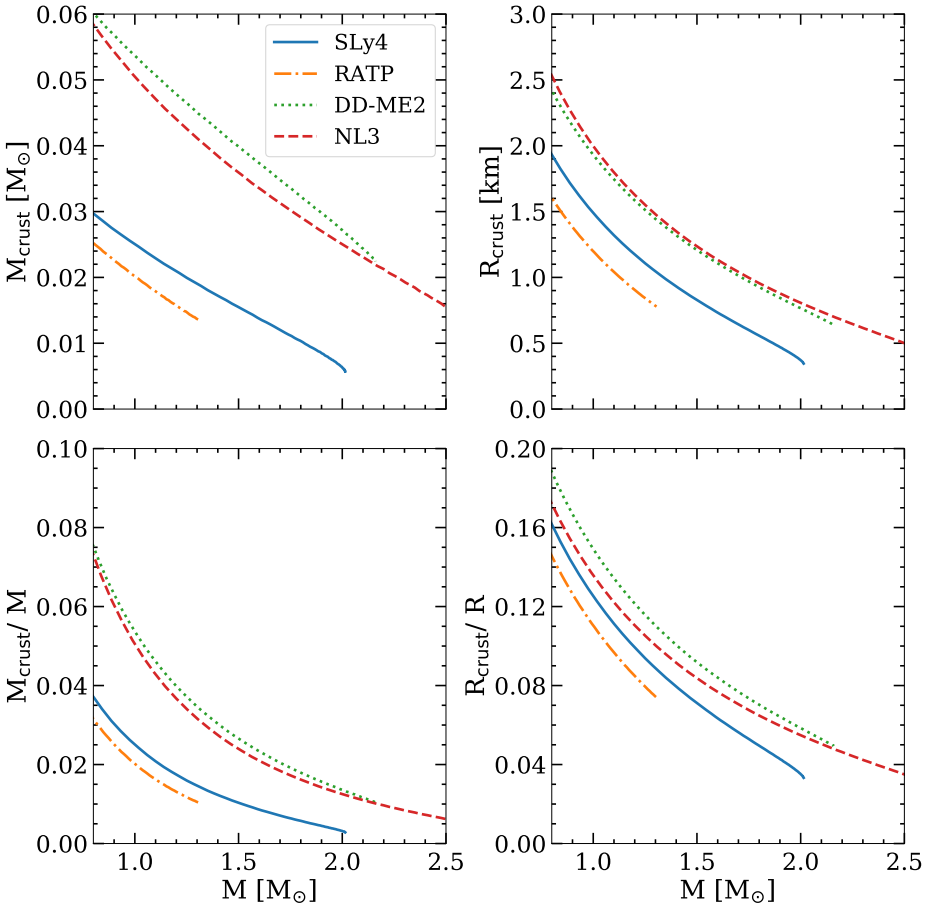

Figure 2.19: Absolute (top panels) and relative (bottom panels) values of the crustal mass (left panels) and thickness (right panels).

I now discuss the results obtained for the tidal deformability. According to Eq. (2.88), the dimensionless tidal deformability is proportional to k_2 and inversely proportional to β^5, with $\beta \propto \frac{M}{R}$. Since the radius does not vary significantly with M for NS with masses $M > 0.5M_\odot$ (see Fig. 2.18), we can expect that the compactness of the star, β, will increase with its mass. Indeed, this is what we can observe in the top panel of Fig. 2.20. On the other hand, the dependence of the Love number k_2 on β is more complicated, as can be seen from Eq. (2.86) and from the lower panel of Fig. 2.20. Interestingly, for all models considered, k_2 has a maximum at around $\beta \approx 0.08 - 0.1$. This value of β corresponds to a mass value of around $0.7M_\odot$. Moreover, Fig. 2.20 also shows that, at the same compactness β, value of k_2

is proportional to the stiffness of the EOS. Indeed, softer EOS are more compressible, hence having smaller response to tidal field, leading to smaller k_2, see also Ref. [171].

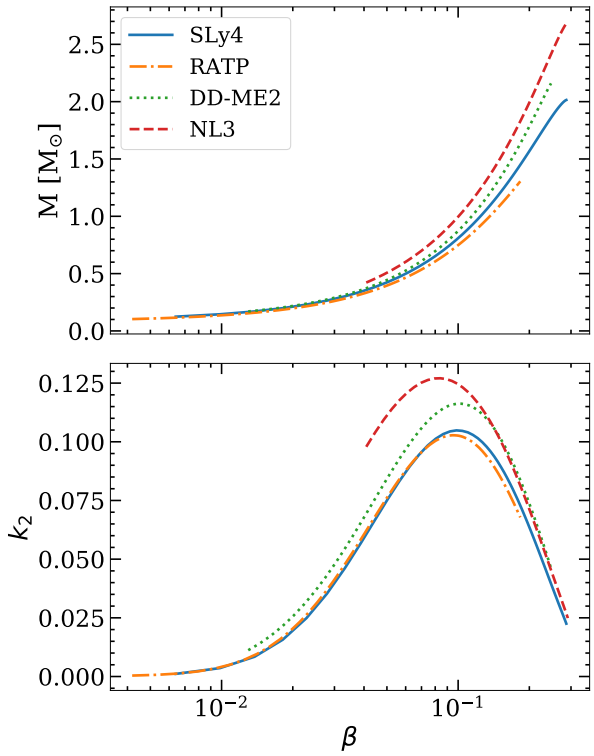

Figure 2.20: Mass (top panel) and the Love number k_2 (bottom panel) as a function of β.

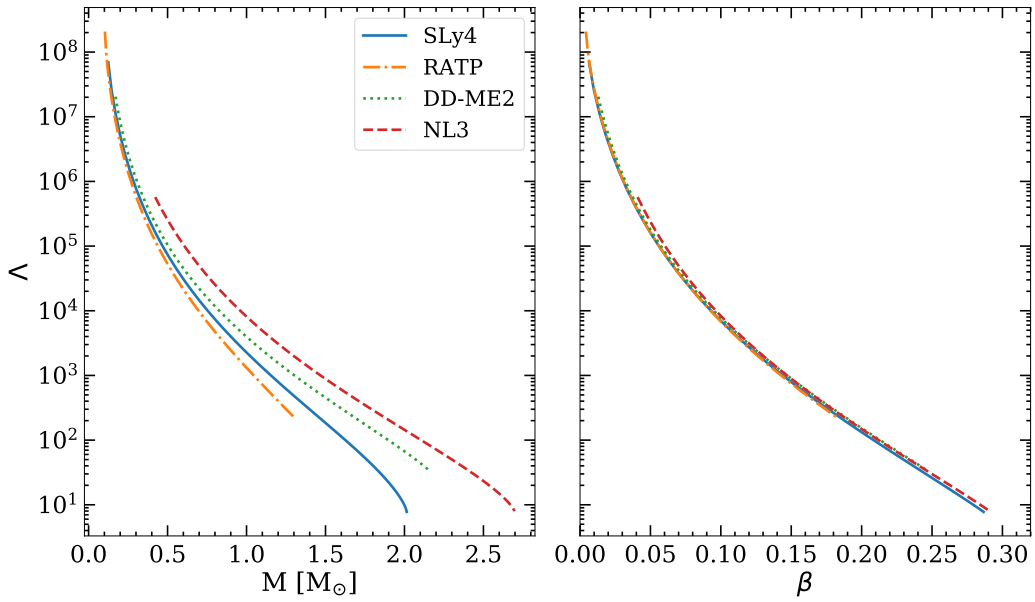

Figure 2.21: Dimensionless tidal deformability as a function of NS mass M (left panel) and compactness β (right panel).

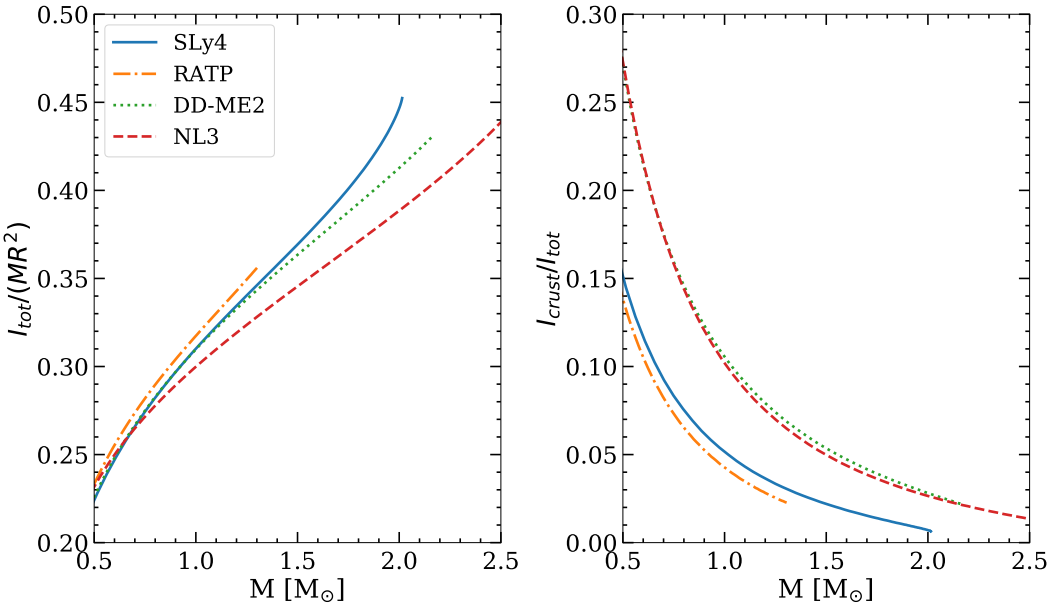

Figure 2.22: Total moment of inertia normalized by MR^2 (left panel), and the fraction contained in the crust (right panel).

As Λ is inversely proportional to β^5, and directly proportional to k_2, the behavior of Λ is governed mostly by β. Thus, we expect Λ to decrease with β and M. This is illustrated in Fig. 2.21. Interestingly, when Λ is plotted against β, the results seem to be model independent. The universal relation between Λ and β was also discussed in the literature, such as in Ref. [176].

The total moment of inertia $I_{\rm tot}$ normalized with MR^2, is depicted in the left panel of Fig. 2.22. One can observe that stiffer EOS generally yield lower $I_{\rm tot}/(MR^2)$. As mentioned above, the crustal moment of inertia is believed to be related to the glitch phenomenon. The value of $I_{\rm crust}/I_{\rm tot}$ is plotted as a function of the M in Fig. 2.22, right panel. We can see that the behavior of $I_{\rm crust}/I_{\rm tot}$ is very similar to that of $M_{\rm crust}/M$. To explain the glitch, $\frac{I_{\rm crust}}{I_{\rm tot}}$ must be larger than 1.4% according to Ref. [177]. If the crustal entrainment is included, then the moment of inertia contained by the crust must be at least 7% [178] or even higher [179]. As we can see from Fig. 2.22, to have such high $\frac{I_{\rm crust}}{I_{\rm tot}}$, the mass of the pulsar must be quite low, specifically below $\sim 1.2M_\odot$ for NL3 and DD-MEδ, and below $0.8M_\odot$ for BSk24. As a result, if the superfluid is limited only to the crust, then it may not be enough to explain the glitch phenomenon. A statistical study on on the prediction for the crustal moment of inertia obtained within the meta-model approach and a CLDM for the crust was performed by Carreau *et al.* 2019 [59]. They concluded that if the entrainment effect is included, the assumption that only the crustal superfluid vortices contribute to the angular momentum transfer is incompatible with the present nuclear physics knowledge.

In this section, the results for the NS observables obtained with different models have been presented and show the model-dependence of such predictions. However, to take into account the uncertainty on our current nuclear-physics knowledge, a statistical study is needed. For this reason, in the next section of this chapter, we confront the nucleonic hypothesis with the

current astrophysical data by performing a Bayesian analysis.

2.3 Nucleonic hypothesis versus astrophysical data

The exceptional progress of multi-messenger astronomy on different astrophysical sources of dense matter has very recently led to quantitative measurements of various NS properties, such as the correlation between mass and radius (M-R) from X-ray timing with NICER [35–38] and the tidal polarizability from GW signals by LIGO/Virgo data [39–41, 180, 181]. These observations, together with the plethora of upcoming data [42], are expected to answer in the next future exciting open questions such as the structure and degrees of freedom of baryonic matter in extreme conditions, and in particular the presence of phase transitions and the existence of deconfined matter in the core of neutron stars [7]. However, the task is complicated by the fact that there is no *ab initio* calculation of ultra-dense matter neither in the hadronic nor the partonic sectors, and therefore effective models are used. The information about the composition of high-density matter is blurred by the uncertainty on the effective energy functional, and similar equations of state can be obtained under different hypotheses on the underlying microphysics [182, 183].

Many works have shown that with the current data, it is still not yet possible to determine the composition in the inner core of NS [184–186]. For this reason, the hypothesis of a purely nucleonic composition of the NS cores cannot be ruled out. To identify the observables pointing towards more exotic constituents, it is important to quantitatively evaluate the space of parameters and observables compatible with the nucleonic hypothesis. With the meta-modeling techniques [64, 65], it is possible to explore the complete parameter space of nucleonic equations of state, and hence predicting the astrophysical observables with uncertainties controlled by our present theoretical and experimental knowledge of nuclear physics. This approach can be viewed as a way to transform experimental and observational constraints into nuclear physics empirical parameters to guide the elaboration of phenomenological and microscopic nuclear models, and it can also be used as a null hypothesis to search for exotic degrees of freedom.

In this section, I present a Bayesian analysis of the semi-agnostic meta-modeling technique of Refs. [59, 64], including both nuclear physics and astrophysical constraints. The corresponding results, which will be shown later on, were published in Ref. [184]. With respect to previous works by different groups [59, 64, 65, 187–190], we included the most recent NICER results [38] which give constraints in the density region where MBPT cannot be applied, and used a fully unified EOS approach, as presented in Sect. 2.1.4, allowing to include in the posterior probabilities the constraints coming from nuclear mass measurements [135]. In Ref. [184], we did not include in the considered constraints the recent skin measurement by PREX II [191] because our model is not presently able to calculate nuclear radii. An extension of this work involving the skin calculation was recently performed in Ref. [192].

2.3.1 Bayesian analysis

Bayesian inference is a method of statistical inference in which Bayes' theorem is used to update the probability for a hypothesis as more evidence or information becomes available.

According to the Bayes' theorem and marginalization, the probability that the hypothesis is true given the data is given by:

$$\text{prob}(\textit{hypothesis}|\textit{data}) \propto \text{prob}(\textit{hypothesis}) \times \text{prob}(\textit{data}|\textit{hypothesis}). \tag{2.96}$$

This theorem is based on the sum and product rules [193]. In Eq. (2.96), prob(*hypothesis*) is called the *prior* probability. It represents our original knowledge/belief about the truth of the hypothesis before being introduced to the data. As the data or information from experiments are given, we can update the prior distribution with the so-called *likelihood* probability, prob(*data*|*hypothesis*). The likelihood gives the probability of observing the measured data if the hypothesis is correct. Finally, we obtain the *posterior* probability, prob(*hypothesis*|*data*) that tells us about the truth of the hypothesis after we know about the data. See Ref. [193] for more details.

In our analysis, the hypothesis can be represented by a set of the empirical parameters $\mathbf{X}$, as explained in Sect. 2.1.1.1. The data will provide us "constraints" on these parameters. Therefore, let us denote them by $\mathbf{c} = \{c_k, k = 1, 2, 3, ...\}$. From Eq. (2.96), we can write our normalized posterior distribution as follows:

$$\text{prob}(\mathbf{X}|\mathbf{c}) = \mathcal{N}\text{prob}(\mathbf{X}) \prod_k \text{prob}(c_k|\mathbf{X}), \tag{2.97}$$

where $\mathcal{N}$ is the normalization factor given by:

$$\mathcal{N} = \left(\int d\mathbf{X} \text{prob}(\mathbf{X}) \prod_k \text{prob}(c_k|\mathbf{X}) \right)^{-1} = (\text{prob}(\mathbf{c}))^{-1}. \tag{2.98}$$

It is important to emphasize the "hypothesis" that we are discussing here is the values of the empirical parameters. Specifically, we want to know the probability of having a certain set of empirical parameters after incorporating all the current information from the data. This should not be mistaken with the nucleonic hypothesis. In other words, Eq. (2.97) gives us the probability of having the empirical parameter set $\mathbf{X}$, and $\mathbf{X}$ is sampled under the nucleonic hypothesis.

Let us denote the nucleonic hypothesis as *model 1* and denote the term on the right-hand side of Eq. (2.98) as prob($\mathbf{c}$|model 1). This quantity is called the *evidence* of model 1. For a given model, the evidence is a constant, and it does not affect the posterior probability distribution. However, if we want to consider different models, such as in model selection studies, then the evidence plays an important role. For instance, let *model 2* denote the hypothesis where we have other degrees of freedom in NS core. Then, the so-called *Bayes factor* can be defined as

$$B(\text{model 1, model 2}|\mathbf{c}) = \frac{\text{prob}(\mathbf{c}|\text{model 1})}{\text{prob}(\mathbf{c}|\text{model 2})}, \tag{2.99}$$

where:

1. if $\log_{10} B > 0$ then model 1 is favored,
2. if $\log_{10} B < 0$ then model 2 is favored,

3. if $\log_{10} B = 0$ then both models are equally probable.

In order to have a reliable evaluation of the Bayes factor, the number of parameters sampled in the two models must be comparable.

In the NS study, the Bayes factor is often used to evaluate the possibility of a phase transition in the NS core (thus model 1 and model 2 would correspond to the nucleonic hypothesis and that of having additional degrees of freedom in the NS core), see e.g., Refs. [185, 186]. However, in the following, only the nucleonic hypothesis is considered, and therefore the value of the evidence is irrelevant. For a discussion on the detectability of a phase transition, see Ref. [194].

2.3.2 Nuclear-physics-informed prior sampling

Table 2.5: Minimum and maximum values of the parameter set $\mathbf{X}$. Table adapted from Ref. [122].

Parameter	Min	Max
$E_{\rm sat}$ [MeV]	-17	-15
$n_{\rm sat}$ [fm^{-3}]	0.15	0.17
$K_{\rm sat}$ [MeV]	190	270
$Q_{\rm sat}$ [MeV]	-1000	1000
$Z_{\rm sat}$ [MeV]	-3000	3000
$E_{\rm sym}$ [MeV]	26	38
$L_{\rm sym}$ [MeV]	10	80
$K_{\rm sym}$ [MeV]	-400	200
$Q_{\rm sym}$ [MeV]	-2000	2000
$Z_{\rm sym}$ [MeV]	-5000	5000
$m^\star_{\rm sat}/m$	0.6	0.8
$\Delta m^\star_{\rm sat}/m$	0.0	0.2
b	1	10

First, we generate uniform distributions of $N_X = 13$ parameters in $\mathbf{X}$ within the ranges indicated in Table 2.5. Hence, $\text{prob}(\mathbf{X}) = 1, \forall \mathbf{X}$. The values of the minimum and maximum of the parameters in the table are chosen based on the information from low-energy nuclear physics data [64, 122, 127]. Since the high-order parameters $Q_{\rm sat,sym}$ and $Z_{\rm sat,sym}$ are poorly constrained, the uncertainties in these parameters in Table 2.5 are very large. Then, each set $\mathbf{X}$ was used as input to obtain the NS EOS within the meta-modeling technique. To have a meaningful prior distribution, we require all parameter sets to result in meaningful solutions for the crust, that is, the minimization of the canonical thermodynamic potential at a given baryon density, as discussed in Sect. 2.1.2, leads to positive gas and cluster densities. In addition, the fit of the surface and curvature parameters $\{\sigma_0, b_s, \sigma_{0c}, \beta\}$ to the AME2016 table must be convergent. These criteria are characterized by the pass-band filter ω_0. Given that the mentioned conditions are satisfied, i.e., $\omega_0 = 1$, the probability of each parameter set $\mathbf{X}$ is then quantified by the goodness of the optimal fit. As a result, the nuclear-physics-informed prior probability is given by:

$$P_1(\mathbf{X}) \propto \omega_0 e^{-\chi^2(\mathbf{X})/2} \text{prob}(\mathbf{X}), \tag{2.100}$$

with

$$\chi^2(\mathbf{X}) = \frac{1}{N_{\rm dof}} \sum_{i=1}^{N_d} \frac{(B^{(i)}_{\rm theo}(\mathbf{X}) - B^{(i)}_{\rm exp})^2}{\Delta B_i^2}, \tag{2.101}$$

see Eq. (2.62), and the sum runs over all the nuclei in the AME2016 [135] mass table. The distributions obtained with this prior represent the most general predictions, within a purely nucleonic composition hypothesis, that are compatible with low energy nuclear physics experiments.

2.3.3 Likelihoods from nuclear physics and astrophysical observables

The prior probability defined in Eq. (2.100) is confronted to different constraints c_k, coming from nuclear physics calculation as well as astrophysical observation data.

The first likelihood we consider comes from the MBPT calculations of the energy per nucleon of SNM and PNM from Ref. [110] based on two- and three-nucleon chiral EFT interactions at N3LO (see Fig. 2.2). These latter calculations are interpreted as a 90% confidence interval. As these bands are very narrow at low densities, we enlarged lower and upper limit of the bands by 5% in order not to discard EOS which are just marginally outside of the bands. The likelihood from these data can be written as:

$$\text{prob}(\text{LD}|\mathbf{X}) = \omega_{\rm LD}(\mathbf{X}), \tag{2.102}$$

in which LD stands for "low density" because this constraint is applied in the low-density region, from 0.02 fm^{-3} to 0.2 fm^{-3}. Furthermore, $\omega_{\rm LD}(\mathbf{X}) = 1$ if the $\mathbf{X}$ is consistent with the EFT bands, and $\omega_{\rm LD}(\mathbf{X}) = 0$ otherwise. Implementing this low density (LD) filter amounts to including in the nucleonic hypothesis the information from *ab initio* nuclear theory.

The second likelihood used in this study is the mass measurement from radio-timing observations of the pulsar PSR J0348+0432 [31], $M_{J03} = 2.01 \pm 0.04 M_\odot$. The probability associated with this measurement is a normal distribution with a mean value of 2.01 and a standard deviation of 0.04:

$$\text{prob}(\text{J03}|\mathbf{X}) = \frac{1}{0.04\sqrt{2\pi}} \int_0^{M_{\rm max}(\mathbf{X})/M_\odot} e^{-\frac{(x-2.01)^2}{2\times 0.04^2}} dx, \tag{2.103}$$

where $M_{\rm max}$ is the maximum mass at equilibrium, determined from the TOV equation (see Sect. 2.2.1).

The third likelihood is the tidal deformability of the binary NS system associated with the gravitational wave event GW170817, detected by LVC [39–42]. From this event, the information on the joint distribution of the combined tidal deformability $\tilde{\Lambda}$ and the mass ratio $q = \frac{m_2}{m_1}$ was deduced (see Fig. 2.23). Conventionally, q is the mass ratio of the lighter component m_2 to the heavier component m_1. Therefore, $q \leq 1$. The constraint from the GW170817 event evaluates the weight of a parameter set based on its prediction for the tidal deformability $\tilde{\Lambda}$ for each q. The likelihood is written as:

$$\text{prob}(\text{LVC}|\mathbf{X}) = \sum_i P_{\rm LVC}(\tilde{\Lambda}(q^{(i)}, \mathbf{X}), q^{(i)}), \tag{2.104}$$

where $P_{\rm LVC}$ is the joint posterior distribution of $\tilde{\Lambda}$ and q taken from Refs. [41, 195]. In Refs. [41, 195], the authors performed a Bayesian inference with four different waveform

models. The distribution for $\tilde{\Lambda}$ and q which we are using for this work is the one obtained with the PhenomPNRT waveform, which is considered as their "reference model". In our analysis, q is chosen to be in the one-sided 90% confidence interval obtained in Ref. [41], $q \in [0.73, 1.00]$. In Ref. [41], it was shown that the chirp mass $\mathcal{M}_c$ of the binary NS system associated to the GW170817 event was accurately determined, $\mathcal{M}_c = 1.186 \pm 0.001 M_\odot$ at the median value with 90% confidence limits. The chirp mass $\mathcal{M}_c$ can be expressed as a function of m_1 and q as:

$$\mathcal{M}_c = \frac{(m_1 m_2)^{3/5}}{(m_1 + m_2)^{1/5}} = \frac{q^{3/5} m_1}{(1+q)^{1/5}}. \tag{2.105}$$

Since the uncertainty in the chirp mass $\mathcal{M}_c$ is negligible, for each value of the mass ratio q, we calculate m_1 directly from the median value of $\mathcal{M}_c$ through Eq. (2.105).

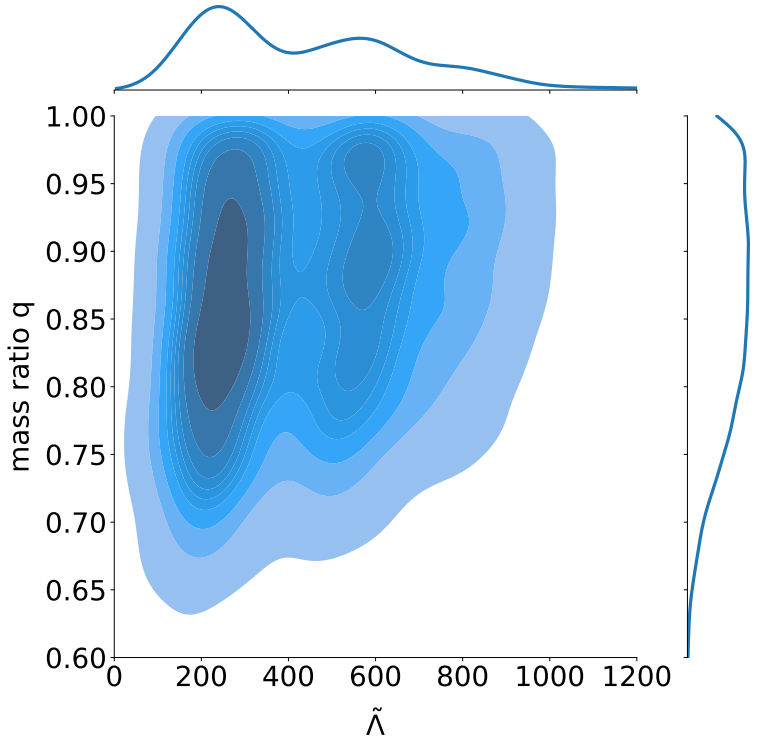

Figure 2.23: Joint distribution of the combined tidal deformability $\tilde{\Lambda}$ with the mass ratio q inferred from GW170817. Figure generated using data from Ref. [195].

The last likelihood comes from the X-ray pulse-profile measurements of PSR J0030+0451 mass, $M_{\rm J00} = 1.44^{+0.15}_{-0.14} M_\odot$, and radius, $R_{\rm J00} = 13.02^{+1.24}_{-1.06}$ km from Ref. [36] and the radius measurement with NICER and XMM-Newton data [38] of the PSR J0740+6620 pulsar with mass $M_{\rm J07} = 2.08 \pm 0.07 M_\odot$ [52], $R_{\rm J07} = 13.7^{+2.6}_{-1.5}$ km [38]. The NICER likelihood probability is given by:

$$\text{prob}(\text{NICER}|\mathbf{X}) = \sum_i p_{\rm NICER1}(M_1^{(i)}, R(M_1^{(i)})) \sum_j p_{\rm NICER2}(M_2^{(j)}, R(M_2^{(j)})), \tag{2.106}$$

where $p_{\rm NICER1}(M, R)$ is the two-dimensional probability distribution of mass and radius for the pulsar PSR J0030+0451 obtained using the waveform model with three uniform oval

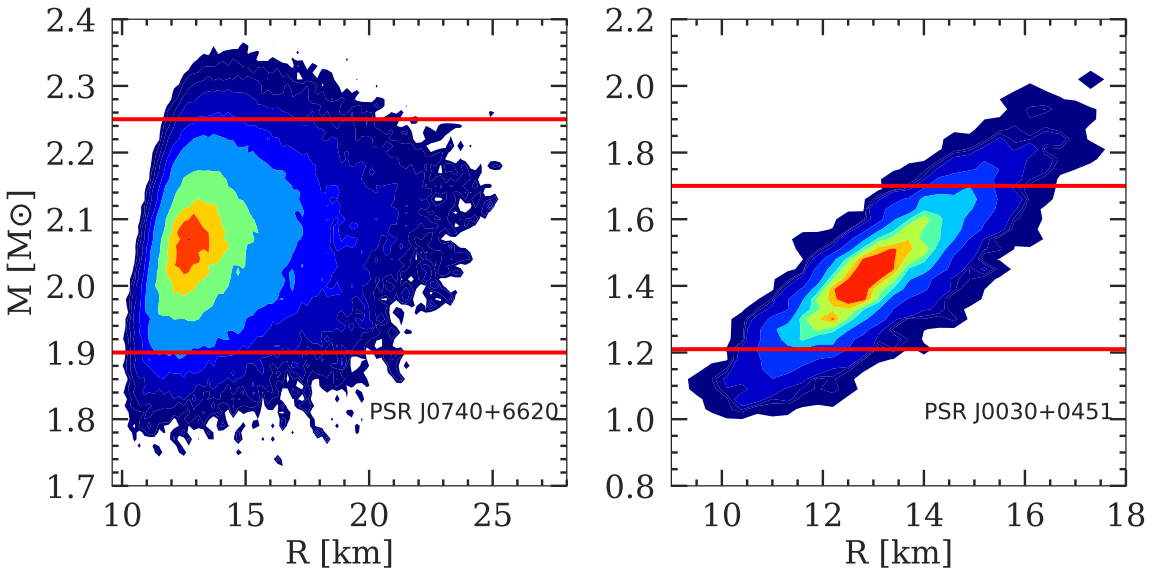

Figure 2.24: Joint mass-radius distribution of PSR J0740+6620 (left panel) generated with data taken from Ref. [105] and of PSR J0030+0451 with data taken from Ref. [104]. The red horizontal lines in each figure indicate the range chosen for M_1 and M_2. See text for details.

spots by Miller *et al.* in Refs. [36, 104] (see the right panel of Fig. 2.24); and $p_{\rm NICER2}(M,R)$ is the probability distribution for PSR J0740+6620 using NICER and XMM-Newton data by Miller *et al.* [38, 105] (see the left panel of Fig. 2.24). The intervals of M_1 and M_2 chosen are sufficiently large so that they cover most of the associated joint mass-radius distributions, $M_1 \in [1.21, 1.70]\, M_\odot$ and $M_2 \in [1.90, 2.25]\, M_\odot$.

2.3.4 Analysis of the posterior

Depending on the likelihood that we consider, the resulting posterior distributions are different. In order to see the impact of different constraints on the nuclear-physics-informed prior, whose probability is given by Eq. (2.100), we consider three different posterior distributions. They are:

- **LD**: This posterior contains parameters selected according to our present nuclear-physics knowledge (both from experiments and theory, see Eqs. (2.100) and (2.102)). The posterior probability can be written as:

$$P_2(\mathbf{X}) = \text{prob}(\mathbf{X}|\text{LD}) \propto \omega_{\rm LD}(\mathbf{X}) P_1(\mathbf{X}), \tag{2.107}$$

- **HD + LVC**: With this distribution, we can identify the impacts from astrophysical data, particularly the maximum mass and tidal deformability constraints. The posterior probability of this distribution is written as:

$$P_3(\mathbf{X}) = \text{prob}(\mathbf{X}|\text{HD}, \text{LVC}, \text{J03}) \propto \omega_{\rm HD}(\mathbf{X}) \text{prob}(\text{J03}|\mathbf{X}) \text{prob}(\text{LVC}|\mathbf{X}) \text{P}_1(\mathbf{X}). \tag{2.108}$$

  Here, $\omega_{\rm HD}$ is also a pass-band type filter similar to the $\omega_{\rm LD}$ filter in Eq. (2.107). Only parameter sets satisfying all the following conditions are retained: causality, thermodynamic stability, and non-negative symmetry energy at all densities. These conditions

are usually violated at high densities, hence the name "HD" filter. Moreover, we expect the conditions on maximum mass and tidal deformability not to be selective on the low-order EOS parameters, but to constitute stringent constraints on the high-density behavior of the EOS. The latter is essentially governed, within the nucleonic hypothesis, by the third and fourth order effective parameters $Q_{\rm sat}$, $Z_{\rm sat}$, $Q_{\rm sym}$ and $Z_{\rm sym}$ [64].

- **All**: Including the three constraints mentioned above together with the likelihood from the joint mass-radius distributions of the two NICER measurements from Refs. [36, 38], the posterior probability for the final distribution is written as:

$$\begin{aligned} P_4(\mathbf{X}) &= \text{prob}(\mathbf{X}|\text{LD}, \text{HD}, \text{LVC}, \text{J03}, \text{NICER}) \\ &\propto \omega_{\rm LD}\omega_{\rm HD}\text{prob}(\text{J03}|\mathbf{X})\text{prob}(\text{LVC}|\mathbf{X})\text{prob}(\text{NICER}|\mathbf{X})P_1(\mathbf{X}). \end{aligned} \tag{2.109}$$

In each distribution, the corresponding posterior distributions of different observables Y are calculated by marginalizing over the EOS parameters as:

$$P(Y) = \prod_{j=1}^{N_X} \int_{X_j^{\rm min}}^{X_j^{\rm max}} dX_j\, P_i(X)\delta\left(Y - Y(\mathbf{X})\right), \tag{2.110}$$

where $i = \{1, 2, 3, 4\}$, and $N_X = 13$ is the number of parameters in the meta-modeling.

In the results, we compare the distributions obtained in the four distributions: prior, LD, HD+LVC, and All, whose probability are defined respectively in Eqs. (2.100), (2.107), (2.108), and (2.109). To insure that the differences in the posterior distributions are induced by the impact of the different constraints, care is taken to have comparable statistics from the four distributions, for each plot shown in this section. Particularly, each distribution contains around 18000 sets of parameters. Moreover, for all shown observables we have checked that increasing in statistics does not affect the results, within the precision chosen for the numerical values given in this work.

2.3.4.1 Implication on NS properties predictions

In this section, I discuss the implication of different likelihoods on the predictions of NS properties within the nucleonic hypothesis.

Table 2.6: Estimations of NS crustal properties for four distributions. The results are presented with medians and 68% confidence limits. Table reproduced from Ref. [184].

	$n_{\rm CC}$ [fm $^{-3}$]	$P_{\rm CC}$ [MeV fm^{-3}]	$R^{1.4}_{\rm crust}$ [km]	$R^{2.0}_{\rm crust}$ [km]
Prior	$0.087^{+0.033}_{-0.037}$	$0.163^{+0.281}_{-0.095}$	$1.13^{+0.25}_{-0.29}$	$0.706^{+0.165}_{-0.191}$
LD	$0.078^{+0.011}_{-0.011}$	$0.385^{+0.104}_{-0.097}$	$1.11^{+0.10}_{-0.14}$	$0.693^{+0.070}_{-0.079}$
HD+LVC	$0.079^{+0.023}_{-0.033}$	$0.141^{+0.202}_{-0.076}$	$1.05^{+0.20}_{-0.20}$	$0.627^{+0.126}_{-0.128}$
All	$0.084^{+0.009}_{-0.010}$	$0.423^{+0.093}_{-0.090}$	$1.15^{+0.10}_{-0.08}$	$0.687^{+0.067}_{-0.067}$

In Fig. 2.25, I display the joint distributions of the crust-core transition density $n_{\rm CC}$ and pressure $P_{\rm CC}$. The chiral EFT calculation plays an important role in the determination

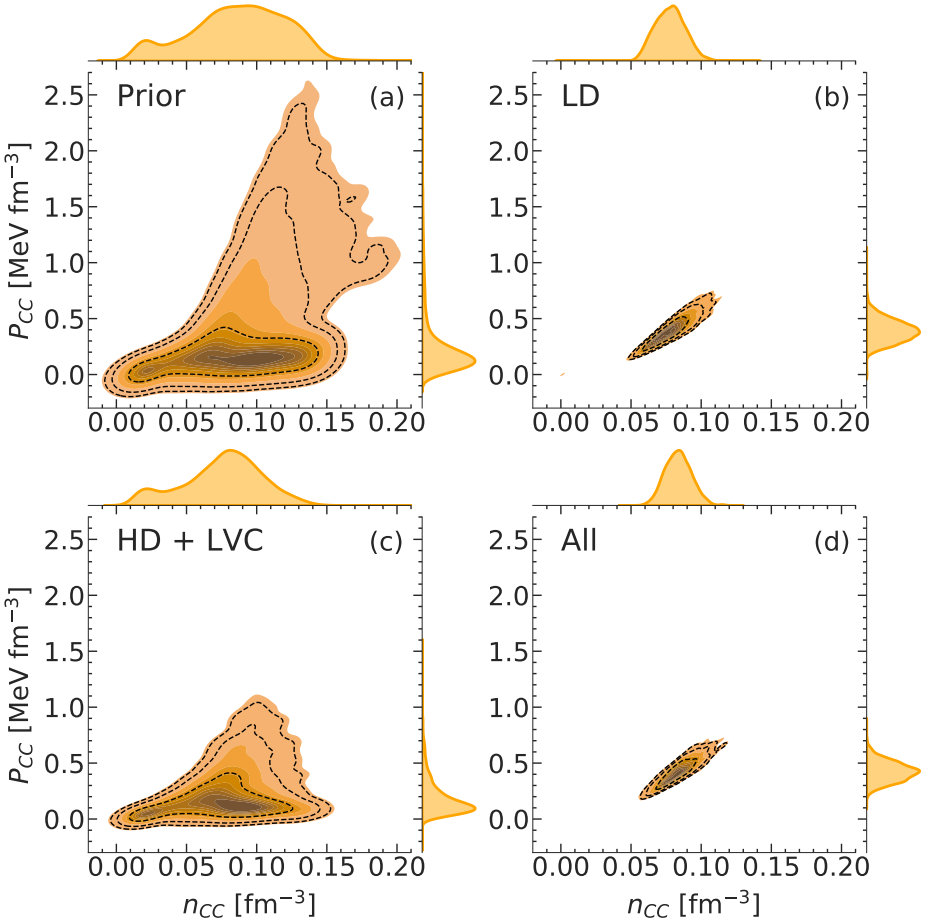

Figure 2.25: Joint probability density plots of crust-core transition density $n_{\rm CC}$ and pressure $P_{\rm CC}$. The dashed black contours in each panel indicate the 68%, 95%, and 99% confidence regions. Figure reproduced from Ref. [184].

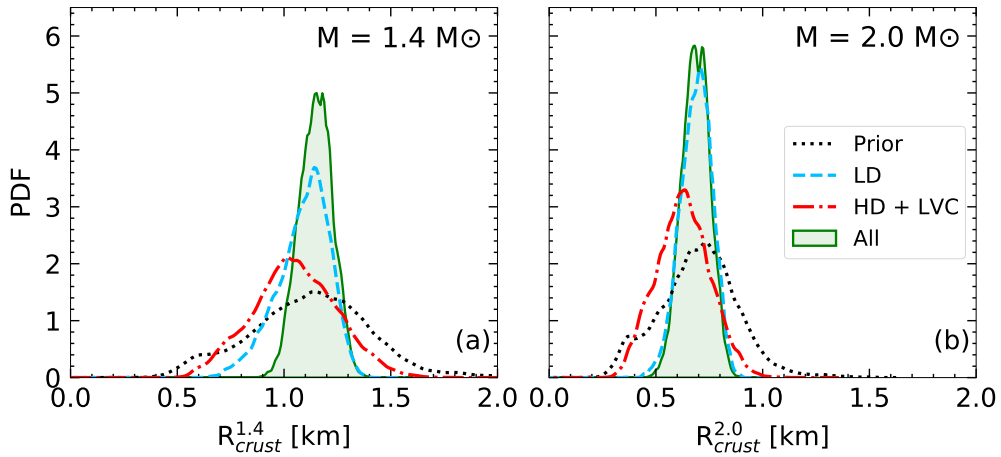

Figure 2.26: Probability density distributions of crust thickness at $M = 1.4M_\odot$ (panel a) and $M = 2.0M_\odot$ (panel b). Figure reproduced from Ref. [184].

of the crust-core transition point, which is evident from the LD distribution in Fig. 2.25b. One can observe that the chiral EFT filter puts stringent limits on both the crust-core transition density $n_{\rm CC}$ and pressure $P_{\rm CC}$; very high and very low values of $n_{\rm CC}$ and $P_{\rm CC}$ are discarded. For the HD+LVC distribution, see Fig. 2.25c, the most noticeable fact is the suppression of models with high transition pressures. However, the probability densities of these models, which violate either causality or thermodynamic stability or positivity of the symmetry energy, are very small, and they lie outside the 95% contour in the prior distribution (see Fig. 2.25a). In other words, the astrophysical constraints on NS maximum mass and tidal deformability have very little effects on the crust-core transition.

The crust-core transition point also determines astrophysical observables associated to the crust, such as the crust thickness, of the moment of inertia [59]. In this study, let us discuss the crust thickness as an illustrative example. Figure 2.26 presents the probability density functions (PDFs) of NS crust thicknesses for $1.4M_\odot$ and $2.0M_\odot$ NS. In both cases, the uncertainties in the LD distributions are narrower compared to the prior, while the effect in the HD+LVC distribution is only marginal. This agrees with our conclusions for the crust-core transition point, that is, the role of the chiral EFT filter is more dominant in the determination of crustal properties. When all constraints are taken into account, crust thicknesses of both $1.4M_\odot$ and $2.0M_\odot$ NS are determined with relative uncertainties up to 10%. For a quantitative estimation of the effects of different filters, in Table 2.6, I present the median crust-core transition density $n_{\rm CC}$ and pressure $P_{\rm CC}$, and the crustal thickness of $1.4M_\odot$ and $2.0M_\odot$ NS together with their 68% confidence limits. Quite conclusively one can infer that the LD chiral EFT filter, among all the considered filters, has the strongest effect on these quantities.

Figure 2.27 shows the sound speed in medium, defined as in Eq. (24) in Ref. [65], as a function of mass density ρ obtained with four different filters at the 50% and 90% confidence intervals, together with the behavior of some selected models [91, 112, 113, 120]. One can observe that for all the filters the most probable EOS remain causal up to very high densities ($\sim 6\rho_{\rm sat}$), even though this requirement is not explicitly imposed in our "Prior" nor the "LD" filter, see panels a and b of Fig. 2.27, respectively. As expected, the behavior of the sound speed is globally structureless. However, we can surprisingly see a trend for a peaked structure, which is typically presented in the literature as a signature of a transition to exotic matter. Nevertheless, this peak could also be caused by the combination of different EOS, not all individual models (see lines in panel d of Fig. 2.27) exhibiting such peak structure. Despite that, the fact that some purely nucleonic EOS show a peak in the sound speed means that this feature cannot be taken as a sign of a phase transition.

Figure 2.28 displays for different filters three shaded regions (from light to dark) sequentially containing 99%, 95%, and 68% confidence intervals for two dimensional distribution for mass and radius of NS. The two black contour lines at low mass and high mass respectively indicate 68% of the mass-radius distributions for PSR J0030+0451 [36] and PSR J0740+6620 [38]. One can observe in panel a of Fig. 2.28 that our prior is already quite compatible with both the recent NICER observations [36, 38]. This explains why the effect of the constraints from NICER is globally small in all our distributions. Moreover, since in panel c of Fig. 2.28, the constraint from the radio-timing mass measurement of the high-

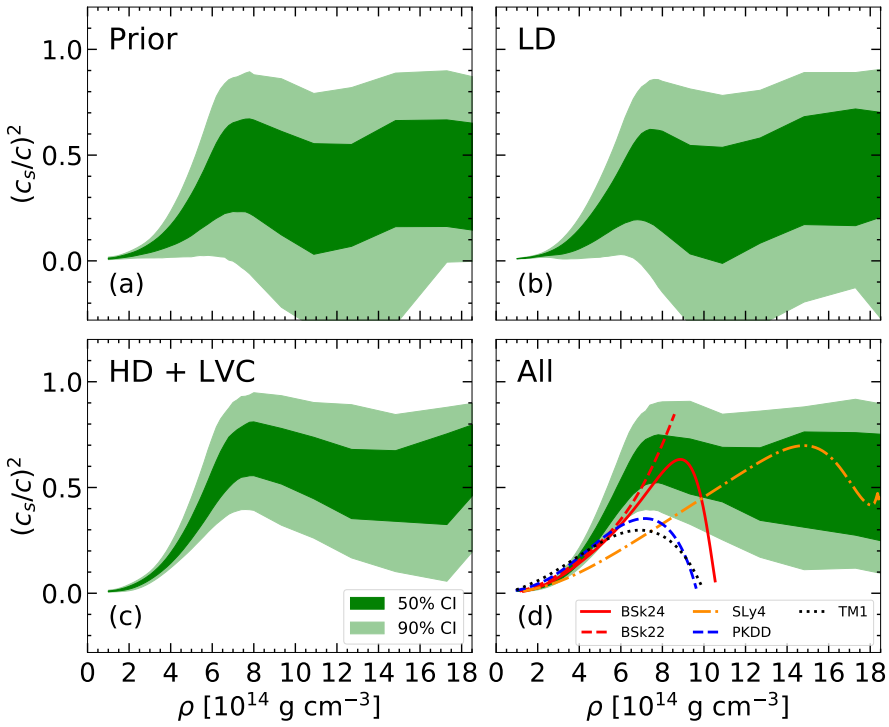

Figure 2.27: 50% (dark green) and 90% (light green) confidence intervals of sound speed $\left(\frac{c_s}{c}\right)^2$ as a function of mass density ρ. Curves in panel d show the sound speed of some selected models [91, 112, 113, 120] up to the central density corresponding to the maximum mass. See text for details. Figure reproduced from Ref. [184].

mass pulsar PSR J0348+0432 is already included beforehand, the impact from the mass of PSR J0740+6620 is negligible in Fig. 2.28d. Additionally, the large uncertainty in the new radius measurement does not help to constrain further the EOS. The compatibility of the NICER measurements and our distributions implies that a nucleonic EOS is flexible enough to reproduce those dense-matter observations. In Ref. [185], Pang *et al.* computed the Bayes factor to study the possibility of having a strong first-order phase transition from nuclear to quark matter in NS. If the data from Miller *et al.* [38] is used, the Bayes factor changes from 0.27 to 0.21. Even though the effect from PSR J0740+6620 is not significant, a decrease in the Bayes factor points to the fact that a first-order phase transition to quark matter is disfavored. Similarly, Legred *et al.* [186] found that the Bayes factor for EOS having multiple stable branches is disfavored against those with one branch; the Bayes factor being 0.146[11] (0.220) with (without) the PSR J0740+6620 measurement. Both these studies disfavor the possibility of a strong phase transition and support the suitability of the hadronic EOS with respect to NS observables, which is in line with our present analysis.

Figure 2.29 presents the marginalized density distributions of NS radii, $R_{1.4}$ and $R_{2.0}$, of the canonical mass $1.4M_\odot$ (panel a) and the typical high mass $2.0M_\odot$ (panel b), respectively. The dashed blue lines represent the PDFs obtained when chiral EFT (LD) filter is applied. We can see that this filter puts a constraint on the upper bound of the distributions. It rejects

[11]The value indicated in this reference was modified in the published version with respect to the first ArXiv version.

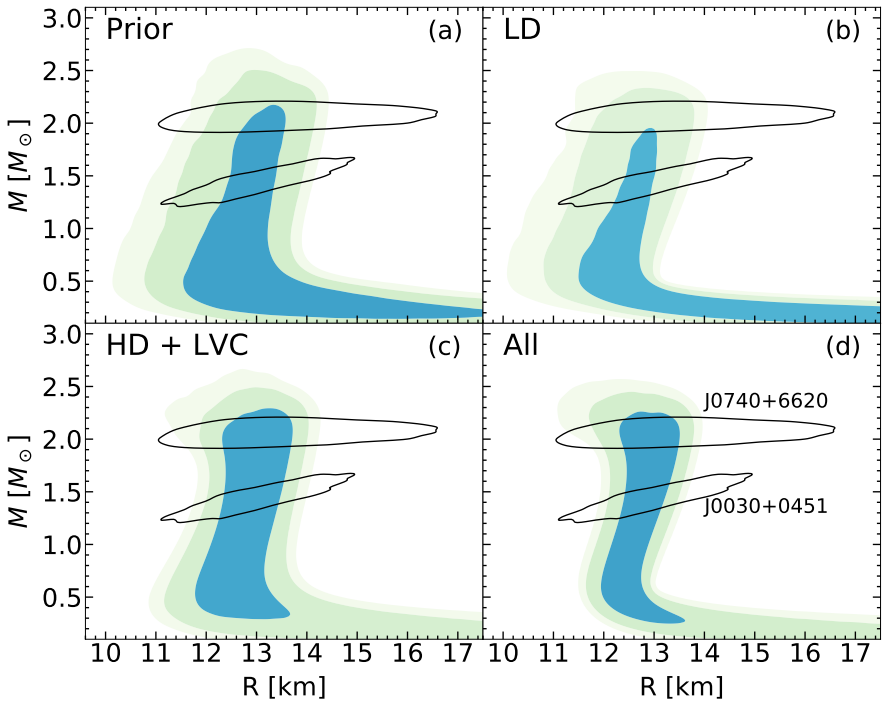

Figure 2.28: Two-dimensional density plots of NS mass M as a function of radius R in comparison with two NICER measurements at 68% (black contours). The three shaded regions in each panel contain 68%, 95%, and 99% of the distribution. See text for details. Figure reproduced from Ref. [184].

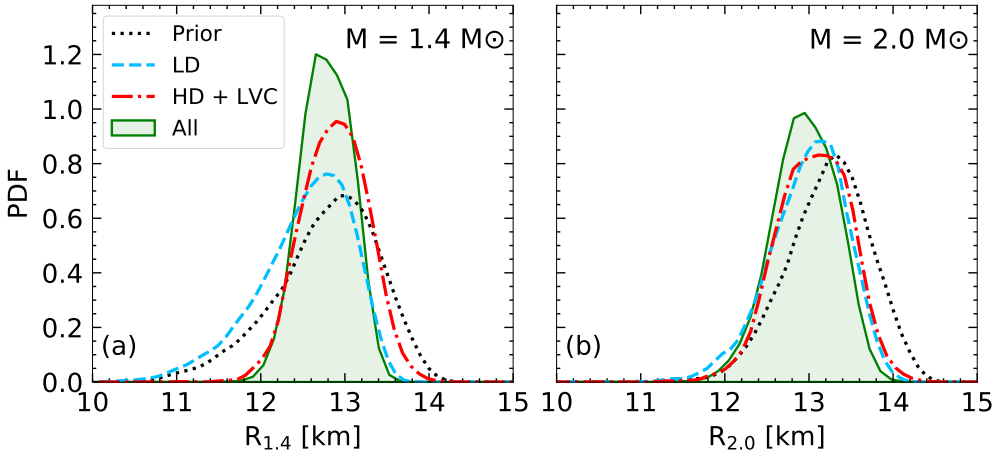

Figure 2.29: Probability density distributions of NS radii at $M = 1.4M_\odot$ (panel a) and $M = 2.0M_\odot$ (panel b). Figure reproduced from Ref. [184].

models with $R_{1.4} \gtrsim 13.6$ km and $R_{2.0} \gtrsim 14.0$ km. In the HD+LVC distribution for $1.4M_\odot$ NS, the constraint from GW170817 softens the EOS, hence constraining the upper bound of $R_{1.4}$, while the requirement on the NS maximum mass filters out very soft EOS, putting a limit to the lower bound of $R_{1.4}$. As a result, these two competing effects provide us with a relatively narrow range on the radius, namely $R_{1.4} \in [11.8, 14.0]$ km (see red dashed-dotted line in panel a). In the case of $R_{2.0}$, the constraint from the radio-timing mass measurement

of PSR J0348+0432 becomes redundant because all distributions must support $2.0M_\odot$ NS resulting in no effect on the lower value of $R_{2.0}$. Therefore, in the HD+LVC distribution of $R_{2.0}$, the constraint only comes from the LVC measurement. Furthermore, this figure also tells us that the impacts on $R_{2.0}$ from the gravitational signal GW170817 and chiral EFT calculation are very similar, even though they affect two different regions of the EOS. Specifically, the former controls the EOS in the NS core, hence the core radius, while the latter dominates the crust EOS, hence the crust thickness. The prediction in the form of median and 68% credible limits for $R_{1.4}$ ($R_{2.0}$) when all constraints are applied together is $12.78^{+0.30}_{-0.29}$ ($12.96^{+0.38}_{-0.37}$) km. In Miller *et al.* [38], the authors employed three EOS models, namely Gaussian, spectral, and piece-wise polytropes. The values of $R_{1.4}$ for these three models are respectively $12.63^{+0.48}_{-0.46}$ km, $12.30^{+0.54}_{-0.51}$ km, and $12.56^{+0.45}_{-0.40}$ km at 68% confidence limit. Despite the difference in EOS sampling methods, these results are in excellent agreement with the results obtained in the present work. Using also the likelihood from PREX-II measurement of the Pb skin, $R^{208}_{\rm skin}$ [191], Ref. [196] obtains $R_{1.4} = 12.75^{+0.42}_{-0.54}$ km, which is also consistent with our prediction.

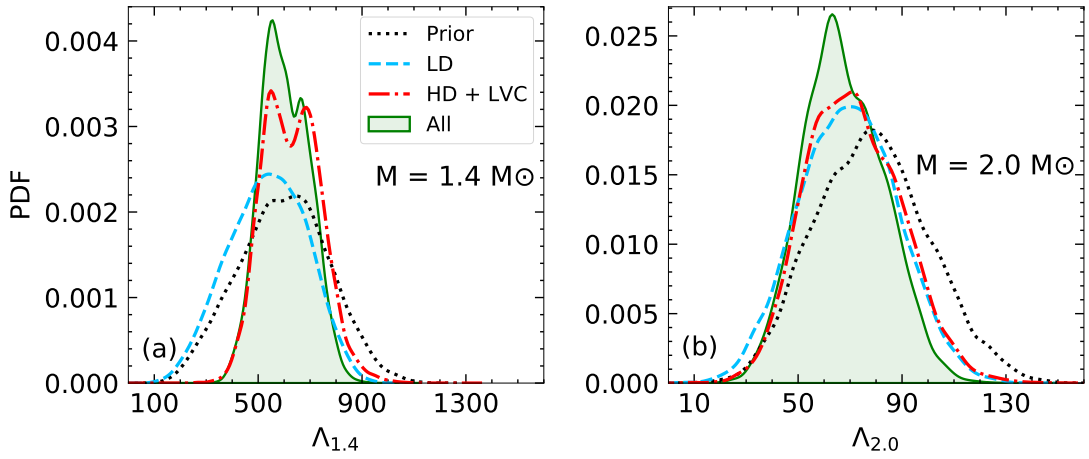

Figure 2.30: Probability density distributions of NS dimensionless tidal deformabilities at $M = 1.4M_\odot$ (panel a) and $M = 2.0M_\odot$ (panel b). Figure reproduced from Ref. [184].

The dimensionless tidal deformability Λ in Eq. (2.88) suggests a relation between Λ and R for a NS of given mass M. However, this relation is not straightforward due to the complex radius dependence of the tidal Love number k_2 [170]. The relation between R and Λ , particularly for the mass $M = 1.4M_\odot$ has been investigated in several works [197–200]. Interestingly, Fig. 2.30 shows that the distributions of $\Lambda_{1.4}$ and $\Lambda_{2.0}$ behave in accordance with the corresponding radius distributions in Fig. 2.29. This may indicate a strong positive correlation between these two quantities. The correlation between $R_{1.4}$ and $\Lambda_{1.4}$ is illustrated in Fig. 2.31.

In addition, we estimated the 90% confidence boundaries of $\Lambda_{1.4}$ ($\Lambda_{2.0}$) to be $\Lambda_{1.4} \in [463, 757]$ ($\Lambda_{2.0} \in [43, 94]$). This prediction of $\Lambda_{1.4}$ agrees excellently with the upper bound extracted from GW170817 signal in Ref. [39] using TaylorF2 model, that is, $\Lambda_{1.4} \leq 800$. The limit in $\Lambda_{1.4}$ has been improved in Ref. [40], in which the more realistic waveform PhenomPNRT was employed, and they obtained $\Lambda_{1.4} \in [70, 580]$ at 90% confidence level for

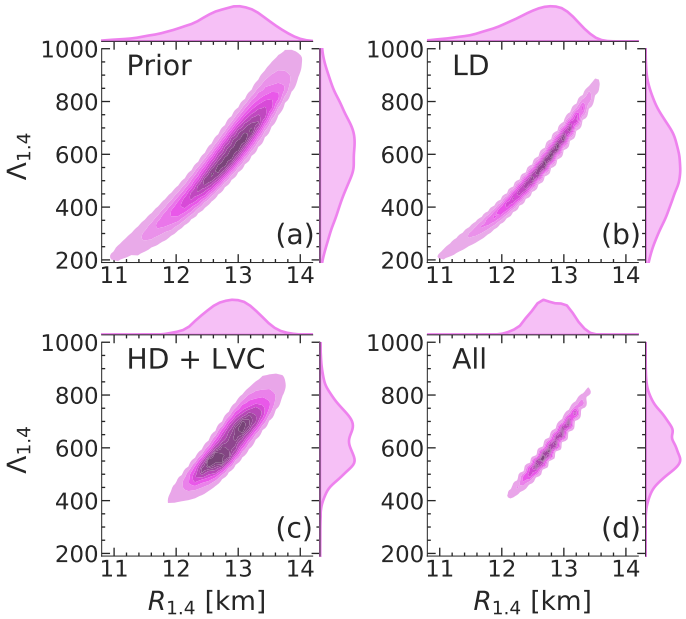

Figure 2.31: Joint probability density plots of NS dimensionless tidal deformability Λ and NS radius R at $M = 1.4M_\odot$ in the four distributions: Prior (panel a), LD (panel b), HD+LVC (panel c), and All (panel d). Figure reproduced from Ref. [201].

the EOS-insensitive analysis [39,40]. Our distribution is still compatible with this result, but it suggests a stiffer EOS in the nucleonic hypothesis.

Another quantity of interest that can be studied is the proton fraction, which is crucial for studying NS cooling. The most efficient cooling mechanism of NS is through the direct Urca (dUrca) neutrino emission process. This process is described by the successive following reactions:

$$n \to p + l + \bar{\nu}_l \tag{2.111}$$

$$p + l \to n + \nu_l, \tag{2.112}$$

where $l = \{e^-, \mu^-\}$. From the momentum and charge conservations, one can derive the expression for the threshold, below which the dUrca process is forbidden:

$$x_{\rm DU} = \frac{1}{1 + (1 + x_{ep}^{1/3})^3}, \tag{2.113}$$

where $x_{ep}(= x_e/x_p)$ is the ratio between electron and proton fraction. Values of $x_{\rm DU}$ can vary in the range from $x_{\rm DU} \simeq 1/9$ in the case of no muons ($x_{ep} = 1$) to $x_{\rm DU} \simeq 0.148$ at the limit of massless muons ($x_{ep} = 0.5$) [90,202].

As I have discussed previously, the proton fraction is sensitive to the isovector energy. Therefore, it can be constrained by the EFT filter, as we can see in Fig. 2.32 (orange band). Nonetheless, the LD filter can only narrow the x_p band in the low-density region. On the other hand, the astrophysical data are active at high densities, but their effect on x_p is not significant, resulting in large uncertainties at high densities. From this figure, we can also see that the dUrca process is predicted to occur at high densities, $\rho \gtrsim 5 \times 10^{14}$ g cm^3.

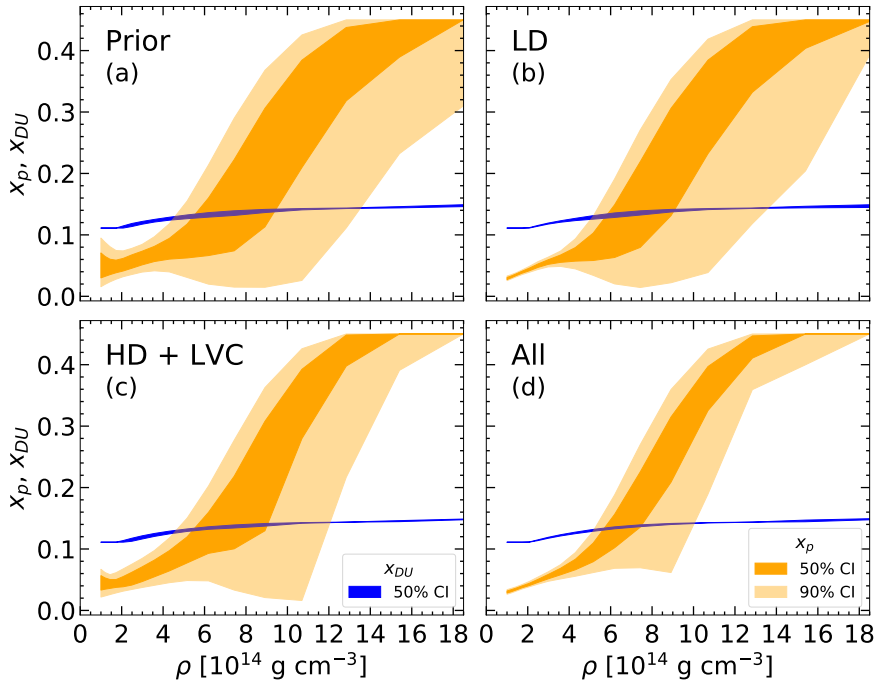

Figure 2.32: Evolution of x_p and $x_{\rm DU}$ as a function of mass-density in the four distributions.

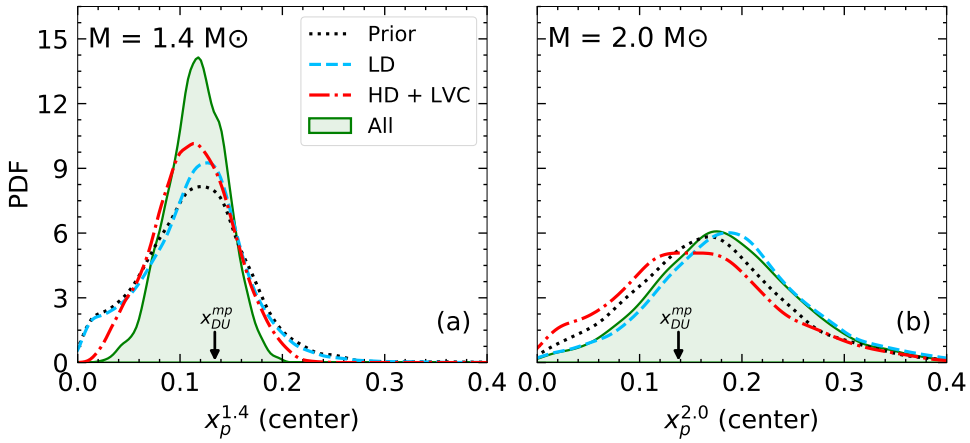

Figure 2.33: Probability density distributions of central proton fractions of NS for a NS with mass $M = 1.4M_\odot$ and $M = 2.0M_\odot$. The arrow in each panel indicates the most probable value of $x_{\rm DU}$. Panel a: $x_{\rm DU}^{\rm mp} \simeq 0.134$. Panel b: $x_{\rm DU}^{\rm mp} \simeq 0.138$. For both values of the NS mass, the values of $x_{\rm DU}^{\rm mp}$ are very similar in the four distributions. See text for details. Figure reproduced from Ref. [184].

Figure 2.33 shows the PDFs of proton fractions calculated at the center of NS with $M = 1.4M_\odot$ and $M = 2.0M_\odot$. The black arrow in each panel indicates the most probable value of $x_{\rm DU}$, calculated for the central density, denoted as $x_{\rm DU}^{\rm mp}$. We found that this quantity is independent of the constraint used (see Fig. 2.32). Furthermore, $x_{\rm DU}^{\rm mp}$ only depends weakly on NS mass, $x_{\rm DU}^{\rm mp} \simeq 0.134$ (0.138) for $M = 1.4$ (2.0) $M_\odot$. For both masses, the distributions of x_p extend to higher values than the corresponding threshold $x_{\rm DU}^{\rm mp}$. Therefore, it is possible for the dUrca process to operate even in NS of mass $1.4M_\odot$. Nevertheless, this fast cooling

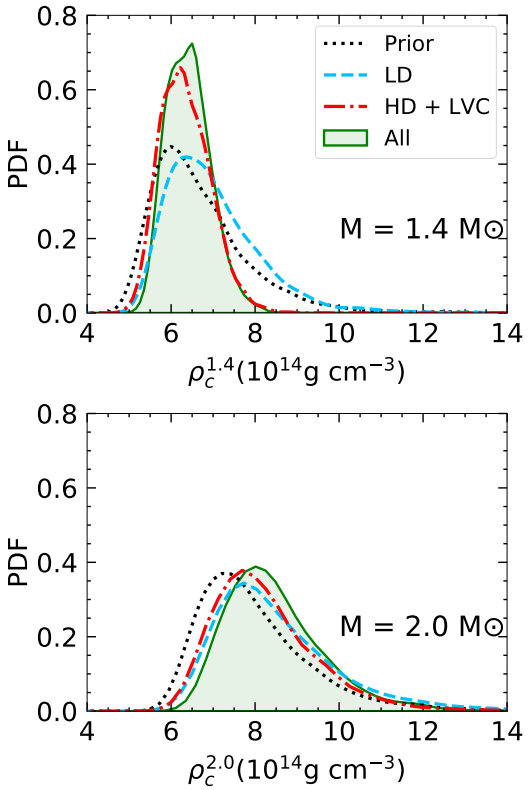

Figure 2.34: Distribution of the central mass density for M=1.4 $M_\odot$ and M=2.0 $M_\odot$ NS.

channel is more likely to happen in heavier NS due to the higher median and deviation of the x_p distribution. Indeed, Fig. 2.34 shows that for $M = 1.4M_\odot$ NS, the central mass density is centered around 6×10^{14} g cm^{-3}, while for $M = 2.0M_\odot$, it is 8×10^{14} g cm^{-3}. Combining this information with that in Fig. 2.32, we can expect both the value and uncertainty of x_p are higher in the heavier NS center.

By integrating the PDF to find the area under the curve for $x_p \geq x_{\mathrm{DU}}^{\mathrm{mp}}$, we estimated the possibility for the dUrca process in NS of mass $1.4M_\odot$ ($2.0M_\odot$) to be approximately 26% (72%). For a more quantitative evaluation, the predictions of NS central proton fractions along with the radius and tidal deformability for NS of mass $1.4M_\odot$ and $2.0M_\odot$ at 68% confidence limit are listed in Table 2.7 .

Table 2.7: Medians and 68% confidence intervals of NS radii, dimensionless tidal deformabilities, and central proton fractions at $M = 1.4M_\odot$ and $M = 2.0M_\odot$. Table reproduced from Ref. [184].

	$R_{1.4}$ [km]	$R_{2.0}$ [km]	$\Lambda_{1.4}$	$\Lambda_{2.0}$	$x_p^{1.4}$	$x_p^{2.0}$
Prior	$12.85^{+0.52}_{-0.69}$	$13.26^{+0.45}_{-0.52}$	601^{+171}_{-182}	78^{+23}_{-22}	$0.115^{+0.047}_{-0.052}$	$0.166^{+0.073}_{-0.070}$
LD	$12.61^{+0.45}_{-0.64}$	$13.03^{+0.39}_{-0.49}$	541^{+151}_{-162}	70^{+19}_{-19}	$0.117^{+0.041}_{-0.052}$	$0.187^{+0.072}_{-0.067}$
HD+LVC	$12.89^{+0.38}_{-0.40}$	$13.07^{+0.42}_{-0.44}$	626^{+114}_{-107}	71^{+20}_{-17}	$0.113^{+0.038}_{-0.039}$	$0.154^{+0.079}_{-0.074}$
All	$12.78^{+0.30}_{-0.29}$	$12.96^{+0.38}_{-0.37}$	598^{+105}_{-85}	66^{+18}_{-14}	$0.117^{+0.027}_{-0.030}$	$0.181^{+0.070}_{-0.065}$

2.3.4.2 Implication on the nucleonic EOS

Previously, I have discussed how the uncertainties in nuclear physics propagate to the uncertainties of different NS predictions. In this section, we will see how different data could help inferring additional properties on the nucleonic EOS.

Figures 2.35 and 2.36 show the probability density distributions (PDFs) of isoscalar and isovector empirical parameters of order $\mathscr{N} < 4$, respectively. As described previously, the distributions labeled as "Prior" are not flat, but they carry the information from the experimental nuclear mass measurement. For example, $E_{\rm sat}$, the energy per particle in SNM at saturation, already has a peaked shape (see Fig. 2.35a) because of this reason. From the HD+LVC distribution, we can see that the astrophysical constraints on NS mass and tidal deformability have almost no effect on the low-order parameters. The impact of the chiral EFT filter on the isoscalar parameters of order $\mathscr{N} < 3$, i.e., $E_{\rm sat}$, $K_{\rm sat}$, along with $n_{\rm sat}$ is not prominent, as can be also seen from Table 2.8; indeed, the LD filter hardly improves the constraints on the aforementioned isoscalar parameters. This can be explained by the fact that the prior intervals of the empirical parameters are chosen based on the current knowledge provided by nuclear physics, in which the deviations of $E_{\rm sat}$, $n_{\rm sat}$, and $K_{\rm sat}$ are already relatively small.

Table 2.8: Medians and 68% confidence limits of EOS empirical parameters of order $\mathscr{N} < 4$ in the four distributions. Table reproduced from Ref. [184].

	$E_{\rm sat}$ [MeV]	$n_{\rm sat}$ [fm^{-3}]	$K_{\rm sat}$ [MeV]	$Q_{\rm sat}$ [MeV]	$E_{\rm sym}$ [MeV]	$L_{\rm sym}$ [MeV]	$K_{\rm sym}$ [MeV]	$Q_{\rm sym}$ [MeV]
Prior	$-16.25^{+0.61}_{-0.46}$	$0.159^{+0.008}_{-0.006}$	231^{+27}_{-28}	-44^{+693}_{-650}	$32.6^{+3.5}_{-3.9}$	42^{+24}_{-22}	-62^{+181}_{-210}	-132^{+1394}_{-1290}
LD	$-15.90^{+0.51}_{-0.50}$	$0.163^{+0.005}_{-0.008}$	239^{+22}_{-30}	-264^{+383}_{-356}	$31.2^{+1.3}_{-1.3}$	43^{+11}_{-9}	-175^{+136}_{-131}	406^{+1026}_{-1116}
HD+LVC	$-16.20^{+0.60}_{-0.47}$	$0.161^{+0.006}_{-0.008}$	231^{+27}_{-27}	321^{+467}_{-596}	$31.4^{+4.0}_{-3.6}$	48^{+18}_{-19}	-2^{+121}_{-113}	502^{+891}_{-1054}
All	$-15.86^{+0.49}_{-0.50}$	$0.163^{+0.006}_{-0.007}$	249^{+15}_{-23}	-41^{+310}_{-267}	$30.9^{+1.3}_{-1.3}$	47^{+9}_{-9}	-74^{+78}_{-65}	1207^{+491}_{-539}

Unlike the lower-order parameters in the isoscalar sector, the isovector counterparts are quite poorly determined by nuclear physics experiments. As a result, once the constraint from the chiral EFT calculation is included, $E_{\rm sym}$, $L_{\rm sym}$ and $K_{\rm sym}$ are strongly affected (see Fig. 2.36 and Table 2.8). Interestingly, the LD filter also has a non-negligible impact on the high-order parameters $Q_{\rm sat}$ and $Q_{\rm sym}$. This is because the chiral EFT calculation gives very precise predictions at very low densities, far from nuclear saturation. In this region, the high-order parameters have a non-negligible contribution to the nuclear matter energy. It was shown by Refs. [121, 142] that constraining the EOS at very low densities $n \sim 0.02 - 0.1$ fm^{-3} is crucial in studying the crust-core transition.

As one may expect, the constraints from NS observables (HD+LVC) play an important role on high-order parameters, such as $Q_{\rm sat}$ and $Q_{\rm sym}$, as well as on the poorly constrained isovector compressibility $K_{\rm sym}$. One can observe that for these parameters, if the HD+LVC filters are included, higher values are preferred in the nucleonic hypothesis, thus disfavoring softer EOS. However, note that this is the net effect of both the $2M_\odot$ radio-timing mass measurement and GW180817 detection. We have checked that without the constraint on the tidal deformability, the resulted nuclear matter energies are even higher, which means that

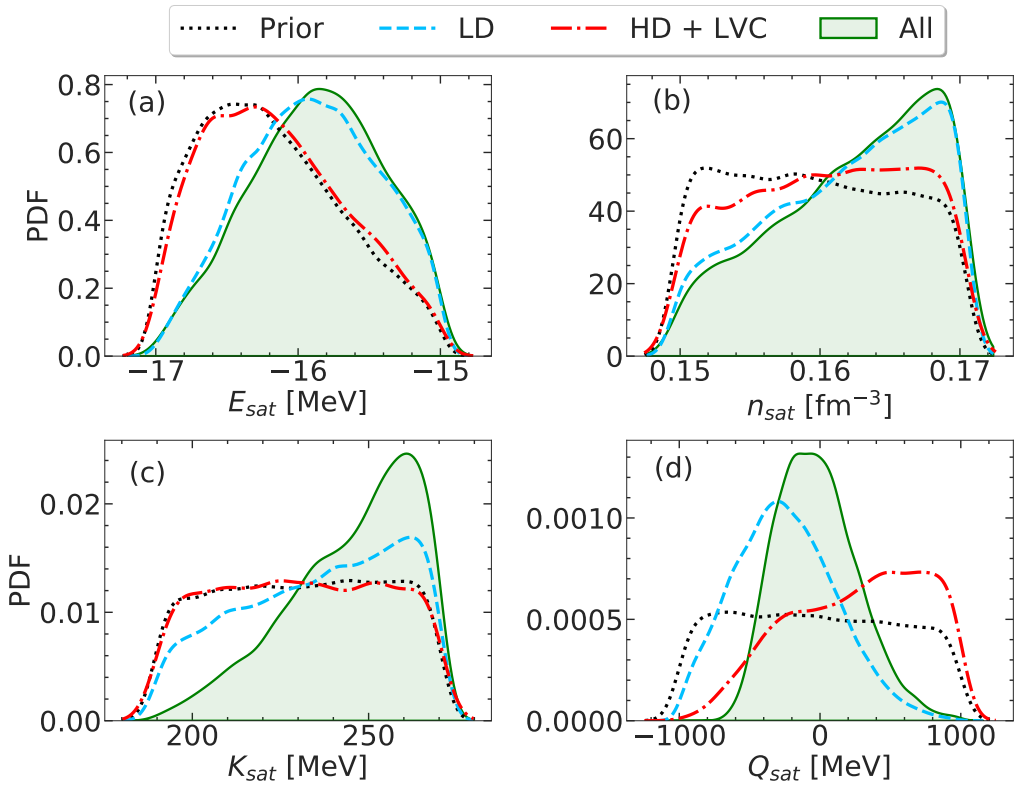

Figure 2.35: Probability density distributions of isoscalar empirical parameters for the prior distribution informed by experimental nuclear masses (black dotted line) and for posteriors of models passing through the low-density (chiral EFT) constraint (blue dashed line), high-density constraints (causality, stability, $e_{\rm sym} \geq 0$, maximum NS mass, and tidal deformability) (red dash-dotted line), and all constraints combined (green shaded region). See text for details. Figure reproduced from Ref. [184].

the constraint from GW170817 softens the EOS and that it is the mass measurement that tends to favor stiffer EOS.

As discussed in details in Ref. [64], the density behavior of realistic functionals can be accurately reproduced up to the central density of massive neutron stars by a Taylor expansion truncated at fourth order, but because of the truncation the parameters of order $\mathscr{N} \geq 3$ have to be considered as effective parameters that govern the high density behavior of the EOS, and do not need to be equal to the corresponding density derivatives at saturation. On the other hand, in the sub-saturation regime, the deviations from the Taylor expansion are accounted for by the low density corrective term that imposes the correct zero density limit [64], see also Eq. (2.16). These two effects being completely independent, the meaning of the third and fourth order parameters as explored by the EFT calculation and the astrophysical observations is not the same, and we can expect that low and high density constraints might point to different values for those parameters. Comparing the dashed and dashed-dotted lines in Fig. 2.35 we can see that indeed low-density constraints impose lower values of $Q_{\rm sat}$ with respect to high-density ones. This means that low-energy experiments aimed at a better measurement of $Q_{\rm sat}$ will not improve our empirical knowledge of the high density EOS. Interestingly, the same is not true for $Q_{\rm sym}$, for which the dotted and dash-dotted distributions

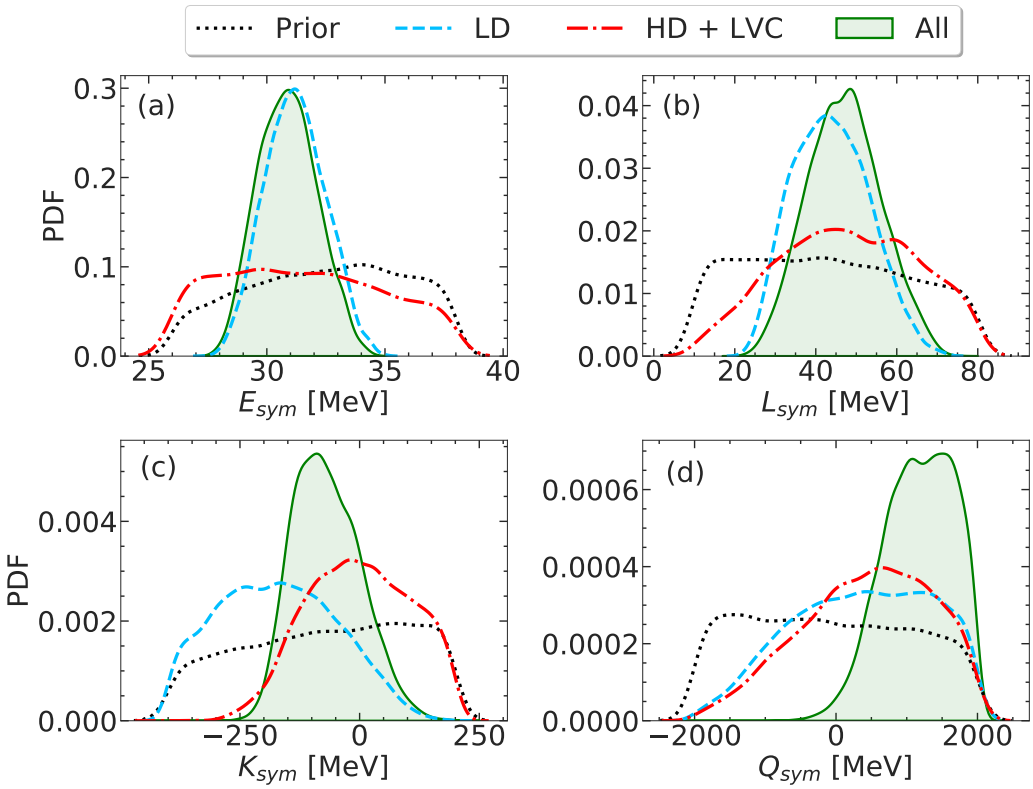

Figure 2.36: Same as Fig. 2.35 but for isovector empirical parameters.

closely overlap. Even if the present constraints are quite loose, it appears that the skewness of the symmetry energy at saturation $Q_{\rm sym}$ gives a fair description of the behavior of the EOS at high density, while a deviation is observed at the level of the compressibility $K_{\rm sym}$. The results for the fourth-order parameters $Z_{\rm sat,sym}$ are not included, because they have very large uncertainties, and very little impact from the different constraints. Furthermore, we will see later on that they have almost no correlations to other parameters or observables.

In Fig. 2.37, the bands for SNM energy per nucleon and symmetry energy are plotted at 50% and 90% confidence intervals for the four posterior distributions described in the previous section. The impact of LD and HD+LVC filters can be observed by looking at panels b and c of Fig. 2.37, respectively. Their effects become notable in different density regimes, as is also evident from the analysis done in Figs. 2.35 and 2.36 and Table 2.8. We can see that $e_{\rm SNM}$ and $e_{\rm sym}$ are relatively well determined up to $\sim 1.5 n_{\rm sat}$.

Unlike the crustal properties, HD+LVC filter is expected to put tighter bounds on global NS properties, which are governed chiefly by the high-density part of the EOS. The effects of different filters on the EOS are shown in Fig. 2.38. The light (dark) orange band indicates 90% (50%) confidence interval. For comparison, the result inferred from the gravitational wave data GW170817 by LVC are also displayed, showing on the x-axis the mass density in CGS units, at 90% level are in dashed blue lines [40]. In Ref. [40] , Abbott *et al.* have sampled their EOS at high density using the spectral parametrization [203]. These EOS are then matched with SLy EOS [204] at around $\sim \rho_{\rm sat}/2$. The authors also put some prior criteria similar to

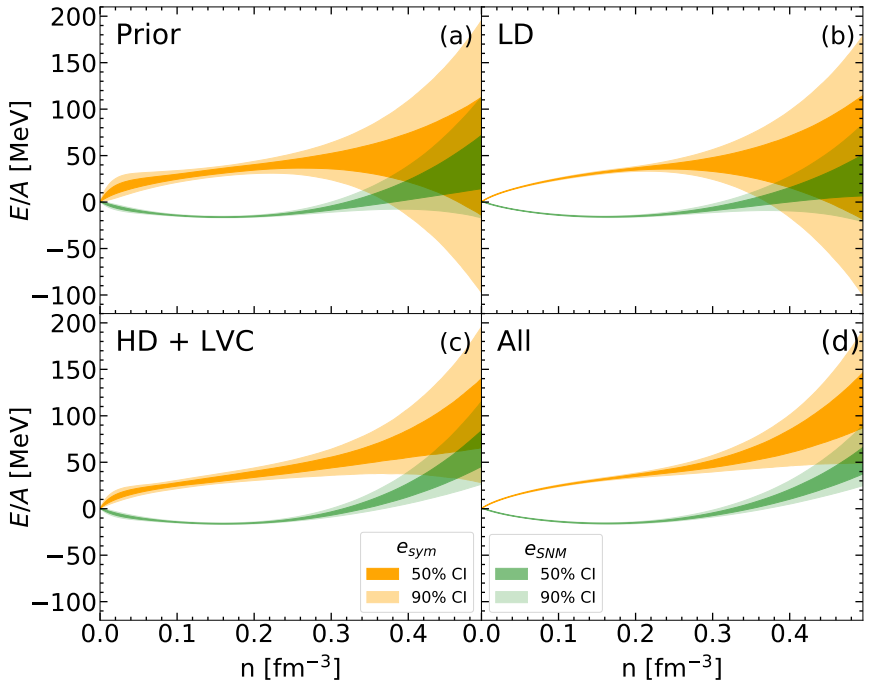

Figure 2.37: 50% (darker color) and 90% (lighter color) confidence intervals of energy per nucleon of symmetric nuclear matter ($e_{\rm SNM}$, green) and symmetry energy ($e_{\rm sym}$, orange) as a function of nuclear matter density n. Figure reproduced from Ref. [184].

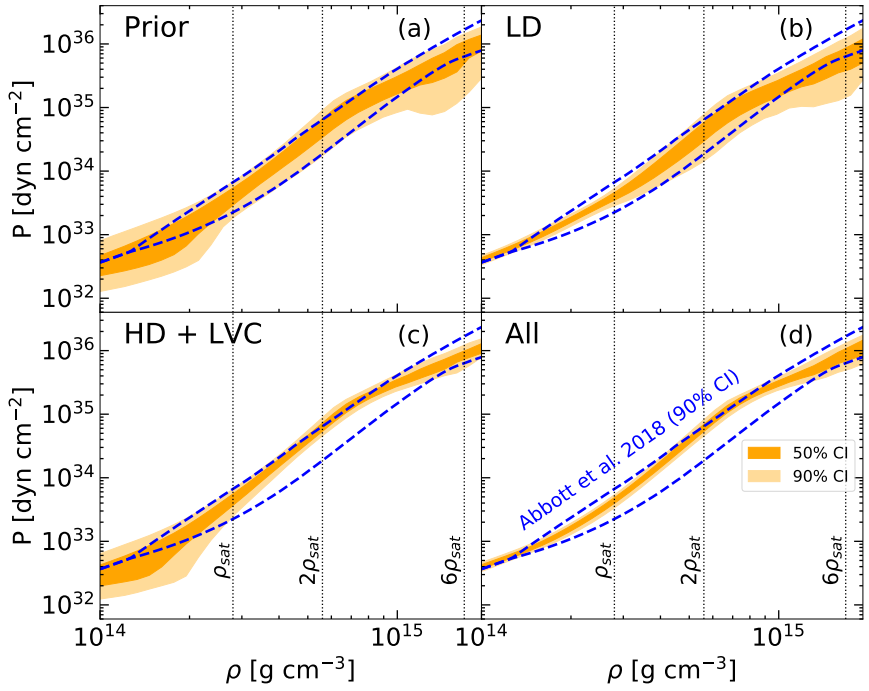

Figure 2.38: 50% (dark orange) and 90% (light orange) confidence intervals of pressure P as a function of mass density ρ in comparison with the 90% confidence interval of the posterior obtained in Abbott *et al.* 2018 [40] (blue dashed lines). See text for details. Figure reproduced from Ref. [184].

our analysis, which are causality, thermodynamic stability, and consistency of NS maximum mass with the observation. For the last condition, they put a sharp limit ($M_{\rm max} \geq 1.97 M_\odot$) instead of using a likelihood like the one used in our analysis (see Eq. (2.103)). However, we have verified that the difference in the maximum NS treatment does not lead to sizable deviation in the final results. In Fig. 2.38a, we can see that our prior distribution is in good agreement with the whole posterior band given by GW170817 event [40]. In our case, the prior distribution carries information from nuclear physics experiments via the chosen prior intervals of empirical parameters as well as the mass fit. This is why the EOS in our prior distribution at low densities is relatively narrow compared to other analyses. Note that the uncertainty below $\rho_{\rm sat}$, appears to be large due to the visual effect of the logarithmic scale in the pressure. Once the chiral EFT filter is applied, this uncertainty is vastly reduced (see Fig. 2.38b), resulting in a very well-constrained band in excellent agreement with the posterior constrained by GW170817 data [40]. Contrarily, the behavior of the EOS at supra-saturation densities is not constrained by the chiral EFT filter. As a result, a larger dispersion is observed at high densities. This dispersion is not as large as in fully agnostic studies [205] because of the nucleonic hypothesis that imposes an analytic behavior of the EOS at all densities. This strong hypothesis can be challenged by astrophysical measurements, and any inconsistency with the observations would reveal the presence of exotic degrees of freedom.

By incorporating the pass-band filter $\omega_{\rm HD}$ as well as the condition on the NS maximum mass in Fig. 2.38c, the deviation in the lower limit of the pressure at density $\rho \gtrsim 10^{15}$ g cm^{-3} observed in the prior, is very much reduced. In particular, the constraint on the NS maximum mass sets a stringent limit on the lower bound of the pressure, and the posterior EOS is shifted significantly towards higher values of pressure. Conversely, the constraint from LVC favors softer EOS, hence setting the limit on the upper bound of the pressure band. In Fig. 2.38d, when all constraints are combined together, we obtain as expected a narrower band for the EOS than the one obtained exclusively from GW170817 data [40]. In addition, we observe that our EOS is lightly stiffer than the one of Ref. [40] at around $2-3\rho_{\rm sat}$. The small width of the EOS and its stiffness are assigned to the semi-agnostic nucleonic prior, which represents current nuclear physics knowledge. Nevertheless, the overall agreement is excellent, thus indicating the compatibility of the nucleonic EOS with the gravitational wave GW170817 data.

Comparing the "HD+LVC" and "All" distributions in panels c and d Fig. 2.38, it can be observed that the inclusion of the new NICER measurement [37, 38] does not show any significant impact on the EOS. Similar conclusions have been drawn in other studies in the literature. In particular, Pang *et al.* [185] carried out a Bayesian analysis using the data from Riley *et al.* [37] and Miller *et al.* [38]. In both cases, they found that the constraint from the radius measurement of PSR J0740+6620 only marginally impacts the EOS. In Ref. [206], Raaijmakers *et al.* performed the Bayesian inference with two EOS parametrizations, namely a piece-wise polytropic model and a speed-of-sound model, and drew similar conclusions. For the constraint on PSR J0740+6620, they employed the data from Riley *et al.* [37], in which the error bar of the radius is smaller than that obtained in Miller *et al.* [38]. They concluded that for the piece-wise polytropic models, the impact on the EOS mainly comes from the high mass value of PSR J0740+6620 because their prior distribution in that mass range is

within the 68% level of the radius measurement (see Fig. 4 in Ref. [206]).

2.3.4.3 Pearson correlation studies

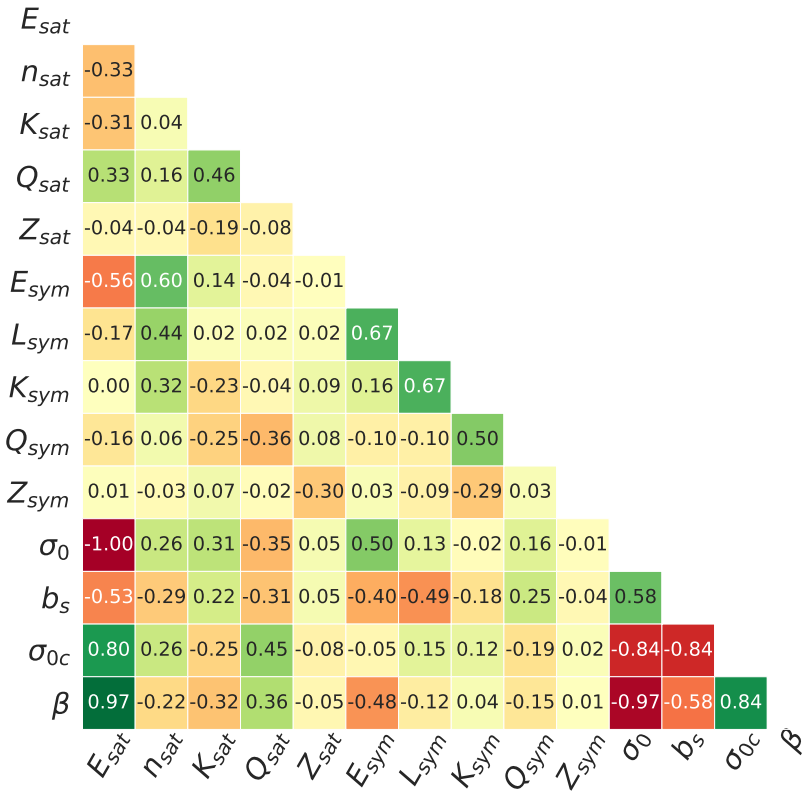

Figure 2.39: Pearson correlation matrix among bulk and surface empirical parameters in the case all filters are applied. Figure reproduced from Ref. [184].

Studying correlations among parameters and observables reveals a lot of information on the many facets of multi-parametric model calculations [141]. The most frequently employed tool for this purpose is the linear Pearson correlation, which is defined for two quantities x and y (x, y can be parameters of the model or any observable calculated from it) as,

$$\mathrm{corr}(x, y) = \frac{\mathrm{cov}(x, y)}{\sigma_x \sigma_y}, \tag{2.114}$$

where $\mathrm{cov}(x, y) = \langle xy \rangle - \langle x \rangle \langle y \rangle$, with $\langle\rangle$ denoting averages, is the covariance between x and y, and σ_x (σ_y) is the standard deviation on x (y).

Figure 2.39 displays the Pearson correlation coefficients among all bulk, surface, and curvature parameters in the case where all constraints are applied. Since the bulk parameters are initially by construction uncorrelated in the flat prior distribution, we can easily assign the induced correlations to the different filters employed. One can see that there is an almost perfect negative correlation between the surface tension of symmetric matter σ_0 and the saturation energy E_{sat}, with $\mathrm{corr}(\sigma_0, E_{\mathrm{sat}}) = -1$. A similar result was found in Ref. [127].

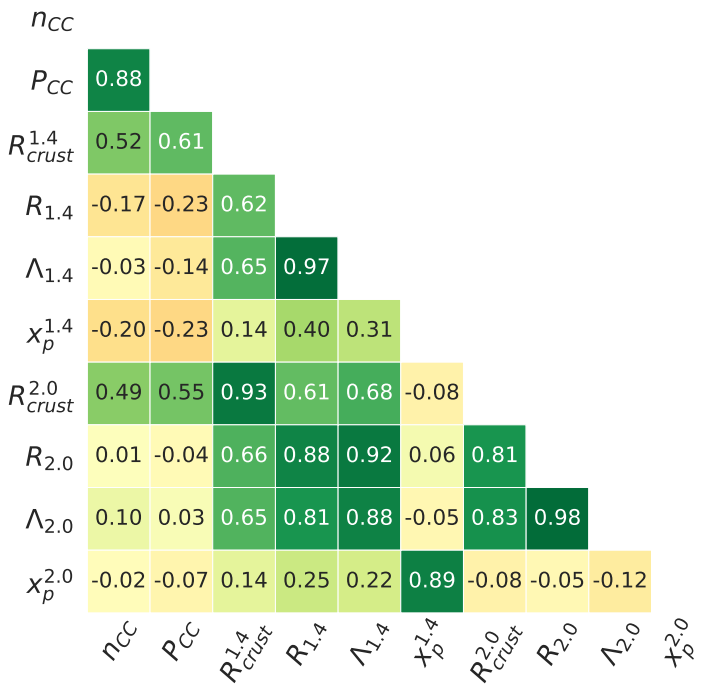

Figure 2.40: Pearson correlation matrix among some observables in the case all filters are applied. Figure reproduced from Ref. [184].

The parameters associated to the curvature (σ_{0c} and β), on the other hand, exhibit strong positive correlations with $E_{\rm sat}$. These correlations appear due to the fit of the surface and curvature parameters to the experimental AME2016 mass table [135]. In addition, if the prior is only constrained by the experimental binding energy of nuclei, we also find a strong correlation between b_s and $E_{\rm sym}$, which are the two main parameters governing the energy of asymmetric nuclear matter. However, once the filter from chiral EFT calculation is applied, $E_{\rm sym}$ is tightly constrained, and hence the correlation gets blurred. Similar to Refs. [65, 127], no significant correlations are found to be induced by the astrophysical constraints. This can be understood from the fact that the astrophysical observations are only sensitive to the beta-equilibrium EOS, and there is a degeneracy between the symmetric EOS parameters and the ones associated to the symmetry energy [207]. The correlations among the bulk parameters shown in Fig. 2.39 thus basically result from the chiral EFT constraint. In particular, the symmetry energy $E_{\rm sym}$ has a moderate (anti)correlation with ($E_{\rm sat}$) $n_{\rm sat}$. Stronger correlations are found among the isovector parameters, which are $\mathrm{corr}(E_{\rm sym}, L_{\rm sym}) = 0.67$ and $\mathrm{corr}(L_{\rm sym}, K_{\rm sym}) = 0.67$. The former is found in several works (see Refs. [127, 189, 208] and references therein for a review), and the latter is also studied in Refs. [209–214]. Slight correlations between high-order parameters, $K_{\rm sat} - Q_{\rm sat}$ and $K_{\rm sym} - Q_{\rm sym}$, are also induced due to the narrow EFT energy bands at very low densities.

Correlations among different observables found in our study are plotted in Fig. 2.40. The strongest correlations in this matrix are the well known ones between radius and dimensionless

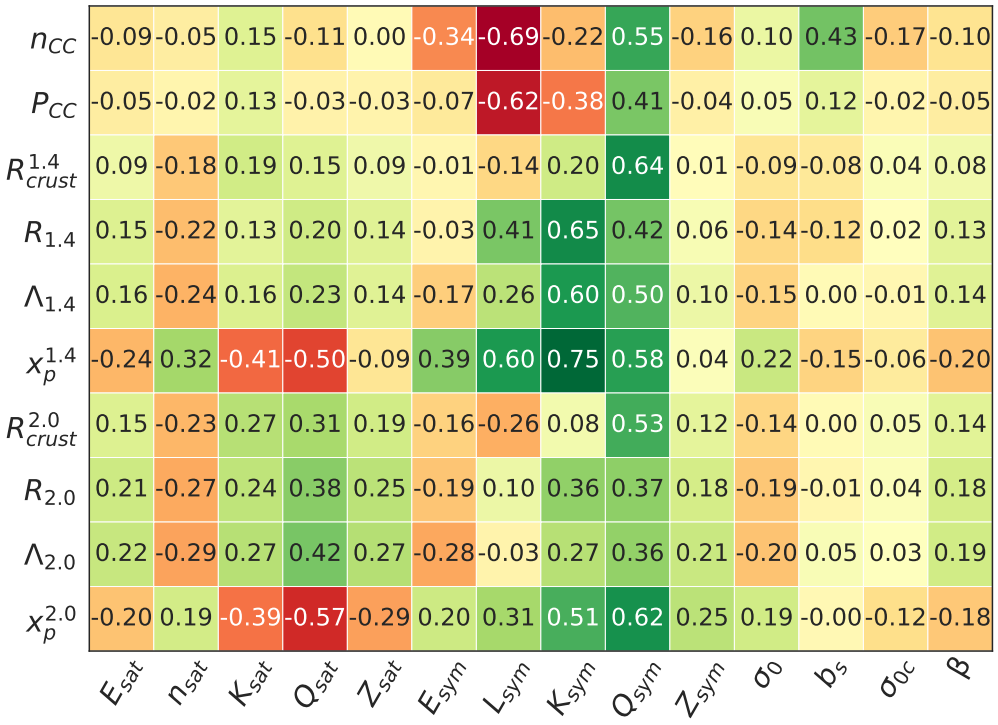

Figure 2.41: Pearson correlation coefficients between some observables with the empirical and surface parameters in the case all filters are applied. Figure reproduced from Ref. [184].

tidal deformability, $\mathrm{corr}(R_{1.4}, \Lambda_{1.4}) = 0.97$ and $\mathrm{corr}(R_{2.0}, \Lambda_{2.0}) = 0.98$. This explains the similarity in the distributions of R and Λ seen in Figs. 2.29 and 2.30, and confirms the result obtained in Fig. 2.31. There is also a strong positive correlation between $n_{\rm CC}$ and $P_{\rm CC}$. This correlation is visible also in the joint distribution plot in Fig. 2.25 (panels b and d). I have mentioned before that the determination of the transition point from the crust to the core is important in predicting crustal observables; this is again confirmed by the correlation coefficients between the crust thickness and the transition density and pressure.

Finally, the correlations between the observables and parameters are shown in Fig. 2.41. For most of the cases, the most influential parameters are from the isovector channel, namely $L_{\rm sym}$, $K_{\rm sym}$, and $Q_{\rm sym}$. The only exception is for the proton fraction, where high-order isoscalar parameters appear to have an impact and exhibit negative correlations. This correlation study clearly demonstrates that astrophysical observables have some marginal influence on the higher order nuclear matter properties, which points towards two conclusions: (a) the low density nuclear physics data have big influence on constraining the lower order parameters; (b) we need more precise astrophysical data to tighten the constraints on higher order parameters. Conversely, to have more accurate prediction on astrophysical properties, we need to reduce the uncertainties in these higher-order parameters from other sources, e.g., heavy ion collisions [215].

2.4 Conclusions

In this chapter, I presented the formalism for constructing unified EOS for NS within the meta-modeling technique. To describe the crust, we employed a CLDM approach, in which the surface parameters are obtained from the fit to the AME2016 mass table. At each given thermodynamic condition, the composition of the crust was obtained at beta equilibrium from the variational procedure. Then, the static NS global and crustal properties were calculated by solving the TOV equations.

To propagate the uncertainties in nuclear physics to the NS predictions, we performed a Bayesian inference. In this analysis, we have jointly analyzed different constraints on the nuclear matter EOS coming from nuclear experiments, *ab initio* nuclear theory, and several new astrophysical observational data, including the very recent simultaneous observation of mass-radius distributions of PSR J0030+0451 and PSR J0740+6620 from the NICER collaboration as well as the observation of tidal deformability in the GW170817 event by LVC. Imposing all these different constraints in a Bayesian framework, we have challenged the hypothesis of a fully analytical (continuous and derivable at all orders) EOS, as obtained in the case where dense baryonic matter is purely constituted of neutrons and protons without any phase transition or exotic degrees of freedom.

Particularly, we have observed that if we have a nuclear-physics-informed prior including the binding energy data of the whole nuclear chart and chiral EFT constraints on low-density SNM and PNM, the posterior for mass-radius of NS are already in line with NICER observations. Contrarily, important bounds on high-density matter are put from radio astronomy observation of NS mass and GW170817 data on tidal deformability. With the present knowledge on astrophysical observations, we predict that the direct Urca cooling is possible with non-negligible probability (27%) even in a NS with mass as low as $1.4M_{\odot}$, which increases much further $\sim 72\%$ for a NS of $2.0M_{\odot}$. This might also be very crucial to (in)validate the nucleonic hypothesis of high-density matter. As all current data on astrophysical observations comply with the nucleonic hypothesis within our metamodel approach, we need more stringent constraints from observations to conclusively establish (or definitively reject) the presence of exotic degrees of freedom in high-density matter.

CHAPTER 3

Inner crust of cold–catalyzed neutron stars

Conventionally, matter in the inner crust of a NS is studied using the WS approximation with the assumption of sphericity. That is, the NS crust is divided into spherical WS cells, each of which contains a spherical nucleus in its center (see Chapter 2). This premise comes from the fact that ordinary nuclei found in terrestrial laboratories are more or less spherical. In the low-density regions of a NS, such as in the outer crust or the outer part of the inner crust, this spherical symmetry of nuclei is well supported by the predominance of nuclear self-energies, namely surface and self-Coulomb energies. As the density increases, the distance between neighboring nuclei decreases, and the lattice contribution in the total Coulomb energy prevails. Accordingly, non-spherical geometries, known as "pasta phases", can appear [12, 216]. The presence of pasta has been robustly predicted in several works [121, 131, 134, 137, 142, 217]. Particularly, it was shown that the pasta layer could contribute up to $\sim 10 - 15\%$ of the crust thickness and to $\sim 50\%$ of the crust mass.

This chapter is organized as follows. In Sect. 3.1, I present a brief introduction to the pasta phases. Particularly, I summarize the recent progress in the studies of these exotic structures (Sect. 3.1.1) and discuss the importance of their possible existence on astrophysical observations (Sect. 3.1.2). Then, I describe how we model pasta phases in Sect. 3.2 and discuss the results obtained using different energy functionals in Sect. 3.3. Interestingly, the properties of the inner crust in the pasta region turn out to be strongly model-dependent. As a result, in Sect. 3.4, we perform a Bayesian inference in order to quantitatively assess the uncertainties of the predictions. Moreover, the influence from the surface as well as the bulk terms are thoroughly discussed. Finally, conclusion can be found in Sect. 3.5. Some of the results presented in this chapter were published in Refs. [121, 142, 217].

3.1 Introduction to the pasta phases

3.1.1 A brief historical overview

From the theoretical point of view, the pasta phases have been explored and discussed in many studies, see, e.g., Refs. [12, 13, 76, 86, 89, 134, 151, 216, 218–225] and references therein. In the following, I present briefly the historical evolution of research on the pasta phases.

The existence of pasta phases, particularly the *bubble* phase, at high densities in the crust was already suggested in the pioneering work on NS matter by Baym, Bethe, and Pethick in 1971 [9]. Specifically, in this paper, the authors stated that when the nucleus occupies more than half of the space in the WS cell, i.e., $u = \frac{V_N}{V_{\rm WS}} \geq 0.5$, it might be more favorable for the nucleus to "turn inside out". In this case, the inner crust would contain a lattice of neutron gas inside bubbles, surrounded by denser nuclear matter. Even though the *bubble* structure also has spherical symmetry, it is different from the standard *sphere* configuration, since in the latter case the denser nuclear matter (the cluster) is located at the center of the WS cell. Therefore, typically, the *bubble* phase is also categorized as "pasta".

In the early 80s, other, non-spherical, shapes, particularly two-dimensional (*rod*, *tube*) and one-dimensional (*slab*) geometries, were further investigated by Ravenhall *et al.* [12] and Hashimoto *et al.* [216]. Within a liquid drop approach, both studies found that the ground state of matter changes from spherical to non-spherical structures, in the following order: spheres → rods → slabs → tubes → bubbles. Due to the resemblance with the Italian pasta, the *rod*, *slab*, and *tube* phases are sometimes also referred to as *spaghetti*, *lasagna*, and *bucatini*. Shortly after these two works, in 1985, William and Koonin [226] performed a microscopic study on these phases using the TF approximation employing the Skyrme III functional, and they also found the same hierarchy for the appearance of pasta. These findings were later confirmed by Lorentz *et al.* [137] using the HF method.

Following these seminal papers, over the last decades, numerous studies have been conducted on nuclear pasta, using different approaches. They include CLDM (see e.g., Refs. [121, 126, 131, 134, 137, 138, 142, 227–229] for recent works), ETF method (e.g., [74, 76, 126, 138, 220, 230–233]), Skyrme-HF calculations (e.g., [234–236]), molecular dynamics calculations (e.g., [10, 222, 237–239]), and HF+BCS method (e.g., [219, 240, 241]). For a review, see also Refs. [28, 58, 128, 218, 242] and references therein.

Besides the five traditional phases of inhomogeneous matter that I have just listed, recently, many works were devoted to investigating more complex structures. For instance, in 2009, Nakazato *et al.* [223] employed a CLDM to study the so-called *gyroid* and *double-diamond morphologies* shapes, which are periodic bicontinuous structures discovered in a block copolymer. Interestingly, they showed that the gyroid phase is expected to appear near the transition from rods to slabs, at a volume fraction similar to that in the polymer system, that is, $u \approx 0.35$. It is natural to expect that the complexity of the structure of inhomogeneous matter could lead to strong implications in the dynamic properties of NS. Indeed, in 2014, with a classical molecular dynamics model, Alcain *et al.* [243] showed that unusual pasta shapes, such as *intertwined lasagna*, could be more efficient in scattering neutrinos of the same momentum than usual pasta. Within the same approach as [243], the topological defects of the pasta slabs were studied in Refs. [237, 238]. Furthermore, another

structure called *nuclear waffles*, was also explored in the work of Ref. [244]. This phase has an interesting topology formed of perforated plates, and it was found to appear in the transition between the spaghetti phase and the lasagna phase. Similar to the previous molecular dynamic studies, this calculation was done at a fixed proton fraction (from 0.1 to 0.4), density ($0.05\ \mathrm{fm}^{-3}$), and temperature (around 1 MeV). At the same thermodynamic conditions (density and temperature), in a system with 40% of protons, a structure called *parking-garage*, inspired by the helical structures found in cell biology, was studied in Ref. [245].

The non-traditional nuclear shapes, such as waffles or defects, seem to appear only at the transition from spaghetti to lasagna and lasagna to bucatini and to correspond to very narrow layers compared to the standard pasta structures [218]. Moreover, the inclusion of the surface and Coulomb energy calculation for these structures is complicated and numerically expensive. For this reason, all the studies mentioned above were performed for selected thermodynamic conditions at fixed density, proton fraction, and temperature. Since our aim is to perform a study of the (cold) NS inner crust in the whole density range and in beta equilibrium, we only consider the five geometries as originally proposed by Ravenhall *et al.* [12], namely spheres, rods, slabs, tubes, and bubbles.

3.1.2 Implication of the pasta phases on astrophysical observations

From the observational point of view, up to now, there is still no direct evidence of the existence of the pasta phases. Nevertheless, the presence of these exotic configurations can potentially have important impacts on various supernovae (SN) and NS phenomena [218,242]. I discuss them in the following.

Neutrino scattering in the collapse phase of SN: In the SN core-collapse dynamics, the interaction between neutrinos and the nucleons/nuclei plays a crucial role. Particularly, it is expected that the neutrino-pasta scattering could affect the onset, the timescale associated to neutrino trapping, as well as the value of the lepton fraction during the collapse [242]. Moreover, it was shown that neutrino excitation of the low-energy modes of the pasta could allow a significant energy transfer to the nuclear medium, possibly reviving the stalled SN shock [246]. As a result, measurements of neutrinos emitted from SN explosion might provide us with indication of the existence of the pasta structure. Indeed, it was shown that the additional opacity from the coherent scattering of neutrinos on pasta slows the neutrino diffusion. Consequently, it increases significantly the neutrino signal at later times of ≥ 10 seconds after the core collapse [247].

NS cooling: The existence of the pasta phases could also affect the cooling of NS by neutrino emission, and this has been postulated and/or investigated by several works, e.g., [137, 222, 237, 248, 249]. For instance, Lorentz *et al.* 1993 [137] suggested that the neutrino generation in NS cooling needed to be reconsidered with the inclusion of the non-spherical nuclear shapes. Particularly, they pointed out that rapid cooling processes such as neutrino-antineutrino pair bremsstrahlung and direct Urca could be affected by the non-spherical nuclear geometries. As mentioned in Chapter 2, the direct Urca is the most efficient cooling process in a NS. However, it is allowed only at sufficiently high densities. Therefore, this process is forbidden in the cores of low-mass NS because of energy and momentum conservation law. In 2004, Gusakov *et al.* [248] calculated the neutrino emissivity in the tube and

bubble phases of the inner crust, and they showed that the direct Urca process is allowed in these two phases. Indeed, thanks to the periodic potential created by the nuclear pasta, the nucleons acquire sufficiently large quasi-momenta to satisfy the momentum conservation in the interaction with neutrinos. Recently, Lin *et al.* [222] presented an improved calculation in this regard using a broad variety of pasta phases and with large-scale molecular dynamics simulations. They found that the neutrino luminosity due to a direct Urca process in the pasta phases can be 3-4 orders of magnitudes larger than that from the modified Urca process in the core. One may therefore expect that data on NS cooling could be used to acquire information on the existence and possibly to constrain the properties of the pasta phases.

Transport properties: Pasta phases can also strongly impact the transport properties of NS, see, e.g., Refs. [55, 56, 237, 238, 250–252], and their existence has been claimed to help explaining the observations of magnetic [56] and thermal evolution [55] of NS. For example, in the observations of the spin-down behavior of rotating NS, it was noticed that very few isolated X-ray pulsars spin with a period exceeding $\approx$ 10 seconds. Since the spin-down process is governed chiefly by the magnetic dipole radiation, it relates closely to the crust transport properties, particularly the electrical resistivity. Specifically, it was shown that the low upper-limit period of isolated X-ray pulsars could be due to the presence of a layer with low electrical conductivity at the bottom of the crust, which would correspond to a layer made up of nuclear pasta [56]. Consequently, this could be a promising indication of the amorphous structure in the crust, whose properties may be constrained by future X-ray timing data.

Crust oscillations: In Ref. [253], it was demonstrated that the nuclear pasta phases have elastic properties of a liquid crystal, rather than a conventional solid[1]. Based on this suggestion, the effect of the pasta layer on the torsional crustal shear mode was subsequently investigated [254, 255]. In particular, Sotani [254] and Gearheart *et al.* [255] showed that because of the presence of the pasta layer, the shear mode frequency is considerably smaller than that expected if one considers only spherical nuclei, thus underlying the role of pasta phases in understanding stellar oscillations. Furthermore, the authors of Ref. [255] showed that the pasta phase could also cause a decrease in the maximum quadrupole ellipticity sustainable by the crust by up to an order of magnitude. Therefore, astrophysical observations of gravitational wave data could possibly probe the presence of pasta phases.

Last but not least, the existence of the pasta phase is also believed to influence the glitch phenomena. Nonetheless, despite the speculation that the non-spherical structure could significantly impact the pinning of superfluid neutron vortices to nuclei [137, 242, 256, 257], to our knowledge, no work has been conducted on this topic so far.

3.2 Modeling of the pasta phases

To study the pasta-phase properties in catalyzed NS, we employ a CLDM, in which the bulk energy is calculated using the meta-modeling approach [64, 65], and the surface parameters are optimized from the AME2016 table [135]. The formalism is the same as that presented in Sect. 2.1.2. In particular, we keep the same set of variational variables (r_N, n_i,

[1] This is the reason why they referred to the pasta layer as "mantle" rather than as part of the "crust".

I, n_p, n_{gn}), which are obtained by solving the system of Eqs. (2.68)-(2.71). The geometry of the nucleus enters in the expression of the cluster energy, see Eq. (2.52). For convenience, let us re-write here the expression:

$$E_i = (A - Z)m_n c^2 + Zm_p c^2 + E_{\rm bulk} + E_{\rm Coul+surf+curv,d}, \tag{3.1}$$

where I have added a subscript d to indicate the terms which depend on the cluster geometry.

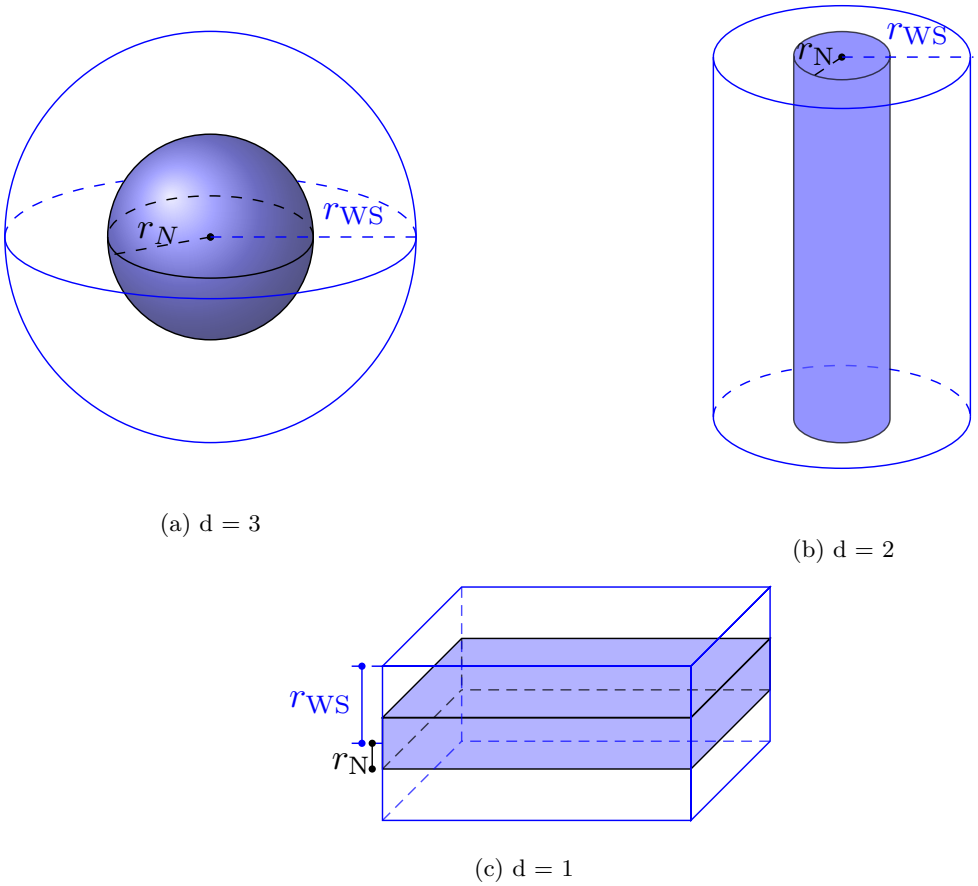

(a) d = 3

(b) d = 2

(c) d = 1

Figure 3.1: Nuclear geometries considered here: $d = 3$ (panel a), $d = 2$ (panel b), and $d = 1$ (panel c). For the *normal* phases (spheres, rods, slabs), the denser nuclear matter occupies the blue region, that is, $l \leq r_N$, where l is the distance from the center (for $d = 3$) or from the symmetry axis (for $d = 2$)/plane (for $d = 1$). For the *inverted* phases (tubes, bubbles), the denser nuclear matter occupies the white region, $r_N < l \leq r_{\rm WS}$.

As mentioned before, in this work, we only consider the five conventional geometries: spheres, rods, slabs, tubes, and bubbles. Thus, the dimensionality d takes integer values: $d = 1$ (slabs), $d = 2$ (rods, tubes), and $d = 3$ (spheres, bubbles). The illustration of these geometries is displayed in Fig. 3.1. In the case of *normal* phases, which are spheres, rods, and slabs, the denser nuclear matter occupies the blue regions, that is, $l \leq r_N$, where l is the distance from the center or from the symmetry axis/plane. On the other hand, in the case of *inverted* phases, which are tubes and bubbles, the location of the denser nuclear matter and the neutron gas is exchanged. Thus, the denser nuclear matter occupies the white region, that is, $r_N < l \leq r_{\rm WS}$. For convenience, let us refer to the blue regions in the case of normal

(inverted) phases as *clusters* (*holes*).

In Sect. 2.1.2, I have respectively defined V_N and u as the volume and volume fraction of the cluster. In this chapter, since we are also considering *holes*, let us generalize V_N to be the volumes of the blue regions of Fig. 3.1, that is, that occupied by either clusters or holes. Therefore:

$$V_N = \begin{cases} \frac{A}{n_i} & \text{for clusters,} \\ V_{\rm WS} - \frac{A}{n_i} & \text{for holes.} \end{cases} \tag{3.2}$$

Then, the volume fraction $u = \frac{V_N}{V_{\rm WS}}$ can be written as

$$u = \begin{cases} \frac{A}{n_i V_{\rm WS}} = \frac{2n_p}{(1-I)n_i} & \text{for clusters,} \\ 1 - \frac{A}{n_i V_{\rm WS}} = 1 - \frac{2n_p}{(1-I)n_i} & \text{for holes.} \end{cases} \tag{3.3}$$

Let $f(u)$ be the volume fraction of the denser phase,

$$f(u) = \frac{2n_p}{(1-I)n_i}, \tag{3.4}$$

then, we can also write $f(u)$ as:

$$f(u) = \begin{cases} u & \text{for clusters,} \\ 1-u & \text{for holes.} \end{cases} \tag{3.5}$$

Therefore, the total energy density in Eq. (2.53) is now written as:

$$\varepsilon_{\rm WS} = \varepsilon_e + \varepsilon_{\rm g}(1 - f(u)) + \frac{E_i}{V_{\rm WS}}. \tag{3.6}$$

We note that $f(u)$ is the same for the case of clusters and holes. Therefore, Eqs. (2.68)-(2.71) still hold for any phase. However, it is worth mentioning that the interaction pressure, defined in Eq. (2.76), in the case of holes not only depends on the Coulomb term but also on the surface and curvature terms. Therefore, the last equality in Eq. (2.76) no longer holds, and in the general case, we can write:

$$P_{\rm int} = \frac{n_p^2}{Z}\frac{\partial E_i}{\partial n_p}. \tag{3.7}$$

From Eq. (3.1), one can see that only the finite-size contributions, namely the surface, curvature, and Coulomb energy, depend on the nuclear shape. Regarding the interface term, the total surface tension σ can be written as a Taylor expansion at first order in the surface curvature $\kappa = \xi_c \frac{d-1}{r_N}$ [258], with $\xi_c = 1$ (-1) for clusters (holes), around the $\kappa = 0$ point as:

$$\sigma = \sigma_s + \kappa\sigma_c, \tag{3.8}$$

where σ_s is the dominant surface term, and σ_c is the curvature correction.

If S_N is the surface area of the pasta, it is straightforward to show that the total surface energy per unit volume can be written as:

$$\varepsilon_{\rm surf+curv,d} = \frac{\sigma S_N}{V_{\rm WS}} = \frac{\sigma V_N}{V_{\rm WS}}\frac{S_N}{V_N} = \frac{ud}{r_N}\sigma = \frac{ud}{r_N}\left(\sigma_s + \xi_c \frac{d-1}{r_N}\sigma_c\right). \tag{3.9}$$

In the above equation, the surface per unit volume for different geometries is written as:

$$\frac{S_N}{V_\mathrm{N}} = \frac{d}{r_N}, \tag{3.10}$$

which are obtained from the following expressions:

$$\left(\frac{S_N}{V_\mathrm{N}}\right)_{d=3} = \frac{4\pi r_N^2}{\frac{4}{3}\pi r_N^3} = \frac{3}{r_N}, \tag{3.11}$$

$$\left(\frac{S_N}{V_\mathrm{N}}\right)_{d=2} = \frac{2\pi r_N^2 + 2\pi h r_N}{\pi h r_N^2} = \frac{2}{r_N}\left(\frac{r_N}{h} + 1\right), \tag{3.12}$$

$$\left(\frac{S_N}{V_\mathrm{N}}\right)_{d=1} = \frac{2L_1L_2 + 2(2r_NL_1 + 2r_NL_2)}{2r_NL_1L_2} = \frac{1}{r_N}\left(1 + \frac{2}{L_1} + \frac{2}{L_2}\right), \tag{3.13}$$

where h (L_1, L_2) is the dimension along the symmetrical axis (plane) for $d = 2$ ($d = 1$). Since the length of rods/tubes and the area of slabs can be considered to be infinite, $h, L_1, L_2 \gg 1$ and $h, L_1, L_2 \gg r_N$. Thus, the limit $h, L_1, L_2 \to \infty$ yields the correct expression in Eq. (3.10).

The surface and curvature can be written separately as:

$$\varepsilon_{\mathrm{surf,d}} = \frac{ud}{r_N}\sigma_s, \tag{3.14}$$

$$\varepsilon_{\mathrm{curv,d}} = \xi_c \frac{ud(d-1)\sigma_c}{r_N^2}, \tag{3.15}$$

as in Refs. [129,131,134]. However, we note that there is a sign typo in the expression of the curvature energy for the inverted phases (tubes and bubbles) in Refs. [131,134]. Indeed, the curvature energies of clusters and holes should have opposite signs, see Refs. [259,260]. The surface and curvature tensions σ_s and σ_c are independent of the geometry and are given by Eqs. (2.57)-(2.58).

The Coulomb energy density reads [12]:

$$\varepsilon_{\mathrm{Coul,d}} = 2\pi \left(e y_p n_i r_N\right)^2 u \eta_{\mathrm{Coul,d}}, \tag{3.16}$$

with:

$$\eta_{\mathrm{Coul},1} = \frac{1}{3}\left[u - 2\left(1 - \frac{1}{2u}\right)\right], \tag{3.17}$$

$$\eta_{\mathrm{Coul},2} = \frac{1}{4}\left[u - \ln u - 1\right], \tag{3.18}$$

$$\eta_{\mathrm{Coul},3} = \frac{1}{5}\left[u + 2\left(1 - \frac{3}{2}u^{1/3}\right)\right]. \tag{3.19}$$

Details of the derivation for the Coulomb term in the WS approximation for the cylindrical and planar geometries are presented in Appendix A.

3.3 Pasta-phase properties

Employing the model described in Sect. 3.2, in this section, I present the properties of the pasta phase which is predicted to appear at the bottom of the inner crust. Particularly,

from the standard variational procedure, solving Eqs. (2.68)-(2.71), we compute microscopic quantities such as size, density, and charge, of the dense component (cluster) and the diluted one (gas) in the WS cell for several thermodynamic conditions. We recall that in beta equilibrium and at zero temperature, the latter condition is characterized by the baryon density n_B only. In addition, we calculate the inner-crust EOS as well as the transition densities between different layers, which are subsequently used as inputs to solve the TOV equations. This allows us to obtain the crustal macroscopic properties, such as the pasta thickness, mass, and moment of inertia. The latter could be of interest for different NS observations, and potentially they could be constrained by the upcoming astrophysical data.

3.3.1 Microscopic properties

Let us start by discussing the microscopic properties of different geometries. Particularly, in Sect. 3.3.1.1, I demonstrate the dependence of the crust equilibrium composition on the nuclear shape using the BSk24 functional. As the pasta phases are predicted to appear in the deepest region of the inner crust, the associated neutron-to-proton ratio is typically high. Consequently, one can expect the emergence of model dependence, and I highlight this aspect in Sect. 3.3.1.2.

3.3.1.1 Geometry dependence

Figure 3.2 shows the evolution as a function of the total baryonic density n_B of our variational variables (r_N, I, n_i, n_{gn}, n_p) and the volume fraction $f(u)$ of the denser phase, obtained with the BSk24 functional. The former are the solutions of the system of Eqs. (2.57)-(2.58) for each given geometry, while the latter is obtained from Eq. (3.4). In general, we can see that r_N, I, and n_i exhibit strong shape-dependence. On the other hand, the surrounding gas densities, n_{gn} and n_p, as well as the volume fraction of the dense nuclear matter phase are almost geometry-independent. Concerning n_i and I, the difference among geometries is larger at low densities, while at $n_B > 0.06$ fm^{-3}, the geometry dependence tends to vanish. As one may expect, the size of the cluster/hole has the strongest geometry dependence. Indeed, the cluster size r_N is determined from the competition between the Coulomb and total surface contributions through the following relation:

$$\varepsilon_{\rm surf} + 2\varepsilon_{\rm curv} = 2\varepsilon_{\rm Coul}. \tag{3.20}$$

Incorporating Eqs. (3.14)-(3.16) in Eq. (3.20), we get:

$$4\pi(ey_pn_i)^2\eta_{\rm Coul,d}(u){r_N}^4 - d\sigma r_N - 2\xi_c d(d-1)\sigma_c = 0, \tag{3.21}$$

From this equation, the cluster/hole radius/half-thickness can be approximated as:

$$r_N \approx \left(\frac{d\sigma_s}{4\pi(ey_pn_i)^2\eta_{\rm Coul,d}(u)}\right)^{1/3}. \tag{3.22}$$

We note that Eq. (3.22) is exact only if there is no curvature term, that is, $\varepsilon_{\rm curv,d} = 0$. However, since the curvature correction is usually negligible compared to the surface term, $\varepsilon_{\rm curv,d} \ll \varepsilon_{\rm surf,d}$, Eq. (3.22) can be considered as a good approximation, and it has been used

in several studies [12, 224, 227]. In our calculation, the curvature term is included, and r_N is obtained numerically and simultaneously with other variational variables.

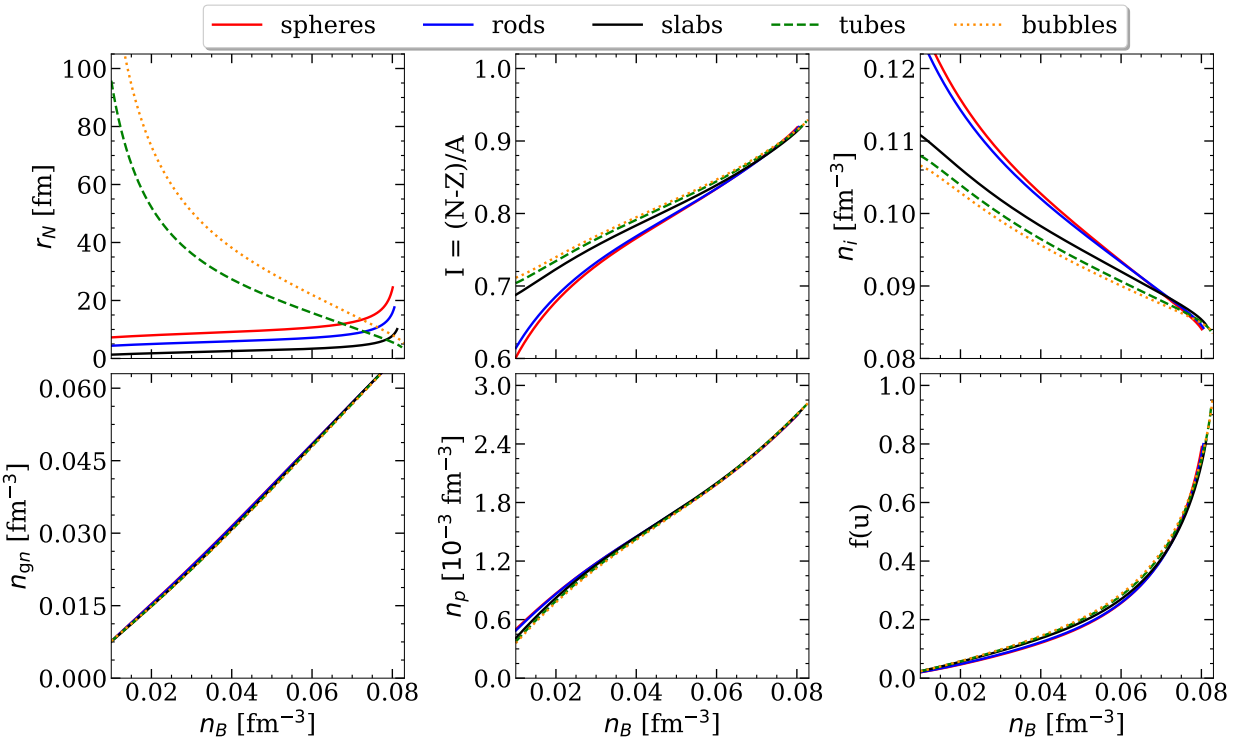

Figure 3.2: Evolution as a function of the total baryonic density n_B of the variational variables (r_N, I, n_i, n_{gn}, n_p) and the volume fraction of the denser phase $f(u)$ obtained for different geometries. The results are obtained with the BSk24 functional.

For the cluster structures, which are spheres (solid red line), rods (solid blue line), and slabs (solid black line), the size r_N increases with n_B. On the contrary, considering the hole configurations, the radius of the gas tubes (dashed green line) and bubbles (dotted orange line), decreases as n_B increases. This result is reasonable because, at low densities, the nuclei are far from each other. Therefore, the WS cell volume is mostly occupied by the neutron gas, hence very large gas bubbles/tubes. As one goes deeper towards the core, the nuclei get closer, and most of the WS cell is filled by the denser nuclear matter. This is the reason why we have larger clusters and smaller holes.

Additionally, from Eq. (3.22), we can deduce that for the same dimensionality d the difference between clusters and holes in the evolution of r_N originates from the term $\eta_{\mathrm{Coul,d}}$. Indeed, the terms σ_s and $y_p n_i$ on the right-hand side of Eq. (3.22) both decrease with n_B independently of the nuclear shape. Conversely, $\eta_{\mathrm{Coul,d}}$ behaves oppositely for clusters and holes. Indeed, the $\eta_{\mathrm{Coul,d}}$ function decreases as a function of the filling factor u, and $\eta_{\mathrm{Coul,d}} \to 0$ as $u \to 1$, as shown in Fig. 3.3. As one can see from the bottom right panel of Fig. 3.2, while $u = f(u)$ increases with n_B in the case of clusters, $u = 1 - f(u)$ decreases with n_B for holes. Thus, in the latter case, $\eta_{\mathrm{Coul,d}}$ is very small at low densities. This explains the very larger values of r_N observed for holes at low n_B (see the top left panel of Fig. 3.2).

Previously, we have seen that given the same dimensionality, different structures (cluster

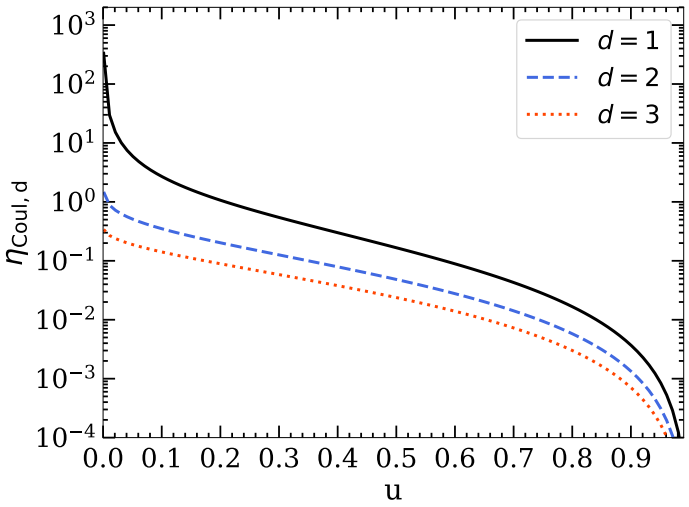

Figure 3.3: Function $\eta_{\mathrm{Coul,d}}$, defined in Eqs. (3.17)-(3.19), as a function of the cluster/hole volume fraction u for different dimensionality d.

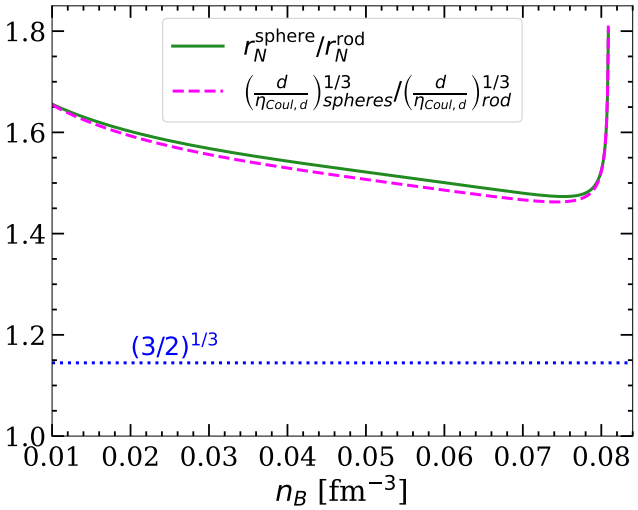

Figure 3.4: The ratio of the optimal radius r_N (solid green line) in comparison with the ratio of $\left(\frac{d}{\eta_{\mathrm{Coul,d}}}\right)^{1/3}$ (dashed magenta line) between spheres and rods. The horizontal dotted blue line indicates the cube root of the ratio of d, $\left(\frac{3}{2}\right)^{1/3} \approx 1.14$.

or hole) can lead to very different values of r_N, according to Eq. (3.22). Now, with the very same equation, we can also explain the dependence of r_N on the dimensionality d for a given structure. In Figs. 3.4 and 3.5, I show the ratio of the optimal radius r_N of spheres with respect to that of rods and slabs (solid green line). We can see that the difference in r_N between these geometries is larger than the cube root of the ratio between the dimensionality d (horizontal dotted blue line). This implies that discrepancy in the radius, $r_{N,d=3}$ with respect to $r_{N,d=1,2}$, is mainly due to the $\eta_{\mathrm{Coul,d}}$ term in Eq. (3.22). Indeed, as we can see in Fig. 3.3, $\eta_{\mathrm{Coul,d}}$ differs significantly between different values of d. From Figs. 3.4 and 3.5, we can see that the ratio of r_N is very close to the ratio of $\left(\frac{d}{\eta_{\mathrm{Coul,d}}}\right)^{1/3}$. Therefore, the

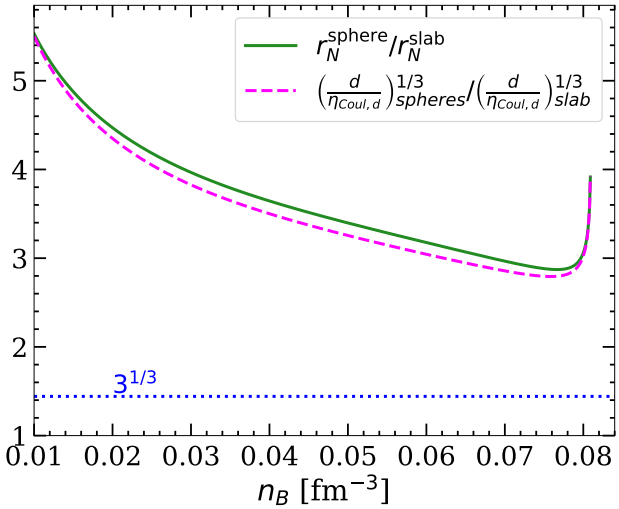

Figure 3.5: Same as Fig. 3.4, but between spheres and slabs.

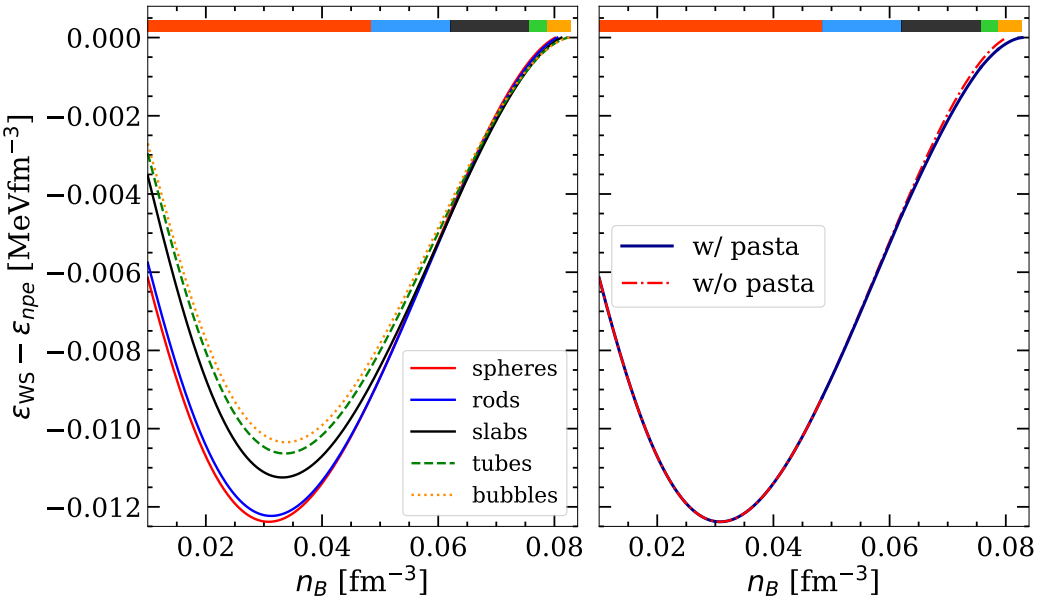

Figure 3.6: Left panel: the difference between the WS-cell energy density $\varepsilon_{\rm WS}$ and that of homogeneous matter in beta equilibrium ε_{npe} as a function of baryon density for five geometries: spheres (solid red lines), rods (solid blue lines), slabs (solid black lines), tubes (dashed green lines), and bubbles (dotted orange lines), for BSk24. Right panel: WS-cell energy-density difference ($\varepsilon_{\rm WS} - \varepsilon_{npe}$) obtained for the most stable geometry (solid blue line) and for only spheres (dash-dotted red line). The horizontal color bar on top of each panel indicates the most favorable geometry at each n_B. See text for details.

contribution of σ_s and $y_p n_i$ (see Eq. (3.22)) is negligible as far as the dependence of r_N on the geometry is concerned.

To check which configuration is favored, in the left panel of Fig. 3.6, I plot the energy difference between the optimal WS-cell energy density $\varepsilon_{\rm WS}$ obtained from the minimization procedure for a given geometry and that for homogeneous matter at β-equilibrium ε_{npe}. The difference is very small at high densities that the different curves are almost indistinguishable

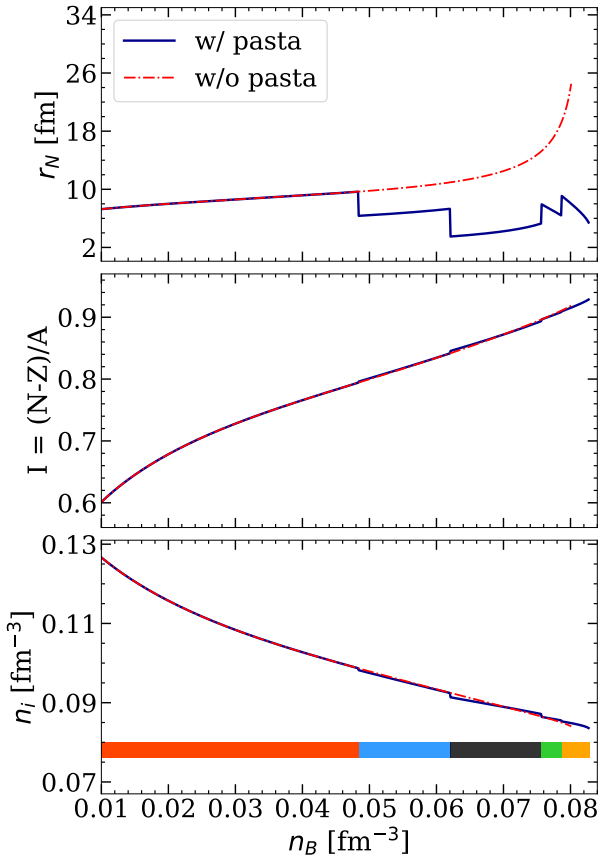

Figure 3.7: Comparison of the optimal cluster/hole size r_N (top panel), isospin I (middle panel), and density n_i (bottom panel) of the denser nuclear matter, obtained with (solid blue line) and without (dash-dotted red line) considering pasta as a function of the total baryonic density n_B using BSk24. The color bar in the bottom panel indicates the most stable geometry at each n_B. See text for details.

at $n_B \gtrsim 0.065$ fm^{-3}. We determine the most stable nuclear shape among the five considered as the one with the lowest $\varepsilon_{\rm WS}$, or equivalently $(\varepsilon_{\rm WS} - \varepsilon_{npe})$. The most favorable geometry at each density is indicated by the color bar on top of the panel. We obtain the same transition order as that found in several work in the literature [12, 137, 216, 226], that is, spheres (red) $\rightarrow$ rods (blue) $\rightarrow$ slabs (black) $\rightarrow$ tubes (green) $\rightarrow$ bubbles (orange). We can see that for the BSk24 functional, pasta appears at a density above around 0.05 fm^{-3} and dissolve into nuclear matter near 0.08 fm^{-3}.

On the right panel of Fig. 3.6, I plot the energy density of the most favored geometry at each n_B (solid blue line) and compare it with that obtained for only spheres (dash-dotted red line). We can see that the deviation between the two cases is tiny. In particular, the energy density obtained with the inclusion of pasta is slightly lower than that with only spheres. As a result, when pasta is considered, the density at which the transition to the core happens is higher, but not remarkably, $n_{\rm CC}^{\rm w/\ pasta} - n_{\rm CC}^{\rm w/o\ pasta} \approx 0.002$ fm^{-3}. Even though the transition between different geometries is quite abrupt, we do not observe discontinuities in $\varepsilon_{\rm WS}$ at the transition points.

However, the discontinuities can be observed in other quantities, such as the crust compo-

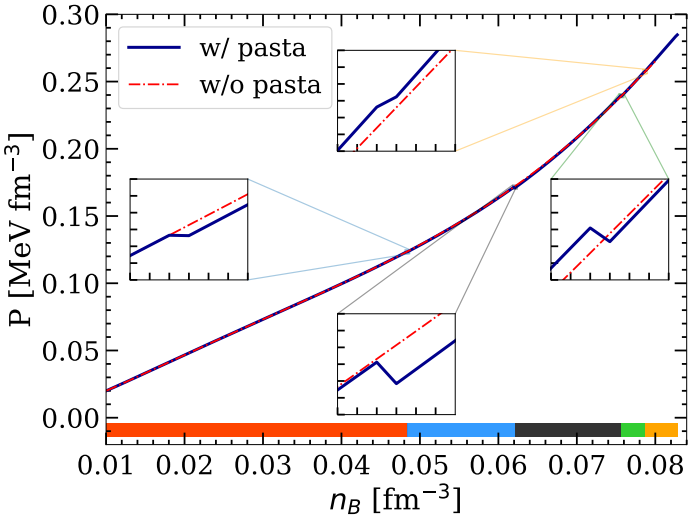

Figure 3.8: Comparison of the crust EOS obtained with (solid blue line) and without (dash-dotted red line) considering pasta as a function of the total baryonic density n_B using BSk24. The insets show a zoom at the transition between the shapes. The tick marks of x- and y-axis in the insects are spaced by respectively 10^{-4} fm^{-3} and 5×10^{-4} MeV fm^{-3}. The color bar at the bottom indicates the most stable geometry at each n_B. See text for details.

sition, as shown in Fig. 3.7. The most visible discontinuities are in the cluster/hole size r_N. When the presence of pasta is included (solid blue line), r_N is significantly smaller than in the case where only spheres are considered (dash-dotted red line). Nevertheless, the difference between the two cases is negligible as far as the isospin I and density n_i of the denser phase are concerned. Similar to r_N, for n_i and I, the jumps at the transition can still be observed, but they are much smaller than for r_N.

Finally, Fig. 3.8 shows that including the pasta structures does not affect significantly the EOS of the inner crust. Therefore, the approximation of sphericity that we made in Chapter 2 is justified for the calculation of the EOS. Nonetheless, we can still observe that at the transition between two successive geometries, there is a small "jump" in the pressure. As mentioned before, this behavior is due to the sudden transition from one shape to another. As a matter of fact, the five geometries that we are considering are very likely oversimplifications of the realistic configurations encountered in the inner crust. For example, before transforming into rods, it is likely that spheres are first deformed to prolate spheroids. Then, the elongation continues until rods are formed. Similarly, intermediate shapes could also be realized at the transition from rods to slabs. We believe that the discontinuities would be smoothed out if these intermediary stages are taken into account.

3.3.1.2 Model dependence

To explore the model dependence of the results, we have examined the equilibrium configurations obtained with different popular nuclear models, corresponding to different bulk parameter sets listed in Tables 2.1. The associated optimal surface parameters are given in Table 3.1. The (σ_0, b_s, $\sigma_{0,c}$, β) parameters have been obtained from the fit of the experimentally measured nuclear binding energies [135], while the p parameter has been optimized

Table 3.1: Optimized surface and curvature parameters for different functionals, for which the bulk parameters are fixed as in Table 2.1. Table reproduced from Ref. [121].

	σ_0 (MeV/fm^2)	b_s	$\sigma_{0,c}$ (MeV/fm)	β	p
BSk24	1.05021	30.32168	0.12147	0.66495	3.00
SLy4	0.98911	19.02416	0.15141	0.75548	3.00
RATP	1.05161	35.22683	0.12488	0.67745	3.00
NRAPR	0.91932	14.68853	0.16594	0.83634	3.00
DD-ME2	1.09358	5.47648	0.11969	0.53966	2.42
DD-MEδ	1.08385	11.38970	0.11810	0.55559	2.73
NL3	1.12493	4.52517	0.12297	0.46301	2.79
PKDD	1.17354	27.70134	0.08008	0.25816	3.00
TM1	1.13817	9.31146	0.11377	0.39118	3.00

to provide a good reproduction of the crust-core transition density of the different functionals, whenever available, or fixed to $p = 3$ otherwise (see Table 3.2 and Refs. [59, 127] for a discussion).

Results are shown in Fig. 3.9, where the different colors correspond to the density regions where different geometries (spheres, rods, slabs, tubes, and possibly bubbles) dominate. The upper edge of each column gives the transition point from the inhomogeneous crust to the homogeneous core, defined as the point where the WS cell energy density, Eq. (3.6), corresponding to the optimal geometry, equals that of homogeneous nuclear matter in beta equilibrium with electrons, see Fig. 3.6. The sequence of the different geometries appears to be model-independent, although not all the considered models predict bubble configurations. Again, it shows that the hierarchy is consistent with previous results (see Ref. [128] for a review). We note that due to the negative curvature energy in the case of inverted configurations, see Eq. 3.15, the tube and bubble phases become more favorable and the density range where the slab phase dominates is reduced compared to the results published in Ref. [121]. However, this sign change does not impact the sphere-pasta transition density, and only slightly increases the crust-core transition density ($\sim 1\%$), see also Table 3.2.

For a given energy functional, it is well known that the precise value of the transition density from the spherical to the non-spherical phases depends on the details of the many-body model used to treat the clustered structure. A comparison with results in the literature is reported in Table 3.2. The first full fourth-order ETF calculations of pasta within the WS approach is the one by Ref. [76] with the BSk24 functional. In that paper, the authors obtained a slightly higher value for the transition density to the rod shape (see Table 3.2), compared to our estimation of 0.048 fm^{-3}. Particularly, without (with) the shell and pairing corrections for spheres, they found the transition density to the pasta phase to be $n_{\rm pasta} = 0.050$ (0.051) fm^{-3}. In Ref. [76], the transition density to the core is not stated explicitly due to a convergence issue occurring at densities above ~ 0.078 fm^{-3}. Therefore, we compare our prediction with that obtained in Ref. [75], where the crust-core boundary was found to happen at 0.081 fm^{-3}. We consider this comparison as a very good agreement, especially considering that beyond-mean field contributions such as pairing, fully neglected here, have been recently shown to affect the composition of the crust [69, 76].

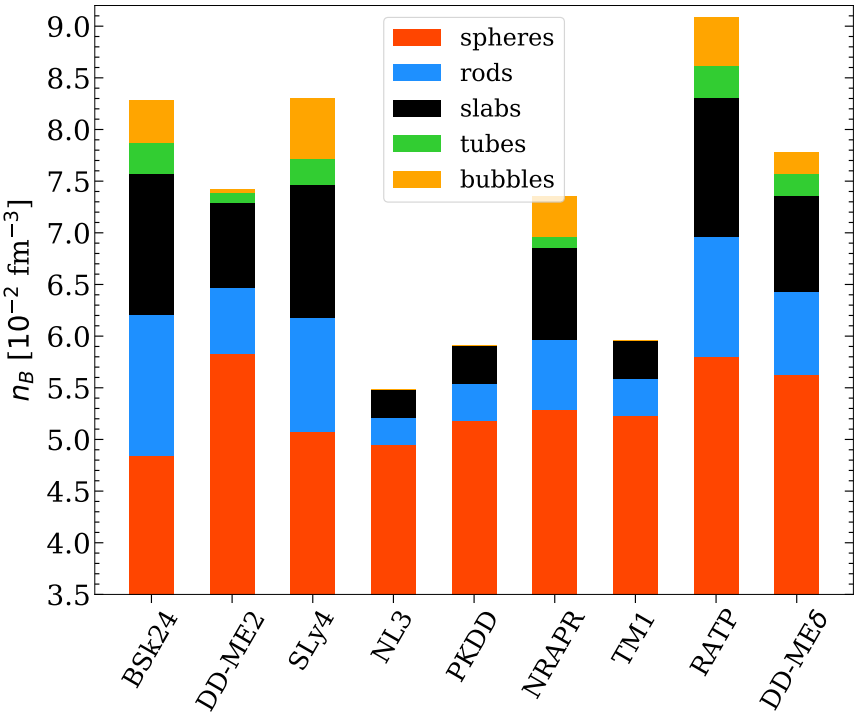

Figure 3.9: Sequence of equilibrium phases and the corresponding transition densities among the geometries for different nuclear functionals. See text for details. Figure adapted from Ref. [121].

In Ref. [76], the microscopic corrections were considered only for spheres and were neglected for pasta. Recently, in Ref. [220], the authors repeated the same calculations but with the Strutinsky-integral and pairing corrections included for the pasta phases. This improvement led to a dramatic effect on the equilibrium shapes. Specifically, due to the positive microscopic corrections for rods, this phase is completely eliminated, and spherical nuclei dominate until ~ 0.077 fm^{-3} where slabs take over. In this case, our CLDM results no longer agree with those using fourth-order ETFSI calculation.

Table 3.2: Transition density from spheres to cylinders ($n_{\rm pasta}$) and from crust to core ($n_{\rm CC}$) for different functionals. For comparison, results from Refs. [74–76,125,126,149,229] are also given. The "-" sign indicates that no transition to pasta is found. Table adapted from Ref. [121].

	$n_{\rm pasta}/n_{\rm CC}$ (10^{-2} fm^{-3})						
Model	This work	Pearson et al. [75,76]	M&U [74]	D&H [125]	Viñas *et al.* [126]	Grill *et al.* [149]	Shchechilin *et al.* [229]
BSk24	4.84/8.28	5.0/8.1					
SLy4	5.07/8.30		6.1/8.1	-/7.6	-/7.6		5.6/7.7
NL3	4.95/5.48					-/5.48	
DD-ME2	5.83/7.42					6.11/7.35	
DD-MEδ	5.63/7.78					6.26/7.66	

In the case of the SLy4 functional, Ref. [74] have employed a slightly less sophisticated second-order ETF approach, and observed a transition to the cylindrical shape at a higher density than the value obtained with our approach for SLy4. However, the thermodynamical potentials corresponding to $d = 3$ and $d = 2$ in Ref. [74] are almost indistinguishable starting from 0.05 fm^{-3}, in good agreement with our results. Furthermore, the crust-core transition point is also in excellent agreement with our findings. At variance with this result, Refs. [126] and [125], who also employ the SLy4 functional, have reported no deviation from the spherical shape within a zeroth-order TF calculation and a CLDM approach, respectively. Moreover, they also obtained a lower density for the crust-core transition. Recently, a calculation of the pasta phases was performed using both the fourth-order ETF method and CLDM based on SLy4 was shown in Ref. [229]. Within the ETF approach, the authors found that the pasta phases composed of rods and tubes cover from ~ 0.056 fm^{-3} to 0.077 fm^{-3}. This result is in reasonable agreement with ours in terms of transition densities. However, concerning the equilibrium shapes, in our calculation, we also found a robust amount of slabs. In the CLDM results, the pasta phases calculated in Ref. [229] almost disappear as the rod form only dominates over spheres in a very narrow density range, from 0.074 fm^{-3} to 0.075 fm^{-3}. The difference with respect to our results might originate from different treatments in the surface energy. Indeed, in Ref. [229], the neutron absorption on the cluster surface is included, while this effect is not considered in our formalism. Moreover, in our calculation, the curvature corrections to the surface tension are taken into account (see Eq. (3.15)), whereas they are not included in Ref. [229]. In beta equilibrium, the difference in energy among the geometries is extremely small (see Fig. 3.6). As a result, an energy correction, even though being very small, could result in considerable change in the appearance of different phases.

Finally, we can also compare our results concerning the relativistic functionals NL3, DD-ME2, and DD-MEδ with the extensive Thomas-Fermi calculations of Ref. [149]. In our approach, we obtain a lower density transition between spheres and cylinders for DD-ME2 and DD-MEδ. For DD-ME2, we obtained the same configuration sequence as in the referred paper (spheres $\rightarrow$ rods $\rightarrow$ slabs), while for DD-MEδ, we also found a small portion of bubble-like structures. As for the NL3 functional, we do find non-spherical shapes, unlike Ref. [149]. As we have stressed before, the transition densities depend significantly on the finite-size contributions. Therefore, by adjusting the parameter p, we are able to reproduce the crust-core transition densities for the mentioned functionals (see Tables 3.1 and 3.2).

Even if the comparison of our work with previous results can be globally considered as satisfactory, Table 3.2 shows that some differences exist between the inner-crust composition of different many-body methods used to compute the energy of clusterized matter, for a fixed EOS (or equivalently: a fixed set of bulk parameters $\mathbf{X}$). This highlights the importance of finite-size contributions to the nuclear energy, which are essential to determine the optimal composition and are not uniquely linked to the bulk matter properties. Indeed, only the bulk parameters $\mathbf{X}$ of our meta-model are adjusted to reproduce a given functional, while we employ a different fitting protocol for the surface (plus curvature) energy. The effects of the surface contribution are studied in greater detail in Sect. 3.4.1.

Complementary information on the inner-crust composition in the presence of non-spherical geometries is given by Fig. 3.10, which reports the total proton fraction in the cell, $Y_p^{\rm tot}$, as a

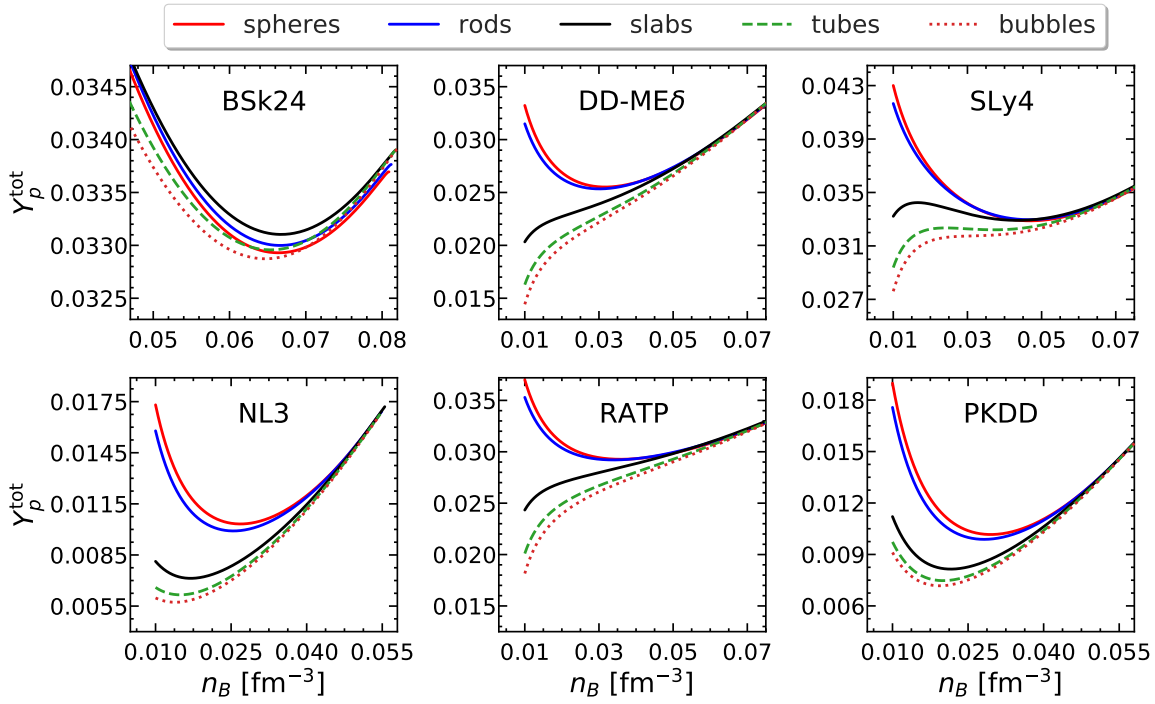

Figure 3.10: Proton fraction in the Wigner-Seitz cell as a function of the baryonic density in the NS crust for different geometries of the clustered structures using different popular nuclear models. See text for details. Figure adapted from Ref. [121].

function of the baryonic density for the different geometries, for a selected set of functionals, as illustrative examples. We can see that some of the functionals exhibit the characteristic parabolic shape already reported by Ref. [76] for the BSk24 model, and the absolute value of the proton fraction is also in reasonable agreement with the findings of Ref. [76]. However, we can also observe that the trend of the proton fraction, the effect of the geometry, and its numerical value throughout the inner crust are very strongly model-dependent.

3.3.2 Macroscopic properties

The consistent minimization of the total energy density $\varepsilon_{\rm WS}$ under the constraint of baryon number conservation for each geometry is crucial in getting the correct configuration for the ground state of matter. This procedure plays an important role in calculations requiring the exact composition as input, such as in calculating transport coefficients [251]. However, as it is well known in any root-finding algorithm, one needs to provide initial guesses as starting values. Since the solutions, especially in r_N, vary with the geometry, as shown in Fig. 3.2, performing this process for all five geometries in a statistical study could be relatively time-consuming. In addition, for the determination of more global quantities, such as thickness, mass, or moment of inertia of the pasta phases, the important ingredients are the EOS and transition densities (or equivalently: the transition pressure). Thus, in Sect. 3.3.2.1, I discuss the so-called spheres-composition approximation we adopted for calculating crustal EOS. With the latter as input, we solve the TOV equations [166, 167] (see also Sect. 2.2.1) and

compute some macroscopic properties, such as mass, thickness, and moment of inertia, for the pasta layer, which I discuss in Sect. 3.3.2.2.

3.3.2.1 Spheres-composition approximation

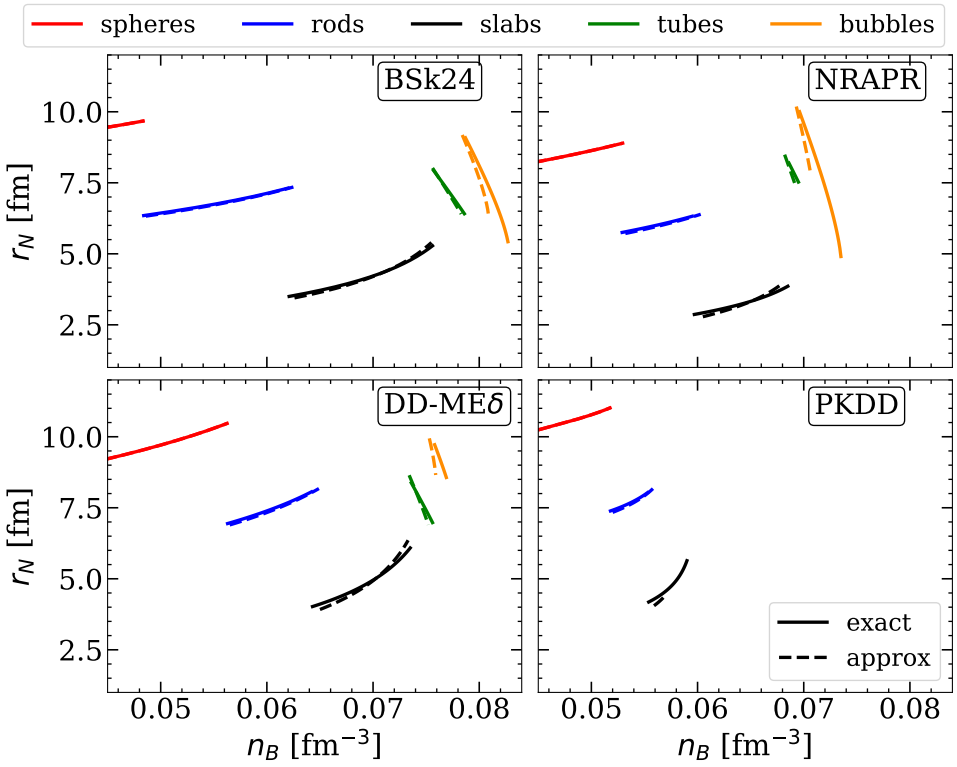

Figure 3.11: Comparison of the optimal radius/half-thickness r_N obtained from the consistent minimization for each geometry ("exact", solid lines) versus those calculated using the spheres-composition approximation ("approx", dashed lines) for four different energy functionals. Different colors correspond to different geometries. See text for details.

In principle, once the nuclear model, defined by the energy functional and the surface parameters, is specified, the pasta structure and composition at a given baryonic density n_B can be determined by a two-step process. First, given a geometry, the energy density of the system is minimized under the condition of baryon number conservation. Then, the equilibrium configuration is defined as the one corresponding to geometry that produces the minimum $\varepsilon_{\rm WS}$. As described in Sect. 2.1.2.2, the first step is equivalent to solving the system of four equations, (2.68)-(2.71), together with Eq. (2.64), for the five variables (r_N, n_i, I, n_p, and n_{gn}). As we have seen in Figs. 3.2 and 3.7, the only considerable difference among the geometries is r_N. Indeed, in Fig. 3.2, we can see that the gas densities, n_p and n_{gn} are almost independent of the geometry. Furthermore, in Fig. 3.7, it is clear that the most favorable values of n_i and I are almost indistinguishable from those obtained for spheres. Therefore, instead of performing the minimization for all five geometries, it is more efficient to solve the equilibrium composition for only spheres. Then, the values of n_i, I, n_p, and n_{gn} computed for spheres are used as inputs to find the size r_N for other geometries from the

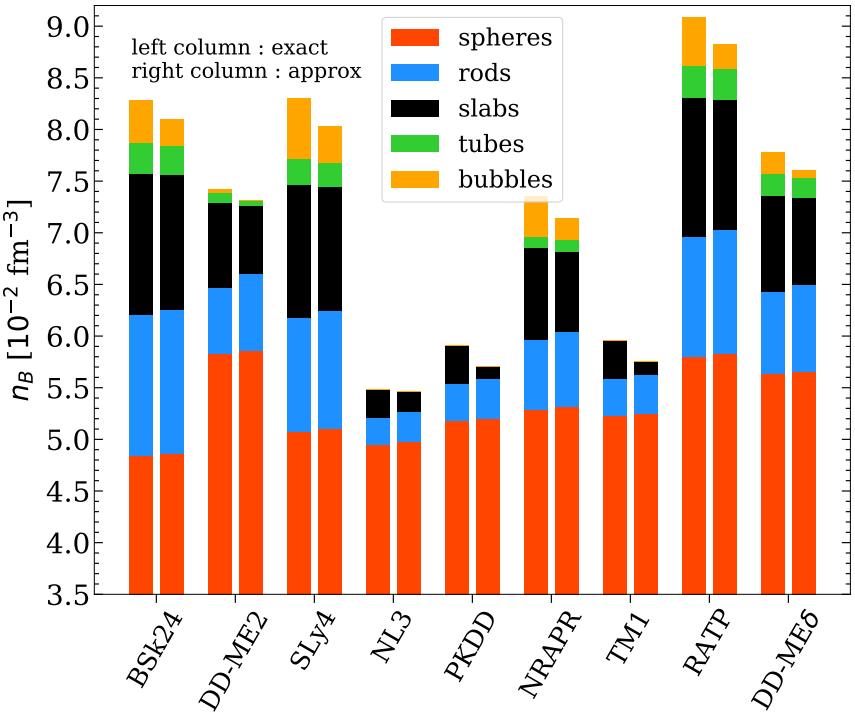

Figure 3.12: Sequence of equilibrium geometries as a function of baryon density n_B for nine different nuclear functionals. The left columns are obtained from the consistent minimization for each geometry, while the right ones are resulted from the spheres-composition approximation. See text for details

virial theorem, Eq. (3.21). Thus, the problem of solving a system of multiple equations is now reduced to only one equation, as was proposed in Ref. [122].

To check the validity of this approximation, in Fig. 3.11, I compare the most favored radius/half-thickness obtained from the full minimization for each geometry (solid lines) with that obtained using the solutions from spheres (dashed lines) for four different models, BSk24, NRAPR, DD-MEδ, and PKDD. We can see that the radii in the region where spheres (red) and rods (blue) dominate are almost identical for all models. This is because values of optimal n_i, I, n_p, and n_{gn} for spheres and rods are very similar (see Fig. 3.2). Considering other geometries, slabs (black), tubes (green), and bubbles (orange), even though the deviation between the two approaches is still visible, it remains small.

The macroscopic properties of the crust are not very sensitive to the detailed composition but to the EOS and the transition points. As we have seen in Fig. 3.8, the impact of the geometry on the EOS is negligible. Moreover, in Fig. 3.12, we can also see that the transition densities among different configurations obtained with the approximation are in excellent agreement with the exact ones. For these reasons, we can conclude that the spheres-composition approximation, which assumes for all geometries the composition obtained for spheres, can be adopted to reduce the computational time when computing global properties of the crust for several models and particularly when performing the Bayesian analysis.

3.3.2.2 Pasta observables

Once we have the information on the EOS and transition points, the pasta observables can be calculated (see also Sect. 2.2.1). In particular, to find the total pasta thickness and mass, the integration of Eqs. (2.81)-(2.82) is performed from $r = 0$ up to the sphere-pasta transition point, $r = R_{\rm core+pasta}$, where $R_{\rm core+pasta}$ is defined as the radius position where $P(r = R_{\rm core+pasta}) = P_{\rm pasta}$, with $P_{\rm pasta}$ being the pressure at the sphere-pasta transition.

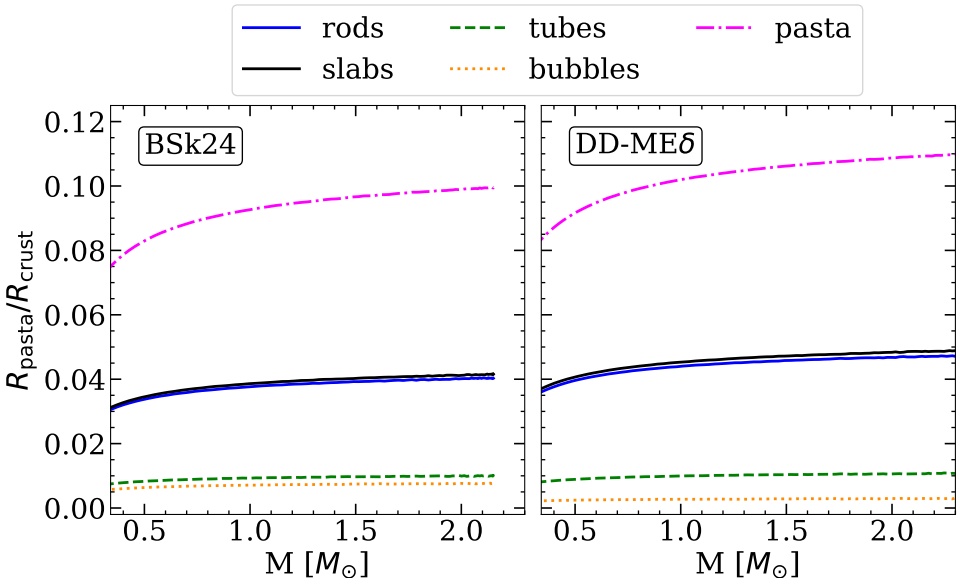

Figure 3.13: The fractional thickness of different pasta phases, rods (solid blue line), slabs (solid black line), tubes (dashed green line), and bubbles (dotted orange line), with respect to the crust obtained for BSk24 (left panel) and DD-MEδ (right panel). The dash-dotted magenta line in each panel indicates the total fractional pasta thickness.

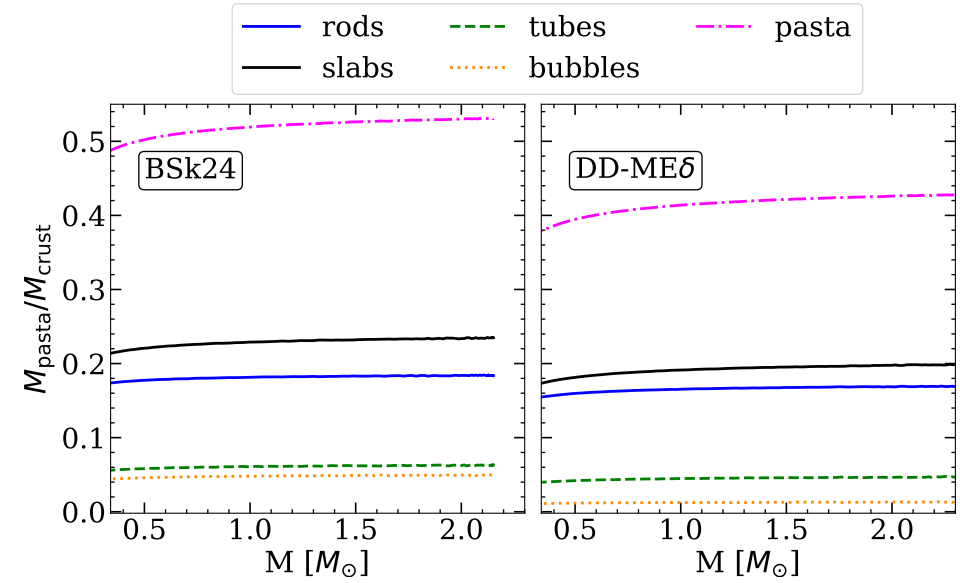

Figure 3.14: Same as Fig. 3.13 but for the pasta fractional mass.

The pasta thickness and mass then can be calculated using:

$$R_{\rm pasta} = R_{\rm core+pasta} - R_{\rm core}, \tag{3.23}$$

$$M_{\rm pasta} = M_{\rm core+pasta} - M_{\rm core}, \tag{3.24}$$

with $R_{\rm core}$ ($M_{\rm core}$) being the core radius (mass), defined as the radius (mass) from the center to the crust-core transition point. Once the transition densities between two most probable configurations are known, see Fig. 3.12, it is also possible to calculate the radius and mass corresponding to each geometry. The results are shown in Figs. 3.13-3.14, where I respectively display, as a function of the NS mass, the fractional radius and mass of different pasta layers to the whole crust for two functionals, BSk24 and DD-MEδ, as illustrative examples. Generally, both figures suggest that the fraction of pasta increase with the NS mass. However, for NS of mass larger than 1.5 $M_\odot$, the increase is only marginal. In total, DD-MEδ predict a slightly larger thickness fraction (11% versus 10%), while BSk24 results in a higher mass fraction ($\sim$ 54% versus $\sim$ 42%). The latter is because the pasta structure corresponding to BSk24 extends to a higher density, as shown in Fig. 3.12.

From the results displayed in this section, we can observe that the predictions for the pasta properties clearly exhibit some model dependence. In order to quantitatively address this issue and determine the influence of the choice of the functionals on the uncertainties of the pasta observables, we perform a Bayesian analysis, which is discussed in the next section.

3.4 Evaluation of the pasta-phase properties uncertainties

We now come to the quantitative determination of the uncertainty on the pasta observables, due to the imperfect knowledge of the nuclear energy functional. To this aim, we perform a Bayesian analysis by largely varying the model parameters $\mathbf{X}$ using flat non-informative priors, and generating posterior distributions with filters that impose both our present low-density (LD) nuclear physics knowledge and high-density (HD) constraints coming from general and NS physics. The ranges of different parameters in the prior distributions are the same as those listed in Table 2.5, except for parameter b. In particular, we observed that the LD filter tends to eliminate high values of b. Therefore, to increase the acceptance rate, for the calculation in this chapter, we varied b from 1 to 6 (previously, b was varied from 1 to 10).

The posterior distribution reads:

$$p_{\rm post}(\mathbf{X}) = \mathcal{N}\omega_{\rm LD}(\mathbf{X})\omega_{\rm HD}(\mathbf{X})\omega_{M_{\rm max}(\mathbf{X})}e^{-\chi^2(\mathbf{X})/2}\omega_0{\rm prob}(\mathbf{X}), \tag{3.25}$$

where prob($\mathbf{X}$) is the flat prior probability and $\mathcal{N}$ is the normalization. Similar to Sect. 2.3, here, the $\omega_{\rm LD}$ filter is given by the chiral EFT calculations of the energy per particle of symmetric and pure neutron matter by Drischler *et al.* [110], which is considered as a 90% confidence interval to account for models marginally consistent with the bands. Since the EFT energy bands become very narrow at low densities, in Ref. [127], the $\omega_{\rm LD}$ filter was applied from ≈ 0.1 fm^{-3}, while in Refs. [121, 142, 217], we have extended this constraint to lower densities, namely in the range $[0.02, 0.2]$ fm^{-3}. I further investigate the effect of such a choice in Sect. 3.4.2.

Let us recall that the $w_{\rm HD}$ filter is defined by imposing:
(i) stability, i.e., the derivative of the pressure with respect to the mass-energy density must be positive, $dP/d\rho_B \geq 0$,
(ii) causality, i.e., the squared speed of sound must be non-negative and smaller than c^2, $0 \leq c_s^2 \leq c^2$,
(iii) a positive symmetry energy at all densities.

Moreover, we also require all EOS in the posterior distribution to result in the maximum NS mass satisfying $M_{\rm max} > M_\mu - M_\sigma = 1.97 M_\odot$, with M_μ (M_σ) being the mean (standard deviation) of the mass measurement from the radio-timing observation of the pulsar PSR J0348+0432 [31], $M_{J03} = 2.01 \pm 0.04 M_\odot$. We found that applying the sharp filter $\omega_{M_{\rm max}}$ and using the likelihood prob($J03|\mathbf{X}$) (Eq. (2.103)) do not result in any noticeable difference, especially in the crustal properties.

A further constraint is given by the condition that the minimization of the energy density of the system, under the constraint of conserving the baryon number, leads to physically meaningful results for the crust, namely positive values for the optimal gas and cluster densities. This condition is represented by ω_0. Finally, the quality of reproduction of the experimental binding energies is defined from the error estimator $\chi^2(\mathbf{X})$ (see Eq. (2.101)).

In this section, I focus our analysis on the impact of the low-density region of the EOS on the pasta observables. Indeed, while the high-density part is crucial to determine global NS properties such as masses and radii, it does not have a predominant role in the region of the crust of interest here [184, 201]. For this reason, unlike Sect. 2.3, the constraints from LVC [39–41] and NICER [35–38] are not included in this section.

3.4.1 The influence of the surface parameters

Within a given nuclear model, the appearance of pasta phases essentially results from the competition between different finite-size contributions. In beta equilibrium, the energy gaps among different geometries are extremely small. Thus, a small difference in the surface term can lead to a different pasta configuration, as discussed in Sect. 3.3.

As we have seen in Sect. 2.1.2.1, the parameter p, which governs the behavior of the surface tension at extreme isospin values (see Fig. 2.10), cannot be constrained by fitting nuclear binding energies. Typically, p is fixed to the value $p = 3$. It was shown that the value $p = 3$ tends to reproduce very well the crust-core transition density obtained with the dynamical method for most of the models [59, 127]. Nevertheless, given the sensitivity of the crustal properties on the surface energy, in this Bayesian analysis, we add p as an extra independent parameter, and randomly generate $p \in [2, 4]$ together with others in the set $\mathbf{X}$.

The first part of this section is devoted to discussing the impact of p. To this aim, in the prior distribution, we generate 10^8 parameter sets $\mathbf{X}$. These prior models are then passed through all the likelihoods/filters mentioned in Eq. (3.25). Particularly, the chiral EFT filter is applied from 0.02 fm^{-3}. Regarding the parameter p, here, we consider both cases: (i) p is fixed to the canonical value, $p = 3$; (ii) $p \in [2, 4]$. In the posteriors, we respectively have 7178 and 7008 parameter sets retained. This suggests that the filters are not selective to the value of p. Indeed, Fig. 3.15 shows that the posterior distribution of the p parameter (blue histogram) is almost flat. This outcome is understandable because p governs the surface

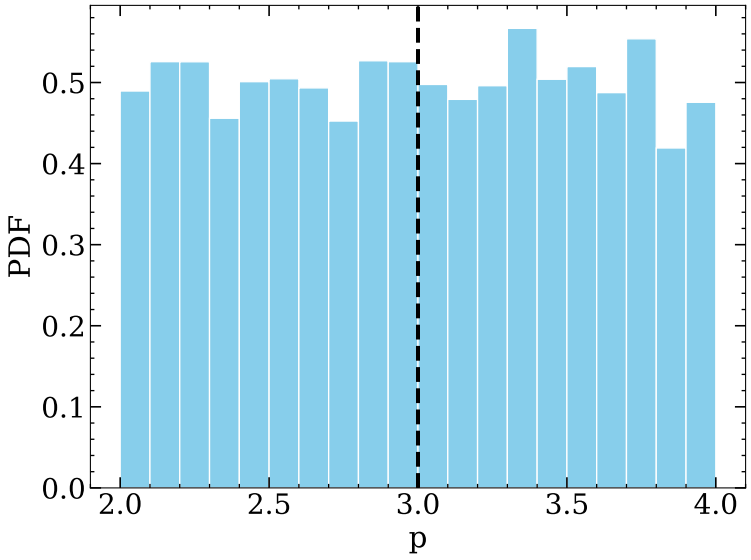

Figure 3.15: Posterior distribution of the p parameter. The vertical dashed black line indicates the canonical value, $p = 3$.

properties, therefore, it can not be constrained by the LD constraint, which controls the nuclear matter behaviors. Furthermore, this parameter enters only the low-density region of the EOS. Consequently, it cannot be constrained by the high-density filters either.

In Sect. 2.1.2.1, I have shown with the BSk24 functional that except for b_s, values of other surface parameters are independent of p (see Fig. 2.10). This statement holds independently of the functional choice, as one can see in Fig. 3.16. Specifically, in this figure, I plot the posterior distributions of σ_0, $\sigma_{0,c}$, β, and b_s corresponding to the case where p is fixed (dashed black lines) in comparison with those obtained when p is allowed to vary (solid blue line). While the distributions of σ_0, $\sigma_{0,c}$, and β are unaffected by p, Fig. 3.16 shows that there is a strong correlation between p and b_s. In fact, from Fig. 2.10, we expect that the correlation between the two parameters is positive. The results shown in Fig. 3.16 suggest that among the five surface parameters, only three, i.e., σ_0, $\sigma_{0,c}$, and β, can be determined from the experimental mass measurements.

Even though the information on the parameter p is decoupled from the nuclear physics experimental data, it impacts the surface tension at high isospin values, see Fig. 2.9. As a result, it can be important in the calculations concerning the inner crust [59, 127]. In Fig. 3.17, I depict the posterior distributions of the crust-core transition density $n_{\rm CC}$ (left panel) and pressure $P_{\rm CC}$ (right panel). It can be observed that fixing the value of p to $p = 3$ eliminates models with low crust-core transition. Nevertheless, the peaks of the distributions are unmodified. Regarding the interface between spheres and pasta, since the associated isospin is not yet extreme, the corresponding transition density and pressure are quite similar in the two cases, as shown in Fig. 3.18. These results imply that by varying p, we allow more models with a small (or even zero) pasta layer. This is displayed in Fig. 3.19. Nonetheless, the probability of these models is negligible compared to the most-probable value.

To explain the models with zero pasta contribution in Fig. 3.19 in the case $p \in [2, 4]$, in

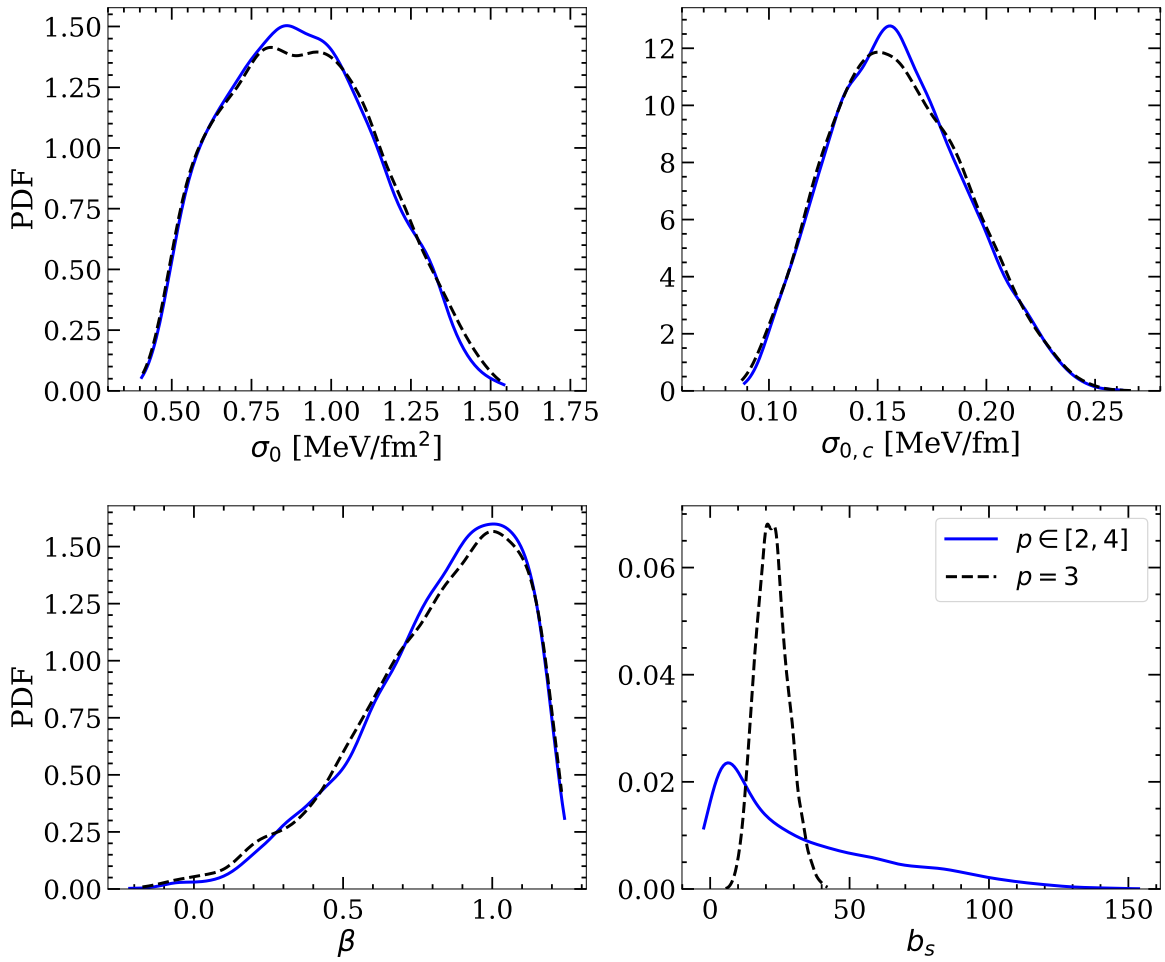

Figure 3.16: Posterior probability density distributions of surface parameters $(\sigma_0, \sigma_{0,c}, b_s, \beta)$ when p is fixed to $p = 3$ (dashed black line) and when p is varied from 2 to 4 (solid blue line).

Fig. 3.20, I plot the probability of having a transition from spheres to one of the possible phases: rods, slabs, tubes, bubbles, or homogeneous matter. Particularly, the rightmost column of each panel indicates the possibility of having a direct transition from spheres to the core without going through any of the pasta structures. When p is varied, $p \in [2, 4]$, (top panel), there are around 0.5% of models in the posterior predicting no transition to pasta. On the other hand, if p is fixed to $p = 3$, then the pasta structure is always predicted (see the bottom panel). Surprisingly, the spherical nuclei do not always transform into rods. In fact, there is approximately 1% of the models with nuclei conversing from spheres to slabs, while 99% them follow the traditional sequence, that is, from spheres to rods.

From the results shown in Figs. 3.17-3.20, we can conclude that even though the transition to the pasta phase is invariant with p, to account for models with relatively low crust-core transition, which correspond to those with small or zero pasta, it is more general to explore p in the range $p \in [2, 4]$ than to fix p to only one unique value[2].

[2]Hereafter, the results presented are always obtained varying $p \in [2, 4]$.

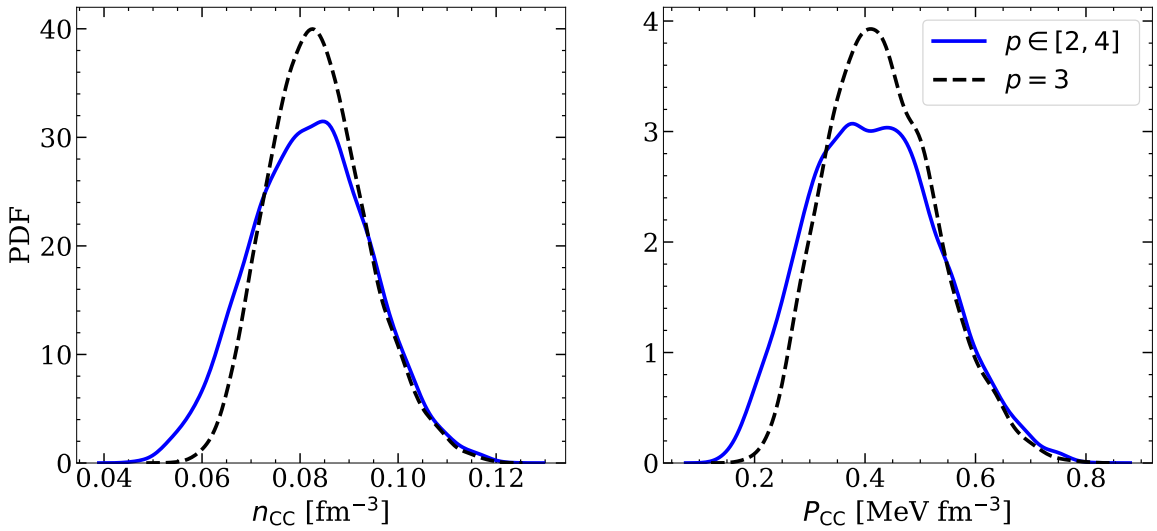

Figure 3.17: Posterior probability density distributions of crust-core transition density (left panel) and pressure (right panel), obtained considering different treatments of the surface parameter p: $p = 3$ (dashed black line) and $p \in [2, 4]$ (solid blue line).

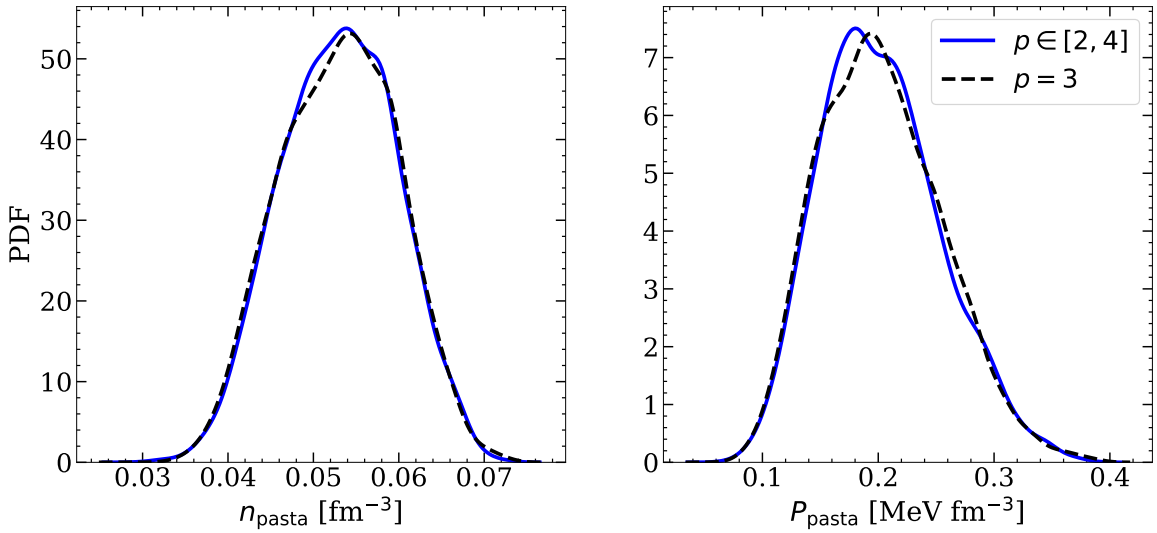

Figure 3.18: Same as Fig. 3.17, but for the sphere-pasta transition.

Table 3.3: Surface and curvature parameters optimized to reproduce the full extended Thomas-Fermi mass table obtained for the BSk24 and SLy4 functionals, by Carreau *et al.* [79] and Furtado & Gulminelli [132], respectively. Table reproduced from Ref. [121].

	σ_0 (MeV/fm^2)	b_s	$\sigma_{0,c}$ (MeV/fm)	β	p
BSk24	0.98636	36.227	0.09008	1.1631	3.0
SLy4	0.99654	49.82	0.061768	y_p+1	3.4

In our study, the properties of the bulk functional are essentially constrained by the EFT calculation, while independent surface parameters are introduced, correlated to the bulk

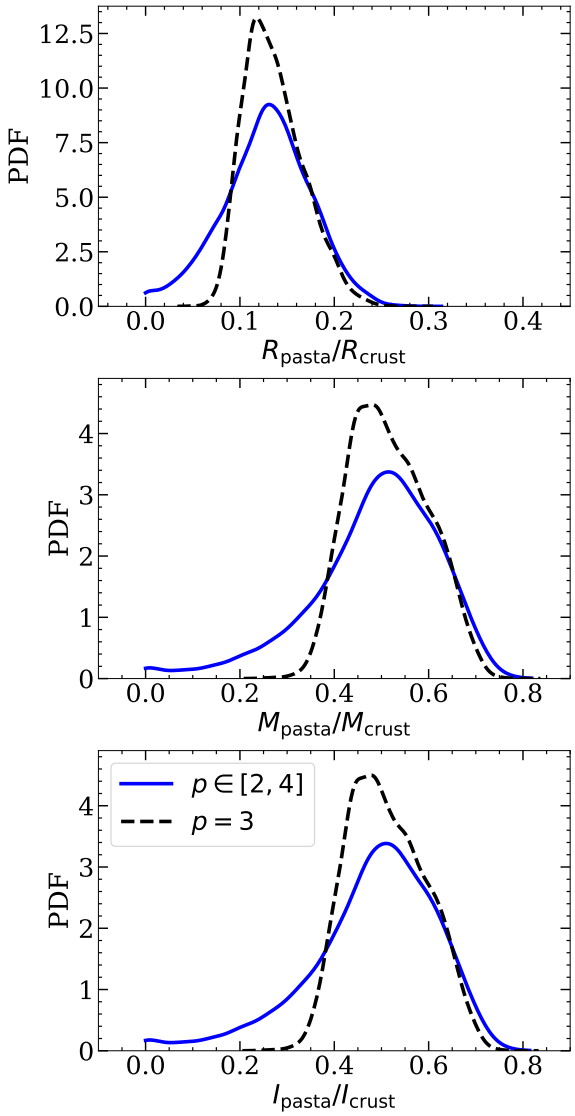

Figure 3.19: Posterior distributions of the fractional thickness (top panel), mass (middle panel), and moment of inertia (lower panel) of the pasta layer with respect to the whole crust, for a neutron star having a mass $M = M_{\rm max}$, obtained with $p = 3$ (dashed black line) and $p \in [2, 4]$ (solid blue line).

properties via the constraint on the reproduction of the nuclear masses. As a consequence, the uncertainties in the bulk parameters induce an uncertainty in the surface properties. This is consistent with the parameter fitting protocol of Skyrme interactions, for which surface properties are governed by extra gradient terms, with respect to the ones associated with the bulk behavior. In the case of relativistic functionals, however, surface properties emerge naturally from the field equations and cannot be independently varied with respect to the bulk. One may then wonder if the 5-parameter expressions, Eqs. (2.57)-(2.58), are general enough to account for the different possible behaviors of the surface tension. The quality and flexibility of this parametrization were partially verified by Newton *et al.* [131], who showed that the seminal crust composition of Ref. [9] can be indeed reproduced with it, and by Furtado & Gulminelli [132], who checked that this functional form can very precisely

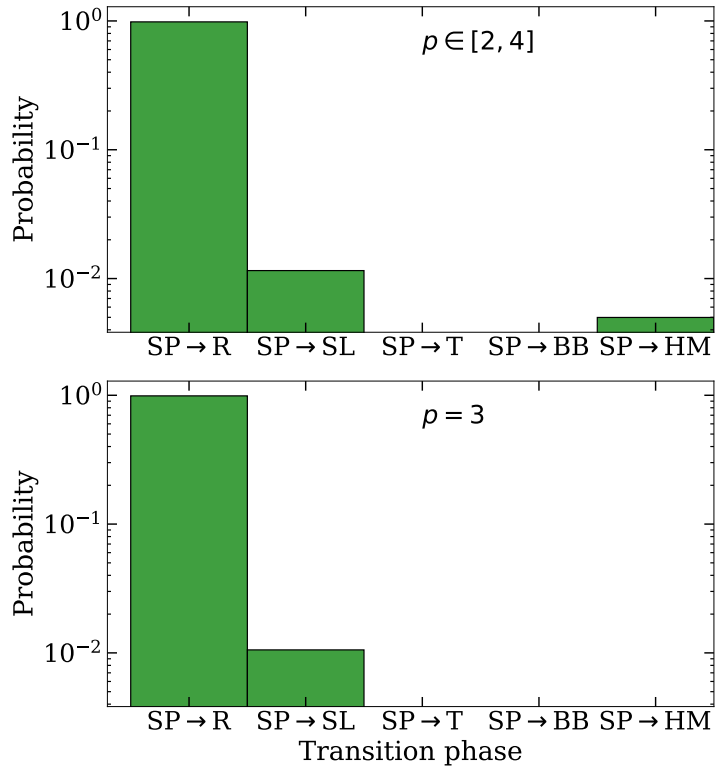

Figure 3.20: Probability of having a transition from spheres to rods (SP→R), spheres to slabs (SP→SL), spheres to tubes (SP→T), spheres to bubbles (SP→BB), and spheres to homogeneous matter (SP→HM) for $p \in [2, 4]$ (top panel) and $p = 3$ (bottom panel).

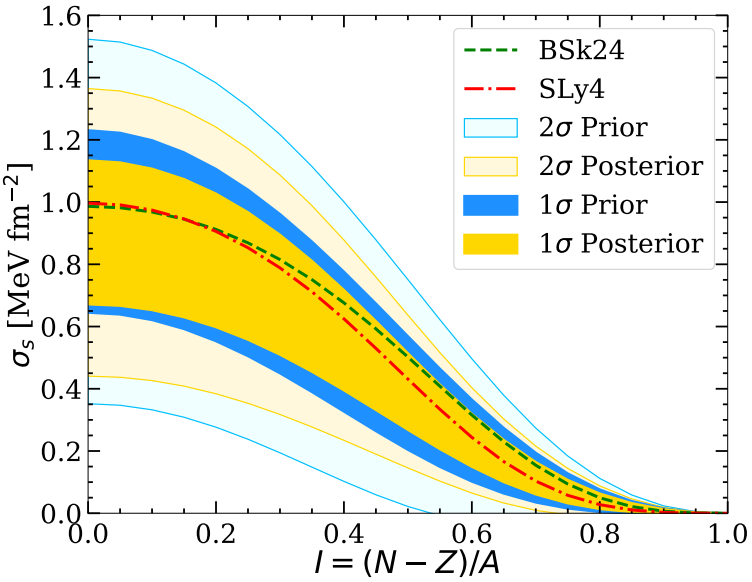

Figure 3.21: 1σ (dark bands) and 2σ bands (light bands) of the surface tension for the prior (blue bands) and posterior (yellow bands) distribution as a function of the cluster isospin I. The dashed green (dash-dotted red) line shows the surface tension obtained for BSk24 by Ref. [79] (SLy4 by Ref. [132]). See text for details.

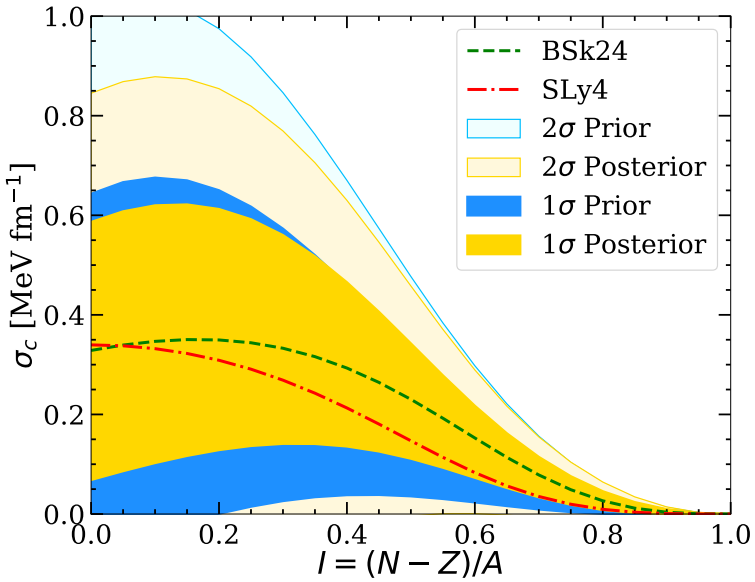

Figure 3.22: Same as Fig. 3.21 but for curvature tension.

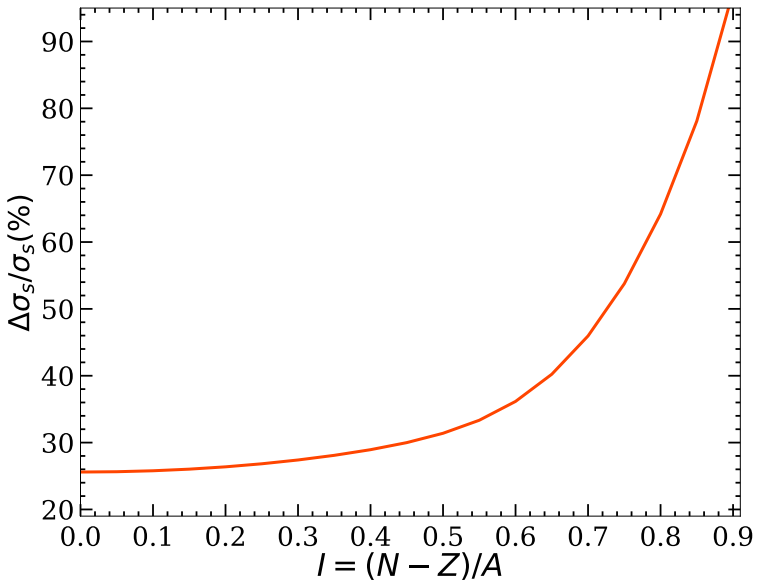

Figure 3.23: Relative uncertainty in the surface tension as a function of the cluster isospin for the posterior distribution.

reproduce extended Thomas-Fermi calculations both for terrestrial nuclei and for beyond dripline crustal nuclei in the case of the SLy4 interaction.

To generalize the discussion, I plot in Figs. 3.21 and 3.22 the 1σ (dark bands) and 2σ (light bands) estimation of the surface and curvature tensions as a function of the isospin of the denser phase, $I = (N-Z)/A$. We can see that the constraint of nuclear masses is not enough to precisely fix the surface tension of symmetric $I \approx 0$ nuclei, even if they correspond to the quasi totality of the measured masses. This can be understood from the degeneracy between

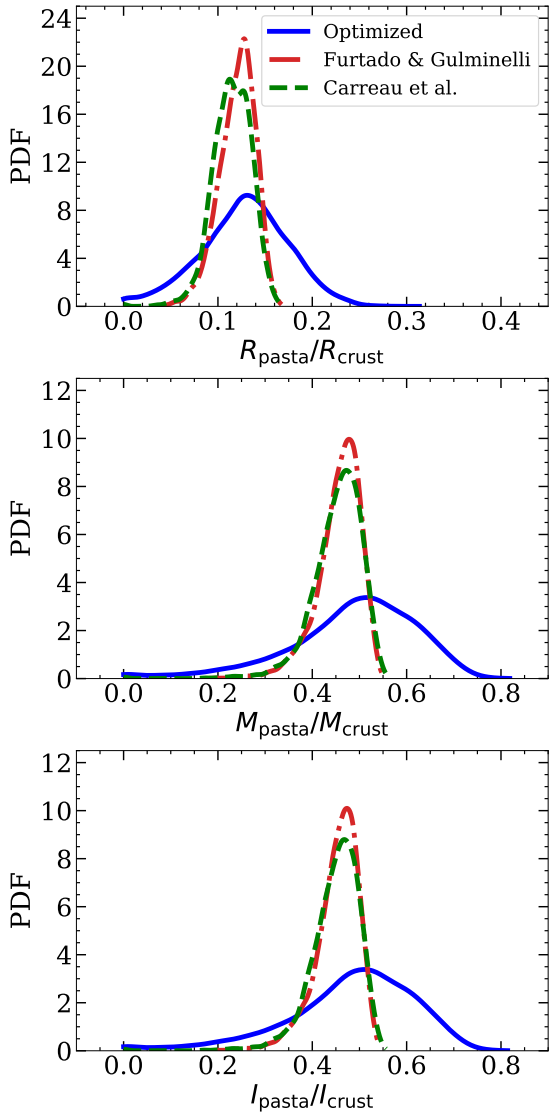

Figure 3.24: Posterior distributions of the fractional thickness (top panel), mass (middle panel), and momentum of inertia (bottom panel) of the pasta layer with respect to the whole crust. Solid blue curves: surface parameters optimized on the energy functional using the AME2016 mass table [135]; dash-dotted red (dashed green) curves: fixed surface parameters from Ref. [132] (Ref. [79]). Figure adapted from Ref. [121].

the surface and the bulk parameters implied by Eq. (2.59), and from the extreme simplicity of the CLDM approximation, which does not include shell and pairing effects. The absolute uncertainty in the surface tension decreases with increasing isospin, due to the constraint that the surface tension should vanish in pure neutron matter. However, this is not the same for the relative uncertainty, that is of the order of $> 20\%$ at the typical proton fraction of the clusters in the inner crust, $I \gtrsim 0.4$ (see Fig. 2.12), and even $\gtrsim 60\%$ for very high isospin values $I \gtrsim 0.8$, much higher than the uncertainty on stable, $I = 0 - 0.3$, nuclei that can be accessed in the laboratory, as shown in Fig. 3.23.

To assess the importance of a self-consistent calculation of surface properties from the assumed bulk energy functional in the modeling of the NS crust, we have performed two

calculations where the surface parameters in the Bayesian analysis are fixed to the values obtained from two different accurate fits of extended Thomas-Fermi calculations of a large pool of nuclei. In the work by Ref. [79], the full BSk24 extended Thomas-Fermi mass table is fitted from dripline to dripline, while the authors of Ref. [132] have used the SLy4 functional, and included in the fit ETF calculations beyond drip, with global proton fractions as low as $Y_p^{\rm WS} = 0.02$. The resulting surface parameters are reported in Table 3.3. These fits lead to surface parameters slightly different from the ones obtained in Table 3.1, because of the larger pool of nuclei included in the optimization. Moreover, in both cases, the extension of the mass table to extremely neutron-rich nuclei has allowed also an optimal determination of the p parameter (see Eq. (2.57)), that governs the extreme isospin behavior of the surface tension and cannot be fixed from the properties of terrestrial nuclei. The surface and curvature tensions corresponding to the parameters fitted by Ref. [79] (dashed green lines) Ref. [132] (dash-dotted red lines) are in very good agreement with the 1σ posterior bands of σ_s (Fig. 3.21) and σ_c (Fig. 3.22) obtained from the optimization of the surface parameters using the AME2016 mass table (dark yellow bands).

The surface tensions in Table 3.3 are more accurately determined than those deduced from the global reproduction of measured nuclear masses (see Table 3.1) and which depend on the empirical $\mathbf{X}$ parameters. However, they are not consistent with the bulk properties of functionals different from BSk24 and SLy4, respectively. The resulting posterior distribution[3] for the pasta obervables is displayed in Fig. 3.24. We can see that the use of a surface tension which is not consistent with the bulk functional (dashed green lines and dash-dotted red lines) leads to a small shift in the most probable values of the represented pasta-layer properties, and an important deformation of the distribution, with a clear underestimation of the uncertainties in the pasta observables.

3.4.2 The influence of the low-density equation of state

The chiral EFT constraint was applied in numerous previous studies of static properties of NS, see Refs. [59, 139, 261, 262]. In these studies, the accent is typically put on the high-density EOS, which is the dominant ingredient of the different astrophysical observables that are integrated over the whole NS volume, such as the tidal polarizability or the NS mass and radius. The compatibility of the functionals with the *ab initio* predictions in the very low-density region below $n \approx 0.05$ fm^{-3} has a negligible influence for these global NS observables, and as such it was often overlooked. In this section, I highlight the importance of low-density EOS in modeling pasta phases by applying the chiral EFT filter in two different density intervals, namely $[0.1, 0.2]$ fm^{-3} and $[0.02, 0.2]$ fm^{-3}. In order to have comparable statistics, when the low-density EFT constraint is applied from 0.1 fm^{-3} instead of 0.02 fm^{-3}, 2×10^6 models are generated in the prior, of which 7714 are retained. Here, the surface parameters are fitted from the AME2016 mass table, with $p \in [2, 4]$.

As long as crustal observables are concerned, the very low-density region, [0.02, 0.1] fm^{-3}, in the chiral EFT calculation is crucial. This is illustrated in Figs. 3.25-3.26, where we respectively represent the posterior distributions of the density and pressure at the crust-

[3] In this analysis, the low-density filter is applied from 0.02 fm^{-3}; out of the 10^8 computed models, 7147 (7024) are retained when the surface parameters are fixed to the values optimized for SLy4 (BSk24).

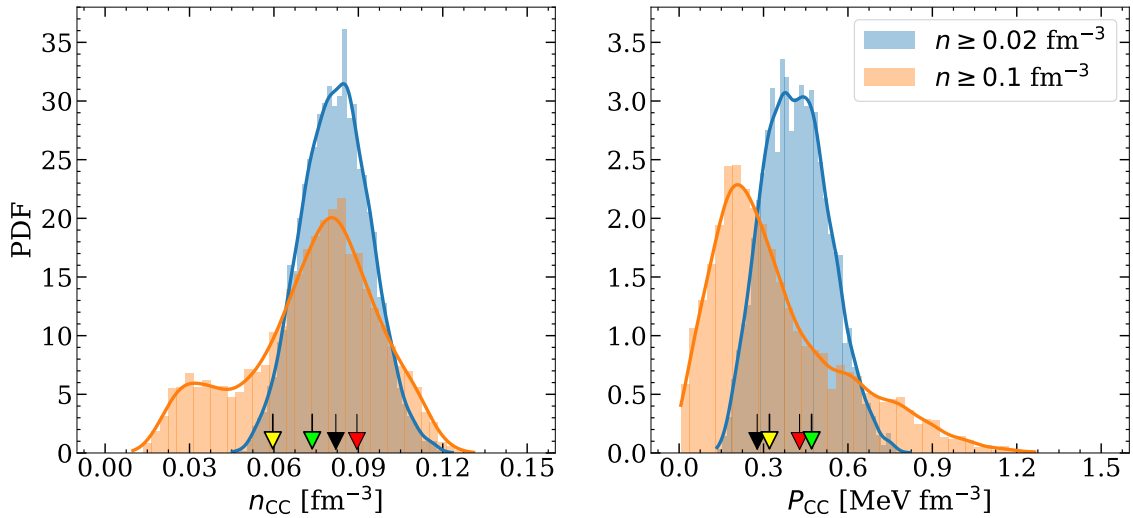

Figure 3.25: Posterior probability density distributions of crust-core transition density (left panel) and pressure (right panel), obtained considering different density intervals for the application of the chiral EFT constraint. Arrows correspond to the predictions of some selected models: BSk24 (black), RATP (red), DD-ME2 (green), and TM1 (yellow). See text for details. Figure adapted from Ref. [121].

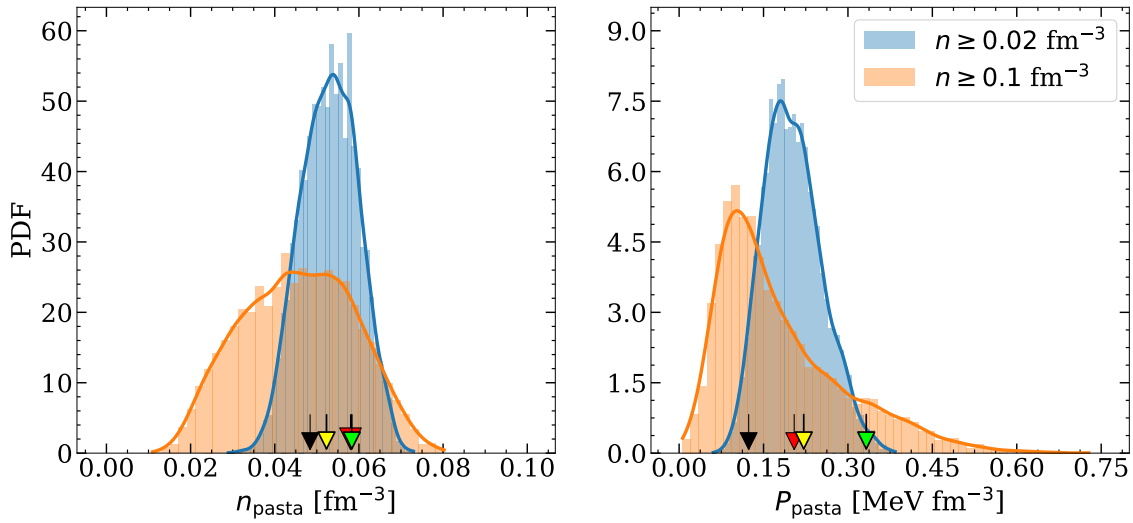

Figure 3.26: Same as Fig. 3.25, but for spheres-pasta transition.

core transition, (n_{CC}, P_{CC}), and the density and pressure at the transition from spherical nuclei to non-spherical pasta structures, (n_{pasta}, P_{pasta}). For comparison, we also indicate by arrows the predictions corresponding to some selected models: BSk24 (black-filled arrow), RATP (red-filled arrow), DD-ME2 (green-filled arrow), and TM1 (yellow-filled arrow). We can see that the very low-density part of the EOS has a notable effect on the determination of the transition points. In particular, an important number of models which correspond to reasonable properties of nuclear matter close to saturation, and therefore fulfill the chiral EFT condition for $n \geq 0.1$ fm^{-3} (orange distributions), are seen to produce very low values for the crust-core and the sphere-pasta transition point.

This implies a very thin crust for the NS and a small or negligible contribution of the pasta

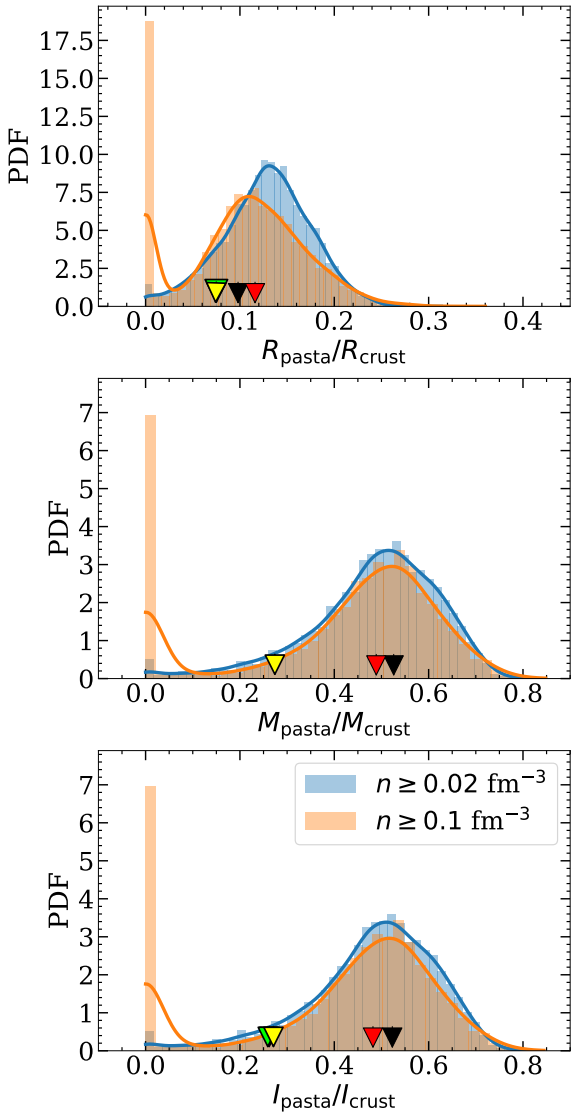

Figure 3.27: Posterior distributions of the fractional thickness (top panel), mass (middle panel), and moment of inertia (lower panel) of the pasta layer with respect to the whole crust, for a neutron star having a mass $M = M_{\rm max}$. The low-density EFT constraints and the arrows corresponding to the predictions of selected models are the same as in Figs. 3.25-3.26. See text for details. Figure adapted from Ref. [121].

phases, as shown in Fig. 3.27, which displays the prediction for the relative crustal thickness associated to the non-spherical pasta structures, $R_{\rm pasta}/R_{\rm crust}$ (top panel), the associated mass, $M_{\rm pasta}/M_{\rm crust}$ (middle panel), and the fraction of the moment of inertia, $I_{\rm pasta}/I_{\rm crust}$ (lower panel). The two choices for the low-density constraints and the arrows indicating the predictions of some selected models (BSk24, RATP, DD-ME2, and TM1) are the same as those adopted in Figs. 3.25-3.26. These observables are computed from the numerical solution of the TOV equations, the crust radius (mass) being calculated as the difference between the total NS radius (mass) and that of the core (we have considered NS having a total mass equal to the maximum mass predicted by each computed model). As it can be seen in Figs. 3.25-3.27, when the chiral EFT constraint is applied from $n \geq 0.02$ fm^{-3}

(blue distributions), almost all models corresponding to a very small (or even null) pasta contribution are filtered out of the posterior distribution. Knowing that the precision and reliability of the *ab initio* calculations improve with decreasing density, we can conclude that our present theoretical understanding of nuclear matter implies that pasta phases should exist in the inner crust of NS.

The results of Figs. 3.25-3.27 clearly show that, as far as the crustal properties are concerned, the treatment of the very low-density region has a sizeable impact. It is interesting to observe that recently, the authors of Ref. [77] conducted a systematic investigation of the composition of the NS inner crust and also underlined the importance of constraining the pure neutron-matter EOS at sub-nuclear densities for a reliable description of NS crusts. Moreover, the important effect of the behavior of the functional at densities below 0.1 fm^{-3} shown by these figures suggests that beyond the influence of the $L_{\rm sym}$ parameter, which has been advanced by numerous studies [158, 159], the high-order parameters might also play a role in the determination of the pasta phase. We, therefore, turn to examine the effect of the chiral EFT filter on the empirical parameters, and the correlation between the transition densities and the behavior of the energy functional at low density.

Figure 3.28 shows the distributions of the energy per baryon (upper panels) and pressure (lower panels) of the different models, for symmetric ($\delta = 0$) and pure neutron matter ($\delta = 1$). The uncertainty bands[4] from Ref. [110] are plotted as dash-dotted black lines, while the violin shapes represent the posterior distributions. Particularly, the models passing the EFT constraints at all densities, i.e., $[0.02, 0.2]$ fm^{-3}, are labeled as "$n \geq 0.02$ fm^{-3}" and represented by coral shapes on the left part of the density axes in all panels. In panels a and c, we compare these distributions with those consistent with the constraints in the density range $n \geq 0.1$ fm^{-3} but not in the interval $[0.02 - 0.1]$ fm^{-3} (green shapes on the right part of the density axes, labeled as "$n \geq 0.1$ fm^{-3} only[5]"). As we have seen in Figs. 3.25 and 3.27, the very low-density regions of the LD filter eliminate models with low crust-core transition density, $n_{\rm CC} < 0.05$ fm^{-3}, and with very small (or zero) pasta contribution. To elaborate on this point, in panels b and d, we compare the distributions satisfying the low-density EFT constraints (labeled "$n \geq 0.02$ fm^{-3}") with those resulting from the filter applied from $n \geq 0.1$ fm^{-3} but predicting a crust-core transition lower than 0.05 fm^{-3}. The latter ones are represented in light blue shapes on the right part of the density axes in panels b and d, labeled as "$n_{\rm CC} < 0.05$ fm^{-3}".

Comparing panels a and b of Fig. 3.28, we can notice that models can violate the EFT constraint both because of a too-soft or a too-stiff energy behavior of pure neutron matter at sub-saturation densities, but it is the excessive stiffness (corresponding to very low neutron energy) that leads to abnormally low transition densities. In the symmetric matter sector, the mass filter is more constraining than the EFT calculation around saturation and the filter is not effective in that region. Going well below saturation, where the mass constraint becomes ineffective, we can observe that the low transition densities are associated to an overbinding of symmetric matter. Looking at the lower panels, we can see that the low transition

[4] We have considered the bands in energy as a 90% confidence interval, that is, the boundaries of the bands represented here are increased by 5% with respect to the original calculations of Ref. [110].

[5] In the posterior distribution where the LD filter is applied in [0.1, 0.2] fm^{-3}, there are some models passing also [0.02, 0.1] fm^{-3}. Here, we want to compare the models passing the EFT bands at all densities, i.e., $[0.02, 0.2]$ fm^{-3}, with those passing the bands only from $[0.1, 0.2]$ fm^{-3}, hence the label "$n \geq 0.1$ fm^{-3} only".

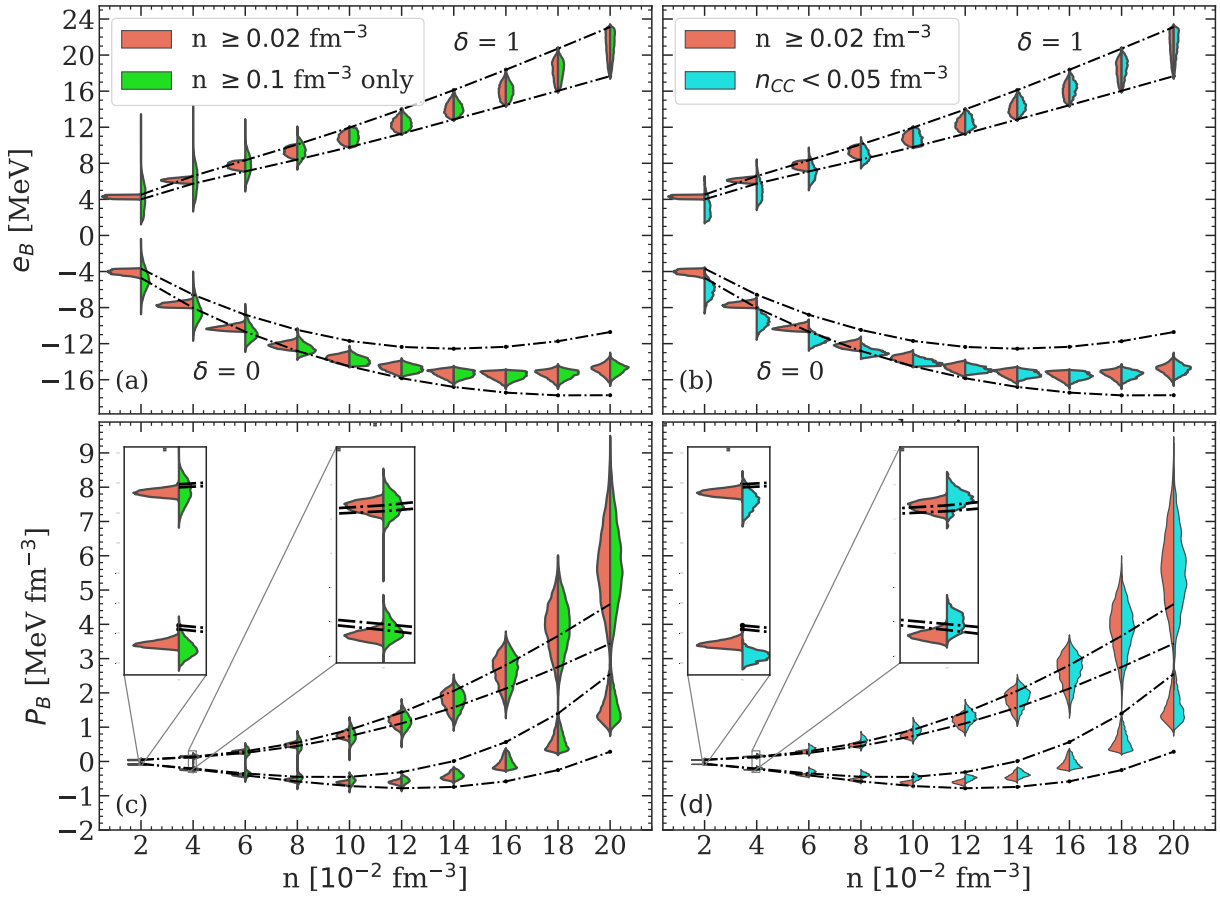

Figure 3.28: Bands of the energy per baryon (top panels) and pressure (bottom panels) of symmetric ($\delta = 0$) and pure neutron matter ($\delta = 1$) as a function of density representing the chiral EFT constraint from [110] (dash-dotted black lines). The probability distributions of models passing the EFT constraints from $n \geq 0.1$ fm^{-3} only (green) and $n \geq 0.02$ fm^{-3} (coral) are represented as a violin-shape on the left panels. On the right panels, we show the same quantities but for models consistent with the bands from $n \geq 0.02$ fm^{-3} (coral) in comparison with those from $n \geq 0.1$ fm^{-3} but predicting a crust-core transition $n_{CC} < 0.05$ fm^{-3} (light blue). The insets in panels (c) and (d) show a zoom of the low-density part. See text for details. Figure adapted from Ref. [142].

densities are globally associated to higher pressures in the sub-saturation region. However, a non-trivial effect is observed at extremely low densities. Indeed we can see that in this regime (right inset in panel c), the effect of the filter is to narrow the distribution of the pressure, without sensibly modifying its shape. As a result, going to even lower densities (left inset in panel c) the pressure is systematically underestimated, showing that the zero-density limit is not correctly reached. This underlines the fact that the zero-density limit as imposed by *ab initio* considerations is not correctly modelled by phenomenological functionals [263, 264]. From panel d, we can see that the violation of the EFT predictions are particularly important in the functionals leading to abnormally low transition densities. These observations lead us to expect that further improvement in the predictions of the pasta properties might be obtained if the low-density behavior will be enforced in the functional through the Yang-Lee expansion following Refs. [263, 264].

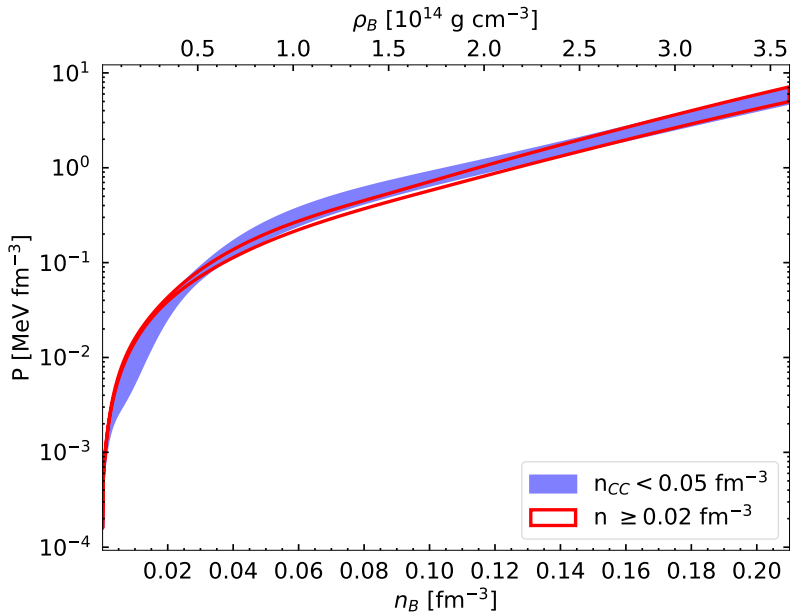

Figure 3.29: 1σ band of the total pressure, defined as in Eq. (2.75), as a function of baryon density n_B (bottom axis) and total mass-energy density ρ_B (top axis), obtained from the posterior distribution of models for which the EFT constraints is applied from $n \geq 0.02$ fm^{-3} (red) and from $n \geq 0.1$ fm^{-3} with a crust-core transition density $n_{CC} < 0.05$ fm^{-3} (blue). Figure adapted from Ref. [121].

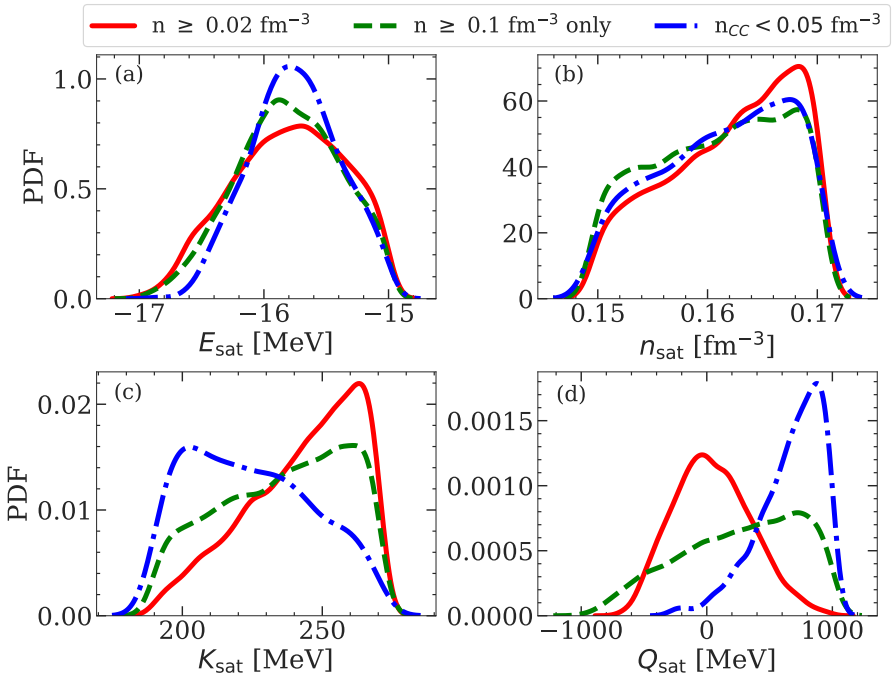

Figure 3.30: Posterior distribution of the isoscalar bulk parameters for models for which the chiral EFT constraint from Ref. [110] are applied from $n \geq 0.02$ fm^{-3} (red solid line), $n \geq 0.1$ fm^{-3} only (green dashed lines), and from $n \geq 0.1$ fm^{-3} but predicting a crust-core transition $n_{CC} < 0.05$ fm^{-3} (dash-dotted blue line). See text for details. Figure adapted from Ref. [142].

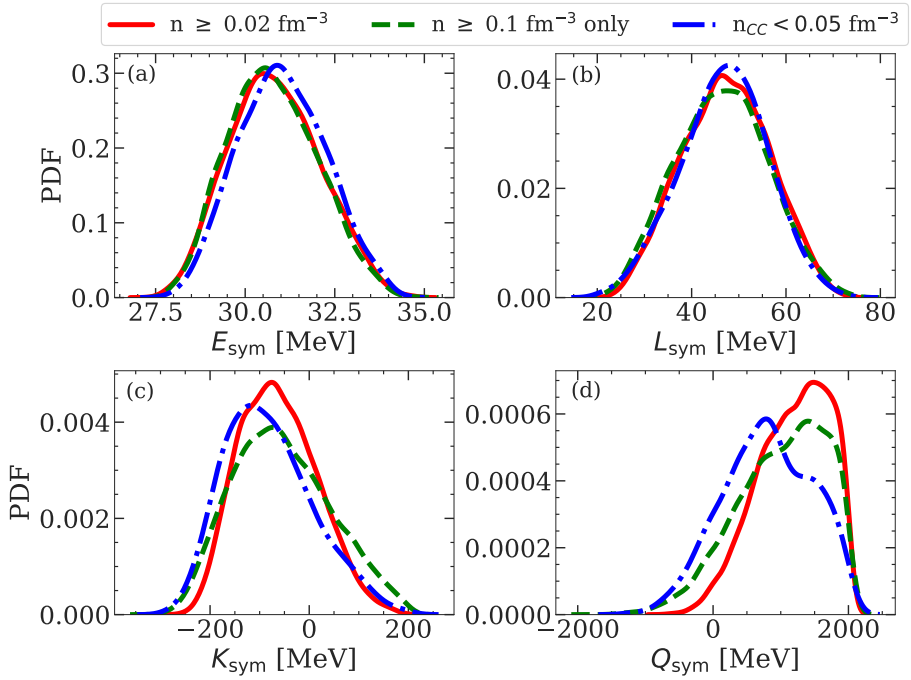

Figure 3.31: Same as in Fig. 3.30 but for the isovector bulk parameters. See text for details.

From the behavior of nuclear matter, one can expect the EOS to manifest in a very similar manner. Indeed, this is demonstrated in Fig. 3.29, where we plot the total pressure in the crust (see Eq. (2.75)) as a function of the baryon density n_B (bottom axis) and mass-energy density ρ_B (top axis). The posterior EOS resulted by applying the EFT bands from $n \geq 0.1$ fm^{-3} and associated with a low crust-core transition density, $n_{CC} < 0.05$ fm^{-3}, is shown in blue at 1σ confidence level. For comparison, the posterior EOS for models which are consistent with the EFT bands from very low densities, $n > 0.02$ fm^{-3}, is depicted in red, also at 1σ level. Figure. 3.29 clearly indicates that models yielding a crust-core transition below 0.05 fm^{-3} reflects in a stiffer EOS in the NS crust in the baryon density range $0.03 \lesssim n_B \lesssim 0.1$ fm^{-3} (or, equivalently in the mass-energy range $0.5 \times 10^{14} \lesssim \rho_B \lesssim 1.8 \times 10^{14}$ g cm^{-3}).

We now examine the impact of this low-density filter on the bulk parameters, whose distributions are plotted in Figs. 3.30 and 3.31 for the isoscalar and isovector parameters, respectively. We can see that no strong impact is observed on the $E_{\rm sat}$ and $n_{\rm sat}$ isoscalar parameter distributions (see panels (a) and (b) in Fig. 3.30), nor on the isovector parameter ones (see Fig. 3.31), except a slight shift of the distributions towards higher values of $K_{\rm sym}$ and $Q_{\rm sym}$ for models filtered from $n \geq 0.02$ fm^{-3}. On the other hand, the low-density filter has a sizeable effect on the higher-order isoscalar parameters $K_{\rm sat}$ and $Q_{\rm sat}$ (see panels (c) and (d) in Fig. 3.30). Indeed, models filtered from $n \geq 0.02$ fm^{-3} (red solid lines) have a more peaked distributions on higher (lower) $K_{\rm sat}$ ($Q_{\rm sat}$) with respect to models predicting $n_{\rm CC} \leq 0.05$ fm^{-3} (dot-dashed blue lines). This behavior can also explain why models yielding low crust-core transition also have lower energy per baryon and higher pressure at sub-saturation density (see Fig. 3.28). Indeed, considering only the lower-order terms in the expansion, the nuclear-

matter energy per nucleon in terms of empirical parameters reads

$$e_B(n,\delta) \approx E_{\rm sat} + \frac{1}{2}K_{\rm sat}x^2 + \frac{1}{6}Q_{\rm sat}x^3 + \delta^2\left(E_{\rm sym} + L_{\rm sym}x + \frac{1}{2}K_{\rm sym}x^2 + \frac{1}{6}Q_{\rm sym}x^3\right) , \tag{3.26}$$

and, for the pressure,

$$P_B(n,\delta) \approx \frac{n_{\rm sat}}{3}(1+3x)^2\left[K_{\rm sat}x + \frac{1}{2}Q_{\rm sat}x^2 + \delta^2\left(L_{\rm sym} + K_{\rm sym}x + \frac{1}{2}Q_{\rm sym}x^2\right)\right] . \tag{3.27}$$

Therefore, roughly speaking, lower average values of $K_{\rm sat}$ and higher values of $Q_{\rm sat}$ result in lower energy per baryon and higher pressure for $x < 0$.

From these results, we can infer that the low-energy part of the functional, and particularly the higher-order isoscalar parameters, have a non-negligible impact on a correct estimation of the transition densities.

3.4.3 Correlations

In the previous sections, we have analyzed the distributions of the different bulk and surface parameters that enter into the modeling of the NS crust. To assess their relative importance in the determination of the pasta properties, we turn to examine the Pearson linear correlation coefficients between the transition properties as well as pasta observables with the bulk and surface parameters. In particular, I show in Fig. 3.32 the correlation coefficient for the crust-core transition density and pressure, $n_{\rm CC}$ and $P_{\rm CC}$, the density and pressure of the transition between spherical and non-spherical configurations, $n_{\rm pasta}$ and $P_{\rm pasta}$, and the relative mass and thickness of the pasta layer with respect to the whole crust, $M_{\rm pasta}/M_{\rm crust}$ and $R_{\rm pasta}/R_{\rm crust}$. For each quantity, the correlations are displayed for the prior, as well as for the posterior distributions. Lines labelled as $n \geq 0.02$ fm^{-3} ($n \geq 0.1$ fm^{-3}) refer to posteriors for which models have been constrained by EFT calculations in the range $[0.02 - 0.2]$ fm^{-3} ($[0.1 - 0.2]$ fm^{-3}).

As for the crust-core transition, we can see that when no constraints are considered ("prior")[6], a correlation of the crust-core transition density (pressure) with $L_{\rm sym}$ ($K_{\rm sym}$ and $Q_{\rm sym}$) is noticed, as already pointed out in Refs. [127, 158]. A (slight) correlation with the second and third derivatives of the symmetry energy, $K_{\rm sym}$ and $Q_{\rm sym}$, is also observed in the prior for the pasta transition. However, only when the physical constraints are applied, further interesting correlations start to appear, particularly with respect to the surface parameters when the models are filtered from $n \geq 0.02$ fm^{-3}. Also, a light correlation with $Q_{\rm sat}$ emerges for models filtered from $n \geq 0.1$ fm^{-3}, while the correlation with the symmetry parameters are preserved. As for the pasta transition density and pressure, we can see that only when the EFT constraint is applied from very low density, more significant correlations emerge. Indeed, otherwise, compensations among the different terms in the functional can occur, thus blurring the correlations. The most relevant bulk parameters seem to be the

[6] Unlike in Chapter 2, here we do not include the likehood from the mass fit in the prior.

energy at saturation, $E_{\rm sat}$, and to a less extent the higher-order derivatives of the symmetry energy $K_{\rm sym}$ and $Q_{\rm sym}$.

Figure 3.32: Pearson correlations between different crustal properties and the bulk, surface, and curvature parameters in the prior and posterior distributions. Two different density intervals for the application of the chiral EFT constraint are considered. See text for details. Figure adapted from Refs. [121, 142].

From Fig. 3.32, we can also observe that both the crust-core transition density and pressure as well as the transition between spherical and pasta configuration are correlated with the surface parameters, particularly when the low-density EFT constraint is enforced from $n \geq 0.02$ fm^{-3}. In particular, the strong correlation of the spheres-pasta transition with $E_{\rm sat}$ might be understood from the important correlation imposed by the mass constraint between $E_{\rm sat}$ and the parameters governing the surface tension at moderate isospin (σ_0, $\sigma_{0,c}$, β). As for the crust-core transition, we can see that it is mainly correlated with the isovector surface parameters, namely b_s and p. Such correlation was already pointed out by Carreau et al. [127], who observed that, when the low-density filter was considered and the p parameter was allowed to vary, the transition point was correlated to the surface properties, and the isovector surface tension was the dominant parameter determining the crust-core transition.

It is encouraging to observe that the fully unconstrained parameter p is not influential at all in the determination of the pasta transition point (see also in Fig. 3.18). As far as this latter is concerned, the most important parameters are instead the curvature parameters, namely $\sigma_{0,c}$ and β, together with σ_0, that are at least in principle more accessible from experiments, if a more refined model of nuclear mass is employed in the future.

Finally, in the last two panels of Fig. 3.32, I also display the correlation for the relative mass and thickness of the pasta layer with respect to the crust. Similar to the case of transition density and pressure, in the absence of physical constraints, that is, in the prior distribution, no very strong correlation can be observed between the bulk parameters and the pasta observables, as expected from the even exploration of the parameter space of our prior distribution. When only the models compatible with our present knowledge of nuclear matter are retained, that is, the posterior, the correlations with the physically significant parameters start to appear, particularly when the LD filter is applied from a very low density. The most relevant parameters are seen to be the energy of symmetric matter $E_{\rm sat}$ and symmetry energy $E_{\rm sym}$ at saturation, as well as the slope of the symmetry energy $L_{\rm sym}$. These parameters are already relatively well constrained by nuclear theory and experiments, but we can expect that their uncertainty will be further reduced in upcoming studies, which will lead to increased precision in the determination of the pasta contribution to the physics of the crust. Regarding the correlation with the surface parameters, since $M_{\rm pasta}/M_{\rm crust}$ and $R_{\rm pasta}/R_{\rm crust}$ carry both information from the spheres-pasta as well as crust-core transitions, correlation can be observed with both (σ_0, $\sigma_{0,c}$, β), which determine the former, and (p, b_s), which is important for the latter.

3.5 Conclusions

In this chapter, we have studied the properties of the pasta phases in cold-catalyzed NS, within the CLDM described in Sect. 2.1.2. Particularly, the bulk properties are obtained using the meta-modeling technique [64, 65], while the surface parameters are fitted from the AME2016 mass table [135]. Five different geometries of matter were considered: spheres, rods, slabs, tubes, and bubbles.

With the BSk24 functional, we first illustrated the geometry dependence of the crust equilibrium composition. We found that while the surrounding gas densities, i.e., $n_e = n_p$

and n_{gn}, are invariant with the geometry, the cluster properties, which are I, n_i, and r_N, exhibit some shape dependence at different extents. Particularly, the strongest geometry dependence appears in the clusters/holes size r_N. Due to the oversimplification in the pasta configuration, we observed discontinuities in the radius/half-thickness associated to the most favorable phase. At each baryon density, if only the most probable configuration is considered, we showed that the composition found for spheres, which are I, n_i, n_p and n_{gn}, can be used to calculate the size of the pasta structure. As a result, we adopted this spheres-composition approximation in calculating the EOS and solving the TOV equations.

Table 3.4: Posterior estimations of the fractional thickness $R_{\rm pasta}/R_{\rm crust}$, moment of inertia $I_{\rm pasta}/I_{\rm crust}$, and mass $M_{\rm pasta}/M_{\rm crust}$ of the pasta layer, normalized to the corresponding crustal quantity, for a neutron star having a mass $M = M_{\rm max}$. The uncertainties indicate 1σ deviations. The chiral EFT filter is applied from either $n = 0.02$ fm^{-3} or $n = 0.1$ fm^{-3}. Table adapted from Ref. [121]

	Posterior	
	$n \geq 0.02$ fm^{-3}	$n \geq 0.1$ fm^{-3}
$R_{\rm pasta}/R_{\rm crust}$	0.128 ± 0.047	0.104 ± 0.063
$I_{\rm pasta}/I_{\rm crust}$	0.480 ± 0.137	0.411 ± 0.212
$M_{\rm pasta}/M_{\rm crust}$	0.485 ± 0.138	0.415 ± 0.214

We also studied the model dependence of the results by employing various nuclear functionals. Even though all the considered models predict the existence of pasta phases, the transition densities among the geometries are strongly model dependent. For this reason, we performed a Bayesian analysis by largely varying the model parameters using uniform priors and generating posterior distributions with filters accounting for both our present low-density nuclear physics knowledge and high-density general and NS physics constraints. We concluded that the most relevant parameters in determining the pasta-phase properties are the lower-order empirical and surface parameters. Furthermore, we found that fixing the surface parameters could lead to an underestimation of the uncertainties in the pasta properties. Moreover, we also highlighted the importance of a consistent calculation between the nuclear functional and surface properties. In addition, by applying the low-density EFT filters on the energy of homogeneous matter on two different density ranges, $[0.1, 0.2]$ fm^{-3} and $[0.02, 0.2]$ fm^{-3}, we showed that the low-density nuclear physics constraints are crucial in determining the crustal and pasta observables. This implies that the higher-order parameters, such as $K_{\rm sat}$ and $Q_{\rm sat}$, also play a role in the determination of crustal properties. Our final predictions for the different pasta observables, namely the fractional thickness $R_{\rm pasta}/R_{\rm crust}$, moment of inertia $I_{\rm pasta}/I_{\rm crust}$, and mass $M_{\rm pasta}/M_{\rm crust}$, of the pasta layer for a NS with a mass equal to its maximum mass, are summarized in Table 3.4.

This formalism for the crust can be extended at finite temperatures, similarly to the approach adopted in Refs. [81] and [80] for the outer and inner crusts, respectively, to account for the so-called impurities. This quantity is of particular interest in different NS phenomena, including NS cooling, and is discussed in Chapter 4.

CHAPTER 4

Inner crust of proto-neutron stars

Generally, the composition of the inner crust is determined under the so-called "cold–catalyzed matter hypothesis", where matter is supposed to be at zero temperature and composed of a periodic lattice of fully ionized and neutron-rich ions, surrounded by unbound neutrons, in beta equilibrium with a highly relativistic electron gas, see the discussion in the Introduction. Such crystalline structure can be divided into identical WS cells [124], with an ion embedded in the center [9, 66], as presented in Chapters 2 and 3. However, this zero-temperature picture may not reflect the real composition of the NS crust [1, 58, 265]. In reality, the initial temperature of PNS after being born from the gravitational core-collapse is very high, $T \sim 10^{11}$ K [1, 266–268] (Fig. 1.1). These PNS are then cooled down mainly via neutrino emission. The cooling of PNS is usually categorized into two main regimes: the short term, which happens at $t \lesssim 60$ seconds from the PNS birth, and the longer term period lasting about millions of years [266]. This chapter focuses on the late stage of the former case, with the assumption that beta equilibrium holds. In particular, we consider PNS after $t \sim 50$ seconds, at which the star is expected to cool to below a few 10^{10} K, and the neutrino mean free path overcomes the stellar radius, leading to neutrino transparency (see Fig. 9 of Ref. [267]). At such temperatures, the PNS crust is expected to be characterized by statistical distributions of different nuclear species in the liquid phase, and the nucleon background can also contain free protons, see e.g., Ref. [7] for a review.

As the star cools down, the temperature decreases, and the width of the nuclear distribution becomes narrower [80]. Thus, at sufficiently low temperatures, where the distribution is sharply peaked, the mixture of different nuclei can be approximated by the most probable one. This approach is called the one-component plasma (OCP) approximation. If the full thermodynamic equilibrium is maintained until the ground state is reached, the NS crust is made of pure layers, each consisting of a one-component Coulomb crystal obtained at zero temperature. However, after the solidification of the crust, the crust composition is believed to be frozen [1, 58]. As a result, the composition of the crust is expected to reflect the situation near the crystallization point $T \sim T_m$, with T_m being the crystallization temperature [58]. Furthermore, depending on the NS cooling timescales, the equilibrium

configuration of the crust could even be frozen at some temperature T_f higher than the crystallization one, $T_f > T_m$ (see e.g., Ref. [265]). Consequently, the impurities induced by the coexistence of different nuclear species would remain, and the one-component picture would become even less reliable. As a result, the nuclear distribution needs to be taken into account in a multi-component plasma (MCP) approach, (see e.g., Refs. [80, 82, 83, 269]).

Due to the intrinsic complexity of the MCP calculation, most approaches to the finite-temperature crust have been performed employing the OCP approximation (see e.g., Refs. [79, 90, 93, 224, 270]). This approximation is justified at relatively low densities and temperatures, where the most probable nucleus is very close to the ground-state OCP composition and the contribution of other ions is typically very small, or as far as average thermodynamic quantities are concerned [84, 269]. Nevertheless, the coexistence of different nuclear species can influence in a significant way the transport properties of the NS crust (see Ref. [251] for a review), and also various NS phenomena, such as magneto-rotational evolution [56] and magneto-thermal evolution [55].

In this chapter, I describe the liquid crust of PNS in both the OCP approximation (Sect. 4.1) and the MCP approach (Sect. 4.2). In particular, I discuss the impact of the cluster center-of-mass motion, which is often neglected in the literature, on the crust equilibrium configuration, as well as its role in breaking the ensemble equivalence between MCP and OCP. Moreover, I also present the investigation on the validity of the OCP approximation and highlight the importance of a fully self-consistent MCP approach. The conclusion can be found in Sect. 4.3. We note that the possible presence of pasta phases is not included in this study.

4.1 One-component plasma approximation

Similar to the case of zero-temperature limit (see Chapters 2 and 3), in the OCP or single-nucleus approximation at finite temperature, the inner crust of a NS can be considered to be composed of identical WS cells, each of which includes a fully ionized ion of mass $M_i = (A - Z)m_n + Zm_p$, surrounded by uniform distributions of electrons and dripped nucleons. At finite temperatures, the nucleon background contains not only free neutrons but also free protons. Let us denote the density of the dripped protons by n_{gp}. In the liquid phase that we are interested in, the ion is no longer located at the center of the cell, but it can explore the whole volume. Nevertheless, because of the OCP approximation, a WS volume can still be defined as the optimal volume encompassing each (moving) ion and is obtained from the condition of charge neutrality.

In this section, I elaborate on the results published in Ref. [270]. Specifically, in Sect. 4.1.1, I detail the derivation of the ion effective mass in an incompressible, irrotational, and non-viscous fluid by employing a standard hydrodynamic approach. Two boundary conditions, corresponding to two assumptions on the penetrability of the ion, are considered separately in Sects. 4.1.1.1 and 4.1.1.2. Then, different terms in the ion free energy are presented in Sect. 4.1.2. In particular, after outlining the expression of the bulk, Coulomb, surface, and curvature free-energy terms in Sects. 4.1.2.1 and 4.1.2.2, special attention is given to the derivation of the translational free energy in Sect. 4.1.2.3. Finally, I introduce the formalism

for the liquid PNS inner crust in Sect. 4.1.3, in which the results at beta equilibrium and fixed total proton fraction are shown respectively in Sects. 4.1.3.1 and 4.1.3.2.

4.1.1 Studying the ion motion with a hydrodynamic approach

In the following, I review the derivation of the effective mass of an ion moving in an incompressible, irrotational, and non-viscous fluid, within an ideal hydrodynamic approach, as already proposed in the literature for a different application [271–276]. Two different boundary conditions, which correspond to the assumptions that the ion is (i) an impenetrable hard sphere, and (ii) a permeable sphere, are considered.

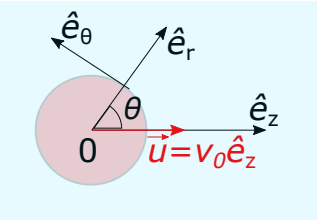

Figure 4.1: Sketch of the motion of the ion (red sphere) in a uniform background, with the considered system of reference. $\hat{e}_z$, $\hat{e}_r$, and $\hat{e}_\theta$ indicate the unit vectors. Figure reproduced from Ref. [270].

Let the z-axis be the direction of the sphere velocity $\vec{u}$ (see Fig. 4.1), then, $\vec{u}$ can be written as:

$$\vec{u} = v_0 \hat{e}_z. \tag{4.1}$$

Assuming that nuclear matter both inside and outside the ion is incompressible and irrotational, there exists a velocity potential $\Phi(\vec{r}) = \Phi_{\rm in}(\vec{r}) + \Phi_{\rm out}(\vec{r})$, with $\vec{r}$ being the vector from the sphere center, and $\Phi_{\rm in}(\vec{r})$ ($\Phi_{\rm out}(\vec{r})$) being the potential inside (outside) the cluster, satisfying the continuity equation for an incompressible fluid, i.e., the Laplace equation:

$$\nabla^2 \Phi(\vec{r}) = 0, \tag{4.2}$$

and the associated velocity field $\vec{v}$ can be written as:

$$\vec{v} = \vec{v}_{\rm in} + \vec{v}_{\rm out} = \nabla\Phi. \tag{4.3}$$

As the flow is azimuthally symmetric, the velocity potential $\Phi(\vec{r})$ only depends on the radial distance r and the polar angle θ (see Fig. 4.1):

$$\Phi(\vec{r}) = \Phi(r, \theta), \tag{4.4}$$

leading to the following Laplace equation in the spherical coordinate:

$$\frac{1}{r^2}\frac{\partial}{\partial r}\left(r^2 \frac{\partial \Phi}{\partial r}\right) + \frac{1}{r^2 \sin\theta}\frac{\partial}{\partial \theta}\left(\sin\theta \frac{\partial \Phi}{\partial \theta}\right) = 0. \tag{4.5}$$

Using the standard separable ansatz, $\Phi(r, \theta) = R(r)\Theta(\theta)$, Eq. (4.5) becomes:

$$\frac{1}{R(r)}\frac{d}{dr}\left(r^2 \frac{dR(r)}{dr}\right) + \frac{1}{\Theta(\theta)\sin\theta}\frac{d}{d\theta}\left(\sin\theta \frac{d\Theta(\theta)}{d\theta}\right) = 0. \tag{4.6}$$

Then, one can split the Laplace equation in Eq. (4.6) into two separate ordinary differential equations:

$$\frac{1}{R(r)}\frac{d}{dr}\left(r^2\frac{dR(r)}{dr}\right) = \zeta, \tag{4.7}$$

$$\frac{1}{\Theta(\theta)\sin\theta}\frac{d}{d\theta}\left(\sin\theta\frac{d\Theta(\theta)}{d\theta}\right) = -\zeta, \tag{4.8}$$

with ζ being a constant. It is well known that ζ is chosen to be $l(l+1)$ such that Eqs. (4.7)-(4.8) are equivalent to differential equations whose solutions are available. Particularly, concerning the radial part, we can rewrite Eq. (4.7) as

$$r^2R''(r) + 2rR'(r) - l(l+1)R(r) = 0. \tag{4.9}$$

We can identify Eq. (4.9) with the Euler-Cauchy equation, whose solution reads

$$R^{(l)}(r) = \mathcal{A}r^l + \frac{\mathcal{B}}{r^{l+1}}, \tag{4.10}$$

where $\mathcal{A}$ and $\mathcal{B}$ are constants to be determined from the specific boundary conditions. Similarly, for the angular part, we have:

$$\frac{1}{\sin\theta}\frac{d}{d\theta}\left(\sin\theta\frac{d\Theta(\theta)}{d\theta}\right) + l(l+1)\Theta(\theta) = 0, \tag{4.11}$$

which can be recognized as the Legendre equation in the variable of $\cos\theta$. Therefore,

$$\Theta^{(l)}(\theta) = P_l(\cos\theta), \tag{4.12}$$

where P_l is the Legendre polynomial. Combining Eqs. (4.10) and (4.12), the solution for the velocity potential has the following form:

$$\Phi_{\rm k}^{(l)}(r,\theta) = P_l(\cos\theta)\left(\mathcal{A}_{\rm k}^{(l)}r^l + \frac{\mathcal{B}_{\rm k}^{(l)}}{r^{l+1}}\right), \tag{4.13}$$

where $\mathrm{k} = \{\mathrm{in}, \mathrm{out}\}$, and the general equation for the Laplace equation in the spherical coordinate, Eq. (4.5), can be written as the sum of all the solutions,

$$\Phi_{\rm k}(r,\theta) = \sum_{l=0}^{\infty} P_l(\cos\theta)\left(\mathcal{A}_{\rm k}^{(l)}r^l + \frac{\mathcal{B}_{\rm k}^{(l)}}{r^{l+1}}\right). \tag{4.14}$$

4.1.1.1 Ion as an impenetrable hard sphere

Let us first consider the ion as an impenetrable hard sphere. If the center of the reference frame coincides with the center of the ion, the radial velocity on the surface of the sphere must vanish:

$$\begin{aligned} v_{r,\rm k}(r_N,\theta) - v_0\cos\theta &= 0, \\ \frac{\partial}{\partial r}\Phi_{\rm k}(r,\theta)\Big|_{r=r_N} - v_0\cos\theta &= 0, \end{aligned} \tag{4.15}$$

where $v_{r,\mathrm{k}}$ is the radial component of the velocity field $\vec{v}_{\mathrm{k}}$. Using the expression of the velocity potential in Eq. (4.14), we obtain:

$$\sum_{l=0}^{\infty} \left.\frac{dR_k^{(l)}(r)}{dr}\right|_{r=r_N} P_l(\cos\theta) - v_0\cos\theta = 0, \tag{4.16}$$

implying that $l = 1$. As a result, the velocity potentials inside and outside the cluster can be expressed as

$$\Phi_{\mathrm{in}}(r,\theta) = \left(\mathcal{A}_{\mathrm{in}} r + \frac{\mathcal{B}_{\mathrm{in}}}{r^2}\right)\cos\theta, \tag{4.17}$$

$$\Phi_{\mathrm{out}}(r,\theta) = \left(\mathcal{A}_{\mathrm{out}} r + \frac{\mathcal{B}_{\mathrm{out}}}{r^2}\right)\cos\theta. \tag{4.18}$$

Since $\Phi_{\mathrm{in}}(r,\theta)$ should not diverge as $r \to 0$, the second term on the right-hand side of Eq. (4.17) should be zero, leading to

$$\mathcal{B}_{\mathrm{in}} = 0. \tag{4.19}$$

To determined the coefficient $\mathcal{A}_{\mathrm{in}}$, one can use the condition that the velocity field is constant inside the ion,

$$\vec{v}(r \le r_N, \theta) = \nabla\Phi_{\mathrm{in}} = \vec{u}, \tag{4.20}$$

and it is straightforward to show that:

$$\mathcal{A}_{\mathrm{in}} = v_0. \tag{4.21}$$

Concerning Φ_{out}, the constants $\mathcal{A}_{\mathrm{out}}$ and $\mathcal{B}_{\mathrm{out}}$ are determined by imposing that in the crust reference frame, the nucleon fluid is at rest far from the ion, $\vec{v}(r \to \infty, \theta) = \vec{0}$, and the sphere is impenetrable, meaning that the ion "pushes" the external nucleon fluid along in the same direction of motion, that is, $v_{r,\mathrm{out}}(r \to r_N, \theta) = u_r$ (equivalent to Eq. (4.15)), where $v_{r,\mathrm{out}} = \frac{\partial}{\partial r}\Phi_{\mathrm{out}}(r,\theta)$ and $u_r = v_0\cos\theta$ are the radial components of $\vec{v}$ and $\vec{u}$, respectively. Thus, the boundary conditions for Φ_{out} can be written as:

$$\lim_{r\to\infty} \Phi_{\mathrm{out}}(r,\theta) = 0, \tag{4.22}$$

$$\left.\frac{\partial}{\partial r}\Phi_{\mathrm{out}}(r,\theta)\right|_{r=r_N} - v_0\cos\theta = 0. \tag{4.23}$$

Equation (4.22) implies that:

$$\mathcal{A}_{\mathrm{out}} = 0, \tag{4.24}$$

and from Eq. (4.23), one can write:

$$-2\mathcal{B}_{\mathrm{out}}\frac{1}{r_N^3}\cos\theta - v_0\cos\theta = 0, \tag{4.25}$$

leading to the following expression for the coefficient $\mathcal{B}_{\mathrm{out}}$:

$$\mathcal{B}_{\mathrm{out}} = \frac{-v_0 r_N^3}{2}. \tag{4.26}$$

As all the coefficients are determined, the potential field Φ can be written as:

$$\Phi(r,\theta) = \begin{cases} v_0 r\cos\theta & \text{if } r \leq r_N \ , \\ -\frac{v_0 r_N^3}{2r^2}\cos\theta & \text{if } r > r_N \ . \end{cases} \tag{4.27}$$

The kinetic energy associated to the flow can therefore be calculated using:

$$\begin{aligned} E_k(\vec{v}) &= \frac{1}{2}\int_V d^3\vec{r}\rho_b(r)|\nabla\Phi|^2 \\ &= \frac{1}{2}\int_V d^3\vec{r}\rho_b(r)\nabla\cdot(\Phi\nabla\Phi) \ , \end{aligned} \tag{4.28}$$

where $\rho_b(r)$ is the local (baryonic) mass density, and the integral is extended to the total volume. The former can be expressed as

$$\rho_b(r) = \begin{cases} \rho_{b,i} & \text{if } r \leq r_N \ , \\ \rho_{b,\mathrm{g}} & \text{if } r > r_N \ , \end{cases} \tag{4.29}$$

with $\rho_{b,i} = M_i/V_N$ being the mass density of the ion and $\rho_{b,\mathrm{g}} = m_p n_{gp} + m_n n_{gn}$ being that of the outside fluid.

Furthermore, from the first to the second line of Eq. (4.28), we have used the following relation:

$$\nabla\cdot(\Phi\nabla\Phi) = \Phi\nabla^2\Phi + \nabla\Phi\cdot\nabla\Phi = |\nabla\Phi|^2. \tag{4.30}$$

Applying the divergence theorem[1], the kinetic energy in Eq. (4.28) reads:

$$E_k = \frac{1}{2}\oint_S dS\rho_{b,i}\Phi_{\mathrm{in}}\left(\nabla\Phi_{\mathrm{in}}\cdot\hat{e}_r\right) - \frac{1}{2}\oint_S dS\rho_{b,\mathrm{g}}\Phi_{\mathrm{out}}\left(\nabla\Phi_{\mathrm{out}}\cdot\hat{e}_r\right). \tag{4.31}$$

Considering the first term on the right-hand side of Eq. (4.31), which corresponds to the kinetic energy inside the ion, one can write:

$$E_{k,\mathrm{in}} = \frac{1}{2}\oint_S dS\rho_{b,i}\Phi_{\mathrm{in}}\left(\nabla\Phi_{\mathrm{in}}\cdot\hat{e}_r\right), \tag{4.32}$$

$$= \frac{\rho_{b,i}}{2}2\pi r_N^2\int_0^\pi d\theta\sin\theta(v_0 r_N\cos\theta)(v_0 cos\theta), \tag{4.33}$$

$$= -\pi r_N^3 v_0^2\rho_{b,i}\int_0^\pi d(\cos\theta)(\cos\theta)^2, \tag{4.34}$$

$$= -\pi r_N^3 v_0^2\rho_{b,i}\frac{(\cos\theta)^3|_0^\pi}{3} = \frac{2}{3}\pi r_N^3 v_0^2\rho_{b,i}, \tag{4.35}$$

$$= \frac{1}{2}M_i v_0^2, \tag{4.36}$$

as expected.

[1]The divergence theorem reads: $\int_V d^3\vec{r}\nabla\cdot\vec{F} = \oint_S dS\vec{F}\cdot\vec{n}$, where $\vec{F}$ is a continuously differentiable vector field, and $\vec{n}$ is the outer unit normal vector. The right-hand side of the equation is a closed integral over the surface S, while the left-hand side gives the volume integral of the divergence of the field over the volume V inside the surface.

Concerning the kinetic energy associated to the flow of the nucleon background, we have:

$$E_{k,\mathrm{out}} = -\frac{1}{2}\oint_S dS\rho_{b,\mathrm{g}}\Phi_{\mathrm{out}}\left(\nabla\Phi_{\mathrm{out}}\cdot\hat{e}_r\right), \tag{4.37}$$

$$= -\frac{\rho_{b,\mathrm{g}}}{2}2\pi r_N^2\int_0^\pi d\theta\sin\theta\left(-\frac{v_0 r_N^3}{2r_N^2}\cos\theta\right)\left(\frac{2v_0 r_N^3}{2r_N^3}\cos\theta\right), \tag{4.38}$$

$$= -\frac{1}{2}\pi r_N^3 v_0^2\rho_{b,\mathrm{g}}\int_0^\pi d(\cos\theta)(\cos\theta)^2, \tag{4.39}$$

$$= \frac{1}{3}\pi r_N^3\rho_{b,\mathrm{g}}v_0^2 = \frac{\gamma}{2}\frac{1}{2}M_i v_0^2. \tag{4.40}$$

Here, γ denotes the ratio of the nucleon background mass density to that of the cluster:

$$\gamma \equiv \frac{\rho_{b,\mathrm{g}}}{\rho_{b,i}}. \tag{4.41}$$

Then, the total kinetic energy of the system is given by:

$$E_k = E_{k,\mathrm{in}} + E_{k,\mathrm{out}}, \tag{4.42}$$

$$= \frac{1}{2}M_i(\frac{\gamma}{2}+1)v_0^2 = \frac{1}{2}M_i^\star v_0^2. \tag{4.43}$$

Thus, if the ion is an impenetrable hard sphere, then its effective mass can be expressed as:

$$M_i^\star = M_i\left(1+\frac{1}{2}\gamma\right), \tag{4.44}$$

which reduces to $M_i^\star = M_i$ if the ion is in vacuum ($\gamma = 0$). Therefore, modeling the ion as an impenetrable hard sphere leads to an increase in the ion effective mass. Making the further approximation that the neutron and proton mass be equal, $m_n \approx m_p$, one retrieves Eq. (2.43) of Ref. [11] (although in the latter work the outside medium also includes alpha particles). Additionally, if there are no dripped protons, that is, $\gamma = n_{gn}/n_i$, one recovers the picture of the neutron fluid flowing around the cluster, as mentioned in Ref. [272].

4.1.1.2 Ion as a permeable sphere

From the microscopic point of view, the cluster and the dripped nucleons are portions of the same fluid (nuclear matter) with different densities and proton-to-neutron ratios. Therefore, one expects that some portion of the nucleons in the cluster participate in the flow of the external fluid. This situation was studied by Refs. [273, 274]. In particular, in the referred works, the authors considered the ion and the dripped neutrons as a single fluid and, as opposed to the hard-sphere image, they assumed the cluster to be fully permeable. This latter is also an extreme picture because one only expects the nucleons in the cluster to participate in the external flow only if they are loosely bound. A more realistic picture would probably be intermediate between these two extreme scenarios, whereby a fraction of nucleons in the cluster can 'freely' move with the external fluid (see also Fig. 7 in Ref. [275]).

Let ρ_b^{f} denote the mass density of the nucleons inside the ion that participate in the flow. Therefore, $\rho_{b,i} - \rho_b^{\mathrm{f}}$ is the mass density of neutrons plus protons moving together in the cluster.

The boundary conditions in the case of a partially-permeable ion are given by:

$$\Phi_{\rm in}(r_N,\theta) = \Phi_{\rm out}(r_N,\theta), \tag{4.45}$$

$$\rho_b^{\rm f}\left(\frac{\partial\Phi_{\rm in}}{\partial r} - v_0\cos\theta\right)\bigg|_{r=r_N} = \rho_{b,{\rm g}}\left(\frac{\partial\Phi_{\rm out}}{\partial r} - v_0\cos\theta\right)\bigg|_{r=r_N}, \tag{4.46}$$

$$\lim_{r\to\infty}\Phi_{\rm out}(r,\theta) = 0. \tag{4.47}$$

In the above equations, Eq. (4.45) ensures the continuity of the velocity potential at the ion surface. The second equation, Eq. (4.46), represents the conservation of the baryon mass along the radial flow. From this equation, we can also deduce that $l = 1$. Similar to the case of a hard sphere, Eq. (4.47) gives the asymptotic behavior of the velocity field at infinity, which also implies $\mathcal{A}_{\rm out} = 0$. Moreover, the non-divergence of $\Phi_{\rm in}$ at $r \to 0$ requires $\mathcal{B}_{\rm in} = 0$. As a result, we can write the solution of the Laplace equation as:

$$\Phi_{\rm in}(r,\theta) = \mathcal{A}_{\rm in} r\cos\theta, \tag{4.48}$$

$$\Phi_{\rm out}(r,\theta) = \frac{\mathcal{B}_{\rm out}}{r^2}\cos\theta. \tag{4.49}$$

Replacing Eqs. (4.48)-(4.49) into Eqs. (4.45)-(4.46), we have:

$$\mathcal{A}_{\rm in} r_N = \mathcal{B}_{\rm out}\frac{1}{r_N^2}, \tag{4.50}$$

$$\rho_b^{\rm f}\left(\mathcal{A}_{\rm in} - v_0\right) = -\rho_{b,{\rm g}}\left(\frac{2\mathcal{B}_{\rm out}}{r_N^3} + v_0\right). \tag{4.51}$$

Solving for $\mathcal{A}_{\rm in}$ and $\mathcal{B}_{\rm out}$, we obtain:

$$\mathcal{A}_{\rm in} = \frac{\rho_b^{\rm f} - \rho_{b,{\rm g}}}{\rho_b^{\rm f} + 2\rho_{b,{\rm g}}} v_0, \tag{4.52}$$

$$\mathcal{B}_{\rm out} = \mathcal{A}_{\rm in} r_N^3 = \frac{\rho_b^{\rm f} - \rho_{b,{\rm g}}}{\rho_b^{\rm f} + 2\rho_{b,{\rm g}}} v_0 r_N^3. \tag{4.53}$$

Finally, the velocity potential inside and outside the permeable ion has the form:

$$\Phi(r,\theta) = \begin{cases} \frac{\delta^{\rm f}-\gamma}{\delta^{\rm f}+2\gamma}\; r\; v_0\cos\theta & \text{if } r < r_N\ , \\ \frac{\delta^{\rm f}-\gamma}{\delta^{\rm f}+2\gamma}\; \frac{r_N^3}{r^2}\; v_0\cos\theta & \text{if } r > r_N\ , \end{cases} \tag{4.54}$$

where we define $\delta^{\rm f} \equiv \rho_b^{\rm f}/\rho_{b,i}$ and γ is expressed as in Eq. (4.41).

Repeating the same steps as in Sect. 4.1.1.1, we can show that the total kinetic energy of the system has the following expression:

$$E_k(\vec{v}) = \frac{1}{2}M_i v_0^2\left[1 - \delta^{\rm f} + \frac{(\delta^{\rm f}-\gamma)^2}{\delta^{\rm f}+2\gamma}\right] = \frac{1}{2}M_i^\star v_0^2\ , \tag{4.55}$$

where we define the effective mass of the ion as:

$$M_i^\star = M_i\left[1 - \delta^{\rm f} + \frac{(\delta^{\rm f}-\gamma)^2}{\delta^{\rm f}+2\gamma}\right]\ . \tag{4.56}$$

If $\delta^{\rm f} > \gamma/4$, we can see that the effective mass of the cluster is reduced compared to the bare one. In other words, the cluster moves in the medium with a reduced speed. In the limiting $\delta^{\rm f} = 0$ case, corresponding to the situation where no neutrons participate in the external flow, and all neutrons move with the protons in the cluster, one recovers Eq. (4.44). In the limiting $\delta^{\rm f} = 1$ case, meaning that all nucleons in the cluster participate in the "free" motion and the cluster is completely permeable to the flow of the outside fluid, one retrieves Eq. (12) of Ref. [274], which has the correct high-density physical limit, namely $M_i^\star \to 0$ for $\gamma \to 1$ (uniform homogeneous system),

$$M_i^\star = M\frac{(1-\gamma)^2}{1+2\gamma}\ . \tag{4.57}$$

We can see that the expression in Eq. (4.56) is general, where different chosen values of $\delta^{\rm f}$ lead to various prescriptions for the ion effective mass. The use of the renormalization of the ion mass in the translational free energy is discussed in Sect. 4.1.2.3.

4.1.2 Cluster free energy in the liquid phase

When the inner crust is in the liquid phase, the collective degrees of freedom are translational. At variance with the cluster energy in cold–catalyzed NS, Eq. (2.52), the cluster free energy F_i at a temperature above the crystallization can be written as:

$$F_i = (A-Z)m_n c^2 + Zm_p c^2 + F_{\rm bulk} + F_{\rm Coul+surf+curv} + F_{\rm trans}, \tag{4.58}$$

where $F_{\rm bulk} = \frac{A}{n_i}\mathcal{F}_B(n_i, I, T)$ is the cluster bulk free energy[2]; $F_{\rm Coul+surf+curv}$ is the sum of the Coulomb, surface, and curvature energies at finite temperatures; and the last term, $F_{\rm trans}$, accounts for the translational degrees of freedom of the cluster. I discuss these terms in detail in the following sections.

4.1.2.1 Nuclear matter free energy in the mean-field approximation

Computation of the cluster and the surrounding nuclear-matter bulk free-energy terms requires knowledge of the free-energy density of homogeneous nuclear matter, $\mathcal{F}_B(n, \delta, T)$, at a total baryonic density[3] $n = n_n + n_p$ and isospin asymmetry $\delta = (n_n - n_p)/n$. To this aim, we use the self-consistent mean-field thermodynamics [11, 152]. In this approach, the free energy is decomposed into a "potential" and a "kinetic" part:

$$\mathcal{F}_B(n, \delta, T) = \mathcal{V}(n, \delta) + \mathcal{F}_{\rm kin}(n, \delta, T), \tag{4.59}$$

where the temperature dependence encoded in the term $\mathcal{F}_{\rm kin}$ is the same as in a system of independent quasi-particles with effective single-particle energies $e_q = \frac{p^2}{2m_q^\star}$ (p being the momentum and $q = n, p$ labeling neutrons and protons) and with shifted effective chemical potentials $\tilde{\mu}_q$ that account for the self-consistent interaction. Regarding the "potential" term, we still employ the meta-modeling approach proposed in Refs. [64, 65], $\mathcal{V} = \mathcal{V}_{\rm MM}^{\mathcal{N}=4}$, as in Eq. (2.15).

[2] In this chapter, the uppercase F, the lowercase f, and $\mathcal{F}$ to denote the free energy per cell, the free energy per nucleon, and the free energy per unit volume, respectively.

[3] Here, n_p refers to the proton density in the homogeneous matter, while elsewhere when treating inhomogeneous matter, $n_p = Z/V_{\rm WS}$.

The Fermi-Dirac distribution of an interacting fermion system reads:

$$f_{\rm FD}(e_q, T, \tilde{\mu}_q) = \frac{1}{1+\exp\left(\frac{e_q-\tilde{\mu}_q}{k_B T}\right)}, \tag{4.60}$$

in which the auxiliary chemical potential is related to the thermodynamical one, $\mu^0_{{\rm HM},q} = \left(\frac{\partial \mathcal{F}_B}{\partial n_q}\right)_{n_{q'}}$ ($n_{q'}$ being the number density of the other species), through:

$$\tilde{\mu}_q = \mu^0_{{\rm HM},q} - U_q, \tag{4.61}$$

where U_q is the mean-field potential. Here, $\mu^0_{{\rm HM},q}$ is used to denote the chemical potential without the nucleon rest mass, $\mu^0_{\rm HM} = \mu_{{\rm HM},q} - m_q c^2$ (see Eq. (2.29) for the case at zero temperature). Let $\mathcal{H}$ be the total energy density of the nuclear matter system,

$$\mathcal{H} = \mathcal{V}(n,\delta) + \sum_{\bar{q}=n,p} \mathcal{E}^{\bar{q}}_{\rm kin}, \tag{4.62}$$

$$= \mathcal{V}(n,\delta) + \sum_{\bar{q}=n,p} \frac{\hbar^2 \tau_{\bar{q}}}{2m^\star_{\bar{q}}}, \tag{4.63}$$

then the mean-field potential U_q is defined as:

$$U_q = \left(\frac{\partial \mathcal{H}}{\partial n_q}\right)_\tau = \left(\frac{\partial \mathcal{V}}{\partial n_q}\right)_{n_{q'}} + \sum_{\bar{q}=n,p} \mathcal{E}^{\bar{q}}_{\rm kin} m^\star_{\bar{q}} \left(\frac{\partial\left(1/m^\star_{\bar{q}}\right)}{\partial n_q}\right)_{n_{q'}}, \tag{4.64}$$

where the partial derivatives with respect to n_n (n_p) are computed keeping n_p (n_n) constant.

The particle number density, n_q, is related to the corresponding auxiliary chemical potential $\tilde{\mu}_q$ through the following relation:

$$n_q = \int_0^\infty \rho(e_q) f_{\rm FD}(e_q) de_q, \tag{4.65}$$

where $\rho(e_q)$ is the density of fermionic energy states,

$$\rho(e_q) = \frac{1}{2\pi^2}\left(\frac{2m^\star_q}{\hbar^2}\right)^{3/2} \sqrt{e_q}\,. \tag{4.66}$$

In the above equation, $m^\star_q(n_q, n_{q'})$ is the density-dependent nucleon effective mass, defined in Eq. (2.11). With Eqs. (4.60) and (4.66), one can demonstrate that Eq. (4.65) is equivalent to:

$$n_q = \frac{1}{2\pi^2}\left(\frac{2m^\star_q}{\hbar^2}\right)^{3/2} \int_0^\infty \frac{\sqrt{e_q}}{1+\exp\left(\frac{e_q-\tilde{\mu}_q}{k_B T}\right)} de_q, \tag{4.67}$$

Defining the nucleon thermal wavelength as

$$\lambda_q = \left(\frac{2\pi\hbar^2}{k_{\rm B} T m^\star_q}\right)^{1/2}, \tag{4.68}$$

the particle number density in Eq. (4.67) can be written as:

$$n_q = \int_0^\infty de_q \frac{\rho(e_q)}{1+\exp\left\{\frac{e_q-\tilde{\mu}_q}{k_{\rm B}T}\right\}} = \frac{2}{\lambda_q^3} F_{1/2}\left(\frac{\tilde{\mu}_q}{k_{\rm B}T}\right), \tag{4.69}$$

in which $F_{1/2}$ denotes the Fermi-Dirac integral:

$$F_j(x) = \frac{1}{\Gamma(j+1)} \int_0^\infty \frac{t^j dt}{1+e^{t-x}}, \tag{4.70}$$

where $j > -1$.

To evaluate the $\mathcal{F}_{\rm kin}(n, \delta, T)$ term, we can use the thermodynamic relation

$$\mathcal{F}_{\rm kin} = \sum_{q=n,p} \mathcal{E}^q_{\rm kin} - T\mathcal{S}^q_{\rm kin}, \tag{4.71}$$

where $\mathcal{E}^q_{\rm kin}$ and $\mathcal{S}^q_{\rm kin}$ are the kinetic energy and entropy densities, respectively, of a system of independent particles with single-particle energy $e_q = p^2/2m^\star_q$. The kinetic energy density corresponding to particles of type q at density n_q is given by:

$$\mathcal{E}^q_{\rm kin} = \int_0^\infty de_q \frac{e_q \rho(e_q)}{1+\exp\left\{\frac{e_q-\tilde{\mu}_q}{k_{\rm B}T}\right\}} = \frac{3k_{\rm B}T}{\lambda_q^3} F_{3/2}\left(\frac{\tilde{\mu}_q}{k_{\rm B}T}\right). \tag{4.72}$$

The entropy is defined from the partial grand canonical thermodynamic potential $\Phi^q_{\rm kin}$ as:

$$\mathcal{S}^q_{\rm kin} = -\left.\frac{\partial \Phi^q_{\rm kin}}{\partial T}\right|_{\tilde{\mu}_q}. \tag{4.73}$$

Using the expression of the grand canonical thermodynamic potential density $\Phi^q_{\rm kin}$,

$$\begin{aligned}\Phi^q_{\rm kin} &= -k_{\rm B}T \int_0^\infty \ln\left[1+\exp\left\{\left(-\frac{e_q-\tilde{\mu}_q}{k_B T}\right)\right\}\right] \rho(e_q) de_q \\ &= -\frac{2}{3}\mathcal{E}^q_{\rm kin}\ ,\end{aligned} \tag{4.74}$$

we obtain:

$$\mathcal{S}^q_{\rm kin} = \frac{5}{3}\frac{\mathcal{E}^q_{\rm kin}}{T} - \frac{\tilde{\mu}_q}{T} n_q. \tag{4.75}$$

Incorporating Eqs. (4.75) and (4.72) into Eq. (4.71), the final result for $\mathcal{F}_{\rm kin}$ reads:

$$\mathcal{F}_{\rm kin} = \sum_{q=n,p} \left[\frac{-2k_{\rm B}T}{\lambda_q^3} F_{3/2}\left(\frac{\tilde{\mu}_q}{k_{\rm B}T}\right) + n_q \tilde{\mu}_q\right]. \tag{4.76}$$

Finite-temperature mean-field theory [11, 152] implies that the free energy density $\mathcal{F}_{\rm kin}$ given by Eq. (4.76) represents the correct "kinetic" term entering Eq. (4.59), provided that the relation between the effective chemical potential $\tilde{\mu}_q$ and the thermodynamic potential μ^0_q is satisfied, as written in Eq. (4.61).

Numerically, the nuclear matter free energy in our calculation is determined as follows. Given the component number densities n_q of the system, the associated chemical potential $\tilde{\mu}_q$ is calculated using Eq. (4.69). Then, inserting the obtained value of $\tilde{\mu}_q$ into Eq. (4.76), one gets the kinetic-free-energy density $\mathcal{F}_{\rm kin}$. Using the meta-modeling formalism described in Chapter 2, with Eq. (2.15) for the potential term, one obtaines the total nuclear matter free-energy density $\mathcal{F}_B$ from Eq. (4.59). In addition, the mean-field potential U_q, Eq. (4.64), and thereby the physical chemical potential $\mu^0_{{\rm HM},q} = \tilde{\mu}_q + U_q$ (with rest mass: $\mu_{{\rm HM},q} = \tilde{\mu}_q + U_q + m_q c^2$) can be determined.

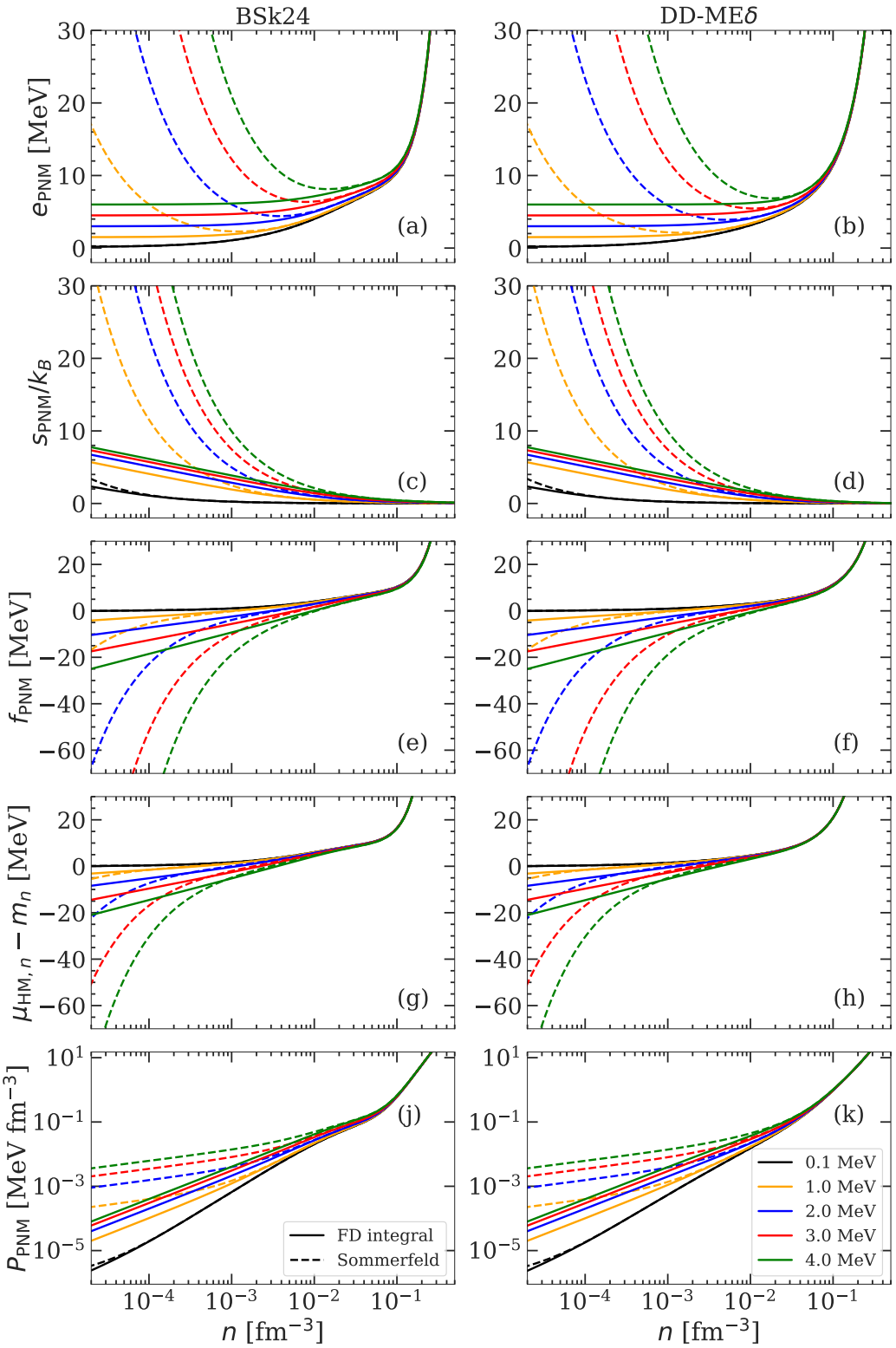

Figure 4.2: Evolution as a function of the total nuclear matter density n of different thermodynamic quantities —energy per nucleon (panels a and b), entropy per nucleon (panels c and d), free energy per nucleon (panels e and f), neutron chemical potential without rest mass (panels g and h), and pressure (panels j and k)— for pure neutron matter obtained using the complete Fermi-Dirac integral (solid lines) and the second-order Sommerfeld approximation (dashed lines) at five different temperatures. Two functionals are considered: BSk24 (left panels) and DD-MEδ (right panels).

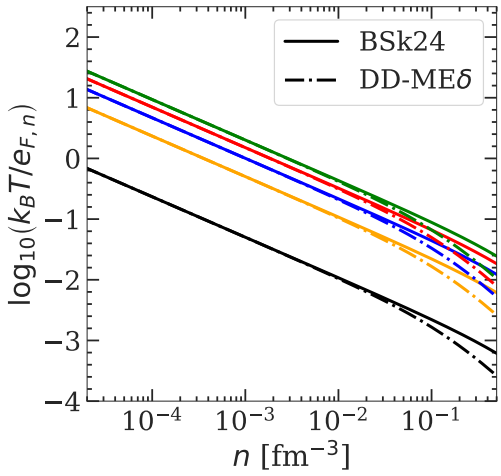

Figure 4.3: Ratio (in logarithmic scale) of the temperature to the neutron Fermi energy as a function of the nuclear matter density n for pure neutron matter. The solid (dash-dotted) lines are obtained for BSk24 (DD-MEδ) for five different temperatures: 0.1 MeV (black), 1.0 MeV (orange), 2.0 MeV(blue), 3.0 MeV (red), and 4.0 MeV (green).

Finally, the nuclear pressure reads:

$$P_B = \sum_{q=n,p} n_q \mu^0_{\mathrm{HM},q}(n,\delta) - \mathcal{F}_B(n,\delta) = \sum_{q=n,p} n_q(\mu_{\mathrm{HM},q}(n,\delta) - m_q c^2) - \mathcal{F}_B(n,\delta). \tag{4.77}$$

In the degenerate limit, $\frac{\tilde{\mu}_q}{k_BT} \gg 1$ or equivalently $k_BT \ll e_{F,q}$, with $e_{F,q}$ being the Fermi energy,

$$e_{F,q} = \frac{\hbar^2 k_{F,q}^2}{2m_q^\star} = \frac{\hbar^2(3\pi^2 n_q)^{2/3}}{2m_q^\star}, \tag{4.78}$$

the complete Fermi-Dirac integrals can be approximated by the Sommerfeld expansions. At the second order, one can show that

$$\tilde{\mu}_q \approx e_{F,q}\left[1 - \frac{\pi^2}{12}\left(\frac{k_BT}{e_{F,q}}\right)^2\right], \tag{4.79}$$

$$\mathcal{E}^q_{\mathrm{kin}} \approx \frac{3}{5} n_q e_{F,q}\left[1 + \frac{5\pi^2}{12}\left(\frac{k_BT}{e_{F,q}}\right)^2\right], \tag{4.80}$$

$$\mathcal{S}^q_{\mathrm{kin}} \approx \frac{\pi^2}{2} n_q \frac{k_B^2 T}{e_{F,q}}, \tag{4.81}$$

$$\mathcal{F}^q_{\mathrm{kin}} \approx \frac{3}{5} n_q e_{F,q}\left[1 - \frac{5\pi^2}{12}\left(\frac{k_BT}{e_{F,q}}\right)^2\right]. \tag{4.82}$$

Once these quantities are determined, the pressure P_B and the physical chemical potential $\mu_{\mathrm{HM},q}$ in the Sommerfeld approximation can be calculated using the relations in Eqs. (4.77) and (4.61), respectively, see also Ref. [277].

To evaluate the validity of the approximations in Eqs. (4.79)-(4.82), in Fig. 4.2, I compare different thermodynamic quantities corresponding to PNM calculated using the complete

Fermi-Dirac integrals (solid lines) with those obtained using the second-order Sommerfeld expansions (dashed lines) for BSk24 (left panels) and DD-MEδ (right panels) at different temperatures. We can easily see that the approximations produce good results at high densities and low temperatures. Particularly, at $k_BT = 0.1$ MeV (black lines), the second-order Sommerfeld expansions are sufficient to describe the nuclear-matter properties, even at very low densities, $n < 10^{-4}$ fm^{-3}, while at $k_BT = 1.0$ MeV (orange lines), the approximations are valid at $n > 10^{-3}$ fm^{-3}. Therefore, the Sommerfeld expansions can be used for calculating different thermodynamic properties of both neutron gas and nuclear matter inside the ion in the inner crust at temperatures below 1 MeV. Nevertheless, in our calculation, temperatures of interest are typically above 1 MeV and could even reach up to 4 MeV. Moreover, the proton gas, whose density is very low, $\sim 10^{-7} - 10^{-4}$ fm^{-3}, is also considered. Because of these two reasons, the Sommerfeld expansions are no longer valid, and the complete Fermi-Dirac integrals must be used. Indeed, at low densities, the approximations considerably overestimate the energy (panels a and b), entropy (panels c and d), and pressure (panels j and k). Conversely, they noticeably underestimate the free energy (panels e and f) and chemical potentials (panels g and h). This can be understood from Eqs. (4.79)-(4.82) and Fig. 4.3. Specifically, at low densities and high temperatures, the ratio $\frac{k_BT}{e_{F,n}}$ is large because the Fermi energy is small (see Eq. (4.78)). As a result, the chemical potential and free energy (energy and entropy) are underestimated (overestimated).

In this study and in the results shown in the following sections, we mainly use the empirical parameters corresponding to BSk24 [112]. Moreover, to study the model dependence of the results, we also employ the SLy4 [113] and DD-MEδ [117] functionals. The empirical parameters of these models are listed in Table 2.1. These three interactions were selected because they all fulfill the basic constraints from nuclear theory, nuclear experiments, and NS observables, and at the same time, they reasonably cover present uncertainties on the nucleonic energy functionals [121, 184], see also Fig. 2.2.

4.1.2.2 Interface energy at finite temperatures

To model the inhomogeneities in the inner crust, in Eq. (4.58) the bulk free energy $F_{\rm bulk}$ is complemented by Coulomb, surface, and curvature contributions:

$$F_{\rm Coul+surf+curv} = V_{\rm WS}(\mathcal{F}_{\rm Coul} + \mathcal{F}_{\rm surf} + \mathcal{F}_{\rm curv}) \ . \tag{4.83}$$

The Coulomb term gives the electrostatic proton–proton, proton–electron, and electron–electron interaction energies. If there is no proton gas and assuming a spherical geometry for the WS cell, the Coulomb energy is derived as in Appendix A. In the case where the proton gas is accounted for, we can use the same formalism, except for replacing $n_e \to (n_e - n_{gp})$ and $n_{\rm ip} \to (n_{\rm ip} - n_{gp})$ in Eq. (A.25), and we can show that

$$\mathcal{F}_{\rm Coul} = 2\pi(en_ir_N)^2 \left(\frac{1-I}{2} - \frac{n_{gp}}{n_i}\right)^2 u\eta_{\rm Coul}(u), \tag{4.84}$$

in which the function $\eta_{\rm Coul}$ accounting for the electron screening is given by Eq. (2.55).

Regarding the surface and curvature energy density, we employ the same expression as in Eq. (2.56), but with a modification on the surface and curvature tensions (see Eqs. (2.27)-

(2.28) in Ref. [90]):

$$\sigma_{\mathrm{s,c}}(I,T) = \sigma_{\mathrm{s,c}}(I,T=0)h(T), \tag{4.85}$$

where

$$h(T) = \begin{cases} 0 & \text{if } T > T_c \ , \\ \left[1 - \left(\frac{T}{T_c}\right)^2\right]^2 & \text{if } T \leq T_c \ , \end{cases} \tag{4.86}$$

and T_c is the critical temperature given by Eq. (2.31) in Ref. [90].

$$k_B T_c(y_p) = 87.76 \left(\frac{K_{\mathrm{sat}}}{375 \text{ MeV}}\right)^{1/2} \left(\frac{0.155 \text{ fm}^{-3}}{n_{\mathrm{sat}}}\right)^{1/3} y_p(1-y_p) \text{ MeV}. \tag{4.87}$$

The behavior of the critical temperature as a function of the cluster proton fraction y_p is plotted in Fig. 4.4 for three different functionals: BSk24 (solid black line), SLy4 (dash-dotted blue line), and DD-MEδ (dashed orange line). We can observe that for all three considered models, $k_B T_c$ increases from 0 to $\sim$ 18 MeV as y_p increases from 0 to 0.5. Therefore, in the outer layer of the inner crust, where the clusters are relatively symmetric, the impact of the temperature on the surface and curvature tensions is negligible. On the other hand, at the bottom of the crust, where $y_p < 0.1$, the PNS temperature and the critical temperature may have the same order of magnitude, thus, the surface and curvature tension are expected to be reduced.

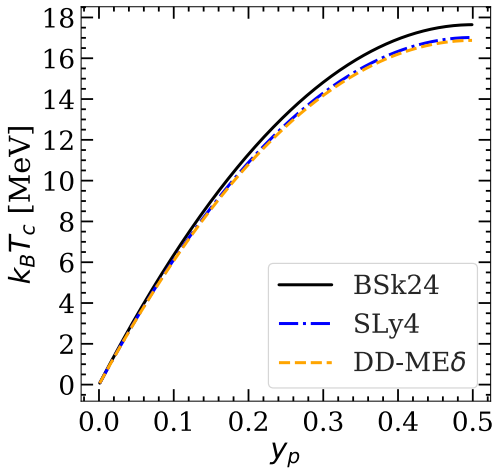

Figure 4.4: Critical temperature as a function of the cluster proton fraction y_p, obtained for BSk24 (solid black line), SLy4 (dashed-dotted blue line), and DD-MEδ (dashed orange line).

4.1.2.3 Translational free energy

Since the temperatures of interest in this work are those above the melting point, clusters are expected to be in the liquid phase. As a result, it is necessary to account for their translational degrees of freedom.

If the effect of the fluid of dripped nucleons is neglected, the free energy corresponding to the translational motion reduces to the standard expression of an ideal gas [1]:

$$F_{\mathrm{trans}} = k_{\mathrm{B}} T \ln\left(\frac{1}{V_{\mathrm{WS}}} \frac{\lambda_i^3}{g_s}\right) - k_{\mathrm{B}} T. \tag{4.88}$$

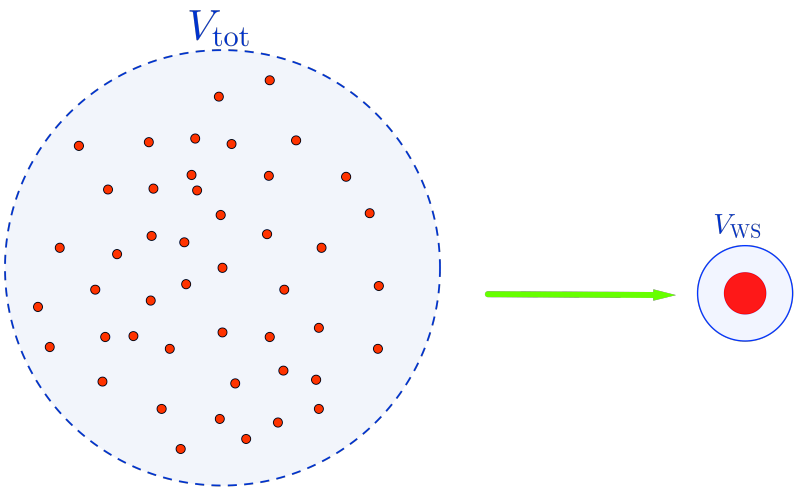

Figure 4.5: Left: a system of $N_{\rm tot}$ identical ions in a (macroscopic) volume $V_{\rm tot}$. Right: an ion in a (microscopic) volume $V_{\rm WS}$ (right).

This expression is easily obtained considering a system of $N_{\rm tot}$ identical ions in a volume $V_{\rm tot}$. In the thermodynamic limit, $N_{\rm tot} \to \infty$, $V_{\rm tot} \to \infty$, and $N_{\rm tot}/V_{\rm tot} \to 1/V_{\rm WS}$ (see Fig. 4.5 for an illustration). The partition function for the center-of-mass motion of a non-relativistic classical particle can be written as

$$\begin{aligned} Z_1^{\rm cl} &= \sum_{\vec{p}} \exp\left\{\left(-\frac{p^2}{2M_i k_B T}\right)\right\} \\ &= g_s V_{\rm tot}\left(\frac{M_i}{h}\right)^3 \int \exp\left\{\left(-\frac{M_i v^2}{2k_{\rm B}T}\right)\right\} d^3v = \frac{V_{\rm tot} g_s}{\lambda_i^3}, \end{aligned} \tag{4.89}$$

where $\lambda_i = \sqrt{\frac{2\pi\hbar^2}{M_i k_{\rm B} T}}$ is the ion thermal wavelength, and $g_s = 2J_i + 1$ is the ground-state spin degeneracy, which is set to unity independently of the ion species, because $J_i = 0$ for even-even nuclei, which are most abundant in the crust. This expression is valid in the non-degenerate Boltzmann limit, corresponding to $\lambda_i^3 \ll V_{\rm WS}$. For a system of $N_{\rm tot}$ identical and indistinguishable clusters, the total partition sum reads:

$$Z_{\rm tot}^{\rm cl} = \frac{(Z_1^{\rm cl})^{N_{\rm tot}}}{N_{\rm tot}!}. \tag{4.90}$$

Therefore, the translational free energy for each cluster can be obtained using the relation

$$F_{\rm trans} = \frac{-k_B T \ln Z_{\rm tot}^{\rm cl}}{N_{\rm tot}}, \tag{4.91}$$

$$F_{\rm trans} = \frac{k_B T}{N_{\rm tot}}\left(\ln(N_{\rm tot}!) - N_{\rm tot}\ln\left(Z_1^{\rm cl}\right)\right). \tag{4.92}$$

Applying the Stirling approximation for $N_{\rm tot} \gg 1$:

$$\ln(N_{\rm tot}!) \approx N_{\rm tot}\ln(N_{\rm tot}) - N_{\rm tot}, \tag{4.93}$$

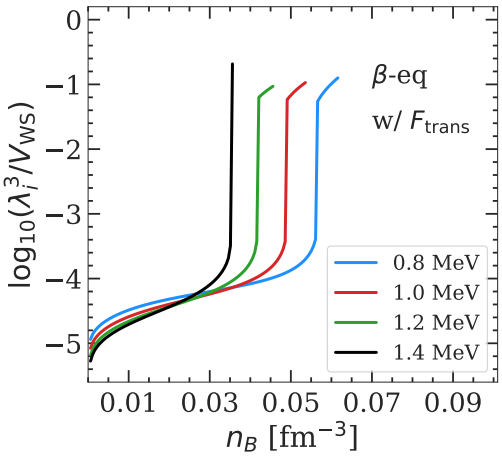

Figure 4.6: Ratio (in logarithmic scale) of the ion thermal wavelength to the WS cell volume as a function of the baryonic density n_B for the BSk24 model at four different temperatures: $k_{\rm B}T = 0.8$ MeV (blue line), $k_{\rm B}T = 1.0$ MeV (red line), $k_{\rm B}T = 1.2$ MeV (green line), and $k_{\rm B}T = 1.4$ MeV (black line). The results are obtained at beta equilibrium using the ideal-gas translational energy, Eq. (4.88). Figure adapted from Ref. [270].

we can rewrite Eq. (4.92) as:

$$\begin{aligned} F_{\rm trans} &\approx \frac{k_B T}{N_{\rm tot}} \left(N_{\rm tot} \ln(N_{\rm tot}) - N_{\rm tot} - N_{\rm tot} \ln\left(Z_1^{\rm cl}\right) \right), \\ &\approx k_B T \ln\left(\frac{N_{\rm tot}}{V_{\rm tot}} \frac{\lambda_i^3}{g_s} \right) - k_B T. \end{aligned} \tag{4.94}$$

At the thermodynamic limit, $N_{\rm tot}/V_{\rm tot} \to 1/V_{\rm WS}$, and Eq. (4.88) is immediately found. From this expression, we can observe that due to the indistinguishability achieved in the OCP approximation, the translational free energy for each ion depends on the volume available to itself, and the WS cell for each ion can still be defined even when the crust is in the liquid phase.

To check the validity of the non-degenerate limit for the calculation of the translational free energy, Eq. (4.88), I show in Fig. 4.6 the ratio of the ion thermal wavelength cubed, λ_i^3, to the WS cell volume as a function of the inner-crust baryon number density n_B for the BSk24 model in beta equilibrium and for four different temperatures. It can be observed that, although the ratio $\lambda_i^3/V_{\rm WS}$ remains smaller than 1 throughout the inner crust, the non-degenerate Boltzmann limit tends to break at high densities and higher temperatures in the vicinity of the crust-core transition.

The derivation of Eq. (4.88) also shows that this expression is only valid in the limit of heavy ions, that is, those with $M_i/m_n \gg 1$, and if ions are considered as point-like particles moving in vacuum. The first of these conditions is well realized in the inner crust, but the latter two clearly become more doubtful as density increases. A first obvious correction to Eq. (4.88) that was considered in the literature since the first works on the finite-temperature crust [11, 90] is to consider a reduced volume $V_{\rm f}$ for the center-of-mass motion:

$$V_{\rm WS} \to V_{\rm f} = \frac{4}{3}\pi (r_{\rm WS} - r_N)^3 \,, \tag{4.95}$$

with $r_{\rm WS}$ being the WS cell radius.

Moreover, in a PNS inner crust, nuclei are surrounded by a distribution of dripped protons and neutrons. At the bottom of the inner crust, the densities of these fluids are comparable to the nuclear internal density and, as a result, the cluster bare mass M_i should be replaced by an effective mass $M_i^\star$, accounting for the modification of the free flow in a nuclear medium. The derivation of the effective mass of the cluster moving in a uniform nucleon medium modeled as an ideal fluid, with different hypotheses as to the fluid properties of the cluster, was presented in Sect. 4.1.1.

Repeating the calculation of the translational partition sum of Eq. (4.89) —using Eq. (4.55) for the thermal kinetic energy— leads to an expression identical to Eq. (4.88), with the substitution $M_i \to M_i^\star$. Including both the corrections on the finite-size effect of nuclei and the effective mass, the translational free energy per WS cell can be written as

$$F^\star_{\rm trans} = k_{\rm B}T \ln\left(\frac{1}{V_{\rm f}}\frac{\lambda_i^{\star 3}}{g_s}\right) - k_{\rm B}T, \tag{4.96}$$

where $\lambda_i^\star = \sqrt{\frac{2\pi\hbar^2}{M_i^\star k_{\rm B}T}}$, with $M_i^\star$ given by Eq. (4.56). Exclusively for the calculation of the ion effective mass in the translational free energy, the following approximations are made:
(i) $m_n \approx m_p$. This leads to $\delta^{\rm f} \approx n^{\rm f}/n_i$, with $n^{\rm f}$ being the number density of nucleons in the cluster participating in the superfluid flow.
(ii) $n_{gp} \approx 0$. This leads to $\gamma \approx \frac{n_{gn}}{n_i}$. Neglecting the possible contribution from proton unbound states appears to be a reasonable approximation at the relatively low temperatures considered in this work, as will be shown in Sect. 4.1.3 (see Fig. 4.13).

Three different prescriptions for $M_i^\star$, corresponding to three chosen values of $\delta^{\rm f}$ are considered:

1. the limiting case $\delta^{\rm f} = 0$, leading to Eq. (4.44), corresponding to a solid cluster fully impermeable to the surrounding nuclear medium;
2. the limiting case $\delta^{\rm f} = 1$, corresponding to the single-fluid calculation by Ref. [274], see Eq. (4.57);
3. the intermediate case $\delta^{\rm f} = \gamma$, leading to:

$$M_i^\star = M_i\,(1-\gamma)\,. \tag{4.97}$$

We can expect that the latter case, which considers that the translational motion concerns protons, bound neutrons, and neutrons in unbound resonant states, while all neutrons occupying continuum states constitute the external fluid, is more realistic. Indeed, the mobility of the nucleons is given by their velocity flux at the Fermi surface [278]. As such, this is only defined for "conduction" nucleons with single-particle wave functions, which do not vanish at the WS boundary, that is, continuum states as defined in Ref. [136]. Although the prescription of e-clusters in Eq. (4.97) is rough, it is found to give an accurate estimation of the total number of unbound non-resonant states obtained from a microscopic HF [136] calculation in the whole density region corresponding to the inner crust (see also e.g., Fig. 9 in Ref. [275]). In the presence of a periodic potential, corresponding to the solid phase where

the relative motion between ions and neutron (super)fluid is driven by star rotation rather than thermal ion motion, the Bragg scattering of free neutrons gives rise to the entrainment effect. This effect alters the number of neutrons entrained by the cluster compared to the expected number in the e-cluster. Typically, this effect reduces the number of effectively free neutrons, leading to an increase in the effective mass of the ions [279, 280], even if it has been reported that in certain cases, the entrainment effect may increase the number of freely moving neutrons [275], particularly in the slab phase in the neutron-star crust [281, 282]. However, this entrainment effect can be disregarded in the current context as the system in the liquid phase is disordered [283], and therefore, the periodic potential does not exist. Thus, it is reasonable to assume that the conduction neutrons coincide with the continuum states. Furthermore, Ref. [82] showed that the factorization of the partition sum that is needed to theoretically obtain the extended nuclear statistical equilibrium models used to produce the general-purpose equation of state [7, 284, 285] is only possible if the cluster mass appearing in the translational part is the e-cluster mass, $A_e = A(1 - n_{\rm g}/n_i)$.

For comparison with Fig. 4.6, in Fig. 4.7, I show the ratio of the ion thermal wavelength cubed, $(\lambda_i^\star)^3$, to the WS cell volume $V_{\rm WS}$ (top panels) as a function of the inner-crust baryonic density n_B for the BSk24 model at beta equilibrium and at two different temperatures: 1.0 MeV (left panels) and 2.0 MeV (right panels). Three different prescriptions of $M_i^\star$ are considered, corresponding to the three listed cases of $\delta^{\rm f}$. One can observe that, in this case, the ratio $(\lambda_i^\star)^3/V_{\rm WS}$ remains always $\ll 1$. Moreover, near the crust-core transition, it is smaller than that obtained for the case of the ideal-gas case. This is because in the ideal-gas case when the clusters dissolve near the crust-core transition point, A and $V_{\rm WS}$ become small (because of the sharp decrease in the cluster mass and proton number; see also Fig. 4.8 and related discussion), and therefore the ratio $(\lambda_i)^3/V_{\rm WS}$ is relatively large. On the other hand, when $F^\star_{\rm trans}$ is used, the clusters remain large until high n_B (see also Figs. 4.12 and 4.14), yielding a greater cluster mass and WS volume, resulting in a smaller thermal-wavelength-cubed-to-WS-cell-volume ratio. However, the ratio of $(\lambda_i^\star)^3$ to the reduced volume $V_{\rm f}$ (bottom panels in Fig. 4.7) increases towards the crust-core transition, reaching ≈ 0.5 almost independently of the temperature and effective-mass estimation. This shows that the non-degenerate limit implicit in Eq. (4.96) is always a reasonable approximation, albeit less justified at the highest densities.

In the following sections, I investigate the effects of the translational free energy on the PNS inner-crust properties by performing the calculations employing both the ideal-gas expression (see Eq. (4.88)) and the expression accounting for the finite-size and in-medium corrections (see Eq. (4.96)).

4.1.3 Crust equilibrium equations at finite temperatures

At a given thermodynamic condition, defined by the baryonic density n_B and temperature T if beta equilibrium is assumed[4], the total free energy density of the system can be written as

$$\mathcal{F} = \mathcal{F}_e + \mathcal{F}_{\rm g}(1-u) + \frac{F_i}{V_{\rm WS}}, \tag{4.98}$$

[4]In the case where the total proton fraction $Y_p^{\rm tot}$ is fixed, the thermodynamic condition is defined by the baryonic density n_B, the temperature T, and $Y_p^{\rm tot} = n_e/n_B$.

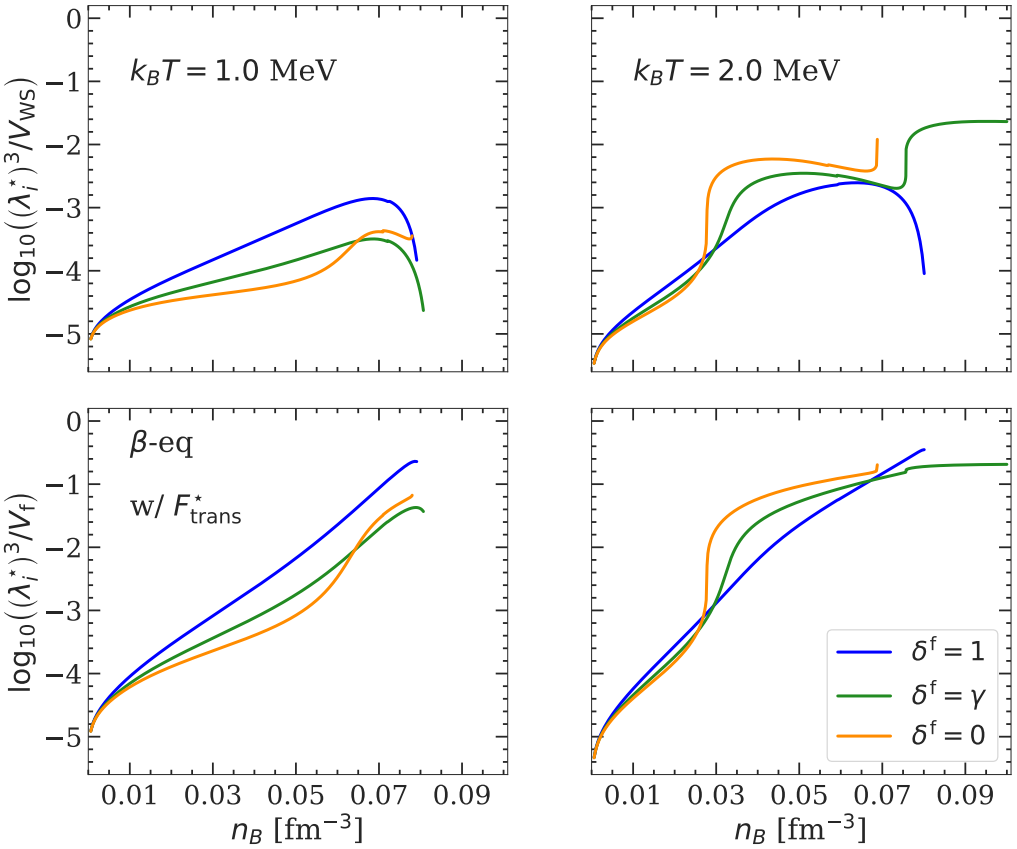

Figure 4.7: Ratio (in logarithmic scale) of the ion thermal wavelength to the WS cell volume (top panels) and to the reduced volume (bottom panels) as a function of the baryonic density n_B for the BSk24 model, using three different prescriptions for the ion effective mass, at two different temperatures: $k_{\rm B}T = 1.0$ MeV (left panels) and $k_{\rm B}T = 2.0$ MeV (right panels). The results are obtained at beta equilibrium using the translational energy $F^\star_{\rm trans}$, Eq. (4.96), accounting for the in-medium correction. Figure adapted from Ref. [270].

where $\mathcal{F}_e$ is the electron gas free energy density calculated using Eq. (2.65) in Ref. [1], $\mathcal{F}_{\rm g} = \mathcal{F}_B(n_{\rm g}, \delta_{\rm g}, T) + m_n c^2 n_{gn} + m_p c^2 n_{gp}$ is the free energy density of uniform nuclear matter (including the rest masses of nucleons) at baryonic density $n_{\rm g} = n_{gn} + n_{gp}$, isospin asymmetry $\delta_{\rm g} = \frac{n_{gn} - n_{gp}}{n_{gn} + n_{gp}}$, and temperature T (see Sect. 4.1.2.1 for more details), and F_i is the cluster free energy (see Sect. 4.1.2 for details). The excluded-volume term breaking the additivity of the free energy in Eq. (4.98), $-u\mathcal{F}_{\rm g}$, has also been shown to account for the subtraction of the gas states from the nuclear partition sum, which avoids double counting of unbound single-particle states [82, 286].

With the presence of the proton gas, the baryon number conservation reads:

$$\begin{aligned} n_B &= \frac{A_{\rm WS}}{V_{\rm WS}} \\ &= \frac{A + (n_{gn} + n_{gp})\left(V_{\rm WS} - \frac{A}{n_i}\right)}{V_{\rm WS}} \\ &= \frac{A}{V_{\rm WS}}\left(1 - \frac{n_{gn} + n_{gp}}{n_i}\right) + n_{gn} + n_{gp}. \end{aligned} \tag{4.99}$$

With $n_p = \frac{Z}{V_{\rm WS}}$ being the average density of bound protons[5] over the WS-cell volume, Eq. (4.99) is equivalent to:

$$n_B = \frac{2n_p}{(1-I)}\left(1 - \frac{n_{\rm gn}+n_{\rm gp}}{n_i}\right) + n_{\rm gn} + n_{\rm gp}. \tag{4.100}$$

The condition of charge neutrality reads:

$$\begin{aligned} n_e &= \frac{Z + n_{\rm gp}(V_{\rm WS} - \frac{A}{n_i})}{V_{\rm WS}} \\ &= n_p + n_{\rm gp}\left(1 - \frac{A}{n_i V_{\rm WS}}\right), \end{aligned} \tag{4.101}$$

thus,

$$n_e = n_p + n_{\rm gp}\left(1 - \frac{2n_p}{n_i(1-I)}\right). \tag{4.102}$$

The minimization of the total free energy density $\mathcal{F}$ in Eq. (4.98) needs to satisfy the two constraints coming from the conservation of the baryonic number (Eq. (4.100)) and the charge neutrality (Eq. (4.102)). As a result, one can introduce two Lagrange multipliers, γ_1, and γ_2, such that the function to be minimized can be expressed as

$$\begin{aligned} \Omega = &\frac{2n_p}{1-I}\frac{F_i}{A} + \left[1 - \frac{2n_p}{(1-I)n_i}\right]\mathcal{F}_{\rm g} + \mathcal{F}_e \\ &+ \gamma_1\left[n_B - \frac{2n_p}{1-I}\left(1 - \frac{n_{\rm gn}+n_{\rm gp}}{n_i}\right) - n_{\rm gn} - n_{\rm gp}\right] \\ &+ \gamma_2\left[n_e - n_p - n_{\rm gp}\left(1 - \frac{2n_p}{n_i(1-I)}\right)\right]. \end{aligned} \tag{4.103}$$

Minimizing Ω with respect to $n_{\rm gn}$:

$$\left.\frac{\partial\Omega}{\partial n_{\rm gn}}\right|_{r_N, I, n_i, n_p, n_{\rm gp}, n_e} = 0, \tag{4.104}$$

$$\frac{2n_p}{1-I}\frac{\partial}{\partial n_{\rm gn}}\left(\frac{F_i}{A}\right) + \left[1 - \frac{2n_p}{(1-I)n_i}\right]\frac{\partial\mathcal{F}_{\rm g}}{\partial n_{\rm gn}} - \left[1 - \frac{2n_p}{(1-I)n_i}\right]\gamma_1 = 0, \tag{4.105}$$

thus:

$$\gamma_1 = \frac{\partial\mathcal{F}_{\rm g}}{\partial n_{\rm gn}} + \frac{2n_p n_i}{n_i(1-I) - 2n_p}\frac{\partial(F_i/A)}{\partial n_{\rm gn}}. \tag{4.106}$$

Similarly, minimizing Ω with respect to $n_{\rm gp}$:

$$\left.\frac{\partial\Omega}{\partial n_{\rm gp}}\right|_{r_N, I, n_i, n_p, n_{\rm gn}, n_e} = 0, \tag{4.107}$$

$$\frac{2n_p}{1-I}\frac{\partial}{\partial n_{\rm gp}}\left(\frac{F_i}{A}\right) + \left[1 - \frac{2n_p}{(1-I)n_i}\right]\frac{\partial\mathcal{F}_{\rm g}}{\partial n_{\rm gp}} - \left[1 - \frac{2n_p}{(1-I)n_i}\right](\gamma_1 + \gamma_2) = 0, \tag{4.108}$$

[5] It is worth reminding that n_p defined here, corresponding to the inhomogeneous crust, is not the same as the homogeneous proton density in Sect. 4.1.2.1

and we obtain:

$$\gamma_2 = \frac{\partial \mathcal{F}_{\rm g}}{\partial n_{gp}} + \frac{2n_p n_i}{n_i(1-I)-2n_p}\frac{\partial (F_i/A)}{\partial n_{gp}} - \gamma_1. \tag{4.109}$$

Defining μ_n and μ_p as

$$\mu_n \equiv \frac{\partial \mathcal{F}_{\rm g}}{\partial n_{gn}} + \frac{2n_p n_i}{n_i(1-I)-2n_p}\frac{\partial (F_i/A)}{\partial n_{gn}}, \tag{4.110}$$

$$\mu_p \equiv \frac{\partial \mathcal{F}_{\rm g}}{\partial n_{gp}} + \frac{2n_p n_i}{n_i(1-I)-2n_p}\frac{\partial (F_i/A)}{\partial n_{gp}}, \tag{4.111}$$

the Lagrange multipliers can be written as

$$\gamma_1 = \mu_n, \tag{4.112}$$

$$\gamma_2 = -\mu_n + \mu_p. \tag{4.113}$$

On the right-hand side of Eqs. (4.110)-(4.111), we can easily see that the first terms are the chemical potentials of the unbound nucleons (including the nucleon rest masses), $\mu_{gn(gp)} = \mu_{{\rm HM},n(p)}(n_{\rm g},\delta_q) \equiv \left(\frac{\partial \mathcal{F}_{\rm g}}{\partial n_{gn(gp)}}\right)_{n_{gp(gn)}}$, while the last terms account for the in-medium modification induced by the Coulomb screening and the center-of-mass translation.

4.1.3.1 Composition at beta equilibrium

In this section, I discuss the impact of the translational free energy on the properties of the inner crust assuming that beta equilibrium holds, which is believed to be the case in the PNS at moderate temperatures (see Ref. [7] and references therein). In this case, we minimize the function Ω defined in Eq. (4.103) with respect to the variational variables (r_N, I, n_i, n_p, n_{gn}, n_{gp}, n_e). Details of the derivation are presented in Appendix C. The equilibrium system of equations for the PNS inner crust at beta equilibrium is given by:

$$\mu_p + \mu_e = \mu_n, \tag{4.114}$$

$$\frac{\partial (F_i/A)}{\partial r_N} = 0, \tag{4.115}$$

$$n_i^2 \frac{\partial}{\partial n_i}\left(\frac{F_i}{A}\right) = P_{\rm g}, \tag{4.116}$$

$$\frac{F_i}{A} + (1-I)\frac{\partial}{\partial I}\left(\frac{F_i}{A}\right) = \mu_n - \frac{P_{\rm g}}{n_i}, \tag{4.117}$$

$$2\left[\frac{\partial}{\partial I}\left(\frac{F_i}{A}\right) - \frac{n_p}{1-I}\frac{\partial}{\partial n_p}\left(\frac{F_i}{A}\right)\right] = \mu_n - \mu_p, \tag{4.118}$$

where $P_{\rm g} = \mu_n n_{gn} + \mu_p n_{gp} - \mathcal{F}_{\rm g}$ is the pressure of the dripped nucleons, and $\mu_e = \partial \mathcal{F}_e/\partial n_e$ is the electron chemical potential. It is to be noted that, because of the definition of the chemical potentials μ_n and μ_p, see Eqs. (4.110)-(4.111), the pressure term $P_{\rm g}$ is not just the pressure of a self-interacting nucleon gas, but also includes in-medium effects.

At each given (n_B, T), this system of five coupled equations, Eqs. (4.114)-(4.118), is solved numerically together with the two constraints from the baryon number conservation,

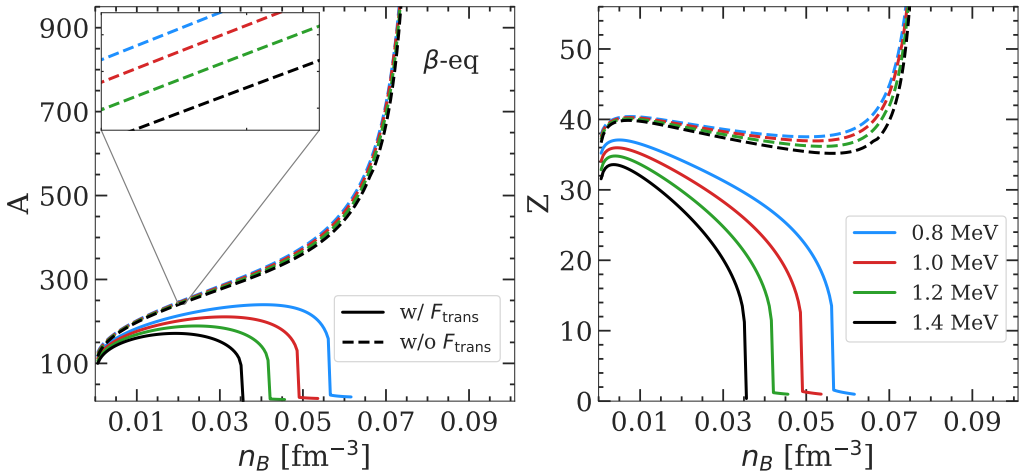

Figure 4.8: Cluster mass number A (left panel) and proton number Z (right panel) as a function of the baryonic density n_B for the BSk24 model at four different temperatures: $k_{\rm B}T = 0.8$ MeV (blue lines), $k_{\rm B}T = 1.0$ MeV (red lines), $k_{\rm B}T = 1.2$ MeV (green lines), and $k_{\rm B}T = 1.4$ MeV (black lines). The solid (dashed) lines are obtained when the translational energy, defined by Eq. (4.88), is (not) included. Figure adapted from Ref. [270].

Eq. (4.100), and charge neutrality, Eq. (4.102), yielding the equilibrium composition, (r_N, I, n_i, n_p, n_{gn}, n_{gp}, and n_e).

We can start by considering the standard ideal-gas expression for the translational motion, Eq. (4.88), while the excluded volume and effective mass corrections are addressed later in this section. The calculation is performed using the BSk24 at four selected values of temperature: $k_{\rm B}T = 0.8$, 1.0, 1.2, and 1.4 MeV. Indeed, T. Carreau *et al.* [79], who calculated the melting temperature using BSk24, showed that these temperatures are sufficiently high for the crust to be in the liquid phase. Figure 4.8 shows the evolution of the cluster mass number A (left panel) and proton number Z (right panel) with the baryonic number density n_B for the chosen temperatures. Let us recall that since only spherical nuclei are considered here, A is related to the variational variables r_N and n_i through the relation $A = 4\pi r_N^3 n_i/3$, and $Z = A(1-I)/2$. To demonstrate the notable influence of the translational free energy $F_{\rm trans}$, Eq. (4.88), I show in Fig. 4.8 the results obtained including (solid lines) and neglecting (dashed lines) the $F_{\rm trans}$ term in Eq. (4.58). Let us first discuss the case without $F_{\rm trans}$ (dashed lines). In this case, Eq. (4.115) is equivalent to the equation of the Baym virial theorem [9], with an additional curvature term, $\mathcal{F}_{\rm surf} + 2\mathcal{F}_{\rm curv} = 2\mathcal{F}_{\rm Coul}$. From this equation, the cluster mass number A can be deduced as

$$A \approx \frac{\sigma_{\rm s}(I,T)}{e^2(\frac{1-I}{2} - \frac{n_{gp}}{n_i})^2 n_i \eta_{\rm Coul}(u)} \ . \tag{4.119}$$

As mentioned in Chapter 3, Eq. (4.119) provides a good approximation in the whole crust because $\mathcal{F}_{\rm curv} \ll \mathcal{F}_{\rm surf}$ for all nuclei. As T increases, the surface tension decreases, see Eq. (4.85). Consequently, A decreases with temperature, as shown in the inset of the upper panel of Fig. 4.8. Similar behavior is observed in Z as well. On the other hand, the denominator of the right-hand side of Eq. (4.119) is a decreasing function of the baryonic density n_B. However, since nuclei become more neutron-rich deeper in the crust, the surface

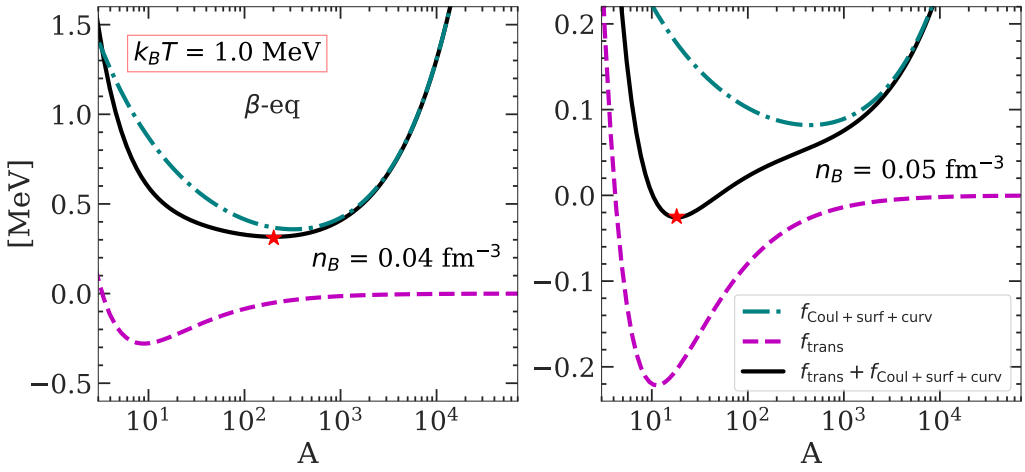

Figure 4.9: Coulomb, surface, and curvature energies per nucleon, $f_{\mathrm{Coul+surf+curv}}$ (dash-dotted teal lines), translational free energy per nucleon, f_{trans} (dashed violet lines), and their sum (solid black lines) as a function of A at $k_{\mathrm{B}}T = 1$ MeV and $n_B = 0.04$ fm^{-3} (left panel) and $n_B = 0.05$ fm^{-3} (right panel) for the BSk24 model. The red star in each panel indicates the solution for A from the minimization. Figure adapted from Ref. [270].

Table 4.1: Crust-core transition density, n_{CC}, and pressure, P_{CC}, for the BSk24 functional at different temperatures with (w/) and without (w/o) the inclusion of the translational free energy F_{trans}. Table reproduced from Ref. [270].

$k_{\mathrm{B}}T$ (MeV)		0.8	1.0	1.2	1.4
n_{CC} (fm^{-3})	w/ F_{trans}	0.062	0.054	0.046	0.036
	w/o F_{trans}	0.079	0.079	0.078	0.078
P_{CC} (MeV/fm^3)	w/ F_{trans}	0.160	0.133	0.111	0.078
	w/o F_{trans}	0.260	0.257	0.255	0.256

tension $\sigma_{\mathrm{s}}(I,T)$ also decreases with n_B. As a consequence, the trend of A versus n_B cannot be straightforwardly deduced and strongly depends on the detailed behavior of σ_{s}, that is, on the nuclear model. From Fig. 4.8, one can see that for the considered temperatures and functional, the behavior of the denominator prevails, hence the increase of cluster mass. For Z, this is not always the case because the isospin I also increases with n_B. Taking into account the translational motion F_{trans} (solid lines in Fig. 4.8) significantly reduces both the mass and proton numbers of the cluster. Specifically, at high densities the cluster completely dissolves, that is, $Z < 1$. Analogously to the calculation without the translational term, the cluster size decreases with temperature. However, the density at which the transition from inhomogeneous to homogeneous matter occurs is much lower than that obtained without F_{trans}. In particular, if we neglect (include) F_{trans}, for all the considered temperatures, the crust-core transition occurs at around $n_{\mathrm{CC}} \approx 0.08$ fm^{-3} ($n_{\mathrm{CC}} \approx 0.04 - 0.06$ fm^{-3}), as can be seen from Table 4.1.

We can understand this behavior by analyzing the minimization equation of the total free energy per nucleon with respect to r_N (or equivalently: A), Eq. (4.115). From the definition

of F_i in Eq. (4.58), Eq. (4.115) can be written as

$$\frac{\partial(f_{\rm Coul+surf+curv} + f_{\rm trans})}{\partial r_N} = 0, \tag{4.120}$$

where $f = F/A$ denotes the free energy per nucleon. This equation shows that we can have heavy or light clusters depending on the competition between $f_{\rm Coul+surf+curv}$, which favors the former ones (as we have seen above), and $f_{\rm trans}$, which favors the latter ones. Indeed, it is easy to show that $f_{\rm trans}$ is minimized at

$$A \approx A_0 = \exp\left[\frac{2}{5}\ln\left(C_0\frac{n_i u}{T^{3/2}}\right) + \frac{3}{5}\right] \ , \tag{4.121}$$

where $C_0 = \hbar^3/g_s\,(2\pi/m_n k_{\rm B})^{3/2}$.

Replacing realistic values for n_i and u in Eq. (4.121), one can show that, for temperatures equal or above 1 MeV, $A_0 < 30$. This point is further illustrated in Fig. 4.9, which displays $f_{\rm Coul+surf+curv}$ (dash-dotted teal lines), $f_{\rm trans}$ (dashed violet lines), and their sum (solid black lines) as a function of A at $k_{\rm B}T = 1$ MeV for two selected densities: $n_B = 0.04$ fm^{-3} (left panel) and $n_B = 0.05$ fm^{-3} (right panel). The other variables (I, n_i, n_p, n_{gn}, n_{gp}, n_e) are fixed to the values obtained from the minimization at the given (n_B, T). From this figure, we can see that, indeed, $f_{\rm Coul+surf+curv}$ is minimized for large clusters ($A > 100$), whereas $f_{\rm trans}$ is minimized for very small ones, $A \approx 10$. At higher density, as matter becomes more neutron-rich, both the Coulomb and the surface energies per baryon decrease. Thus, the impact of the translational motion prevails. Moreover, $f_{\rm trans}$ obviously dominates at high temperatures. Consequently, the net effect is that the translational free energy becomes more important at high temperatures and densities, as shown in Figs. 4.10-4.11. This explains why small clusters are found in this regime in Fig. 4.8 when the translational energy is accounted for in the minimization procedure.

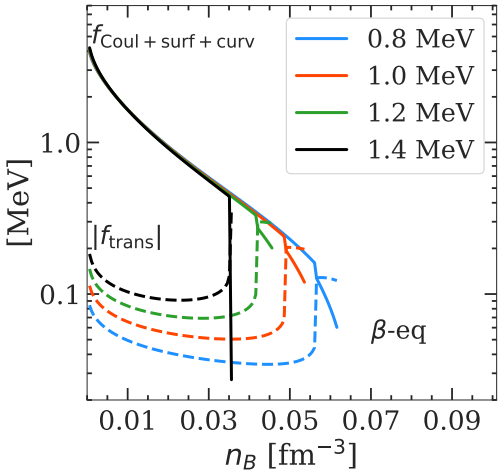

Figure 4.10: The sum of surface, curvature, and Coulomb free energies per nucleon (solid lines) and the absolute value of the translational free energy per nucleon(dashed lines) as a function of the baryonic density n_B for the BSk24 model at four different temperatures: $k_{\rm B}T = 0.8$ MeV (blue lines), $k_{\rm B}T = 1.0$ MeV (red lines), $k_{\rm B}T = 1.2$ MeV (green lines), and $k_{\rm B}T = 1.4$ MeV (black lines).

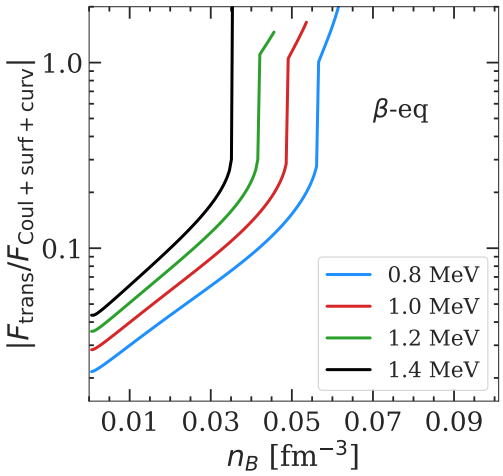

Figure 4.11: Absolute value of the ratio of the translational free energy to the sum of surface, curvature, and Coulomb free energies as a function of the baryonic density n_B for the BSk24 model at four different temperatures: $k_{\rm B}T = 0.8$ MeV (blue line), $k_{\rm B}T = 1.0$ MeV (red line), $k_{\rm B}T = 1.2$ MeV (green line), and $k_{\rm B}T = 1.4$ MeV (black line). Figure adapted from Ref. [270].

The surprising results of Figs. 4.8-4.11 are obtained using the oversimplified ideal-gas expression, Eq. (4.88), which is only justified at rather high temperatures and relatively low densities, see Fig. 4.6. One can expect that the inclusion of the cluster effective mass, as well as the reduction of the available volume for the translational motion, will reduce the impact of the center-of-mass motion. This is shown in Fig. 4.12, where the cluster mass number A and proton number Z are plotted as a function of the baryonic number density n_B for the BSk24 model at $k_{\rm B}T = 1.0$ MeV (left panels) and $k_{\rm B}T = 2.0$ MeV (right panels). For all the considered values of $\delta^{\rm f}$, including $F^{\star}_{\rm trans}$, Eq. (4.96), still noticeably shrinks the size of the cluster with respect to the case where the collective degrees of freedom are neglected. However, the effect is not as dramatic as when the ideal-gas expression, Eq. (4.88), is used (see also Fig. 4.8). The latter is true both when $M^{\star}_i < M_i$, that is, when $\delta^{\rm f} > 0$, and when $M^{\star}_i > M_i$, that is, in the case where $\delta^{\rm f} = 0$. As one may expect, the influence of the translational free energy becomes larger with increasing temperature, as can be seen by comparing the left and right panels. The effect is also larger with decreasing $\delta^{\rm f}$. As already mentioned, among the three prescriptions of the ion effective mass discussed in Sect. 4.1.1, the most realistic one would be when all neutrons in the continuum states participate in the flow, i.e. $\delta^{\rm f} = \gamma$. Therefore, in the following, I show the results only for this case, that is, Eq. (4.97) is used in $F^{\star}_{\rm trans}$, Eq. (4.96).

Interestingly, in the case $\delta^{\rm f} = \gamma$ (dash-dotted green line in Fig. 4.12), we can observe a transition to small proton-mass clusters, $Z \sim 2$, at $k_BT = 2.0$ MeV (right panels) and $n_B > 0.075$ fm^{-3}, and this configuration persists even at $n_B > 0.1$ fm^{-3}. As it is shown in Fig. 4.13, the neutron and proton cluster densities (solid lines), $n_{in} = n_i(1+I)/2$ and $n_{ip} = n_i(1-I)/2$, of these light configurations are very similar to those of the surrounding homogeneous nuclear medium (dashed lines). From the physical point of view, these small-amplitude and small-wavelength inhomogeneities might correspond to correlations or resonant states that are expected to exist in nuclear matter but are not captured in the homogeneous matter mean-

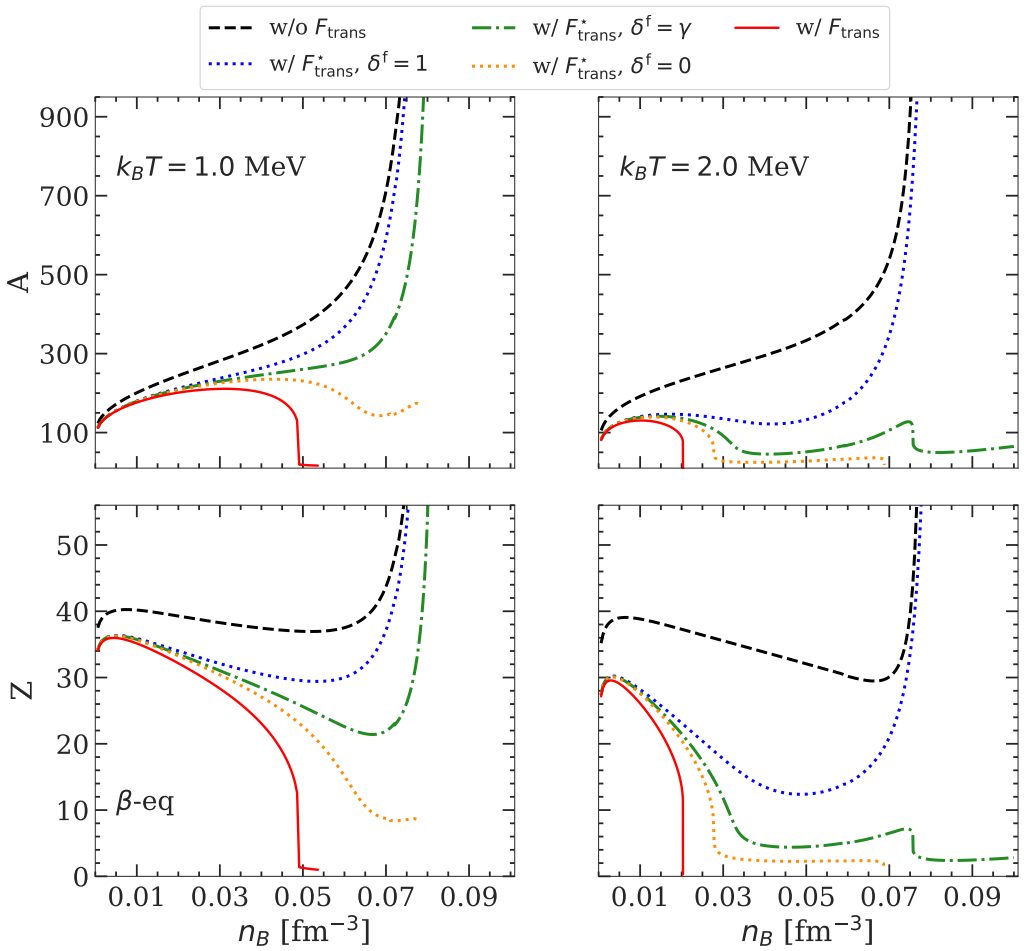

Figure 4.12: Cluster mass number A (upper panels) and proton number Z (lower panels) as a function of the baryonic density n_B for the BSk24 model at two different temperatures: $k_{\rm B}T = 1.0$ MeV (left panels) and $k_{\rm B}T = 2.0$ MeV (right panels). Different prescriptions for the translational free energy are considered. See text for details. Figure adapted from Ref. [270].

field approximation. However, in this density region, there is no clear distinction between inhomogeneous and homogeneous matter. Therefore, this transition to low-Z clusters can be identified as the interface between the crust and the core.

Figure 4.14 displays the cluster mass number A and proton number Z as a function of the baryonic number density n_B for three values of temperature: $k_{\rm B}T = 1.0$ MeV (left panels), 1.5 MeV (middle panels), and 2.0 MeV (right panels) for the BSk24 [112] (black lines), SLy4 [113] (blue lines), and DD-MEδ [117] (orange lines) models. The A and Z obtained with (without) the translational energy $F^{\star}_{\rm trans}$ are shown with solid (dashed) lines. While the results are almost model-independent, they vary significantly with the temperature. For all the considered models, with the more realistic expression $F^{\star}_{\rm trans}$, at 1 MeV very heavy clusters ($A > 400$) are favored until the transition to the core, whereas, at higher temperatures, the crust-core transition occurs at lower densities. The latter behavior can be expected due to the increase in the translational degrees of freedom.

To better understand this finding, we can notice that the mass number $A^{\star}_0$ at which

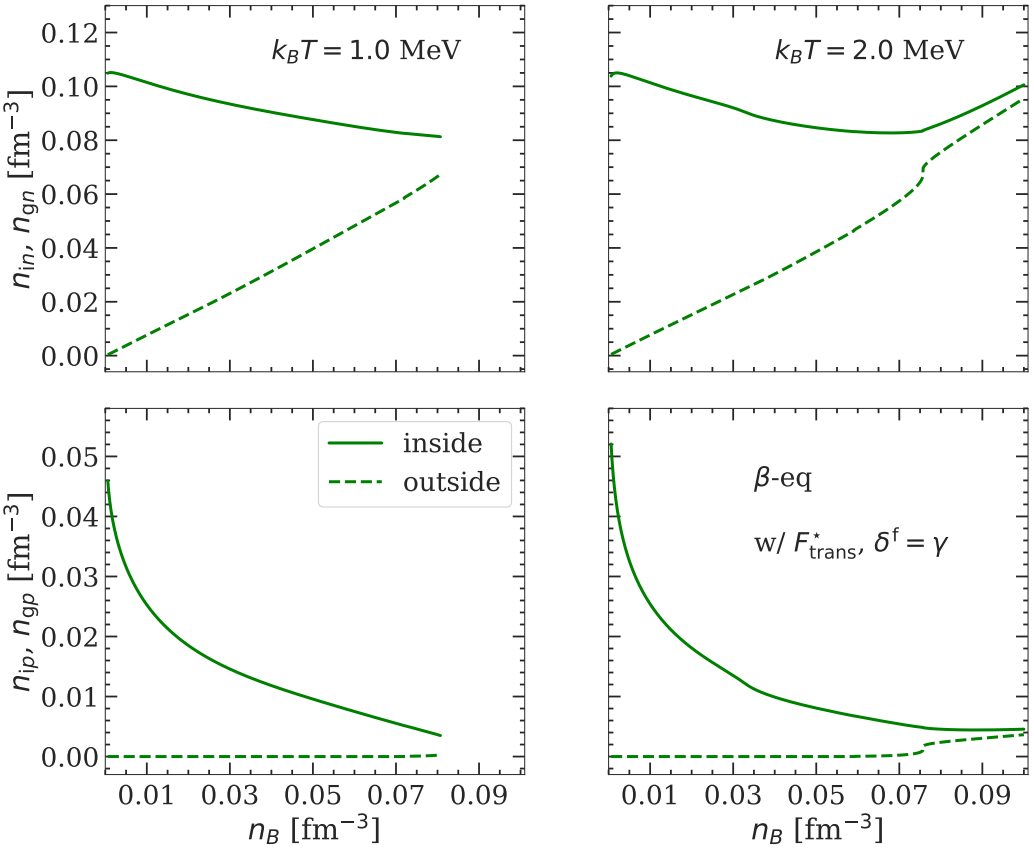

Figure 4.13: Neutron (upper panels) and proton (lower panels) densities inside (solid lines) and outside (dashed lines) the cluster as a function of the baryonic density n_B for the BSk24 model at two different temperatures: $k_{\rm B}T = 1.0$ MeV (left panels) and $k_{\rm B}T = 2.0$ MeV (right panels). The effective translational free energy $F^\star_{\rm trans}$ is included, with $\delta^{\rm f} = \gamma$. Figure adapted from Ref. [270].

$F^\star_{\rm trans}/A$ is minimized has the same functional form as in Eq. (4.121), that is:

$$A_0^\star = \exp\left[\frac{2}{5}\ln\left(C_0\frac{n_i u}{T^{3/2}g(u,\gamma)}\right) + \frac{3}{5}\right], \tag{4.122}$$

where:

$$g(u,\gamma) = \left(\sqrt{1-\gamma}(1-u^{1/3})\right)^3. \tag{4.123}$$

The behavior of $A_0^\star$ thus depends on the competition between the $T^{3/2}$ and the $g(u,\gamma)$ factors. As n_B increases, the ratio γ between the density outside and inside the ion increases and approaches 1 near the crust-core transition, thus reducing the effect of the translational term. If the volume fraction occupied by the ion u also increases (approaching 1), which is the case at relatively small temperatures, $1/g$ can be a very large number, and large clusters are still favored even if the translational free energy is accounted for (see left panels in Fig. 4.14). However, at higher temperatures, $k_BT \gtrsim 1.5$ MeV, the translational effect becomes more significant, and the cluster volume fraction decreases near the crust-core transition, thus leading to the appearance of small clusters when $F^\star_{\rm trans}$ is included.

The impact of the excluded-volume approach on the transition from clusterized to homogeneous matter was also discussed by Ref. [287]. In the latter work, a strong increase

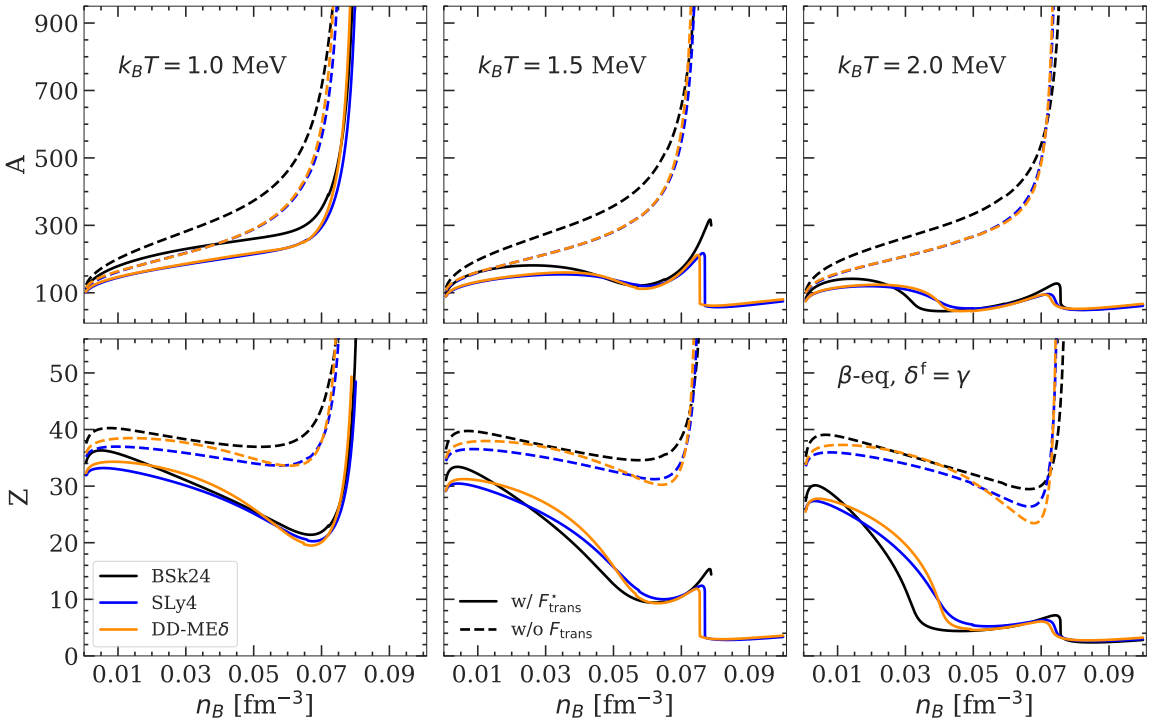

Figure 4.14: Cluster mass number A (upper panels) and proton number Z (lower panels) as a function of the baryonic density n_B for the BSk24 (black lines), SLy4 (blue lines), and DD-MEδ (orange lines) models at three different temperatures: $k_{\rm B}T = 1.0$ MeV (left panels), $k_{\rm B}T = 1.5$ MeV (middle panels), and $k_{\rm B}T = 2.0$ MeV (right panels). The solid (dashed) lines are obtained with (without) the effective translational energy $F^{\star}_{\rm trans}$, Eq. (4.96), with $\delta^{\rm f} = \gamma$. Figure adapted from Ref. [270].

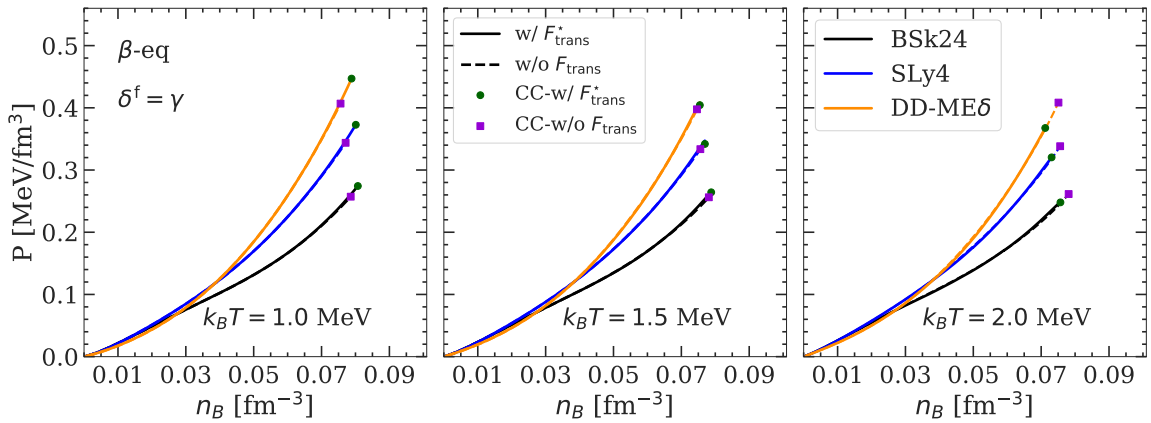

Figure 4.15: Same as Fig. 4.14, but for the pressure P versus the baryonic number density n_B. The green dots (violet squares) mark the crust-core transition with (without) $F^{\star}_{\rm trans}$. Figure adapted from Ref. [270].

(and even divergence) of the pressure, resulting in the transition to uniform matter when the excluded-volume mechanism was implemented, was noticed, and a solution was proposed, namely a generalization of the excluded-volume approach. In our case, this same divergence that is brought by the term $(1 - u^{1/3})^{-3}$ in Eq. (4.122) is moderated by finite-temperature effects, yielding instead the appearance of lighter, essentially unbound clusters.

Table 4.2: Crust-core transition density, $n_{\rm CC}$, and pressure, $P_{\rm CC}$, for the BSk24, SLy4, and DD-MEδ models at different temperatures with (w/) and without (w/o) the inclusion of the translational free energy $F^{\star}_{\rm trans}$ for the case $\delta^{\rm f} = \gamma$. Table adapted from Ref. [270].

Model		BSk24			SLy4			DD-MEδ		
k_BT (MeV)		1.0	1.5	2.0	1.0	1.5	2.0	1.0	1.5	2.0
$n_{\rm CC}$ (fm^{-3})	w/ $F^{\star}_{\rm trans}$	0.081	0.079	0.076	0.080	0.077	0.073	0.079	0.075	0.071
	w/o $F^{\star}_{\rm trans}$	0.079	0.078	0.078	0.077	0.076	0.076	0.076	0.075	0.075
$P_{\rm CC}$ (MeV/fm^3)	w/ $F^{\star}_{\rm trans}$	0.274	0.264	0.248	0.373	0.342	0.320	0.447	0.404	0.368
	w/o $F^{\star}_{\rm trans}$	0.257	0.256	0.261	0.344	0.334	0.338	0.407	0.398	0.408

The effect of the modified translational free energy, $F^{\star}_{\rm trans}$, on the compositions (A, Z) is significant at all densities in the PNS inner crust. Specifically, at the highest temperature considered, $k_{\rm B}T = 2.0$ MeV, the reduction in A and Z with respect to a calculation where the translational energy is neglected or excluded from the variational equation with respect to the cluster size, as in the works by Refs. [90,288], is of the order of > 400 in A and > 20 in Z. Therefore, for calculations of the (liquid) inner crust where an accurate description of the composition is needed, the translational free energy should be taken into account. In contrast to the ideal-gas approximation, the inclusion of in-medium effects in the translational free energy does not lead to an early dissolution of the clusters, as can be seen by comparing Figs. 4.8 and 4.14. Instead, at all the considered temperatures, clusters are favored over homogeneous nuclear matter up to $n_B \gtrsim 0.07$ fm^{-3}.

On the other hand, in most cases, the impact of the translational free energy term is reduced on more global quantities like the equation of state. This is demonstrated in Fig. 4.15, where the total pressure P is plotted as a function of the baryon number density n_B in the inner crust. We can see that, for all the considered models, including or not the in-medium modified translational free energy $F^{\star}_{\rm trans}$ yields almost identical results, the solid and dashed curves in Fig. 4.15 being almost indistinguishable. The crust-core interface is indicated by green dots (violet squares) for the case where $F^{\star}_{\rm trans}$ is (not) taken into account. The crust-core transition was determined by comparing the WS free energy density of the inhomogeneous crust to that of homogeneous (or quasi-homogeneous) matter at beta equilibrium (see also Fig. 4.14). At $k_BT = 1.0$ MeV (top panel), the translational degrees of freedom favor clusters over homogeneous matter by lowering the free energy density of the system. Thus, the crust-core transition is moved to higher density (and pressure) when this term is accounted for. On the other hand, the situation is reversed for $k_BT = 1.5$ MeV (middle panel) and 2.0 MeV (bottom panel). This is understood from the fact that the most favorable clusters decrease in size as the temperature increases, leading to a progressive "melting" in the surrounding medium. Thus, the resulting crust-core transition is very close to or even lower than that obtained by neglecting the translational free energy contribution. Values of the crust-core transition density and pressure are reported in Table 4.2.

4.1.3.2 Composition at a fixed proton fraction

In the case of beta equilibrium, the cluster proton fraction falls rapidly as the density increases, from ~ 0.4 at the outermost layer to ~ 0.05 at the bottom of the PNS inner crust.

As a result, the contribution from the Coulomb, surface, and curvature energies decline dramatically, and the effect from the translational degrees of freedom in this region becomes significant, leading to the reduction of the cluster mass and proton number, as discussed in Sect. 4.1.3.1. One would expect that the drastic effects observed in the beta-equilibrium case are hindered if the cluster proton fraction remains relatively high at all densities. To verify this, in this section, I consider the case where the total proton fraction is fixed. The latter is of interest for astrophysical scenarios, either where the total proton fraction can be assumed to be roughly constant, as in some regions of the supernova collapsing core in the neutrino-trapped regime (e.g., [289,290]; see also Ref. [291]), or for the computation of general-purpose EOS, where calculations are performed for given (fixed) values of density n_B, temperature T, and total proton (or electron) fraction $Y_p^{\rm tot}$ (see e.g., Refs. [90, 288, 292, 293]; see also Refs. [7, 284] for an overview of general-purpose EOS computation). For this reason, several studies have been devoted to calculations at finite temperature and fixed proton fraction ($Y_p^{\rm tot} \approx 0.1 - 0.5$), particularly for conditions relevant to supernova matter (e.g., [293–296]).

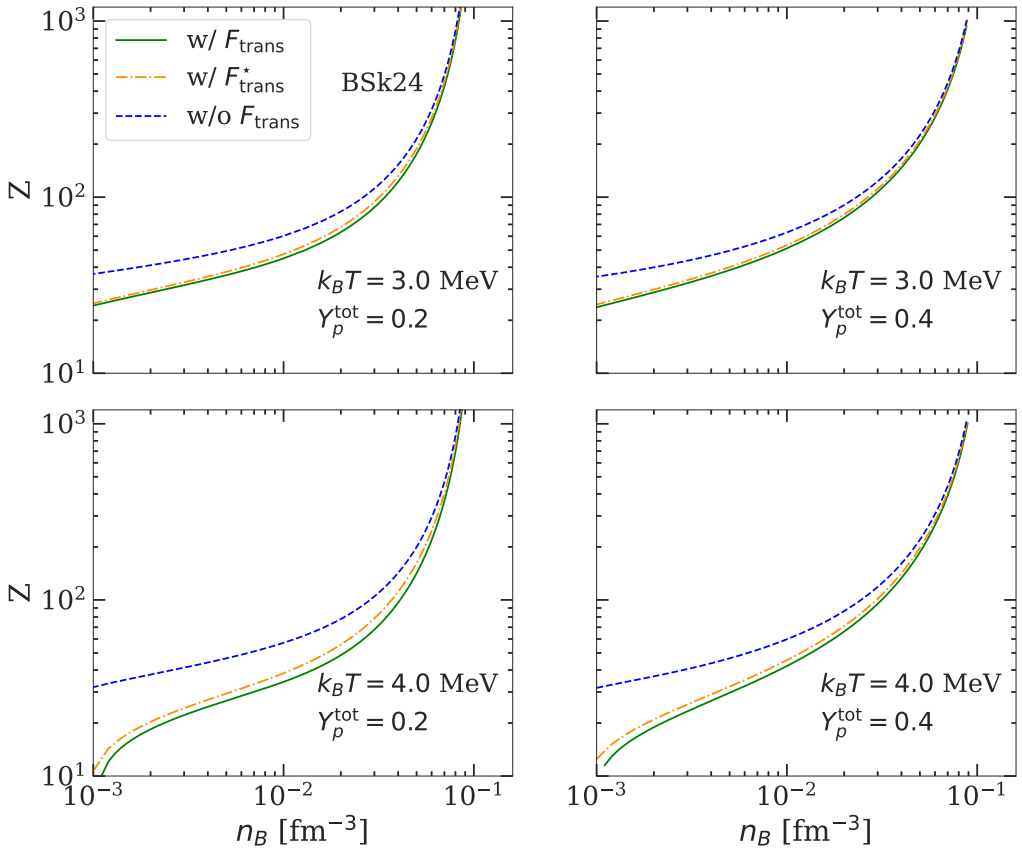

Figure 4.16: Proton number in the cluster as a function of baryon density n_B obtained with $F_{\rm trans}$ (solid green lines), with $F^{\star}_{\rm trans}$ where $\delta^{\rm f} = \gamma$ (dash-dotted orange lines), and without translational term (dashed blue lines).

At a fixed total proton fraction $Y_p^{\rm tot} = n_e/n_B$, Eq. (4.114) associated to beta equilibrium no longer holds, and the equilibrium state of matter for each given thermodynamic condition (n_B, T, $Y_p^{\rm tot}$) is determined by solving the system of four variational equations, Eqs. (4.115)-

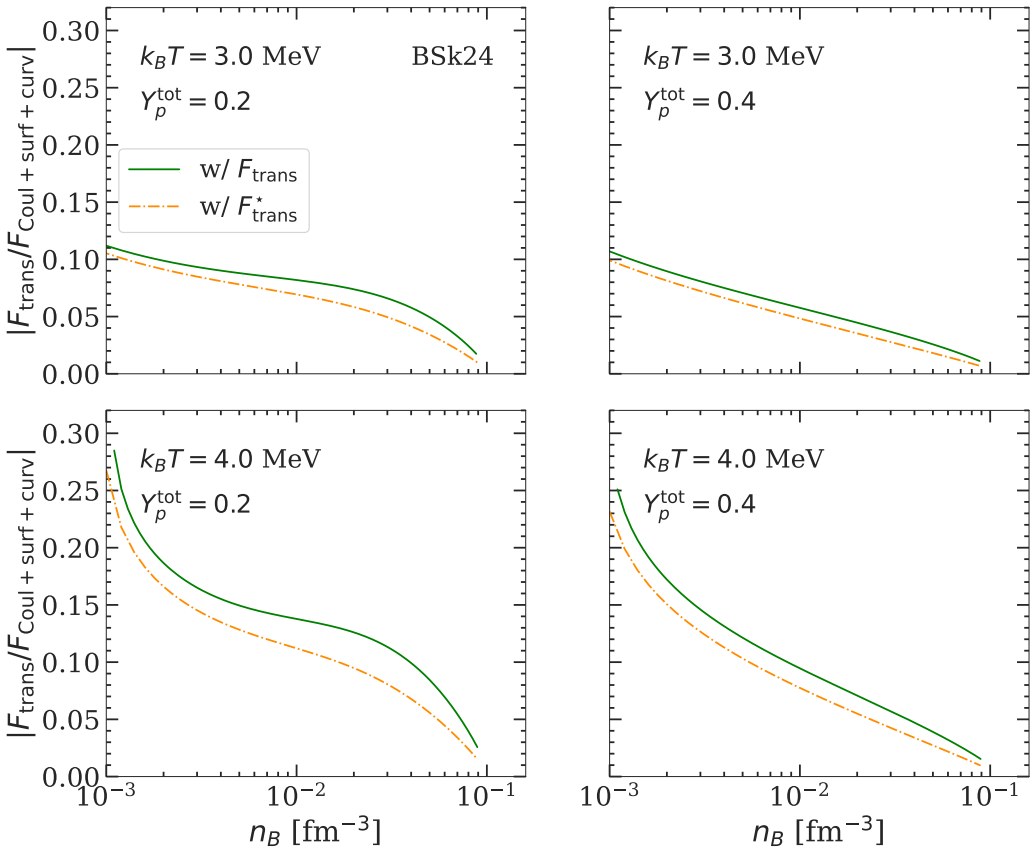

Figure 4.17: Absolute values of translational free energy ($F_{\rm trans}$ or $F^\star_{\rm trans}$) divided by the sum of finite-size energy (surface, curvature and Coulomb). Solid green lines are obtained with the ideal-gas translational term $F_{\rm trans}$, and dash-dotted orange lines correspond to $F^\star_{\rm trans}$, Eq. (4.96), with $\delta^{\rm f} = \gamma$.

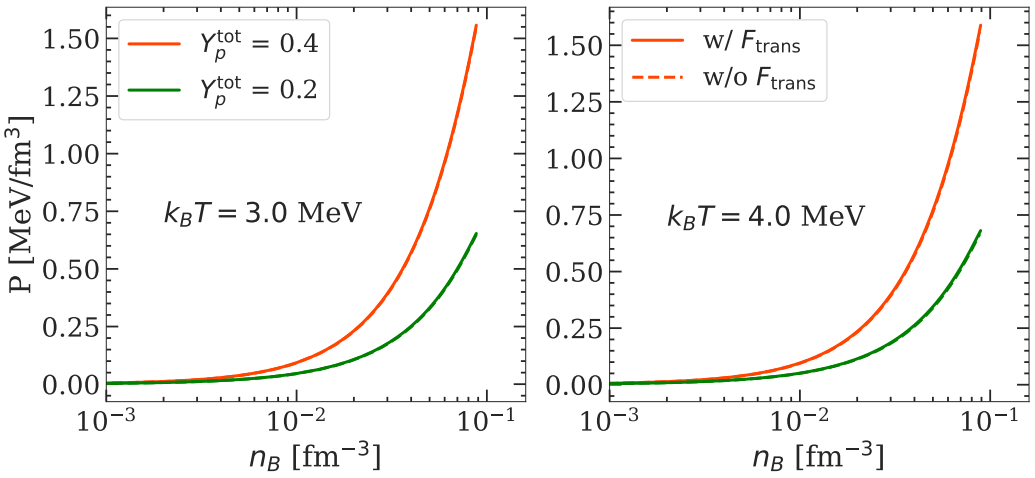

Figure 4.18: Pressure P versus the baryonic density n_B for the BSk24 model at $Y_p^{\rm tot} = 0.4$ (red lines) and $Y_p^{\rm tot} = 0.2$ (green lines) for $k_{\rm B}T = 3.0$ MeV (left panel) and $k_{\rm B}T = 4.0$ MeV (right panel), obtained with (solid line) and without the (ideal-gas) translational energy. Figure adapted from Ref. [270].

(4.118), together with the equations of baryon number conservation, Eq. (4.100), and charge

neutrality, Eq. (4.102).

Figure 4.16 displays the cluster proton number Z as a function of n_B at $k_\mathrm{B}T = 3.0$ MeV (upper panels) and $k_\mathrm{B}T = 4.0$ MeV (lower panels) at two selected total proton fractions: $Y_p^\mathrm{tot} = 0.2$ (left panels) and $Y_p^\mathrm{tot} = 0.4$ (right panels). Results are shown both for the case where the translational free energy is neglected (dashed lines) and for the two different prescriptions for the translational free energy term considered in this work: F_trans, Eq. (4.88) (solid lines), and $F^\star_\mathrm{trans}$, Eq. (4.96), with $\delta^\mathrm{f} = \gamma$ (dash-dotted lines). Similarly to the beta-equilibrium case discussed in Sect. 4.1.3.1, both prescriptions, F_trans and $F^\star_\mathrm{trans}$, have the effect of reducing the cluster size. In particular, this effect is larger at lower n_B and Y_p^tot, and higher T. However, in the scenario where the proton fraction is fixed, the impact of the translational free energy is only slightly reduced when the in-medium corrections on the cluster volume and on the effective mass are taken into account, as can be seen by comparing the solid and the dash-dotted lines in Fig. 4.16.

More strikingly, the role of the translational free energy is overall much less important than in the beta-equilibrium case. When the translational term is included, the clusters still survive up to around 0.1 fm^{-3}, unlike in beta equilibrium (see Table 4.1 and Fig. 4.14). This can be understood by analyzing the absolute ratio between the translational, F_trans (solid lines) and $F^\star_\mathrm{trans}$, and the finite-size free energies, $|F_\mathrm{trans}/F_\mathrm{Coul+surf+curv}|$, shown in Fig. 4.17. Indeed, as already mentioned in Sect. 4.1.3.1, the cluster size results from the competition between these two terms. For the fixed proton fractions we consider, which are however higher than those obtained in beta equilibrium, the finite-size term dominates at all densities, particularly at higher n_B, higher Y_p^tot, and lower T, which explains the reduced impact of F_trans in these regimes observed in Fig. 4.16. One can thus expect that the effect of the translational free energy remains negligible on the equation of state also in the fixed proton fraction scenario, as can indeed be seen in Fig. 4.18.

4.2 Multi-component plasma approach

As it was shown in Ref. [80], at temperatures close to the crystallization point, the nuclear distribution in the outer region of the inner crust is sufficiently narrow that it can be represented by a single heavy nucleus obtained from the OCP approximation. However, at other thermodynamic conditions, where the distribution gets broader and the abundance of light clusters becomes prominent, this approximation is no longer reliable. As a result, the coexistence of all nuclear species needs to be taken into account [82, 85, 88].

In this section, I present in detail the MCP formalism and the results of our work in Ref. [269]. In this work, the modeling of matter in nuclear statistical equilibrium is a further extension of the formalism from Refs. [81] and [80] to deeper regions in the inner crust as well as to higher temperatures, with the employment of a more realistic description for the center-of-mass motion. Moreover, we also go beyond the perturbative approach used in Ref. [80] and perform a fully self-consistent MCP calculation, where the cluster distribution and the gas variables are calculated consistently with the constraints of baryon number conservation and charge neutrality. Indeed, in Ref. [80], the nuclear distributions were calculated using a perturbative implementation of the nuclear statistical equilibrium, as first proposed in

Ref. [83]. In this perturbative treatment, for a given baryon density n_B and temperature T, the beta-equilibrium composition is firstly found in the OCP approximation. This procedure yields the (OCP) neutron and proton chemical potentials which are subsequently used in the computation of the ion abundances. Although not fully self-consistent, this approach has the advantage of leading to a very fast convergence, with reduced computational cost with respect to a full nuclear statistical equilibrium treatment (see e.g., Refs. [82, 88, 285]). However, the applicability of such perturbative approach needs a more thorough assessment at high densities, in the deeper regions of the crust, and at relative high temperatures, above the crystallization temperature.

Our MCP analysis is performed at temperatures in the range from 1 MeV to 2 MeV, where the crust is expected to be in the liquid phase [79] and the beta-equilibrium condition should be realized. This section is organized as follows: The derivation of the cluster distribution is described in Sect. 4.2.1, while the total pressure of the inhomogeneous matter in the MCP calculation is given in Sect. 4.2.2. In Sect. 4.2.3, I present the translational-free-energy term in the MCP picture. Then, the comparison between the MCP and OCP approaches is discussed in Sect. 4.2.4. Numerical results are presented in Sect. 4.2.5, where the perturbative MCP approach is shown in Sect. 4.2.5.1, the self-consistent MCP calculations are presented Sect. 4.2.5.2, and the outcomes for the impurity parameter are displayed in Sect. 4.2.5.3.

4.2.1 Derivation of the cluster distribution

In the MCP approach, the NS inner crust at each thermodynamic condition is an ensemble of different nuclear species, denoted by $(j) \equiv (A^{(j)}, Z^{(j)})$[6], in WS cells of volume $V_{\rm WS}^{(j)}$. At finite temperatures, a free proton gas could also be present as included in the OCP calculation in Sect. 4.1. However, as we have seen in Fig. 4.13, for the considered temperature regimes, $k_{\rm B}T \lesssim 2.0$ MeV, the proton gas density remained very small for almost all densities, about 10^{-3} fm^{-3} at most at the bottom of the crust, and its effects on the EOS and the crust composition are negligible. For this reason, the presence of the free protons is neglected in the MCP formalism, as was done in Ref. [80].

Assuming that the electron and neutron gases are uniformly distributed in all cells, we have: $n_{gn}^{(j)} = n_{\rm gn}$ and $n_e^{(j)} = n_e$. In addition, to avoid the interaction between different cells, let us suppose that charge neutrality holds in each of them:

$$n_e = n_p = n_p^{(j)} = \frac{Z^{(j)}}{V_{\rm WS}^{(j)}}. \tag{4.124}$$

Let $n_N^{(j)}$ be the ion density of a species $(A^{(j)}, Z^{(j)})$, the frequency of occurrence or probability of the component (j) is given by $p_j = n_N^{(j)} \langle V_{\rm WS} \rangle$, with the bracket notation $\langle\rangle$ indicating ensemble averages. The normalization condition for the probability reads

$$\sum_j p_j = 1, \tag{4.125}$$

implying

$$\sum_j n_N^{(j)} = \frac{1}{\langle V_{\rm WS} \rangle}. \tag{4.126}$$

[6] We vary $Z \in [2, 100]$, and for each Z, $A \in [2Z, 30Z]$.

The total free energy density of the system is given by:

$$\mathcal{F}^{\rm MCP} = \sum_j n_N^{(j)} \left(F_i^{(j)} - V_N^{(j)} \mathcal{F}_{\rm g} \right) + \mathcal{F}_{\rm g} + \mathcal{F}_e \ , \tag{4.127}$$

where $\mathcal{F}_{\rm g} = \mathcal{F}_B(n = n_{\rm gn}, \delta_{\rm g} = 1, T) + n_{\rm gn} m_n c^2$ is the free-energy density of the neutron gas. The minimization of this total free energy density $\mathcal{F}^{\rm MCP}$ is subject to the constraints of baryon number conservation and charge neutrality:

$$n_B - n_{\rm gn} - \sum_j n_N^{(j)} \left(A^{(j)} - n_{\rm gn} V_N^{(j)} \right) = 0. \tag{4.128}$$

$$n_p - \sum_j n_N^{(j)} Z^{(j)} = 0, \tag{4.129}$$

As a result, two Lagrange multipliers, ξ_1 and ξ_2, can be introduced, and the function to be minimized becomes:

$$\begin{aligned} \Omega^{\rm MCP} = {} & \mathcal{F}_{\rm g} + \mathcal{F}_e + \sum_j n_N^{(j)} \left(F_i^{(j)} - V_N^{(j)} \mathcal{F}_{\rm g} \right) \\ & + \xi_1 \left(n_p - \sum_j n_N^{(j)} Z^{(j)} \right) \\ & + \xi_2 \left(n_B - n_{\rm gn} - \sum_j n_N^{(j)} \left(A^{(j)} - n_{\rm gn} V_N^{(j)} \right) \right) . \end{aligned} \tag{4.130}$$

Minimizing $\Omega^{\rm MCP}$ with respect to n_p $(=n_e)$ and $n_{\rm gn}$, we obtain the following expressions for ξ_1 and ξ_2:

$$\xi_1 = -\frac{\partial \mathcal{F}_e}{\partial n_p} - \sum_j n_N^{(j)} \frac{\partial F_i^{(j)}}{\partial n_p} = -\left(\mu_e + \Delta\mu_e \right), \tag{4.131}$$

$$\xi_2 = \frac{\partial \mathcal{F}_{\rm g}}{\partial n_{\rm gn}} + \frac{\sum_j n_N^{(j)} \left(\partial F_i^{(j)} / \partial n_{\rm gn} \right)}{1 - \sum_j n_N^{(j)} V_N^{(j)}} \equiv \mu_n. \tag{4.132}$$

The second term on the right-hand side of Eq. (4.131), $\Delta\mu_e = \sum_j n_N^{(j)} \frac{\partial F_i^{(j)}}{\partial n_p}$, arises from the dependence of the cluster free energy on the electron-gas density via the Coulomb screening term. Moreover, we can also see that μ_n is not the same as that of the neutron background, but it also includes the in-medium effect:

$$\mu_n = \frac{\partial \mathcal{F}_{\rm g}}{\partial n_{\rm gn}} + \Delta\mu_n, \tag{4.133}$$

with

$$\Delta\mu_n = \frac{\sum_j n_N^{(j)} \left(\partial F_i^{(j)} / \partial n_{\rm gn} \right)}{1 - \sum_j n_N^{(j)} V_N^{(j)}}. \tag{4.134}$$

The condition of charge neutrality in Eq. (4.129) is equivalent to $\sum_j n_N^{(j)} V_{\rm WS}^{(j)} = 1$. Using this relation in Eq. (4.134), at the limit where the distribution is made of only one component,

we can easily show that $\Delta\mu_n \to \frac{(\partial F_i/\partial n_{\rm gn})}{V_{\rm WS}-V_N}$, and the neutron chemical potential in Eq. (4.132) has the same expression as that in Eq. (4.110).

Since the neutron gas and the electron gas free-energy densities, $\mathcal{F}_{\rm g}$ and $\mathcal{F}_e$, are independent of $n_N^{(j)}$, we only need to consider the terms related to ions. Substituting ξ_1 and ξ_2 by their corresponding expressions in Eqs. (4.131)-(4.132), the function to be minimized becomes:

$$\begin{aligned}\Omega_i^{\rm MCP} = &\sum_j n_N^{(j)}\left(F_i^{(j)} - V_N^{(j)}\mathcal{F}_{\rm g}\right)\\ &+ (\mu_e + \Delta\mu_e)\sum_j n_N^{(j)} Z^{(j)} - \mu_n \sum_j n_N^{(j)}\left(A^{(j)} - n_{\rm gn}V_N^{(j)}\right).\end{aligned} \tag{4.135}$$

It is worth noticing that the ion free energy, $F_i^{(j)}$, has the same form as in Eq. (4.58), but the contribution from the translation must be replaced by:

$$F_{\rm trans}^{\star,(j),{\rm MCP}} = k_B T \ln\left(\frac{n_N^{(j)}}{\bar{u}_{\rm f}}\frac{(\lambda_i^{\star,(j)})^3}{g_s^{(j)}}\right) - k_B T, \tag{4.136}$$

where $g_s^{(j)} = 1\ \forall j$, and $\bar{u}_{\rm f}$ is the fraction of the average free volume, and the effective thermal wavelength of the ion in Eq. (4.136) is given by

$$\lambda_i^{\star,(j)} = \sqrt{\frac{2\pi\hbar^2}{M_i^{\star,(j)} k_{\rm B} T}}, \tag{4.137}$$

where

$$M_i^{\star,(j)} = M_i^{(j)}(1-\gamma^{(j)})\ , \tag{4.138}$$

with $\gamma^{(j)} = n_{\rm gn}/n_i^{(j)}$ being the ratio between the neutron gas density and the cluster internal density. In the same spirit as Ref. [87], the fraction of the average free volume $\bar{u}_{\rm f}$ is given by:

$$\bar{u}_{\rm f} = 1 - \sum_j n_N^{(j)} V_N^{(j)}\ . \tag{4.139}$$

Details on $F_{\rm trans}^{\star,(j),{\rm MCP}}$ are given in Sect. 4.2.3.

Performing the variation on $\Omega_i^{\rm MCP}$ in Eq. (4.135) with respect to $n_N^{(j)}$, we obtain:

$$F_i^{(j)} - V_N^{(j)}\mathcal{F}_{\rm g} + \sum_{j'} n_N^{(j')}\frac{\partial F_i^{(j')}}{\partial n_N^{(j)}} + (\mu_e + \Delta\mu_e)Z^{(j)} - \mu_n\left(A^{(j)} - n_{\rm gn}V_N^{(j)}\right) = 0. \tag{4.140}$$

Using $\sum_{j'} n_N^{(j')}\frac{\partial F_i^{(j')}}{\partial n_N^{(j)}} = k_B T$, and denoting $\mathcal{R}^{(j)} = \Delta\mu_e Z^{(j)}$, Eq. (4.140) becomes:

$$\begin{aligned}F_i^{(j)} - V_N^{(j)}\mathcal{F}_{\rm g} - F_{\rm trans}^{\star,(j),{\rm MCP}} + k_B T\ln n_N^{(j)} - k_B T\ln\bar{u}_{\rm f} + k_B T\ln\left(\frac{(\lambda_i^{\star,(j)})^3}{g_s^{(j)}}\right) + \mathcal{R}^{(j)}\\ + \mu_e Z^{(j)} - \mu_n\left(A^{(j)} - n_{\rm gn}V_N^{(j)}\right) = 0,\end{aligned} \tag{4.141}$$

leading to the following expression for the ion density $n_N^{(j)}$:

$$n_N^{(j)} = \bar{u}_{\rm f} \exp\left\{\left(-\frac{\tilde{\Omega}_i^{(j)}}{k_B T}\right)\right\}. \tag{4.142}$$

From Eq. (4.141), it is straightforward to demonstrate that $\tilde{\Omega}_i^{(j)}$ can be written as:

$$\tilde{\Omega}_i^{(j)} = F_i^{(j),\star} - V_N^{(j)}\mathcal{F}_{\rm g} + \mathcal{R}^{(j)} + \mu_e Z^{(j)} - \mu_n\left(A^{(j)} - n_{\rm gn}V_N^{(j)}\right). \tag{4.143}$$

where

$$F_i^{(j),\star} = F_i^{(j)} - F_{\rm trans}^{\star,(j),{\rm MCP}} + k_B T \ln\left(\frac{(\lambda_i^{\star,(j)})^3}{g_s^{(j)}}\right). \tag{4.144}$$

The term $\mathcal{R}^{(j)}$ in Eq. (4.143) is the so-called *rearrangement term*. It was shown that this term is important to guarantee the thermodynamic consistency of the model and to recover the ensemble equivalence between the MCP and OCP approaches (see e.g., Refs. [80, 81, 83, 89]). As mentioned before, $\mathcal{R}^{(j)}$ accounts for the modification in the electron chemical potential due to the dependence of the Coulomb energy on the electron density:

$$\begin{aligned}
\mathcal{R}^{(j)} &= Z^{(j)}\Delta\mu_e \ , \\
&= Z^{(j)}\sum_{j'} n_N^{(j')}\frac{\partial F_i^{(j')}}{\partial n_p} \ , \\
&= Z^{(j)}\sum_{j'} n_N^{(j')}\frac{\partial F_{\rm Coul}^{(j')}}{\partial n_p} \ , \\
&= V_{\rm WS}^{(j)}\sum_{j'} n_N^{(j')}V_{\rm WS}^{(j')}P_{\rm int}^{(j')} \ , \\
&= V_{\rm WS}^{(j)}\bar{P}_{\rm int} \ ,
\end{aligned} \tag{4.145}$$

in which $P_{\rm int}^{(j')}$ is the pressure contributed by the Coulomb interaction,

$$P_{\rm int}^{(j')} = \frac{n_p^2}{Z^{(j')}}\frac{\partial F_{\rm Coul}^{(j')}}{\partial n_p} \ . \tag{4.146}$$

and $\bar{P}_{\rm int}$ reads:

$$\bar{P}_{\rm int} = \sum_{j'} n_N^{(j')}V_{\rm WS}^{(j')}P_{\rm int}^{(j')}. \tag{4.147}$$

We can notice that the rearrangement term, Eq. (4.145), is not exactly equivalent to that derived in Ref. [80].

In order to determine the cluster distribution $n_N^{(j)}$, it is essential to know n_p, $n_{\rm gn}$, $\Delta\mu_n$, $\bar{u}_{\rm f}$, and $\bar{P}_{\rm int}$, in which the three latter terms themselves require the knowledge of $n_N^{(j)}$, leading to a self-consistent problem. Therefore, for each given baryon density and temperature, the system of five equations, Eqs. (4.128), (4.129), (4.134), (4.139), and (4.147), with $n_N^{(j)}$ given by Eq. (4.142) are solved simultaneously. This procedure results in the gas variables and cluster distribution fulfilling the baryon number conservation and charge neutrality conditions at the input thermodynamic condition (n_B, T).

4.2.2 Total pressure in MCP

Considering a WS cell containing species (j), the total pressure corresponding to this cell can be written as

$$P^{(j)} = P_{gn} + P_e + P_i^{(j)}, \tag{4.148}$$

where the gas and electron pressures are the same in all cells since both gases are uniformly distributed in the whole volume, and $P_i^{(j)}$ is the ion pressure,

$$P_i^{(j)} = P_{\rm trans}^{\star,(j)} + P_{\rm int}^{(j)}, \tag{4.149}$$

in which $P_{\rm int}^{(j)}$ is the interaction pressure and is given by Eq. (4.146), while $P_{\rm id}^{(j)}$ is contributed by the center-of-mass motion:

$$P_{\rm trans}^{\star,(j)} = P_{\rm trans}^{\star} = \frac{k_{\rm B}T}{\bar{u}_{\rm f}\langle V_{\rm WS}\rangle} \ . \tag{4.150}$$

Now, to derive the total pressure in MCP, one can start from the definition of pressure, i.e., $P = -\left.\frac{\partial F}{\partial V}\right|_{N,T}$, and obtain:

$$P^{\rm MCP} = -\left.\frac{\partial\langle F^{\rm MCP}\rangle}{\partial\langle V_{\rm WS}\rangle}\right|_{p_j,T} , \tag{4.151}$$

$$= P_{gn} + P_e + P_{\rm trans}^{\star} + \frac{\partial\langle F_{\rm Coul}\rangle}{\partial\langle V_{\rm WS}\rangle}, \tag{4.152}$$

$$= P_{gn} + P_e + P_{\rm trans}^{\star} + \frac{n_p^2}{\langle Z\rangle}\sum_j p_j \frac{\partial F_{\rm Coul}^{(j)}}{\partial n_p}, \tag{4.153}$$

where $P_{gn} = \mu_{gn}n_{gn} - \mathcal{F}_{\rm g}$ ($P_e = \mu_e n_e - \mathcal{F}_e$) is the neutron gas (electron) pressure [7]. Finally, using the relations in Eq. (4.147), we obtain:

$$P^{\rm MCP} = P_{gn} + P_e + P_{\rm trans}^{\star} + \bar{P}_{\rm int}. \tag{4.154}$$

As it was already pointed out by Ref. [81], the total pressure in MCP is not equal to the the average pressure over all species, i.e., $P^{\rm MCP} \neq \sum_j p_j P^{(j)}$.

4.2.3 Translational free energy of ions in the MCP

The translational-free-energy term appearing in Eq. (4.58), $F_{\rm trans}^{\star,(j),{\rm MCP}}$, accounts for the center-of-mass motion of each ion in the liquid MCP. In the OCP description (see Sect. 4.1.2.3), clusters at each thermodynamic condition are not only identical but also indistinguishable, and the translational free energy per ion can be associated to a single microscopic WS-cell volume, such that all WS cells are independent, and the charge neutrality holds in each cell. In this approximation, when the finite-size effect is taken into account, the free volume of each ion is that given by Eq. (4.95):

$$V_{\rm f}^{\rm OCP} = \frac{4}{3}\pi(r_{\rm WS} - r_N)^3 \ , \tag{4.155}$$

[7] One should notice that the pressure term denoted by P_{gn} corresponds to pure neutron gas, that is, it does not include in-medium effects.

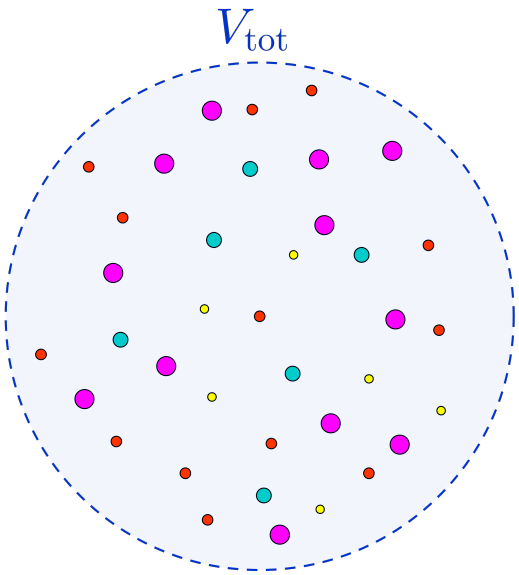

Figure 4.19: Schematic illustration of a system of $N_{\rm tot} = \sum_j N^{(j)}$ different species (j) in a (macroscopic) volume $V_{\rm tot}$.

where I have added the superscript "OCP".

On the contrary, in the MCP picture, at each $(n_B,\ T)$, the system contains a mixture of different species (see Fig. 4.19). Let $N^{(j)}$ be the number of (indistinguishable) ions of species (j), the total number of particles in the system is $N_{\rm tot} = \sum_j N^{(j)}$, and the occurrence frequency is $p_j = \frac{N^{(j)}}{N_{\rm tot}}$. If we (temporarily) neglect the finite size of the clusters, then the translational free energy for an ion of species (j) has the same form as in Eq. (4.94), but with $N_{\rm tot}$ being replaced by $N^{(j)}$:

$$F_{\rm trans}^{(j),\rm MCP} \approx k_B T \ln\left(\frac{N^{(j)}}{V_{\rm tot}}\frac{\left(\lambda_i^{(j)}\right)^3}{g_s}\right) - k_B T\ , \tag{4.156}$$

$$= k_B T \ln\left(\frac{p_j N_{\rm tot}}{V_{\rm tot}}\frac{\left(\lambda_i^{(j)}\right)^3}{g_s}\right) - k_B T\ , \tag{4.157}$$

$$= k_B T \ln\left(\frac{p_j}{\langle V_{\rm WS}\rangle}\frac{\left(\lambda_i^{(j)}\right)^3}{g_s}\right) - k_B T. \tag{4.158}$$

We can see that the available volume per ion $\langle V_{\rm WS}\rangle = V_{\rm tot}/N_{\rm tot}$ in the MCP mixture is an average quantity, and it is the same for all species. Thus, unlike the OCP picture, in the MCP approach, the microscopic volume associated with the center-of-mass motion of each ion does not coincide with the corresponding WS-cell volume, $\langle V_{\rm WS}\rangle \neq V_{\rm WS}^{(j)}$. As a result, in the latter, the WS approximation is relaxed, and therefore, when the finite-size effect is considered, the average free volume $\langle V_{\rm f}\rangle$ can be obtained by subtracting from $\langle V_{\rm WS}\rangle$ the

average volume occupied by the different ions:

$$\langle V_{\rm f}\rangle = \langle V_{\rm WS}\rangle - \langle V_N\rangle = \sum_j p_j V_{\rm f}^{(j)}, \tag{4.159}$$

where

$$V_{\rm f}^{(j)} = \frac{4}{3}\pi\left(r_{\rm WS}^{(j)3} - r_N^{(j)3}\right) , \tag{4.160}$$

Using $\langle V_{\rm f}\rangle = \bar{u}_{\rm f}\langle V_{\rm WS}\rangle$ (see the definition of $\bar{u}_{\rm f}$ in Eq. (4.139)), and accounting also for the fact that the bound nucleons inside each ion can be in relative motion with respect to the unbound neutron gas leads to Eq. (4.136) for the translational free energy.

In Ref. [81], it was noticed that, because of the different expressions of the translational energy in the OCP and MCP approach, a first deviation from the linear mixing rule appears. As a consequence, the total free-energy of the ions is not just the sum of the OCP ion free-energies, but an extra term arises, known in the literature as the mixing entropy (see Eq. (21) in Ref. [81]; see also Ref. [297]). This is still the case here, but the additional (non-ideal) "mixing entropy" term now reflects the in-medium (excluded-volume) effects included in the translational energy $F_{\rm trans}^{\star,(j),{\rm MCP}}$,

$$F_i^{(j)} = F_i^{(j),{\rm OCP}} + k_B T \ln\left[p_j \frac{Z^{(j)}}{\langle Z\rangle}\frac{\left(1-u^{(j)1/3}\right)^3}{\bar{u}_{\rm f}}\right] . \tag{4.161}$$

4.2.4 MCP versus OCP

To compare the MCP and OCP approaches, we need to evaluate the most probable configuration in the MCP. The latter corresponds to the maximum probability, $p_j^{\rm max}$, or equivalently the minimum grand-canonical potential, $\tilde{\Omega}_i^{(j),{\rm min}}$. Since the gas densities are invariant with cells, the minimization is performed only with respect to the three variables associated with the cluster, i.e., $r_N^{(j)}$, $I^{(j)}$, and $n_i^{(j)}$, yielding the following system of equations:

$$(n_i^{(j)})^2\frac{\partial(F_i^{\star,(j)}/A^{(j)})}{\partial n_i^{(j)}} - \frac{r_N^{(j)}n_i^{(j)}}{3}\frac{\partial(F_i^{(j),\star}/A^{(j)})}{\partial r_N^{(j)}} = P_{\rm g}, \tag{4.162}$$

$$\frac{r_N^{(j)}}{3A^{(j)}}\frac{\partial F_i^{\star,(j)}}{\partial r_N^{(j)}} + (1-I^{(j)})\frac{\partial(F_i^{\star,(j)}/A^{(j)})}{\partial I^{(j)}} = \mu_n - \frac{P_{\rm g}}{n_i^{(j)}}, \tag{4.163}$$

$$2\frac{\partial(F_i^{\star,(j)}/A^{(j)})}{\partial I^{(j)}} - \frac{\bar{P}_{\rm int}}{n_p} = \mu_e, \tag{4.164}$$

where $P_{\rm g} = \mu_n n_{gn} - \mathcal{F}_{\rm g} = P_{gn} + \Delta\mu_n n_{gn}$ is the neutron pressure, including the in-medium effects.

The OCP equilibrium equations, Eqs. (4.114)-(4.118), without the free proton gas, can be

written as:

$$n_i^2 \frac{\partial}{\partial n_i}\left(\frac{F_i}{A}\right) = P_{\rm g}\ , \tag{4.165}$$

$$\frac{F_i}{A} + (1-I)\frac{\partial}{\partial I}\left(\frac{F_i}{A}\right) = \mu_n - \frac{P_{\rm g}}{n_i}\ , \tag{4.166}$$

$$2\left[\frac{\partial}{\partial I}\left(\frac{F_i}{A}\right) - \frac{n_p}{1-I}\frac{\partial}{\partial n_p}\left(\frac{F_i}{A}\right)\right] = \mu_e\ , \tag{4.167}$$

$$\frac{\partial (F_i/A)}{\partial r_N} = 0\ . \tag{4.168}$$

It is easy to show that Eqs. (4.162)-(4.164) for the most probable ion in the MCP are equivalent to the first three OCP variational equations Eqs. (4.165)-(4.167) if the following conditions are satisfied:
(i) $F_i^{\star,(j)}$ is the same as in the OCP, i.e., $F_i^{\star,(j)} = F_i^{(j),\rm OCP} = F_i$. This is the case if the non-linear mixing term, which arises due to the translational motion [81,82], see Sect. 4.2.3, is negligible;
(ii) the gas densities, n_{gn} and n_e, as well as $\Delta\mu_n$ and $\bar{P}_{\rm int}$, are identical to the OCP values. This is expected to be realized if the ion distributions are strongly peaked on a unique ion species, such that the averages in Eqs. (4.134) and (4.147) can be approximated to a single term corresponding to the OCP solution.

The validity of these conditions, which are necessary for the OCP approximation to give a satisfactory description of the finite-temperature configuration, are discussed in Sect. 4.2.5.1. The extra OCP condition Eq.(4.168) is identical to the well-known Baym virial theorem [9] which holds for a nucleus in the vacuum. This condition arises from the fact that, for a given thermodynamic condition, there is systematically one more independent variable in the OCP with respect to the MCP. Indeed, the WS cell volume in the MCP is simply defined by charge conservation, while in the OCP it corresponds to an additional variable that has to be variationally determined.

In a CLD picture, for a given mass A and atomic number Z, a nuclear species is also characterized by its radius, r_N, or equivalently its density $n_i = 3A/(4\pi r_N^3)$, which can in principle fluctuate from cell to cell in the MCP equilibrium. Changing variables from (r_N, I, n_i) to (A, Z, n_i), the ion radius distribution of a given (A, Z) nucleus is expressed as

$$p_{AZ}(r_N) = \mathcal{N} n_N(A^{(j)} = A, Z^{(j)} = Z, r_N), \tag{4.169}$$

where $\mathcal{N}$ is a normalization. This distribution will be peaked at a value r_N corresponding to $\partial\tilde{\Omega}_i^{(j)}/\partial n_i|_{A^{(j)},Z^{(j)}} = 0$. This gives a pressure equilibrium condition as

$$P_{\rm cl}^\star \equiv \left.\frac{n_i^2}{A}\frac{\partial F_i^\star}{\partial n_i}\right|_{A,Z} = P_{\rm g}. \tag{4.170}$$

This equation is not necessarily compatible with the so called virial condition, or radius minimization ansatz given by

$$\left.\frac{\partial (F_i^\star/A)}{\partial r_N}\right|_{A,Z} = 0. \tag{4.171}$$

As a consequence, even if conditions (i) and (ii) above are met, the minimization equation for the OCP radius, Eq. (4.168), is not necessarily fulfilled in the MCP.

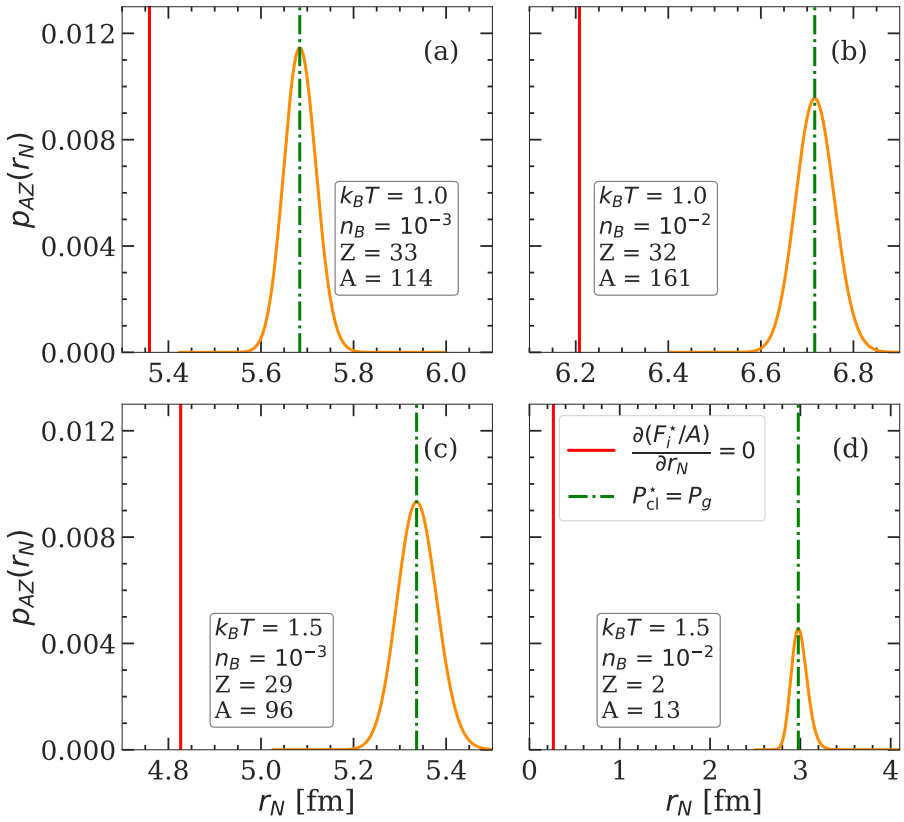

Figure 4.20: Normalized distribution of the cluster radius, $p_{AZ}(r_N)$, (orange solid line) in a full MCP calculation, in comparison with two different equilibrium prescriptions (see text) obtained for the most probable cluster at different temperatures (in MeV) and densities (in fm^{-3}). Figure adapted from Ref. [269].

This first important difference between the OCP and MCP approach is presented in Fig. 4.20, which shows the normalized distribution of the cluster radius for the most probable (A, Z) nucleus obtained at different thermodynamic conditions (orange solid lines) using BSk24 funtional. This distribution is compared with the solution obtained from the condition of pressure equilibrium in Eq. (4.170) (green dash-dotted lines) and that resulting from the minimization of the free energy per nucleon with respect to r_N in Eq. (4.171) (red solid lines). The distributions are obtained using the gas densities and chemical potentials consistent with the baryon number conservation and charge neutrality at each given thermodynamic condition (n_B, T) (see also Sect. 4.2.5.2). From Fig. 4.20, one can also observe that the solution of the pressure equilibrium equation always coincides with the peak of the MCP distribution. This is true not only for the radius of the most probable cluster but also for the $r_N^{(j)}$ of any $(A^{(j)}, Z^{(j)})$ cluster. On the other hand, using Eq. (4.171) to determine the cluster radius fails in reproducing the most probable cluster radius obtained within the MCP approach. In fact, it only produces the correct peak for the most probable cluster if the OCP chemical potentials are used and the contribution from the non-linear mixing term is negligible, as it

was analytically demonstrated in Ref. [83].

The computation of the crust observables considering the cluster distribution in the three-dimensional variable space (A, Z, r_N), is a numerically heavy task. In the literature, most MCP codes for core-collapse simulations either ignore the cluster density degree of freedom (see, e.g., Refs. [82, 87]) or impose the virial condition Eq. (4.171) (see, e.g., Refs. [86, 89]). Since the radius distribution is symmetric and relatively narrow in all thermodynamic conditions studied in the present work, to limit the numerical cost, in the following sections, the radius for each (A, Z) species is fixed from the pressure equilibrium condition Eq. (4.170).

4.2.5 Crust composition at finite temperature in the MCP

In this section, I show the composition and EOS of the inner crust of a PNS in the MCP approach, employing the empirical parameters from the BSk24 functional.

4.2.5.1 Perturbative MCP calculations

To begin, I discuss the results obtained calculating the MCP distribution in a perturbative approach as first proposed in Ref. [83]. The calculation was done as follows. For each (n_B, T), the OCP solution is first calculated by solving the system of equilibrium equations Eqs. (4.165)-(4.168). This yields the OCP composition (that is, $A^{\rm OCP}$, $Z^{\rm OCP}$, and the nuclear radius $r_N^{\rm OCP}$), the OCP chemical potentials, as well as the neutron and electron densities, $n_{\rm gn} = n_{\rm gn}^{\rm OCP}$, $n_e = n_e^{\rm OCP}$, and:

$$\Delta\mu_n \equiv \Delta\mu_n^{\rm OCP} = \left(\frac{\partial F_i/\partial n_{\rm gn}}{V_{\rm WS} - V_N}\right)_{\rm OCP}, \tag{4.172}$$

$$\bar{P}_{\rm int} \equiv \bar{P}_{\rm int}^{\rm OCP} = \left(\frac{n_p^2}{Z}\frac{\partial F_{\rm Coul}}{\partial n_p}\right)_{\rm OCP}, \tag{4.173}$$

$$\bar{u}_{\rm f} \equiv \bar{u}_{\rm f}^{\rm OCP} = \left(\frac{V_{\rm f}}{V_{\rm WS}}\right)_{\rm OCP}. \tag{4.174}$$

With the latter five quantities as input, the ion distribution is obtained from Eq. (4.142), from which the normalized probabilities as a function of A and Z can be obtained, $p_j \equiv p_{AZ} = n_N^{(j)} / \sum_j n_N^{(j)}$.

As discussed in Sect. 4.2.4, the OCP and MCP results should coincide if, in addition, the non-linear mixing term coming from the translational free energy is set to zero. This is illustrated in Fig. 4.21, where the cluster radius r_N (blue lines), proton number Z (red lines), and mass number A (black lines) predicted by OCP (solid lines) are plotted as a function of the input baryon density, n_B, together with the MCP average (dashed lines) and most probable quantities (diamonds). For all the considered densities (from the neutron-drip up to the crust-core transition density) and temperatures, we can see that the most probable A, Z, and r_N coincide with the OCP solutions, and follow very closely the average values, implying that the distributions are centered around the OCP predictions.

This is further shown in Fig. 4.22, which displays the joint distributions of the cluster proton number Z and mass number A for the same temperatures as in Fig. 4.21 and for three selected densities, $n_B = 2 \times 10^{-3}$ fm^{-3} (green contours), $n_B = 10^{-2}$ fm^{-3} (orange

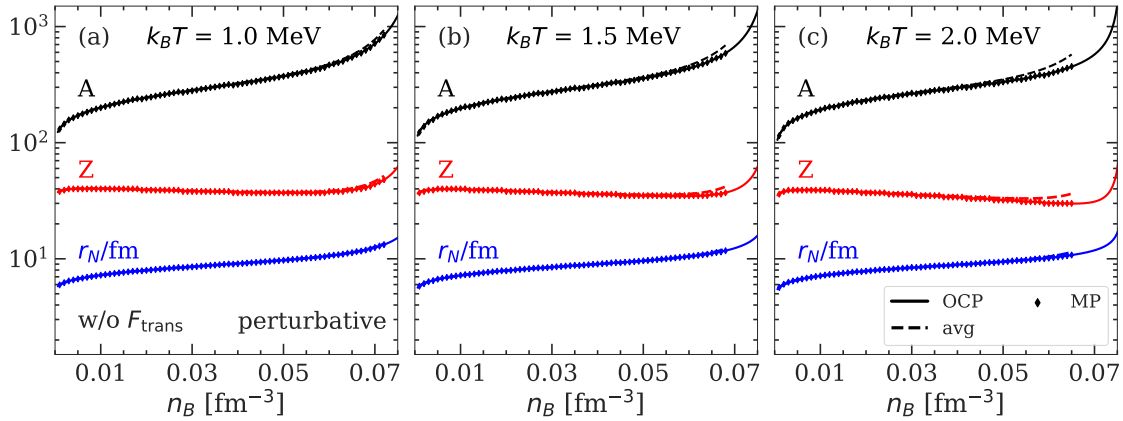

Figure 4.21: Cluster radius r_N (blue), proton number Z (red), and mass number A (black) as a function of the baryon density n_B at different temperatures: $k_BT = 1.0$ MeV (panel a), $k_BT = 1.5$ MeV (panel b), and $k_BT = 2.0$ MeV (panel c). OCP results are shown by full lines, while dashed lines and symbols correspond to the average and the most probable value of the cluster distribution in a perturbative MCP calculation. The translational free energy is not included in the calculations. Figure adapted from Ref. [269].

contours), and $n_B = 2 \times 10^{-2}$ fm^{-3} (blue contours). The distributions are, indeed, Gaussian-like, peaking at the OCP solutions (black stars). We can also observe that, while the proton number Z is relatively constant, the most probable mass number A increases with density, as already noticed in Refs. [79, 270]. Moreover, the width of the distributions gets broader with temperature and density, with lighter clusters being populated at higher T and n_B (see panel c), underlying the importance of considering a full nuclear ensemble instead of a single-nucleus (OCP) approach.

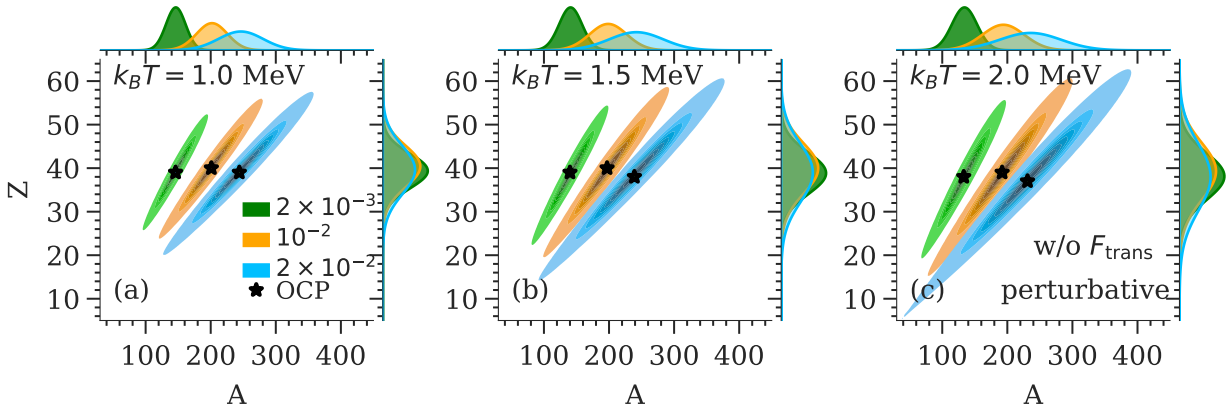

Figure 4.22: Joint distributions of the cluster proton number Z and mass number A for the same temperatures as Fig. 4.21 and for three selected input baryon densities: $n_B = 2 \times 10^{-3}$ fm^{-3} (green contours), $n_B = 10^{-2}$ fm^{-3} (orange contours), and $n_B = 2 \times 10^{-2}$ fm^{-3} (blue contours), in a perturbative MCP calculation. The black stars indicate the OCP solution. The translational free energy is not included in the calculations. Figure adapted from Ref. [269].

Due to the dependence of the cluster free energy on the electron gas density via the Coulomb screening term, the so-called rearrangement term, denoted by $\mathcal{R}^{(j)}$, appears, as in Eq. (4.135). This term is crucial in ensuring the thermodynamic consistency of the model.

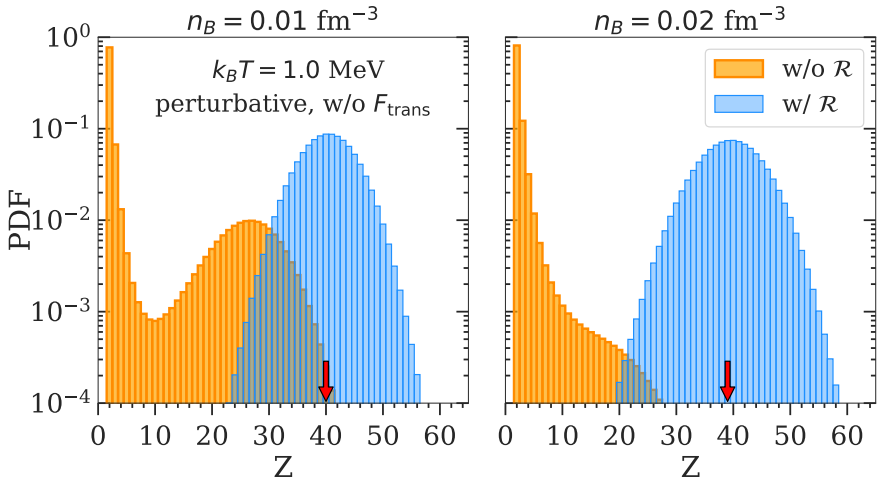

Figure 4.23: Probability density distribution of the proton number Z obtained with (blue) and without (orange) the rearrangement term at 1 MeV for two selected densities $n_B = 0.01$ fm^{-3} (left panel) and $n_B = 0.02$ fm^{-3} (right panel), in a perturbative MCP calculation. The arrows indicate the OCP solution. The translational free energy is not included in the calculations.

Moreover, in calculations where the chemical potentials are approximated by the OCP values, accounting for $\mathcal{R}^{(j)}$ is necessary to recover the ensemble equivalence between the MCP and OCP approaches (see e.g., Refs. [80,81,83,86,89]).This is shown in Fig. 4.23, where I plot the probability density distribution of the proton number Z at 1 MeV for two selected densities: $n_B = 0.01$ fm^{-3} (left panel) and $n_B = 0.02$ fm^{-3} (right panel). The blue (orange) histograms are obtained with (without) the rearrangment term, while the red arrows indicate the OCP solutions. We can see that the rearrangement term significantly impacts the distribution. Particularly, without $\mathcal{R}^{(j)}$, the Z distribution is shifted towards low-Z clusters. Moreover, the effect is more considerable at higher density.

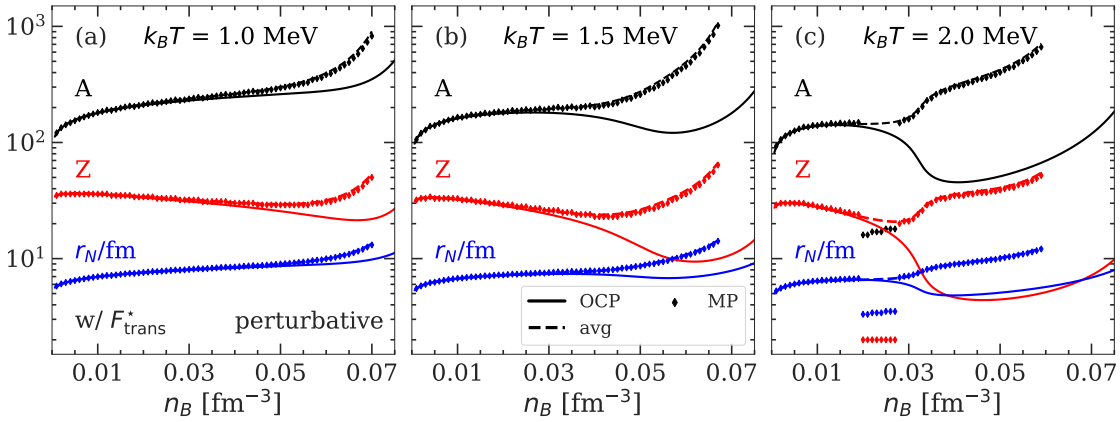

Figure 4.24: Same as in Fig. 4.21 but with the translational free energy, $F^\star_{\rm trans}$, included in both the OCP and perturbative MCP calculations.

Now, let us turn to discuss the influence of the non-linear mixing term, coming from the translational motion. Figure 4.24 shows the evolution with the baryon density of the cluster variables A, Z, and r_N, for the same conditions as in Fig. 4.21, but with the translational

free energy included in both the OCP and the MCP calculations, Eqs. (4.96) and (4.136), respectively. We can see that the different description of the center-of-mass motion induces a discrepancy in the prediction of the two approaches. Indeed, in the OCP approximation, the cluster moves in the reduced ("free") volume $V_{\rm f}^{\rm OCP}$, see Eqs. (4.96) and (4.155), associated to the single WS cell determined from the variational procedure, while in the MCP, clusters of different species are considered to move in the same macroscopic volume, leading to an average "free" volume $\langle V_{\rm f}\rangle$, see Eqs. (4.136) and (4.159). This correlation between the different ion species breaks the linear mixing rule. At lower temperatures (see panel a of Fig. 4.24), the deviation between the MCP and OCP prediction is negligible at densities below about 0.05 fm^{-3}, implying that the influence of the non-linear mixing term is not very important. On the other hand, from panels b and c of Fig. 4.24 we can see that, with increasing temperature, the discrepancy between the two approaches starts to become significant at progressively lower densities. This can be understood from the fact that the contribution of the translational free energy becomes more important at higher T and n_B, as discussed in Sect. 4.1. In particular, we can see that the distributions in the (perturbative) MCP are shifted to bigger clusters with respect to the OCP solution and that the crust-core transition occurs earlier. This is because Eq. (4.168), which yields small clusters in the OCP approximation (see Sect. 4.1), no longer holds in the MCP, as discussed in Sect. 4.2.4. In addition, the contribution of the translational free-energy term in the OCP approximation is more important than that in the MCP. Indeed, in the former, the free volume term is a variable entering the minimization process, whereas $\langle V_{\rm f}\rangle$ in the MCP is the common volume for all nuclear species. As a result, it does not affect the nuclear distribution, see Eqs. (4.143)-(4.144).

The discontinuous behavior of the most probable (A, Z) cluster in Fig. 4.24 is due to the fact that, as the temperature increases, the contribution of very light clusters, such as neutron-rich helium isotopes, becomes increasingly favored. This is shown in Fig. 4.25, which show the two-dimensional distribution of Z and A for different densities at 2.0 MeV. Indeed, we can see that the distribution has a double-peaked structure, and at $n_B = 0.02$ fm^{-3} (middle panel), the helium abundancy (slightly) overcomes the abundancy of the heavy cluster in the iron region predicted by the OCP. Still, it is also visible from Fig. 4.25 that the light-cluster contribution is limited to a small number of helium isotopes, while a large variety of nuclear species has a comparable probability around the $(A^{\rm OCP}, Z^{\rm OCP})$ value. Therefore, if we consider the probabilities of each element Z by integrating the distributions over the isotopic content (that is, over A), the (perturbative) MCP predictions appear in closer agreement with the OCP approximation, at least at relative low densities, as can be seen from Fig. 4.26.

The results presented in this section confirm that the non-linear mixing term induced by the translational energy leads to a breaking of the ensemble equivalence between the OCP and MCP predictions.

The perturbative MCP approach employed here has the clear advantage of computing the full nuclear distributions at a reduced computational cost. However, this approach is not fully self-consistent, because the gas densities and chemical potentials resulting from the OCP solutions might not exactly satisfy the constraints of baryon number conservation and charge neutrality in the MCP, Eqs. (4.128) and (4.129), respectively. For this reason, we have performed fully self-consistent MCP calculations, that are discussed in the next section.

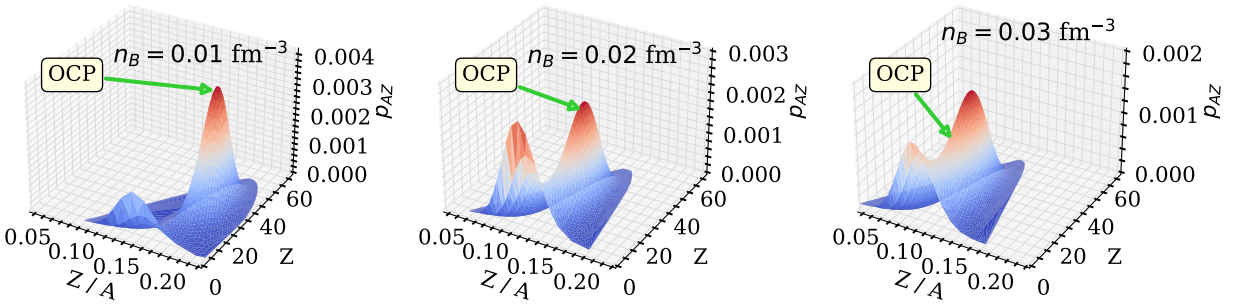

Figure 4.25: Normalized probability p_{AZ} in a perturbative MCP calculation, as a function of the cluster proton number Z and cluster proton fraction Z/A, obtained at temperature $k_BT = 2.0$ MeV for three different baryon densities: $n_B = 0.01$ fm^{-3} (left panel), $n_B = 0.02$ fm^{-3} (middle panel), and $n_B = 0.03$ fm^{-3} (right panel). The green arrow in each panel indicates the corresponding OCP solution. The translational free energy is included in both MCP and OCP. Figure adapted from Ref. [269].

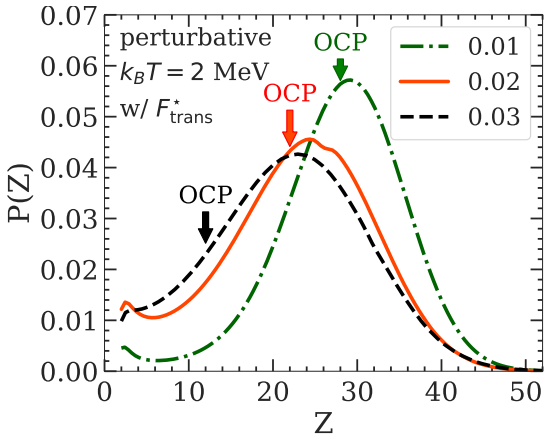

Figure 4.26: Normalized distributions as a function of Z, $P(Z) = \sum_A p_{AZ}$, where p_{AZ} are taken from Fig. 4.25. The legend gives three values of n_B in fm^{-3}. Figure reproduced from Ref. [269].

4.2.5.2 Self-consistent MCP calculations

In this section, I present the results obtained from the fully self-consistent MCP calculations. At each thermodynamic condition, the system of five equations given by Eqs. (4.128), (4.129), (4.134), (4.147), and (4.139), are solved simultaneously with the ion density $n_N^{(j)}$ given by Eq. (4.142), yielding n_{gn}, n_e, $\Delta\mu_n$, $\bar{P}_{\rm int}$, and $\bar{u}_{\rm f}$. The chemical potentials of neutrons, Eq. (4.132), and electrons $\mu_e = {\rm d}\mathcal{F}_e/{\rm d}n_e$ are calculated subsequently. In the following, the translational free energy term, Eq. (4.96) for OCP and Eq. (4.136) for MCP, is always included in the computation of the ion free energy.

In Fig. 4.27, I show the evolution with the baryon number density of the neutron chemical potential μ_n, Eq. (4.132) (panel a), the electron chemical potential potential $\mu_e = {\rm d}\mathcal{F}_e/{\rm d}n_e$ (panel b), the average free-volume fraction $\bar{u}_{\rm f}$, Eq. (4.139) (panel c), and the MCP interaction pressure $\bar{P}_{\rm int}$, Eq. (4.147) (panel d). All these quantities enter the computation of the ion abundances via Eq. (4.143). For illustrative purposes, the results are displayed for only one selected temperature, $k_{\rm B}T = 1.0$ MeV. The solutions from the MCP calculations are

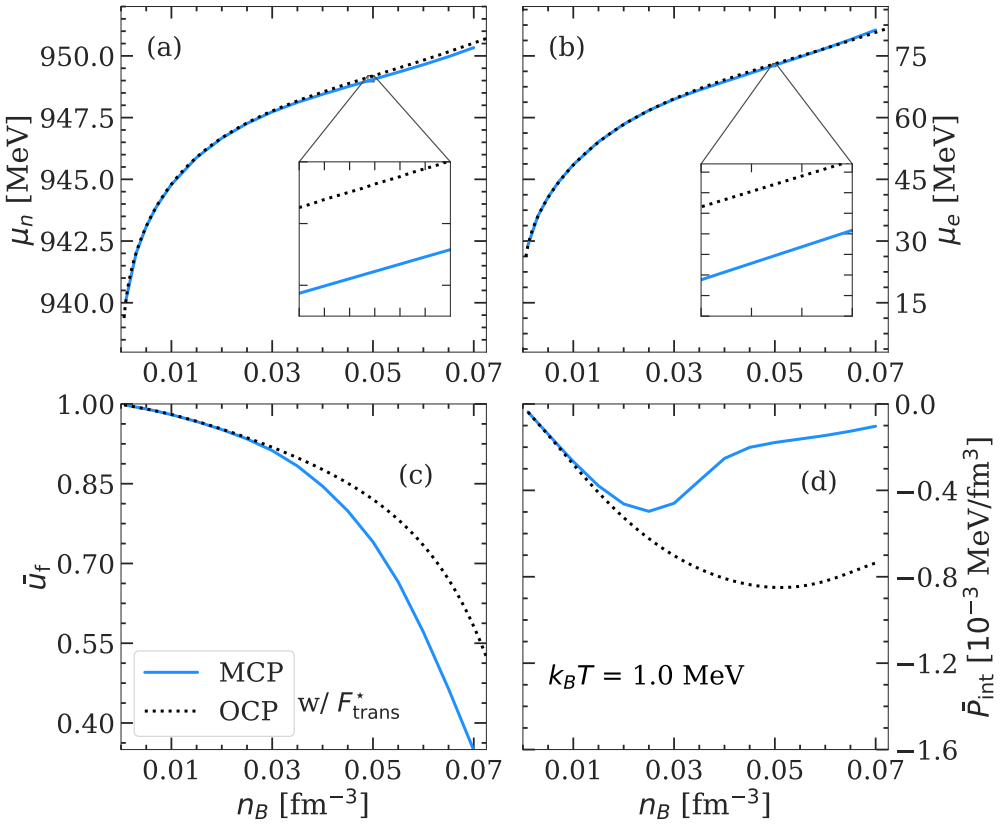

Figure 4.27: Self-consistent MCP solution (solid blue lines) for the neutron chemical potential μ_n (panel a), electron chemical potential μ_e (panel b), average free volume fraction $\bar{u}_f$ (panel c), and MCP interaction pressure $\bar{P}_{int}$ (panel d) as a function of the total baryon density n_B at $k_BT = 1$ MeV. The dotted black lines show the OCP predictions. The tick marks of the x and y axes in the insets of panel a and b are spaced by 2×10^{-4} fm^{-3} and 0.1 MeV, respectively. Figure adapted from Ref. [269].

shown by solid lines, while the dotted lines correspond to the values calculated at the OCP composition, that is, $\mu_n^{OCP}, \mu_e^{OCP}, \bar{u}_f^{OCP}$, and $\bar{P}_{int}^{OCP}$. As we can see from panels a and b, the chemical potentials in the MCP are very similar to those in the OCP approximation; indeed, the two curves are almost indistinguishable. However, from the inset in panel a, we can observe that the neutron chemical potential in the MCP is slightly lower than the OCP counterpart, suggesting that the corresponding gas density is not the same in the two approaches, and in particular that it is smaller in the MCP. The same trend is observed for the electron chemical potential (see panel b in Fig. 4.27), except at densities above 0.06 fm^{-3}, where μ_e calculated in the MCP is slightly above that obtained in the OCP approach, and therefore, the corresponding density is higher in the MCP. Even though the difference between the MCP and OCP chemical potentials is numerically small since these latter enter in the calculation of the ion abundances through the exponential, Eq. (4.142), it could still lead to a significant deviation between the MCP and OCP results, as already noticed in Ref. [82]. From panels c and d in Fig. 4.27, one can see that at relatively low baryon density, $n_B \lesssim 0.02$ fm^{-3}, $\bar{u}_f$ and $\bar{P}_{int}$ computed within the MCP are almost identical to those calculated in the

OCP approximation[8]. We, therefore, can expect that, at low densities and temperatures, the results shown in Fig. 4.24 be a good approximation. On the other hand, at higher densities, the absolute value of the interaction pressure, which directly enters in the computation of the rearrangement term, tends to zero in the MCP approach, while $|\bar{P}_{\rm int}^{\rm OCP}|$ increases. Since the latter is an input in the perturbative MCP, we can expect that the discrepancies between the perturbative and self-consistent MCP approaches would also become more pronounced at higher densities.

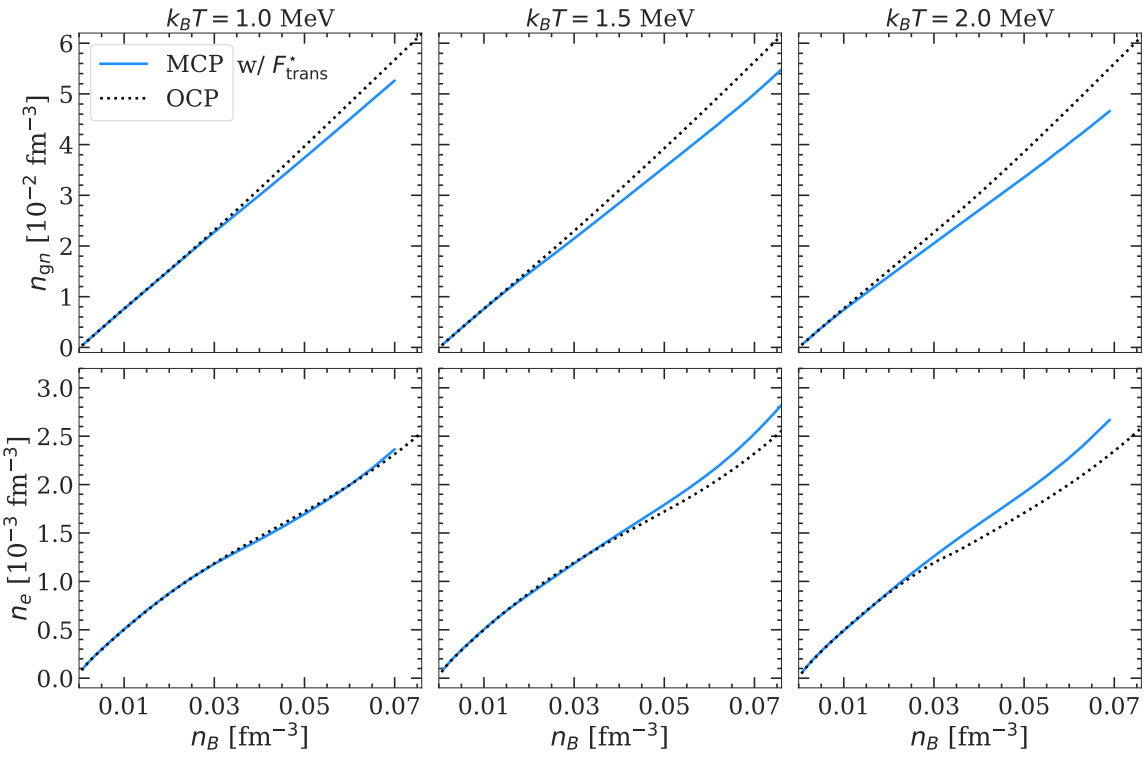

Figure 4.28: Neutron (upper panels) and electron (lower panels) gas densities as a function of the total baryonic density obtained in MCP (solid blue lines) and OCP (dotted black lines) for BSk24 at three different temperatures: $k_BT = 1.0$ MeV (left panels), $k_BT = 1.5$ MeV (middle panels), and $k_BT = 2.0$ MeV (right panels). Figure adapted from Ref. [298].

A complimentary comparison is shown in Fig. 4.28, which displays the densities of free neutrons (upper panels) and electrons (lower panels) as a function of n_B in the OCP (dotted black lines) and MCP (solid blue lines) at three selected temperatures: $k_BT = 1.0$ MeV (left panels), $k_BT = 1.5$ MeV (middle panels), and $k_BT = 2.0$ MeV (right panels). For all three temperatures considered, values of n_{gn} and n_e in MCP and OCP in the low-density region overlap. As the density and temperature increase, the discrepancy between the two approaches becomes larger. This can be understood as follows. At low (n_B, T), the nuclear distribution is narrow and symmetric, and the non-linear mixing term is negligible, as mentioned by Refs. [80–82]. Thus, the average quantities in MCP are close to those calculated assuming only one single nucleus, i.e., $\langle A\rangle \approx A^{\rm OCP}$, $\langle Z\rangle \approx Z^{\rm OCP}$, and $\langle V_{\rm WS}\rangle \approx V_{\rm WS}^{\rm OCP}$. Therefore, the charge neutrality and baryon number conservation constraints imply that

[8]One should notice that $\bar{u}_{\rm f}^{\rm OCP} = u_{\rm f} \equiv V_{\rm f}/V_{\rm WS} \neq V_{\rm f}^{\rm OCP}/V_{\rm WS}$ due to the different definitions of $V_{\rm f}$, see Eq. (4.160) and Eq. (4.155).

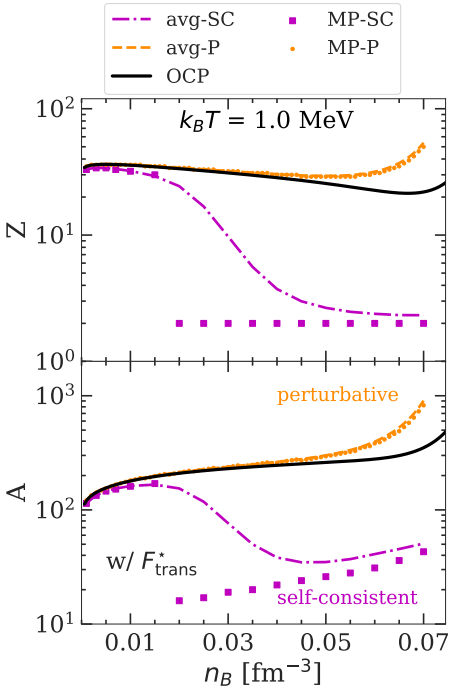

Figure 4.29: Average (dash-dotted violet lines) and most probable (violet squares) values of the cluster Z (upper panel) and A (lower panel) in the self-consistent (SC) MCP calculations as a function of the total baryon density n_B at $k_{\rm B}T = 1$ MeV. The OCP solutions (black solid lines), as well as the average (orange dashed lines) and most probable (orange dots) values in the perturbative (P) MCP are also plotted for comparison. Figure reproduced from Ref. [269].

the gas solutions in the two approaches coincide, and the ensemble equivalence is established. On the other hand, at higher densities and temperatures, the distributions are spread over wider ranges of A and Z, and multiple peaks with comparable probabilities may even emerge [82, 85, 87, 88]. As a consequence, the symmetric shape of the distributions is no longer guaranteed. Furthermore, the peak in MCP can be shifted with respect to the OCP solution because of the non-linear mixing term (see Sect. 4.2.5.1). As a result, $\langle A\rangle \neq A^{\rm OCP}$, $\langle Z\rangle \neq Z^{\rm OCP}$, and $\langle V_{\rm WS}\rangle \neq V_{\rm WS}^{\rm OCP}$, and the gas densities in the two approaches deviate. Interestingly, Fig. 4.28 also shows that the density of unbound neutrons in MCP is always lower than that in OCP (see upper panels). This reduction was also observed in other statistical studies, particularly, Ref. [84] (see their Table 3) and Ref. [82] (see their Figure 13). To be more specific, the former study was performed for core-collapse supernovae matter at a fixed proton fraction, while the latter was calculated for PNS crust at beta equilibrium. In addition, in Ref. [82], the authors showed that the depletion of free nucleons is due to the formation of light clusters. Thus, we can also expect to observe the presence of light nuclei in the MCP.

This is shown in Fig. 4.29 that displays the average (dash-dotted violet lines) and most probable (violet squares) values of Z (upper panel) and A (lower panel) in the self-consistent MCP calculation. These quantities are plotted as a function of n_B at $k_{\rm B}T = 1$ MeV, together with the OCP predictions (black solid lines) and the average (orange dashed lines) and most probable (orange dots) values obtained within the pertubative MCP procedure. Below

about 0.02 fm^{-3}, the results of the three different approaches coincide. However, as the density increases, the outcome of the different methods start to diverge, and therefore the pertubative MCP and OCP predictions become less reliable. These results confirm, on the one hand, the validity of these approximations at relatively low densities, while, on the other hand, highlight the importance of full MCP calculations in the deeper region in the PNS inner crust. We can see that, in the self-consistent MCP calculations, lighter nuclei dominate at high density, in agreement with previous works based on the nuclear statistical equilibrium (see, e.g., Refs. [82, 85]). Conversely, in the OCP and perturbative MCP approximations, heavier clusters survive until the crust-core transition.

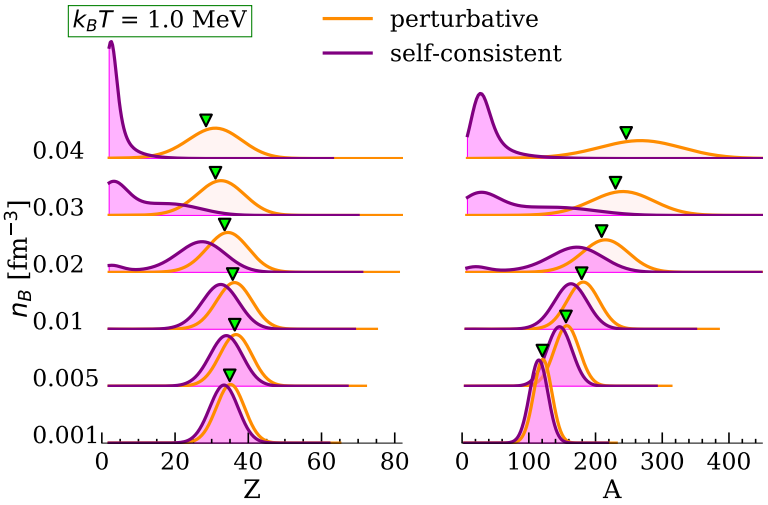

Figure 4.30: Normalized probability distributions of the cluster proton number Z (left panel) and mass number A (right panel) at $k_{\rm B}T = 1$ MeV for different baryon densities, $n_B \in [0.001, 0.04]$ fm^{-3}. The violet distributions are obtained from the self-consistent MCP calculations, while the orange ones correspond the perturbative MCP. The OCP solutions are marked by the green triangles. Figure reproduced from Ref. [269].

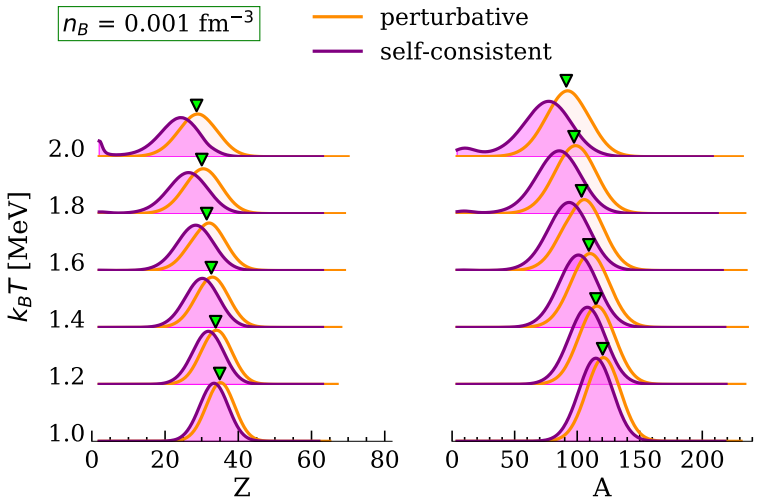

Figure 4.31: Same as Fig. 4.30, but at a fixed baryon density $n_B = 0.001$ fm^{-3} and for different temperatures, $k_{\rm B}T \in [1.0, 2.0]$ MeV.

In order to further investigate this point, I show in Fig. 4.30 the normalized distributions of the cluster proton number Z (left panel) and mass number A (right panel) at different densities in the inner crust, $n_B \in [0.001, 0.04]$ fm^{-3} at $k_{\rm B}T = 1.0$ MeV, for both the self-consistent MCP calculations (violet areas) and the perturbative MCP ones (orange areas). As one may expect, at lower densities, the distributions obtained in the two approaches are almost identical; they are narrow and peaked at the OCP predictions (green triangles). Therefore, employing a perturbative MCP, where the gas variables are fixed from the OCP solution, is a very good approximation in these thermodynamic conditions. As the density increases, at $n_B \approx 0.02 - 0.03$ fm^{-3} the self-consistent MCP distributions are displaced towards lower values of A and Z and even exhibit a double-peaked structure, meaning that lighter clusters co-exist with heavier ones, and their contribution becomes important. In these regimes the OCP and perturbative MCP predictions significantly overestimate the cluster mass and proton number. Eventually, at the bottom of the crust, nuclei with $Z < 5$ and $A < 50$ may even dominate, with Helium being the most probable element, although the tails of the distributions extend up to $Z \simeq 50$ and $A \simeq 400$, implying that heavier nuclei may still be present near the crust-core transition.

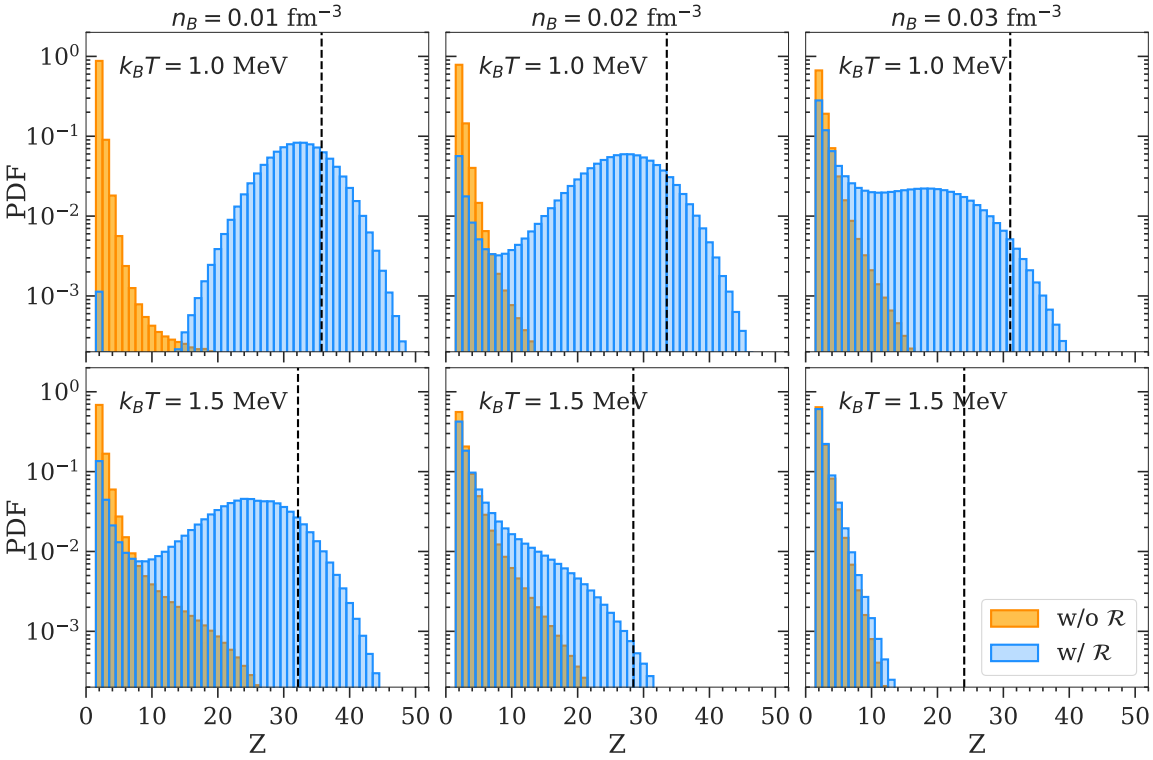

Figure 4.32: Probability density distribution of the ion proton number Z obtained with (blue) and without (orange) including the rearrangement term. Three different densities are considered: $n_B = 0.01$ fm^{-3} (left panels), $n_B = 0.02$ fm^{-3} (middle panels), and $n_B = 0.03$ fm^{-3} (right panels). At each density, the distributions are obtained at two chosen temperatures: $k_BT = 1.0$ MeV (upper panel) and $k_BT = 1.5$ MeV (lower panel). The vertical dashed black line in each panel indicates the OCP solution. The gas densities and chemical potentials are obtained from the self-consistent MCP calculation with the rearrangement term. Figure adapted from Ref. [298].

In order to study the dependence of the results on the temperature, in Fig. 4.31, I show the

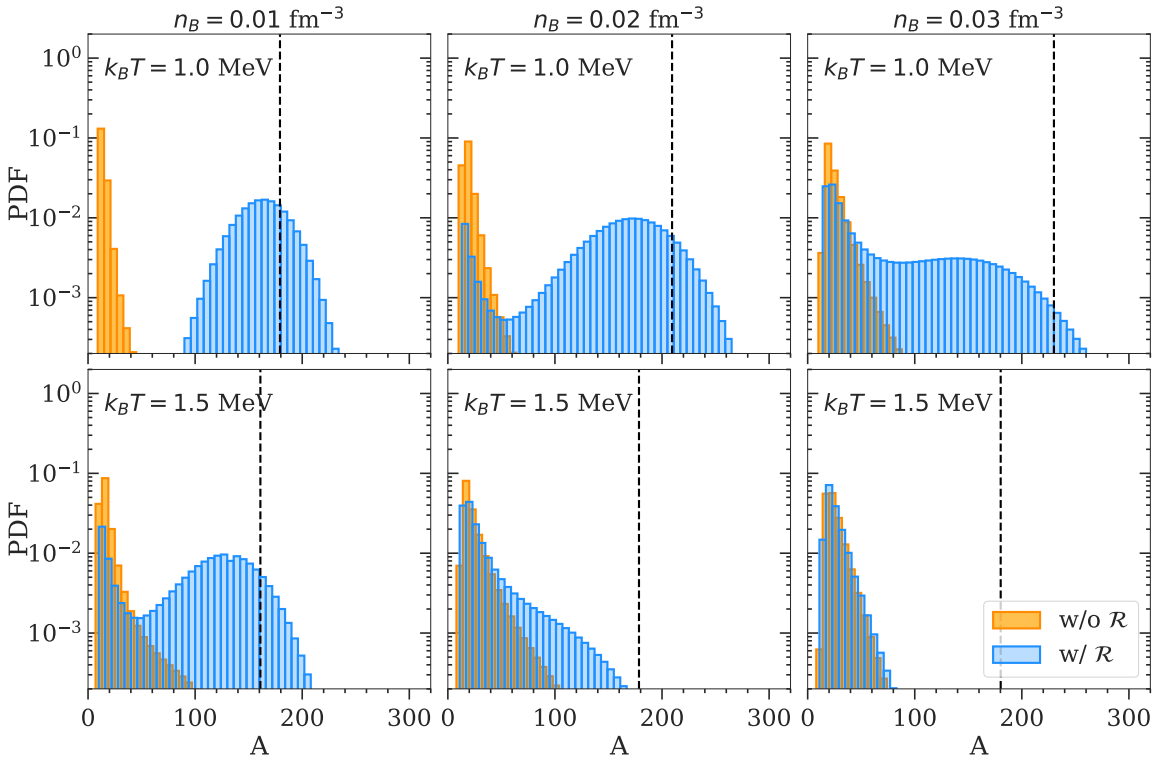

Figure 4.33: Same as Fig. 4.32 but for the ion mass number A. See text for details.

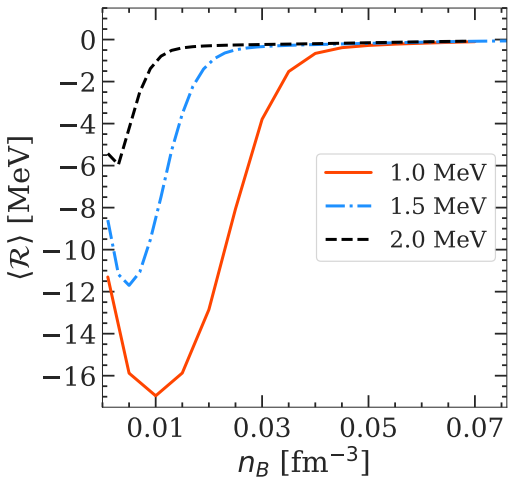

Figure 4.34: Average value of the rearrangement term $\langle\mathcal{R}\rangle$ in the fully self-consistent MCP as a function of the total baryonic density n_B at three different temperatures: $k_BT = 1.0$ MeV (solid red line), $k_BT = 1.5$ MeV (dash-dotted blue line), and $k_BT = 2.0$ MeV (dashed black line). Figure reproduced from Ref. [298].

distributions of Z (left panel) and A (right panel) at $n_B = 0.001$ fm^{-3} in the aforementioned temperature range. As in Fig. 4.30, the results from both the self-consistent MCP calculations (violet areas) and the perturbative MCP ones (orange areas) are displayed and compared with the OCP solutions (green triangles). At lower temperatures, the distribution peaks coincide with the OCP predictions. However, as the temperature increases, more nuclear species are populated, and therefore the distributions flatten and the OCP prediction tends

to overestimate the cluster size. At higher temperatures, $k_{\rm B}T \geq 1.8$ MeV, small clusters start to appear. At 2 MeV, the double-peak structure already observed at high density is clearly visible in the self-consistent MCP calculations, while it is not the case in the perturbative MCP results. Nevertheless, the deviation between the predictions of the two approaches is not as significant as in Fig. 4.30, which suggests that the effect of the density overcomes that on the temperature as far as the resulting distributions are concerned.

To evaluate the importance of the rearrangement term, Eq. (4.145), at the same gas densities and chemical potentials as obtained in the self-consistent MCP (Fig. 4.28), in Figs. 4.32 and 4.33, I display with the blue (orange) histograms the nuclear distributions obtained with (without) $\mathcal{R}^{(j)}$. We can easily see that the impact of this term on the MCP distributions is non-negligible, especially at lower densities and temperatures. Specifically, the distributions without $\mathcal{R}^{(j)}$ (orange) are very much shifted to low Z and A, while the correct distributions are peaked around heavier nuclei (see left panels). Nevertheless, at higher densities and temperatures, where the nuclear distribution is dominated by light degrees of freedom, the effect from $\mathcal{R}^{(j)}$ can be neglected. This is because the rearrangement term, defined in Eq. (4.145), is proportional to the WS volume and the interaction pressure from the Coulomb interaction. When the light clusters are present and dominant in the crust, the associated WS cell volume as well as Coulomb interaction magnitude decrease. As a result, the rearrangement term in this region becomes small, hence not affecting the nuclear distribution. The effect of the rearrangement term in the self-consistent MCP is opposite to that of the perturbative MCP, as shown in Fig. 4.23 and in Ref. [83], in which the effect is larger at higher densities and temperatures.

To elaborate on this point, in Fig. 4.34, I plot the average value of the rearrangement term, $\langle \mathcal{R} \rangle = \langle V_{\rm WS} \rangle \bar{P}_{\rm int}$, as a function of densities for three selected temperatures: $k_B T = 1.0$ MeV (solid red line), $k_B T = 1.5$ MeV (dash-dotted blue line), and $k_B T = 2.0$ MeV (dashed black line). From this figure, we can observe that the absolute value of the rearrangement term decreases with temperature. Moreover, at 1 MeV, $\langle \mathcal{R} \rangle$ is most negative when $n_B = 0.01$ fm^{-3}, and it approaches to zero as the density increases. We should keep in mind that the impact from $\mathcal{R}^{(j)}$ depends on its relative contribution with respect to other terms in $\tilde{\Omega}_i^{(j)}$, see Eq. (4.143), and not on the absolute value. Nevertheless, when $\langle \mathcal{R} \rangle \sim 0$, as it is the case for $k_B T = 1.5$ MeV and $n_B = 0.03$ fm^{-3}, we can safely conclude that the rearrangement term does not play any role in the nuclear distribution. Indeed, this is shown in the bottom right panels of Figs. 4.32 and 4.33.

The results presented in Figs. 4.29-4.31 show that even for temperature as low as 1 MeV, the OCP approximation is no longer reliable in the deepest region of the crust. Therefore, for studies requiring an accurate knowledge of the crust composition, a full MCP calculation is needed. However, the effect is less important as far as more global properties like EOS are concerned. This is illustrated in Fig. 4.35, which present the total pressure (Eq. (4.154)) versus the mass-energy density in the PNS inner crust, for three different temperatures, $k_{\rm B}T = 1$ MeV (red lines), 1.5 MeV (blue lines), and 2 MeV (black lines), for both the MCP (solid lines) and the OCP approximation (dotted lines). Indeed, at $k_{\rm B}T = 1$ MeV, the EOS provided within the self-consistent MCP approach and the OCP approximation are very similar at all densities. At higher temperatures, deviations between the two calculations start

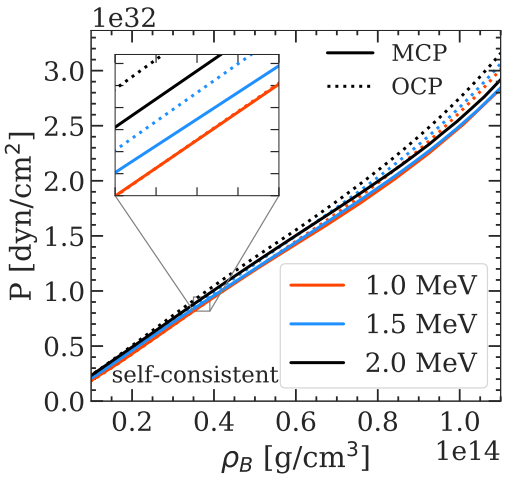

Figure 4.35: Total pressure as a function of mass-energy density ρ_B resulting from the self-consistent MCP calculations (solid lines) at $k_{\rm B}T = 1$ MeV (red lines), 1.5 MeV (blue lines), and 2 MeV (black lines). For comparison, the OCP results are plotted with dotted lines. In the inset, the tick marks on the x and y axis are spaced by 10^{12} g/cm^3 and 2×10^{30} dyn/cm^2, respectively. Figure reproduced from Ref. [269].

to emerge, particularly at high densities. However, these discrepancies amount to $\sim 10\%$ at most in the vicinity of the crust-core transition.

4.2.5.3 Impurity parameter

Many different astrophysical phenomena, such as NS cooling, timing evolution, and accretion, are determined by the transport properties, such as thermal and electrical conductivities, of the crust [251, 299–303]. As electrons act as the primary carriers governing these transport processes, an accurate understanding of electron-ion scattering is essential for determining the crustal transport properties, see e.g., Ref. [251] for a review. Since the crust could cease to be in strong and weak equilibrium at the crystallization temperature T_m or even above depending on the cooling timescales[9], as suggested by Refs. [303, 304], the final composition of the crust could be established at $T \sim T_m$. As a consequence, the lattice is imperfect, and the electron-impurity scattering needs to be taken into account [251, 302, 303]. If the impurities in the solid are weakly correlated, the collision frequency can be split into the sum of the electron-phonon and the electron-impurity scattering contributions according to the Matthiessen's rule [251, 301, 305], i.e., $\nu = \nu_{\rm e-ph} + \nu_{\rm e-imp}$. Particularly, the influence of electron-impurity scattering on the thermal and electrical conductivities can be quantified by the impurity parameter, defined as the variance of the Z distribution [303, 305],

$$Q_{\rm imp} = \langle Z^2 \rangle - \langle Z \rangle^2 \ . \tag{4.175}$$

Nevertheless, it is worth mentioning that the applicability of this splitting rule could be questionable for the case of very large $Q_{\rm imp}$ [301].

In the literature, the presence of impurities is commonly linked to the pasta phases, as they have been observed in molecular dynamics simulations performed at high temperatures, high densities near the crust-core transition, and with a high proton fraction. Particularly,

[9]The timescales are such that thermal equilibrium is always granted.

these studies suggest that $Q_{\rm imp}$ can be of the order of 30-100 [86, 238, 306]. However, it is important to emphasize that the thermodynamic conditions examined in the mentioned works do not align with those encountered in the crust of a NS.

In the calculations of magneto-thermal and timing evolution of NS [55, 56], the value of $Q_{\rm imp}$ as a function of the density is taken as a free parameter. Within our MCP approach, it is possible to self-consistently calculate the impurity parameter for the entire inner crust. Values of $Q_{\rm imp}$ for three temperatures, $k_{\rm B}T = 1.0$ MeV (red lines), $k_{\rm B}T = 1.5$ MeV (blue lines), and $k_{\rm B}T = 2.0$ MeV (black lines) are plotted in Fig. 4.36. Results obtained with the self-consistent (perturbative) MCP calculations are shown as a function of the input baryon density in the crust by solid (dash-dotted) lines. At the lower temperature, $k_{\rm B}T = 1.0$ MeV (red lines), the predictions from the two treatments coincide at lower densities, until $n_B \approx 0.01$ fm^{-3}. With increasing density, the impurity parameter is, at first, larger in the self-consistent MCP approach with respect to the perturbative one. However, at variance with the perturbative MCP predictions, $Q_{\rm imp}$ does not increase monotonically in the self-consistent calculations, but peaks around $n_B \approx 0.025$ fm^{-3}, reaching $Q_{\rm imp} \approx 100$ for the considered BSk24 model, and subsequently decreases at higher densities. A similar behavior is observed for higher temperatures, although the discrepancy between the two treatments and the peak in the impurity parameter appear at smaller densities. This can be understood from the Z distributions shown in the left panel of Figs. 4.30-4.31. Indeed, while the presence of the second peak at small Z for moderate densities increases the variance of Z, the transition to light nuclei at high densities overall decreases the value of the impurity parameter. These findings also show that the impurity parameter calculated within the perturbative MCP approach is underestimated at low densities, and severely overestimated at high densities.

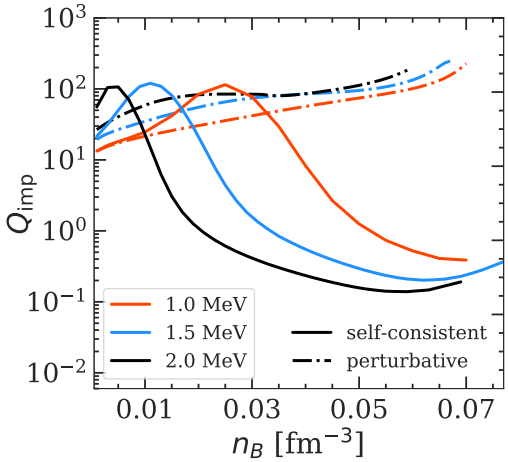

Figure 4.36: Impurity parameter $Q_{\rm imp}$ as a function of the baryon density n_B in the inner crust for $k_{\rm B}T = 1.0$ MeV (red), $k_{\rm B}T = 1.5$ MeV (blue), and $k_{\rm B}T = 2.0$ MeV (black) in the self-consistent MCP calculation (solid lines) in comparison with the results obtained with the perturbative MCP (dash-dotted lines). Figure reproduced from Ref. [269].

In the cooling process of a NS, it is reasonable to suppose the crust composition to be frozen after the solidification of the crust. Neutron absorption or β-decays might still occur at lower temperatures, but pycnonuclear reactions that involve overcoming a Coulomb barrier might

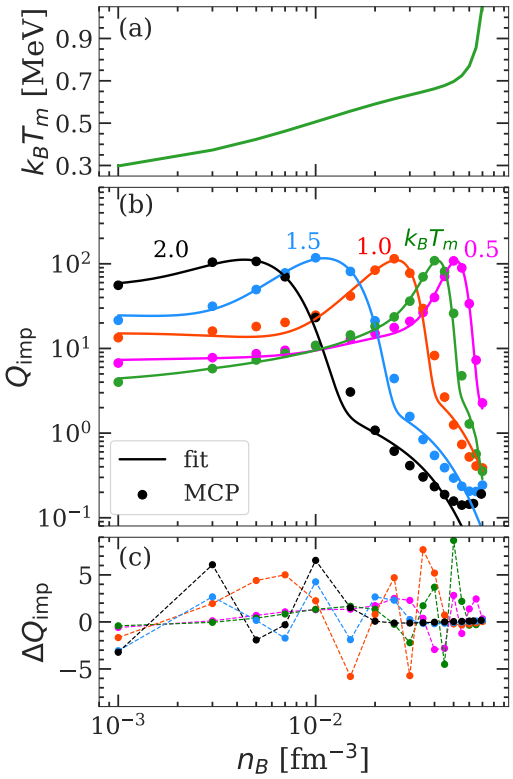

Figure 4.37: Panel a: Crystallization temperature $k_{\rm B}T_{\rm m}$ calculated using Eq. (4.176) as a function of the baryon density n_B. Panel b: Impurity parameter $Q_{\rm imp}$ in the fully self-consistent MCP calculation as a function of n_B evaluated at the crystallization temperature $k_{\rm B}T_{\rm m}$ (green points) and at four fixed temperatures: $k_{\rm B}T = 0.5$ MeV (magenta points), $k_{\rm B}T = 1.0$ MeV (red points), $k_{\rm B}T = 1.5$ MeV (blue points), and $k_{\rm B}T = 2.0$ MeV (black points). Solid lines are obtained from the fit given by Eq. (4.177). Panel c: Error in the fitting formula ($\Delta Q_{\rm imp}$ = calculated $Q_{\rm imp}$ - fit). Figure reproduced from Ref. [269].

be considerably inhibited even above crystallization. A realistic estimate of the temperature at which the ion distribution is frozen and the impurity parameter is settled, would require a comparison between the cooling time and the different reaction rates, which is beyond the scope of the present study. As a reasonable estimate, the impurity parameter of the solid crust can be computed from that obtained at the crystallization temperature of a pure Coulomb plasma [1]:

$$T_{\rm m} \approx \frac{Z^2 e^2}{k_{\rm B} r_{\rm WS} \Gamma_{\rm m}}, \tag{4.176}$$

where Z and $r_{\rm WS}$ correspond to the ground-state composition at zero temperature, and $\Gamma_{\rm m} \approx 175$ is the Coulomb coupling parameter at the melting point. It is interesting to observe that this simple expression was shown in Ref. [79] (see their Fig. 4) to give a good order-of-magnitude estimate of the temperature where the OCP free-energy densities in the liquid equate those of the solid phase.

Values of $k_{\rm B}T_{\rm m}$ from Eq. (4.176) are displayed in panel a of Fig. 4.37: $k_{\rm B}T_{\rm m}$ increases monotonically from ~ 0.3 MeV at $n_B = 10^{-3}$ fm^{-3} to ~ 1.0 MeV at $n_B = 0.07$ fm^{-3} (see also Fig. 4 in Ref. [79]). The corresponding evolution of the impurity parameter in the fully self-consistent MCP calculations at the crystallization point as a function of the baryon density

in the inner crust is shown with green points in panel b of Fig. 4.37. We can see that a high impurity parameter $10 \lesssim Q_{\rm imp} \lesssim 100$ should be expected in the whole inner crust, which could have important consequences in the magneto-thermal evolution of X-ray pulsars, see Refs. [56, 237, 249].

For comparison, I also plot $Q_{\rm imp}$ for four different selected temperatures: $k_{\rm B}T = 0.5$ MeV (magenta points), $k_{\rm B}T = 1.0$ MeV (red points), $k_{\rm B}T = 1.5$ MeV (blue points), and $k_{\rm B}T = 2.0$ MeV (black points). We can see that the general behavior of $Q_{\rm imp}$ is similar for all temperatures, that is, all curves show a peak and a subsequent drop. Indeed, even at a relatively low temperature, $k_{\rm B}T = 0.5$ MeV, $Q_{\rm imp}$ is still reduced at high densities, $n_B \approx 0.06$ fm^{-3}, indicating that the charge distribution is dominated by small Z. Moreover, as expected, a higher $Q_{\rm imp}$ is obtained if the composition is frozen at higher temperatures, but the sharp drop occurs at lower density because of the appearance of light nuclei (see also Figs. 4.30-4.31). However, our results should be considered with care at high densities, because non-spherical pasta structures, which are not considered in the present paper, could appear. Such structures are also expected to be associated with high impurity parameters $Q_{\rm imp} \sim 30$, see Refs. [238, 307]. Also, the CLD description can be questioned for light clusters and a more microscopic treatment of the in-medium modifications might be needed, see Refs. [308] and [309].

Table 4.3: Impurity parameter $Q_{\rm imp}$ in the inner crust for different temperatures. The results are obtained with the fully self-consistent MCP calculation. Table reproduced from Ref. [269].

Density	Temperature (MeV)				
(fm^{-3})	0.5	$k_{\rm B}T_{\rm m}$	1.0	1.5	2.0
0.001	6.73	4.00	13.41	21.52	55.75
0.005	8.67	7.31	18.16	49.65	106.76
0.010	10.74	10.88	24.69	117.81	23.21
0.015	12.85	14.42	41.62	81.21	3.06
0.020	15.02	18.27	84.15	21.20	1.08
0.025	17.68	23.58	114.79	4.41	0.61
0.030	20.89	36.22	77.58	1.57	0.41
0.035	26.62	70.06	29.61	0.84	0.30
0.040	40.09	108.84	8.26	0.54	0.23
0.045	71.04	81.13	2.67	0.39	0.19
0.050	108.29	25.97	1.25	0.29	0.16
0.055	89.51	4.76	0.74	0.24	0.14
0.060	33.78	1.28	0.52	0.21	0.14
0.065	7.29	0.57	0.41	0.20	0.16
0.070	2.27	0.35	0.39	0.24	0.19

The results for the impurity parameters shown in Fig. 4.37 are given in Table 4.3 and will be publicly available to the astrophysics community for implementation in NS simulations. For practical applications to numerical simulations, we also provide a fitting formula,

$$Q_{\rm imp} = \exp\left(a_0 + \sum_{k=0}^{4} x_B^k \sum_{j=1}^{3} a_{kj} x_T^j\right) + \Delta Q \tag{4.177}$$

where $x_B \equiv n_B/{\rm fm}^{-3}$, $x_T \equiv k_{\rm B}T/{\rm MeV}$, $a_0 = 3.328$, a_{kj} are given in Table 4.4, and the

Table 4.4: Fitting parameters a_{kj} in Eq. (4.177) for the impurity parameter. Table reproduced from Ref. [269].

a_{kj}	$j=1$	$j=2$	$j=3$
$k=0$	-2.285×10^{1}	2.205×10^{1}	-5.370
$k=1$	1.818×10^{3}	-1.087×10^{3}	2.000×10^{2}
$k=2$	-9.456×10^{4}	6.849×10^{4}	-2.673×10^{4}
$k=3$	1.730×10^{6}	-5.766×10^{5}	4.969×10^{5}
$k=4$	-1.161×10^{7}	6.356×10^{6}	-1.666×10^{7}

function ΔQ reads:

$$\Delta Q = \frac{f_0\ x_T\ (x_{BT}(n_B,T))^{f_1}}{[(x_{BT}(n_B,T)/f_2+f_3)^4+f_4]\,f(n_B,T)}, \tag{4.178}$$

with $f_0 = 65.55$, $f_1 = 9.046\times10^{-2}$, $f_2 = -6.324$, $f_3 = -1.087\times10^{-2}$, $f_4 = 4.802$. The variable x_{BT} in Eq. (4.178) depends on both n_B and T and is defined as:

$$x_{BT}(n_B,T) \equiv (5+\log_{10} x_B)^2\, x_T\ , \tag{4.179}$$

while $f(n_B,T)$ is given by

$$f(n_B,T) = 1 + x_B x_T^{3/2} \exp\left(\frac{200}{3}x_B - \frac{1}{4}\right). \tag{4.180}$$

The impurity parameter calculated at different temperatures with the fitting expression Eq. (4.177) is shown by solid lines in panel b of Fig. 4.37, while the error with respect to the computed values of $Q_{\rm imp}$ in the MCP approach is displayed in panel c. We can see that the error remains relatively small, $|\Delta Q_{\rm imp}| \approx 5$ at most, in the whole inner-crust density range. Indeed, even if the fit tends to break down at higher densities and higher temperatures (see black and blue lines in panel b of Fig. 4.37 for $n_B \gtrsim 0.05$ fm^{-3}), the error remains very small because of the low values of $Q_{\rm imp} \approx 0.1-0.2$.

4.3 Conclusions

In this chapter, I have focused mainly on studying the properties of the PNS inner crust in late PNS cooling stages, after tens of seconds from the birth of the hot PNS, where the star is expected to cool to a few 10^{10} K, and beta-equilibrium is assumed to hold. At such temperatures, the crust is expected to be in the liquid phase, and the translational free energy of clusters needs to be considered. To describe the cluster energetics, a CLDM approach is employed, in which the nuclear matter quantities are calculated from finite-temperature mean-field thermodynamics with the BSk24 functional, and the surface parameters are optimized consistently with the bulk energy from the fit to the experimental nuclear masses in the AME2016 table.

The first part of the chapter was devoted to analyzing the influence of the translational degrees of freedom in the liquid phase on the properties of finite-temperature ultra-dense stellar matter in the one-component plasma approximation, where the crust is supposed to be

composed of identical WS cells. To this aim, different expressions were derived analytically for the effective mass of the ion modeled with a constant density profile and moving in a uniform nucleon background using a hydrodynamical approach with different boundary conditions. This renormalization of the ion mass to account for the in-medium effects was then included in the translational free energy contribution of the ion energetics. For each given thermodynamic condition, the crust composition was calculated using the standard variational minimization of the total free energy density. It was shown that the cluster size is determined by the competition between the motion of the center-of-mass of the ion and the interface properties, namely, the Coulomb, surface, and curvature energies. Within the temperature range considered in this work (few 10^{10} K), the interface terms favor large clusters constituted of more than ≈ 100 nucleons, while the entropy gain associated to the translational motion is maximal for a gas-like composition of very small ions. Consequently, including the translational free energy in the variational theory can significantly reduce the number of nucleons in the clusters, especially at high temperatures. However, the importance of this effect varies with the scenario. In particular, at beta equilibrium, considering the ions as an ideal gas, the inclusion of the translational free energy leads to a drastic reduction of the cluster proton and mass numbers already at temperatures as low as the crystallization temperature. This implies an early dissolution of clusters in the dense medium, hence a very low crust-core transition density. If one includes the corrections from the cluster size and the in-medium modification considering that only neutrons in the continuum states participate in the flow, then the composition is still modified by the translational motion, but the effect is less drastic than the ideal-gas case. This result, therefore, is important, because the translational degrees of freedom are typically neglected in the literature when modeling the finite-temperature crust for NS cooling simulations. This unexpected influence of the translational entropy on the composition of matter is due to the fact that, in beta equilibrium, the proton fraction at high densities is very small, and the contribution from the Coulomb, surface, and curvature energies does not dominate the translational contribution. Conversely, if the total proton fraction is of the order of 0.2 or more, as typically found in supernova matter, the finite-size energies dominate, and the crust composition is less affected. Indeed, even at temperatures as high as $k_{\mathrm{B}}T = 4$ MeV, heavy clusters are still favored close to the transition to homogeneous matter. In supernova matter, neglecting the translational contribution in the variational treatment, as is done for instance in the popular EOS by Ref. [90], therefore appears to be justified. For both cases, the impacts of the translational degrees of freedom on the EOS is negligible.

The coexistence of different nuclear species in beta equilibrium was investigated in the second part of the chapter, where the calculations were performed employing both a perturbative MCP treatment, with the chemical potentials and gas densities being taken from the OCP calculations, and a fully self-consistent MCP approach. It was shown that, if non-linear mixing terms arising from the center-of-mass motion of the ion are neglected, the most probable clusters in the MCP (perturbative) approach coincide with the OCP predictions throughout the whole inner crust at all considered temperatures. However, as already discussed in Sect. 4.1, this translational free energy term should be taken into account in the calculations of the (liquid) inner-crust composition, leading to a breaking in the ensemble

equivalence. The outcomes also show that the OCP and the perturbative MCP treatments are a good approximation at relatively low densities and temperatures, especially as far as global properties like the EOS are concerned. However, a full self-consistent MCP is needed, particularly in the deeper region of the crust, for reliable predictions of the PNS crust composition. Moreover, the results reveal that, with increasing density and temperature, the abundance of light nuclei becomes important, and eventually dominates the whole distribution. This result has an important effect on the calculation of the impurity parameter, thus potentially on the NS cooling. Despite the discrepancy in the composition predicted in MCP and OCP, overall, the EOS in these two approaches are in good agreement. In general, the pressure in MCP is lower than the OCP counterpart, but the effect is only noticeable in the innermost region and at very high temperatures.

In this study, only spherical clusters were considered. However, non-spherical structures like the so-called nuclear pasta phases may appear at the bottom of the inner crust, and the coexistence of different (non-spherical) structures deserves further study.

CHAPTER 5

Summary and Outlook

The purpose of this thesis is to study the interior structure of (proto-)NS as well as the connections to their observables. To this aim, the nuclear matter properties are characterized within the meta-modeling technique [64, 65], and the inhomogeneities in the crust are described using a compressible liquid drop model. The results in this thesis can be divided into different topics corresponding to different chapters, addressing various topics in NS studies: unified nucleonic EOS of cold–catalyzed neutron stars (Chapter 2), pasta phases in cold–catalyzed neutron stars (Chapter 3), and proto-neutron star inner crust in the liquid phase (Chapter 4).

Chapter 2 starts with the formalism of nuclear matter properties in the meta-modeling approach. First, I verified that the meta-modeling approach can reproduce satisfactorily different non-relativistic and relativistic nucleonic models if the Taylor expansion is truncated at the fourth order, confirming the analysis of Refs. [64, 65]. On top of that, using a large set of functionals, I showed that for symmetric nuclear matter they agree well up to the saturation density, whereas the dispersion becomes larger at higher densities and isopins. Consequently, the core composition, which is obtained in beta equilibrium and within the nucleonic hypothesis, exhibits strong model dependence. To describe the crust, the bulk energy is complemented by the Coulomb, surface, and curvature terms. In particular, the Coulomb energy accounts for the electrostatic interaction in the WS approximation and can be derived analytically. For the surface and curvature tensions, we employed the parameterization from Ref. [133], which is based on Thomas-Fermi calculations at extreme isospin asymmetries and characterized by five surface parameters, $(\sigma_0, \sigma_{0,c}, b_s, \beta, p)$. These parameters were optimized to reproduce the experimental nuclear binding energies in the AME2016 table [135]. Except for light nuclei, the χ^2-fit for the surface parameters was shown to perform well for different functionals, with a relative error of $\sim 1\%$. Nevertheless, since the parameters b_s and p are mostly related to isovector properties of matter, they cannot be constrained very well by experimental nuclear data, leading to significant uncertainties in the inner-crust properties. At each given thermodynamic condition, defined by the total baryonic density, the composition of the crust was obtained using a variational method. Then, a unified EOS was constructed

and used as input to solve TOV equations. In order to assess the uncertainties in our predictions for NS properties, we performed a Bayesian inference, in which the ranges of the empirical parameters in the prior distribution were chosen based on the current knowledge from nuclear physics. In this analysis, the likelihoods were taken from the chiral EFT calculation [110] as well as the updated data from NS observations, i.e., the mass measurement from radio timing by Ref. [31], tidal deformability inferred from the GW170817 event [39–42], and mass-radius distributions provided by the NICER collaboration [35–38]. It is important to emphasize that, in this analysis, we only considered the nucleonic hypothesis, where the baryonic matter in the core is purely constituted of neutrons and protons without any phase transition or other hadronic degrees of freedom. With this Bayesian study, we demonstrated that the information from nuclear physics constrains the EOS at low densities, hence the crustal properties of NS. On the other hand, the data from NS observations constrain the EOS at high densities and therefore determine NS global properties, such as mass, radius, and tidal deformability. Furthermore, the nuclear matter properties compatible with nuclear theory and experiments as well as astrophysical data were also extracted. In addition, the results of this Bayesian study also suggest that the nucleonic hypothesis can reproduce all current data from NS observations. Nevertheless, one should keep in mind that our analysis does not rule out the possibility of having other hadronic species or the transition to quark matter in the NS core. In fact, to evaluate the probability of having other degrees of freedom, one can compute the evidence in the two hypotheses and calculate the so-called Bayes factor, as done in e.g., Refs. [185, 186, 194]. If more stringent data become available in the future, our current Bayesian inference can also be used as a null hypothesis to search for possible exotic degrees of freedom. Moreover, the developments of heavy-ion collision experiments are expected to shed light on high-density nuclear matter properties, and therefore, the uncertainties in our predictions for the NS properties could be reduced. While the foundational framework of this chapter was initially presented in T. Carreau's thesis, I have improved the Bayesian analysis and consistently integrated the latest astrophysical constraints. These improvements have yielded results published in a peer-reviewed article [184] and a conference proceedings [201].

Even though the crust only has a small contribution to the total mass and radius of a NS, it can have significant impacts on different NS phenomena. Particularly, in the innermost region of the crust, non-spherical structures of nuclei called the pasta phases could appear and influence NS cooling, transport properties, etc. The properties of the pasta phases are addressed in Chapter 3. Specifically, we extended the formalism of inhomogeneous matter described in Chapter 2 to include five different geometries: spheres, rods, slabs, tubes, and bubbles, as suggested in Refs. [12, 216]. The microscopic properties, specifically the variational variables $(r_N, I, n_i, n_{gn}, n_p)$ and the cluster volume fraction $f(u)$, of different geometries were calculated from the minimization of the total energy density of the WS cell under the constraints of charge neutrality and baryon number conservation. Using the BSk24 functional, we found that apart from the size r_N, the other quantities corresponding to the most favored geometry are almost identical to those of spheres. In addition, including the pasta structures does not affect the EOS of the inner crust, except for a small jump in pressure at the transition from one geometry to another. To investigate the model dependence of the

results, we carried out the calculation for nine different functionals and found that the composition and the transition densities among the geometries vary significantly with the nuclear model. This is also the case for the macroscopic pasta properties, such as thickness, mass, and moment of inertia. To calculate these latter quantities, we utilized the spheres-composition approximation to obtain the EOS and solve the TOV equations. Similar to Chapter 2, a Bayesian study was performed to quantify the uncertainties in the pasta phase properties. In particular, the posterior distributions resulted from the constraint on the maximum mass ($M_{\rm max} \geq 1.97\ M_\odot$) [31] and the chiral EFT calculation [110]. It was shown that both the bulk and surface properties play an important role in the determination of the pasta phases. To be more specific, we observed that restricting the variation of the surface and curvature parameters could lead to an underestimation of the uncertainties of pasta-phase properties. These results emphasize the importance of the consistency between the surface properties and the nuclear functional. Moreover, by considering two different density ranges for applying the low-density EFT filters on the energy of homogeneous matter, $[0.1, 0.2]$ fm^{-3} and $[0.02, 0.2]$ fm^{-3}, it is interesting to observe that the information from nuclear physics at very low densities are of great importance for a better understanding of astrophysical quantities, particularly the crustal and pasta phase properties. Finally, we estimated that the pasta phases contribute $12.8 \pm 4.7\%$ of the crust thickness and $48.5 \pm 13.8\%$ of the crust mass. One can expect that these uncertainties on the pasta properties could be reduced when further constraints from nuclear physics experiments and theory become available. This chapter of the thesis is entirely original and has resulted in two publications [121, 142] and a conference proceedings [217].

The picture at zero temperature may not reflect the real composition of the neutron-star crust. Indeed, the initial temperature of proto-neutron stars after being born from the gravitational core collapse is of the order of 10^{11} K [1]. These stars then cool down mainly via neutrino emission. After tens of seconds from its birth, a proto-neutron star is expected to cool to a few 10^{10} K and to be transparent to neutrinos [267]. Depending on the cooling rate, the composition in the crust could be frozen at some finite temperature. Under this condition, the crust can be modeled as a multi-component plasma characterized by the coexistence of different ion species in the liquid phase, and the background can also contain free protons. The crust at finite temperature is studied in Chapter 4. The results in this chapter were obtained assuming that nuclei are spherical. Besides, we mainly used the empirical parameters from the BSk24 functional, which was shown to be in good agreement with *ab initio* calculation as well as astrophysical data [121]. Moreover, we built our model from the one-component plasma approximation to the multi-component plasma approach. In the former, the crust is supposed to be composed of identical WS cells, that is, the whole nuclear distribution is represented by a single nucleus, and we focused on demonstrating the effects of the cluster center-of-mass degrees of freedom on the properties of the crust. To obtain a realistic approximation for the translational free energy, the finite-size effect was taken into account, and the effective mass induced by the motion of the ion in the uniform nucleon background was derived using a hydrodynamical approach, assuming nuclear matter inside and outside the ion to be incompressible and irrotational fluid. At beta equilibrium, each thermodynamic condition is defined by the temperature and total baryonic density of

the system. In this case, the cluster size results from the competition between the motion of the center-of-mass of the ion and the interface properties, namely, the Coulomb, surface, and curvature energies. At a temperature of a few 10^{10} K, the latter prefer large clusters ($A \gtrsim 100$), while the translational term is minimized at small clusters ($A \sim 10$). As a consequence, accounting for the center-of-mass motion leads to nucleon depletion in the optimal configuration, and this effect grows with density and temperature. The reduction in A and Z is also observed in the case of a fixed proton fraction, which is relevant for hot and dense supernova matter. However, the impact in the latter case is much less significant than in the case of beta equilibrium. Regarding the crust EOS, the translational free energy only has a negligible influence. The OCP approximation is applicable if the nuclear distribution is very peaked, such as in the outer crust and at temperatures around the crystallization point. However, this is not always the case in other conditions, especially at high densities and temperatures. Therefore, we employed the MCP approach to study the coexistence of different nuclear species in beta equilibrium. Since the contribution from the proton gas is insignificant at the temperatures considered in this work, free protons are neglected in the MCP calculation. Here, we considered both the perturbative – where the gas properties are taken from the OCP approximation – and self-consistent – where the gas properties are computed self-consistently with the charge neutrality and baryon number conservation – cases. With the perturbative MCP treatment, we demonstrated that the equivalence between MCP and OCP is established only if non-linear mixing contribution, which originates from the center-of-mass motion in the case of liquid crust, can be neglected. Nevertheless, since this term becomes more important in deeper layers of the crust and at higher temperatures, the OCP prediction deviates from the most probable configuration in the perturbative MCP calculation. This approach does not guarantee thermodynamic consistency, and therefore, a full self-consistent MCP is needed, particularly in the deeper region of the crust, for reliable predictions of the PNS crust composition. Interestingly, it was shown that with increasing density and temperature, the abundance of light nuclei becomes important, and eventually dominates the whole nuclear distribution. Consequently, the impurity parameter, which is defined as the variance in the charge distribution, shows a peak structure, rather than increasing monotonically. This result could have a potential impact on the NS cooling and transport properties. Regardless of the considerable difference in the composition predicted in different approaches, in general, the EOS in the crust is only modified insignificantly. Particularly, the pressure in MCP is slightly lower than the OCP counterpart, of $\sim 10\%$ at most. Let us stress that our results at high densities should be taken with caution because the CLDM description is known to be not satisfactory for light nuclei. Therefore, a more microscopic treatment with in-medium corrections might be needed for a more reliable prediction. Additionally, non-spherical structures like the pasta phases may appear at the bottom of the inner crust, and the coexistence of different (non-spherical) structures deserves further study. Finally, this study can be extended to calculate the transport properties in the NS crust. For the first time, the MCP calculations beyond the perturbative approach as well as the inclusion of the translational degrees of freedom with the effective mass are performed. The original work described in this chapter has led to two papers in *Astronomy & Astrophysics* [269, 270] and one paper in preparation.

The formalism and numerical tools developed in this work can be utilized and expanded upon in various directions. Specifically, the Bayesian analysis presented in Chapter 2 can be updated to incorporate future astrophysical observations from collaborations like LIGO-Virgo or NICER, enabling a more comprehensive understanding of the high-density region of the EOS. With these potential measurements, we anticipate to have narrower posterior distributions of high-order empirical parameters. Furthermore, it is also possible to integrate valuable information derived from heavy-ion collision experiments, particularly on the properties of asymmetric matter, into the Bayesian studies, as demonstrated by Ref. [103]. Although these constraints are currently not as stringent as desired [103], they hold promise in unveiling the behavior of dense matter in the future, see e.g., Ref. [310]. As a result, one can expect to have more precise determination of high-order empirical parameters, and therefore, more precise predictions for the NS observables. In addition, it is also of great importance to acquire further insights into the EOS at low densities through nuclear physics experiments and theoretical calculations. Indeed, these insights could play a crucial role in reducing uncertainties in the calculations of NS crustal properties, which hold relevance across numerous astrophysical scenarios. Moreover, another possibility for extending this work is the inclusion of other degrees of freedom, such as hyperons and quarks, into the core EOS, as already performed by Refs. [34, 194].

As discussed in Chapter 3, the presence of pasta phases in the crust could have significant implications for various astrophysical phenomena. Consequently, it is reasonable to anticipate that our calculations for the properties of pasta phases can serve as inputs for calculating relevant observables to those phenomena. On the other hand, different observations could potentially impose constraints on the existence as well as characteristics of the pasta phases, see Ref. [254] for an example of constraining the pasta structure with oscillations from giant flares. Furthermore, the formalism presented for pasta phases at zero temperature in Chapter 3 can be extended to finite temperatures, following a similar approach as discussed for spheres in Chapter 4. However, unlike spheres, where the thermal effects, i.e., translations or vibrations, can be derived using standard statistical mechanics (although with non-trivial considerations for finite size and effective mass corrections), addressing the thermal effects of non-spherical nuclei is a more complex and challenging task. Consequently, this topic deserves thorough investigation. Once this aspect is established, the presence of pasta phases can be incorporated into the formalism presented in Chapter 4 for the crust of PNS, in both the OCP and MCP approaches. In the latter approach, it is also possible to assess the influence of pasta phases on the impurity parameter for the beta-equilibrated crust. Additionally, the results obtained from Chapter 4 can be employed to calculate the transport properties, which play vital roles in various NS phenomena. In particular, it is interesting to study the impacts of electron-impurity scattering on thermal and electrical conductivities. Besides, it is also worthwhile to check the validity of the Matthiessen's rule in the high-$Q_{\rm imp}$ regime, similar to the work by Ref. [301], with our consistent MCP formalism. These consistent calculations on the thermal and electrical conductivities then can be used to study the timing properties and magnetothermal evolutions of NS as in Refs. [55, 56].

The code developed during my thesis builds upon the open-source library, NSEoS, created by T. Carreau [175]. Currently, this code is exclusively available on GitLab for internal

members of the Caen Theory group [311]. However, this code was used by other members of the group to build a numerical tool that allows for calculating a unified EOS from an arbitrary core EOS using the meta-modeling technique developed in this thesis. This tool is currently hosted on the IN2P3 GitLab as well as on the LIGO Git, and is used by the LVK collaboration for the data analysis of the O4 data-taking (May 2023). Additionally, I have prepared a comprehensive user documentation, and in the near future, both the code and the user guides will be made accessible to external users.

Appendices

APPENDIX A

Coulomb energy for different geometries in the Wigner-Seitz approximation

A.1 Spherical shapes

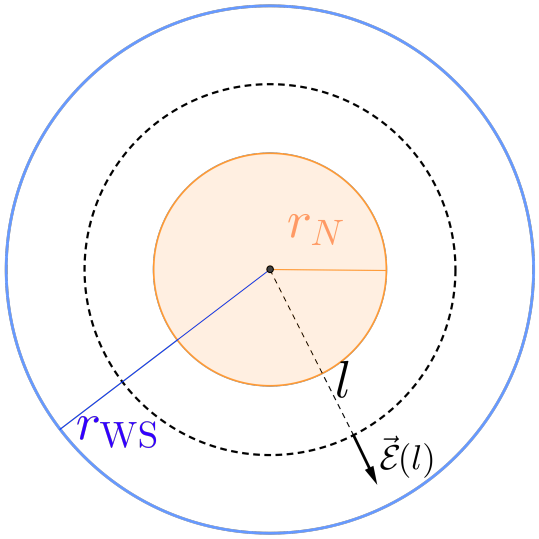

Figure A.1: Sketch of a spherical cluster of radius r_N in a WS cell of radius r_{WS}.

Considering a spherical nucleus of radius r_N located in the center of a WS cell of radius r_{WS}, as depicted in Fig. A.1. The cluster has Z protons, and it is embedded in a uniform electron background of density n_e such that the cell is neutral, $n_e = \frac{Z}{V_{\mathrm{WS}}}$. In order to determine the total Coulomb energy in the WS cell, we need to know the electric potential and electric field.

A.1.1 Electric field

To calculate the electric field at a distance l from the center, we can consider two regions: (i) $0 < l \leq r_N$ and (ii) $r_N < l \leq r_{\rm WS}$. Outside the WS cell, $l > r_{\rm WS}$, there is no electric field due to the charge neutrality in the cell.

* $0 < l \leq r_N$:
From Gauss theorem:

$$\mathcal{E}_1 4\pi l^2 = \frac{e(n_{\rm ip} - n_e)\frac{4\pi}{3}l^3}{\epsilon_0}, \tag{A.1}$$

where $\mathcal{E}_1$ denotes the electric field, ϵ_0 is the dielectric constant of vacuum, e is the elementary charge, and $n_{\rm ip}$ is the proton density inside the cluster, $n_{\rm ip} = \frac{Z}{4\pi r_N^3/3}$. Thus,

$$\mathcal{E}_1 = \frac{e(n_{\rm ip} - n_e)l}{3\epsilon_0}. \tag{A.2}$$

* $r_N < l \leq r_{\rm WS}$:
Similarly,

$$\mathcal{E}_2 4\pi l^2 = \frac{4\pi e(n_{\rm ip} r_N^3 - n_e l^3)}{3\epsilon_0}, \tag{A.3}$$

where $\mathcal{E}_2$ indicates the electric field in this region. We have:

$$\mathcal{E}_2 = \frac{e(n_{\rm ip} r_N^3 - n_e l^3)}{3\epsilon_0 l^2}. \tag{A.4}$$

A.1.2 Electric potential

Let V_1 and V_2 be the electric potentials inside and outside the cluster, respectively. For $r_N < l \leq r_{\rm WS}$:

$$V_2(l) - V_2(r_{\rm WS}) = -\int_{r_{\rm WS}}^{l} \mathcal{E}_2(\bar{r})d\bar{r}, \tag{A.5}$$

$$V_2(l) - 0 = \frac{e}{3\epsilon_0}\int_{l}^{r_{\rm WS}} \left(n_{\rm ip}\frac{r_N^3}{\bar{r}^2} - n_e\bar{r}\right)d\bar{r}, \tag{A.6}$$

$$V_2(l) = \frac{e}{3\epsilon_0}\left[n_{\rm ip}\frac{r_N^3}{l} + \frac{1}{2}n_e l^2 - n_{\rm ip}\frac{r_N^3}{r_{\rm WS}} - \frac{1}{2}n_e r_{\rm WS}^2\right]. \tag{A.7}$$

For $0 < l \leq r_N$:

$$V_1(l) - V_2(r_N) = -\int_{r_N}^{l} \mathcal{E}_1(\bar{r})d\bar{r}, \tag{A.8}$$

$$V_1(l) - V_2(r_N) = \int_{l}^{r_N} \frac{e(n_{\rm ip} - n_e)\bar{r}}{3\epsilon_0}d\bar{r}, \tag{A.9}$$

$$V_1(l) - V_2(r_N) = \frac{e(n_{\rm ip} - n_e)}{3\epsilon_0}\frac{r_N^2 - l^2}{2}, \tag{A.10}$$

$$V_1(l) = \frac{e(n_{\rm ip} - n_e)}{3\epsilon_0}\frac{r_N^2 - l^2}{2} + \frac{e}{3\epsilon_0}\left[n_{\rm ip} r_N^2 + \frac{1}{2}n_e r_N^2 - n_{\rm ip}\frac{r_N^3}{r_{\rm WS}} - \frac{1}{2}n_e l_{\rm WS}^2\right], \tag{A.11}$$

$$V_1(l) = \frac{e}{6\epsilon_0}\left[n_{\rm ip}\left(3r_N^2 - l^2\right) - n_e\left(3r_{\rm WS}^2 - l^2\right)\right]. \tag{A.12}$$

A.1.3 Coulomb energy

The electric potential energy in the Wigner-Seitz approximation can be calculated from

$$E_{\text{Coul}} = E_{\text{Coul},1} + E_{\text{Coul},2}, \tag{A.13}$$

$$E_{\text{Coul}} = \frac{1}{2}\int V_1(n_{ip} - n_e)edV + \frac{1}{2}\int V_2(-n_e)edV, \tag{A.14}$$

For the electric potential energy inside the cluster, $E_{\text{Coul},1}$, we have:

$$E_{\text{Coul},1} = \frac{1}{2}\int V_1(n_{ip} - n_e)edV, \tag{A.15}$$

$$E_{\text{Coul},1} = \frac{1}{2}\int_0^{r_N} \frac{e}{6\epsilon_0}\left[n_{ip}\left(3r_N^2 - l^2\right) - n_e\left(3r_{\text{WS}}^2 - l^2\right)\right](n_{ip} - n_e)e4\pi l^2 dl, \tag{A.16}$$

$$E_{\text{Coul},1} = \frac{4\pi e^2}{12\epsilon_0}(n_{ip} - n_e)\left[n_{ip}\left(r_N^5 - \frac{r_N^5}{5}\right) - n_e\left(r_{\text{WS}}^2 r_N^3 - \frac{r_N^5}{5}\right)\right], \tag{A.17}$$

$$E_{\text{Coul},1} = \frac{V_N(n_{ip} - n_e)e^2}{4\epsilon_0}\left[n_{ip}\frac{4r_N^2}{5} - n_e(r_{\text{WS}}^2 - \frac{r_N^2}{5})\right], \tag{A.18}$$

with $V_N = \frac{4\pi r_N^3}{3}$ being the cluster volume.
Similarly, for the electric potential energy outside the cluster, $E_{\text{Coul},2}$, we have:

$$E_{\text{Coul},2} = -\frac{1}{2}\int V_2 n_e edV, \tag{A.19}$$

$$E_{\text{Coul},2} = -\frac{n_e}{2}\frac{e^2}{3\epsilon_0}\int_{r_N}^{r_{\text{WS}}}\left[n_{ip}\frac{r_N^3}{l} + \frac{1}{2}n_e l^2 - n_{ip}\frac{r_N^3}{r_{\text{WS}}} - \frac{1}{2}n_e r_{\text{WS}}^2\right]4\pi l^2 dl, \tag{A.20}$$

$$E_{\text{Coul},2} = -\frac{4\pi n_e e^2}{6\epsilon_0}\left[n_{ip}r_N^3\frac{r_{\text{WS}}^2 - r_N^2}{2} + \frac{n_e}{2}\frac{r_{\text{WS}}^5 - r_N^5}{5} - \left(n_{ip}\frac{r_N^3}{r_{\text{WS}}} + \frac{1}{2}n_e r_{\text{WS}}^2\right)\frac{r_{\text{WS}}^3 - r_N^3}{3}\right], \tag{A.21}$$

$$E_{\text{Coul},2} = -\frac{V_N n_e e^2}{4\epsilon_0}\left[n_{ip}(r_{\text{WS}}^2 - r_N^2) - n_e\frac{4}{5}\frac{r_{\text{WS}}^5}{r_N^3} - n_e\left(\frac{r_N^2}{5} - r_{\text{WS}}^5\right)\right]. \tag{A.22}$$

Therefore, the total Coulomb energy reads:

$$\begin{aligned} E_{\text{Coul}} =& \frac{V_N(n_{ip} - n_e)e^2}{4\epsilon_0}\left[n_{ip}\frac{4r_N^2}{5} - n_e(r_{\text{WS}}^2 - \frac{r_N^2}{5})\right] + \\ &- \frac{V_N n_e e^2}{4\epsilon_0}\left[n_{ip}(r_{\text{WS}}^2 - r_N^2) - n_e\frac{4}{5}\frac{r_{\text{WS}}^5}{r_N^3} - n_e\left(\frac{r_N^2}{5} - r_{\text{WS}}^5\right)\right]. \end{aligned} \tag{A.23}$$

We can show that Eq. (A.23) is equivalent to:

$$E_{\text{Coul}} = \frac{V_N e^2}{4\epsilon_0}\left[n_{ip}^2\frac{4r_N^2}{5} + n_e^2\frac{4r_{\text{WS}}^5}{5r_N^3} + n_{ip}n_e\left(\frac{2r_N^2}{5} - 2r_{\text{WS}}^2\right)\right], \tag{A.24}$$

$$E_{\text{Coul}} = \frac{3}{5}\frac{V_N^2 e^2 n_{ip}^2}{4\pi\epsilon_0}\frac{1}{r_N}\left[1 + \frac{n_e^2}{n_{ip}^2}\frac{r_{\text{WS}}^5}{r_N^5} - \frac{5}{2}\left(\frac{n_e}{n_{ip}}\frac{r_{\text{WS}}^2}{r_N^2} - \frac{1}{2}\right)\right] \tag{A.25}$$

Using $n_{ip} r_N^3 = n_e r_{\rm WS}^3$, we arrive to the following equation:

$$E_{\rm Coul} = \frac{3}{5}\frac{(Ze)^2}{4\pi\epsilon_0}\frac{1}{r_N}\left[1 + \frac{1}{2}\frac{r_N^3}{r_{\rm WS}^3} - \frac{3}{2}\frac{r_N}{r_{\rm WS}}\right]. \tag{A.26}$$

Let $u = \frac{V_N}{V_{\rm WS}} = \frac{r_N^3}{r_{\rm WS}^3}$, the Coulomb energy can be written as:

$$E_{\rm Coul} = \frac{3}{5}\frac{(Ze)^2}{4\pi\epsilon_0}\frac{1}{r_N}\left[1 + \frac{u}{2} - \frac{3u^{1/3}}{2}\right]. \tag{A.27}$$

In the CGS unit system, $4\pi\epsilon_0 = 1$. Dividing the Coulomb energy $E_{\rm Coul}$ by the WS cell volume, we get the Coulomb energy density:

$$\varepsilon_{\rm Coul} = \frac{E_{\rm Coul}}{V_{\rm WS}} = 2\pi\left(e y_p n_i r_N\right)^2 u \eta_{\rm Coul,3}(u), \tag{A.28}$$

where $y_p = (1-I)/2$ is the cluster proton fraction, and $\eta_{\rm Coul,3}$ is defined as:

$$\eta_{\rm Coul,3}(u) = \frac{1}{5}\left[u + 2\left(1 - \frac{3}{2}u^{1/3}\right)\right]. \tag{A.29}$$

In the case of bubbles, we can follow the same steps as above. Indeed, having a bubbles structure with proton density n_{ip}, in the region $r_N < r < r_{\rm WS}$, in the background of electron of density n_e is equivalent to having a sphere of proton density $n'_{ip} = -n_{ip}$, in the region $r \le r_N$, with a background of electrons of density $n'_e = n_e - n_{ip}$. Thus, Eq. (A.25) becomes:

$$E_{\rm Coul} = \frac{3}{5}\frac{(Ze)^2}{4\pi\epsilon_0}\frac{1}{r_N}\left[1 + \frac{n'^2_e}{n'^2_{\rm ip}}\frac{r_{\rm WS}^5}{r_N^5} - \frac{5}{2}\left(\frac{n'_e}{n'_{\rm ip}}\frac{r_{\rm WS}^2}{r_N^2} - \frac{1}{2}\right)\right]. \tag{A.30}$$

Using the charge neutrality condition, $n'_{ip} r_N^3 = n'_e r_{\rm WS}^3$, one can easily arrive to Eq. (A.27), with $u = \frac{V_N}{V_{\rm WS}}$ being the volume fraction of the hole.

A.2 Cylindrical shapes

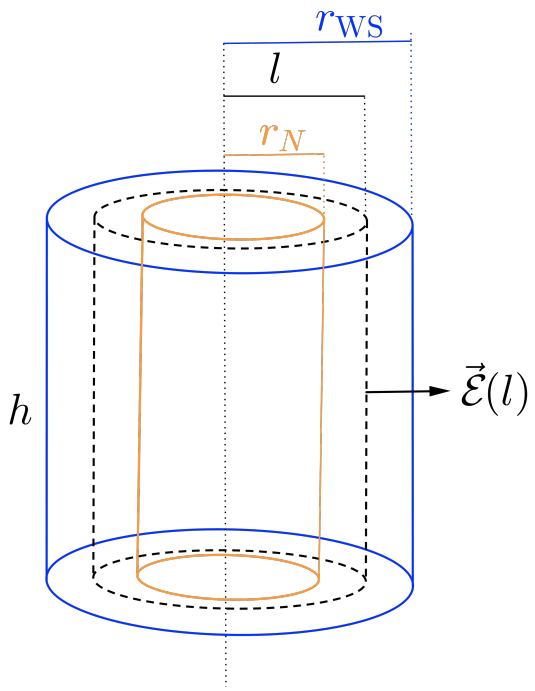

Figure A.2: Sketch of a cylindrical cluster of radius r_N in a WS cell of radius r_{WS}.

A.2.1 Electric field

* $0 < l \leq r_N$:
From Gauss theorem:

$$\mathcal{E}_1 2\pi l h = \frac{e(n_{\mathrm{ip}} - n_e)\pi l^2 h}{\epsilon_0}, \tag{A.31}$$

Thus,

$$\mathcal{E}_1 = \frac{e(n_{\mathrm{ip}} - n_e) l}{2\epsilon_0}. \tag{A.32}$$

* $r_N < l \leq r_{\mathrm{WS}}$:
Similarly,

$$\mathcal{E}_2 2\pi l h = \frac{\pi h e(n_{\mathrm{ip}} r_N^2 - n_e l^2)}{2\epsilon_0}, \tag{A.33}$$

We have:

$$\mathcal{E}_2 = \frac{e(n_{\mathrm{ip}} r_N^2 - n_e l^2)}{2\epsilon_0 l}. \tag{A.34}$$

A.2.2 Electric potential

For $r_N < l \leq r_{\mathrm{WS}}$:

$$V_2(l) - V_2(r_{\mathrm{WS}}) = -\int_{r_{\mathrm{WS}}}^{l} \mathcal{E}_2(\bar{r})d\bar{r}, \tag{A.35}$$

$$V_2(l) - 0 = \frac{e}{2\epsilon_0}\int_{l}^{r_{\mathrm{WS}}} \left(n_{\mathrm{ip}}\frac{r_N^2}{\bar{r}} - n_e\bar{r}\right)d\bar{r}, \tag{A.36}$$

$$V_2(l) = \frac{e}{2\epsilon_0}\left[n_{\mathrm{ip}}r_N^2 \ln\frac{r_{\mathrm{WS}}}{l} + \frac{1}{2}n_e l^2 - \frac{1}{2}n_e r_{\mathrm{WS}}^2\right]. \tag{A.37}$$

For $0 < l \leq r_N$:

$$V_1(l) - V_2(r_N) = -\int_{r_N}^{l} \mathcal{E}_1(\bar{r})d\bar{r}, \tag{A.38}$$

$$V_1(l) - V_2(r_N) = \int_{l}^{r_N} \frac{e(n_{\mathrm{ip}} - n_e)\bar{r}}{2\epsilon_0}d\bar{r}, \tag{A.39}$$

$$V_1(l) - V_2(r_N) = \frac{e(n_{\mathrm{ip}} - n_e)}{2\epsilon_0}\frac{r_N^2 - l^2}{2}, \tag{A.40}$$

$$V_1(l) = \frac{e(n_{\mathrm{ip}} - n_e)}{2\epsilon_0}\frac{r_N^2 - l^2}{2} + \frac{e}{2\epsilon_0}\left[n_{\mathrm{ip}}r_N^2 \ln\frac{r_{\mathrm{WS}}}{r_N} + \frac{1}{2}n_e r_N^2 - \frac{1}{2}n_e r_{\mathrm{WS}}^2\right], \tag{A.41}$$

$$V_1(l) = \frac{e}{2\epsilon_0}\left[n_{\mathrm{ip}}\left(\frac{1}{2}r_N^2 - \frac{1}{2}l^2 + r_N^2 \ln\frac{r_{\mathrm{WS}}}{r_N}\right) - \frac{1}{2}n_e\left(r_{\mathrm{WS}}^2 - l^2\right)\right]. \tag{A.42}$$

A.2.3 Coulomb energy

$$E_{\mathrm{Coul}} = E_{\mathrm{Coul},1} + E_{\mathrm{Coul},2}, \tag{A.43}$$

$$E_{\mathrm{Coul}} = \frac{1}{2}\int V_1(n_{\mathrm{ip}} - n_e)ehdS + \frac{1}{2}\int V_2(-n_e)ehdS, \tag{A.44}$$

For the electric potential energy inside the cluster, $E_{\mathrm{Coul},1}$, we have:

$$E_{\mathrm{Coul},1} = \frac{1}{2}\int V_1(n_{\mathrm{ip}} - n_e)ehdS, \tag{A.45}$$

$$= \int_0^{r_N} \frac{e}{4\epsilon_0}\left[n_{\mathrm{ip}}\left(\frac{1}{2}r_N^2 - \frac{1}{2}l^2 + r_N^2 \ln\frac{r_{\mathrm{WS}}}{r_N}\right) - \frac{1}{2}n_e\left(r_{\mathrm{WS}}^2 - l^2\right)\right](n_{\mathrm{ip}} - n_e)e2\pi hldl, \tag{A.46}$$

$$= \frac{\pi he^2}{2\epsilon_0}(n_{\mathrm{ip}} - n_e)\left[n_{\mathrm{ip}}\left(-\frac{1}{8}r_N^4 + \frac{1}{2}r_N^4 \ln\frac{r_{\mathrm{WS}}}{r_N}\right) + n_e\frac{1}{8}r_N^4\right], \tag{A.47}$$

$$= \frac{V_N(n_{\mathrm{ip}} - n_e)e^2}{2}\left[n_{\mathrm{ip}}\left(-\frac{1}{8}r_N^2 + \frac{1}{2}r_N^2 \ln\frac{r_{\mathrm{WS}}}{r_N}\right) + n_e\frac{1}{8}r_{\mathrm{N}}^2\right], \tag{A.48}$$

with $V_N = \pi h r_N^2$ being the cluster volume.

Similarly, for the electric potential energy outside the cluster, $E_{\text{Coul},2}$, we have:

$$E_{\text{Coul},2} = -\frac{1}{2}\int V_2 n_e e h dS, \tag{A.49}$$

$$= -\frac{n_e}{2}\frac{e^2}{2\epsilon_0}\int_{r_N}^{r_{\text{WS}}}\left[n_{\text{ip}} r_N^2 \ln\frac{r_{\text{WS}}}{l} + \frac{1}{2}n_e l^2 - \frac{1}{2}n_e r_{\text{WS}}^2\right] 2\pi h l dl, \tag{A.50}$$

$$= -\frac{\pi h n_e e^2}{2\epsilon_0}\left[-n_{\text{ip}}\frac{1}{2}r_N^4 \ln\frac{r_{\text{WS}}}{r_N} + \frac{1}{8}n_e\left(r_{\text{WS}}^4 - r_N^4\right)\right], \tag{A.51}$$

$$= -\frac{V_N n_e e^2}{2\epsilon_0}\left[-n_{\text{ip}}\frac{1}{2}r_N^2 \ln\frac{r_{\text{WS}}}{r_N} + \frac{1}{8}n_e\left(\frac{r_{\text{WS}}^4}{r_N^2} - r_N^2\right)\right]. \tag{A.52}$$

Thus, using the charge neutrality condition $n_e r_{\text{WS}}^2 = n_{\text{ip}} r_N^2$, and $u = \frac{r_N^2}{r_{\text{WS}}^2} = \frac{n_e}{n_{\text{ip}}}$:

$$E_{\text{Coul}} = \frac{V_N e^2 r_N^2}{8\epsilon_0}\left[n_{\text{ip}} n_e - n_{\text{ip}}^2 - n_{\text{ip}}^2 \ln u\right] \tag{A.53}$$

$$= \frac{1}{2}V_N (e r_N n_{\text{ip}})^2 \pi (u - 1 - \ln u), \tag{A.54}$$

$$= 2\pi V_N (e r_N y_p n_i)^2 \eta_{\text{Coul},2}, \tag{A.55}$$

where

$$\eta_{\text{Coul},2} = \frac{1}{4}(u - 1 - \ln u). \tag{A.56}$$

The Coulomb energy density for cylindrical shape is then given by

$$\varepsilon_{\text{Coul}} = \frac{E_{\text{Coul}}}{V_{\text{WS}}} = 2\pi (e r_N y_p n_i)^2 u \eta_{\text{Coul},2} \tag{A.57}$$

A.3 Planar shape

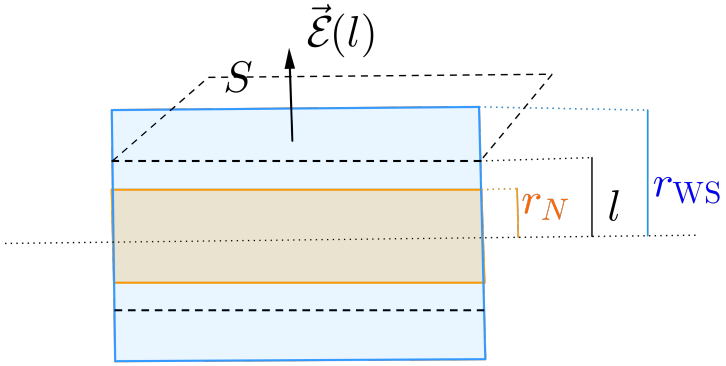

Figure A.3: Sketch of a slab of half-thickness r_N in a WS cell of half-thickness r_{WS}.

A.3.1 Electric field

* $0 < l \leq r_N$:
From Gauss theorem:

$$\mathcal{E}_1 S = \frac{e(n_{\text{ip}} - n_e) S l}{\epsilon_0}, \tag{A.58}$$

Thus,

$$\mathcal{E}_1 = \frac{e(n_{ip} - n_e)l}{\epsilon_0}. \tag{A.59}$$

* $r_N < l \leq r_{\rm WS}$:
Similarly,

$$\mathcal{E}_2 S = \frac{e(n_{ip} r_N - n_e l)S}{\epsilon_0}, \tag{A.60}$$

We have:

$$\mathcal{E}_2 = \frac{e(n_{ip} r_N - n_e l)}{\epsilon_0}. \tag{A.61}$$

A.3.2 Electric potential

For $r_N < l \leq r_{\rm WS}$:

$$V_2(l) - V_2(r_{\rm WS}) = -\int_{r_{\rm WS}}^{l} \mathcal{E}_2(\bar{r}) d\bar{r}, \tag{A.62}$$

$$V_2(l) - 0 = \frac{e}{\epsilon_0}(n_{ip} r_N - n_e \bar{r}) d\bar{r}, \tag{A.63}$$

$$V_2(l) = \frac{e}{\epsilon_0}\left[n_{ip} r_N (r_{\rm WS} - l) - \frac{1}{2} n_e (r_{\rm WS}^2 - l^2)\right]. \tag{A.64}$$

For $0 < l \leq r_N$:

$$V_1(l) - V_2(r_N) = -\int_{r_N}^{l} \mathcal{E}_1(\bar{r}) d\bar{r}, \tag{A.65}$$

$$V_1(l) - V_2(r_N) = \int_{l}^{r_N} \frac{e(n_{ip} - n_e)\bar{r}}{\epsilon_0} d\bar{r}, \tag{A.66}$$

$$V_1(l) - V_2(r_N) = \frac{e(n_{ip} - n_e)}{\epsilon_0}(r_N - l), \tag{A.67}$$

$$V_1(l) = \frac{e(n_{ip} - n_e)}{\epsilon_0}\frac{r_N^2 - l^2)}{2} + \frac{e}{\epsilon_0}\left[n_{ip} r_N (r_{\rm WS} - r_N) - \frac{1}{2} n_e (r_{\rm WS}^2 - r_N^2)\right], \tag{A.68}$$

$$V_1(l) = \frac{e}{\epsilon_0}\left[-\frac{n_{ip}}{2}(r_N^2 + l^2) + \frac{n_e}{2}(l^2 + r_{\rm WS}^2\right], \tag{A.69}$$

where I have used the charge neutrality condition, $n_{ip} r_N = n_e r_{\rm WS}$

A.3.3 Coulomb energy

$$E_{\rm Coul} = E_{\rm Coul,1} + E_{\rm Coul,2}, \tag{A.70}$$

$$E_{\rm Coul} = \frac{1}{2}\int V_1 (n_{ip} - n_e) e 2S dl + \frac{1}{2}\int V_2 (-n_e) e 2S dl, \tag{A.71}$$

For the electric potential energy inside the cluster, $E_{\text{Coul},1}$, we have:

$$E_{\text{Coul},1} = \frac{1}{2}\int V_1(n_{ip} - n_e)e2Sdl, \tag{A.72}$$

$$= \int_0^{r_N} \frac{e}{\epsilon_0}\left[-\frac{n_{ip}}{2}(r_N^2 + l^2) + \frac{n_e}{2}(l^2 + r_{\text{WS}}^2)\right](n_{ip} - n_e)eSdl, \tag{A.73}$$

$$= \frac{2Se^2}{2\epsilon_0}(n_{ip} - n_e)\left[-\frac{1}{2}n_{ip}\left(r_N^3 + \frac{1}{3}r_N^3\right) + \frac{1}{2}n_e\left(\frac{r_N^3}{3} + r_{\text{WS}}^2 r_N\right)\right], \tag{A.74}$$

$$= \frac{V_N(n_{ip} - n_e)e^2}{2\epsilon_0}\left[-\frac{2}{3}n_{ip}r_N^2 + \frac{1}{2}n_e\left(\frac{r_N^2}{3} + r_{\text{WS}}^2\right)\right], \tag{A.75}$$

Similarly, for the electric potential energy outside the cluster, $E_{\text{Coul},2}$, we have:

$$E_{\text{Coul},2} = -\frac{1}{2}\int V_2 n_e e2Sdl, \tag{A.76}$$

$$= -\frac{n_e e^2}{\epsilon_0}\int_{r_N}^{r_{\text{WS}}}\left[n_{ip}r_N(r_{\text{WS}} - l) - \frac{1}{2}n_e(r_{\text{WS}}^2 - l^2)\right]Sdl, \tag{A.77}$$

$$= -\frac{2Sn_e e^2}{2\epsilon_0}\left[\frac{1}{2}n_{ip}r_N^3 + n_e\left(\frac{r_{\text{WS}}^3}{6} - \frac{r_{\text{WS}}^2 r_N}{2} - \frac{r_N^3}{6}\right)\right], \tag{A.78}$$

$$= \frac{-V_N n_e e^2}{2\epsilon_0}\left[\frac{1}{2}n_{ip}r_N^2 + n_e\left(\frac{r_{\text{WS}}^3}{6r_N} - \frac{r_{\text{WS}}^2}{2} - \frac{r_N^2}{6}\right)\right]. \tag{A.79}$$

Thus

$$E_{\text{Coul}} = \frac{V_N e^2}{2\epsilon_0}\left(-\frac{2}{3}n_{ip}^2 r_N^2 + n_{ip}n_e\left(\frac{r_N^2}{3} + \frac{r_{\text{WS}}^2}{3}\right)\right), \tag{A.80}$$

$$= \frac{2\pi V_N e^2}{4\pi\epsilon_0}\frac{r_N^2 n_{ip}^2}{3}\left[-2 + \frac{n_e}{n_{ip}}\left(1 + \frac{r_{\text{WS}}^2}{r_N^2}\right)\right], \tag{A.81}$$

$$= 2\pi V_N(e y_p n_i r_N)^2 \eta_{\text{Coul},1}, \tag{A.82}$$

where

$$\eta_{\text{Coul},1} = \frac{1}{3}\left(-2 + u + \frac{1}{u}\right) \tag{A.83}$$

The Coulomb energy density for a slab is given by

$$\varepsilon_{\text{Coul}} = \frac{E_{\text{Coul}}}{V_{\text{WS}}} = 2\pi(e r_N y_p n_i)^2 u \eta_{\text{Coul},1} \tag{A.84}$$

From Eqs. (A.28), (A.57), and (A.84), we can write the Coulomb energy density in the WS approximation for a geometry d as:

$$\varepsilon_{\text{Coul}} = \frac{E_{\text{Coul}}}{V_{\text{WS}}} = 2\pi(e r_N y_p n_i)^2 u \eta_{\text{Coul,d}}. \tag{A.85}$$

This expression holds for both *clusters* and *holes* structure.

APPENDIX B

Variational equations for cold–catalyzed neutron-star crusts

In this chapter, I present in details the steps for obtaining the system of equilibrium equations of a cold-catalyzed NS crust.

B.1 Outer crust

For the outer crust, there is no free neutron gas. Therefore, the total energy density in each WS cell is expressed as:

$$\varepsilon_{\rm WS} = \varepsilon_e + \frac{E_i}{V_{\rm WS}}. \tag{B.1}$$

The baryonic number conservation can be written as:

$$n_B = \frac{A}{V_{\rm WS}} = \frac{2n_p}{1-I}. \tag{B.2}$$

Under this constraint, one can introduce a Lagrange multiplier λ_o, and the function to be minimized reads:

$$\Omega_o = \varepsilon_e + \frac{E_i}{V_{\rm WS}} - \lambda_o \frac{2n_p}{1-I}. \tag{B.3}$$

Inserting Eq. (B.2) into Eq. (B.3) we have:

$$\Omega_o = \varepsilon_e + n_B \frac{E_i}{A} - \lambda_o \frac{2n_p}{1-I}. \tag{B.4}$$

The equilibrium equations are obtained by minimizing Ω_o in Eq. (B.4) with respect to four chosen variables: r_N, n_i, I, and n_p.

The minimization with respect to r_N reads:

$$\left.\frac{\partial \Omega_o}{\partial r_N}\right|_{n_i, I, n_p} = 0. \tag{B.5}$$

Replacing Eq. (B.4) into Eq. (B.5) leads to:

$$\frac{\partial}{\partial r_N}\left(\frac{E_i}{A}\right) = 0. \tag{B.6}$$

The minimization with respect to the cluster density n_i gives:

$$\left.\frac{\partial \Omega_o}{\partial n_i}\right|_{r_N, I, n_p} = 0. \tag{B.7}$$

This is equivalent to:

$$\frac{\partial}{\partial n_i}\left(\frac{E_i}{A}\right) = 0. \tag{B.8}$$

To obtain the expression of λ_o, we can minimize Ω_o with respect to the cluster isospin asymmetry I:

$$\left.\frac{\partial \Omega_o}{\partial I}\right|_{r_N, n_i, n_p} = 0. \tag{B.9}$$

Substituting the expression of Ω_o into Eq. (B.9), we get:

$$n_B \frac{\partial}{\partial I}\left(\frac{E_i}{A}\right) - \lambda_o \frac{2n_p}{(1-I)^2} = 0. \tag{B.10}$$

Using Eq. (B.2), one can show that:

$$n_B \frac{\partial}{\partial I}\left(\frac{E_i}{A}\right) - \lambda_o \frac{n_B}{(1-I)} = 0. \tag{B.11}$$

From Eq. (B.11), it is straightforward that λ_o can be written as:

$$\lambda_o = (1-I)\frac{\partial}{\partial I}\left(\frac{E_i}{A}\right). \tag{B.12}$$

Finally, minimizing Ω_o with respect to n_p:

$$\left.\frac{\partial \Omega_o}{\partial n_p}\right|_{r_N, n_i, I} = 0. \tag{B.13}$$

This equation results in:

$$\frac{\partial \varepsilon_e}{\partial n_e} + n_B \frac{\partial}{\partial n_p}\frac{E_i}{A} - \lambda_o \frac{2}{1-I} = 0, \tag{B.14}$$

$$\mu_e + \frac{2n_p}{1-I}\frac{\partial}{\partial n_p}\frac{E_i}{A} - \lambda_o \frac{2}{1-I} = 0. \tag{B.15}$$

In the above equation, the charge neutrality, i.e., $n_p = n_e$ and baryonic number conservation, Eq. (B.2), were used. Substituting the expression of λ_o in Eq. (B.12) we get:

$$2\left[\frac{\partial}{\partial I}\left(\frac{E_i}{A}\right) - \frac{n_p}{1-I}\frac{\partial}{\partial n_p}\left(\frac{E_i}{A}\right)\right] = \mu_e. \tag{B.16}$$

In summary, to get the composition of the outer crust, we solve for the four variables (r_N, n_i, I, and n_p) from a system of four equations:

$$\frac{2n_p}{1-I} = n_B, \tag{B.17}$$

$$\frac{\partial}{\partial r_N}\left(\frac{E_i}{A}\right) = 0, \tag{B.18}$$

$$\frac{\partial}{\partial n_i}\left(\frac{E_i}{A}\right) = 0 \tag{B.19}$$

$$2\left[\frac{\partial}{\partial I}\left(\frac{E_i}{A}\right) - \frac{n_p}{1-I}\frac{\partial}{\partial n_p}\left(\frac{E_i}{A}\right)\right] = \mu_e. \tag{B.20}$$

B.2 Inner crust

Similarly, for the inner crust, one needs to add the neutron gas density $n_{\rm gn}$ as an extra variable, and the energy density of the WS cell becomes:

$$\varepsilon_{\rm WS} = \varepsilon_e + \varepsilon_{\rm g}(1-u) + \frac{E_i}{V_{\rm WS}}, \tag{B.21}$$

The baryonic number conservation reads:

$$\begin{aligned} n_B &= \frac{A + n_{\rm gn}(1-u)V_{\rm WS}}{V_{\rm WS}} \\ &= \frac{A}{V_{\rm WS}} + n_{\rm gn}(1-u) \\ &= \frac{2Z}{(1-I)V_{\rm WS}} + n_{\rm gn}(1-u), \\ &= \frac{2n_p}{(1-I)} + n_{\rm gn}(1-u). \end{aligned} \tag{B.22}$$

The volume fraction u can be expressed as:

$$u = \frac{V_N}{V_{\rm WS}}, \tag{B.23}$$

$$u = \frac{A/n_i}{V_{\rm WS}}, \tag{B.24}$$

$$u = \frac{2Z}{(1-I)n_i V_{\rm WS}}, \tag{B.25}$$

$$u = \frac{2n_p}{n_i(1-I)}. \tag{B.26}$$

Therefore, the total baryonic number can be re-written as:

$$n_B = \frac{2n_p}{1-I}\left(1 - \frac{n_{\rm gn}}{n_i}\right) + n_{\rm gn}. \tag{B.27}$$

Similar to Sect. B.1, we can minimize $\varepsilon_{\rm WS}$ in Eq. (B.21) with the constraint in Eq. (B.27) by introducing a Lagrange multiplier λ_i:

$$\Omega = \varepsilon_{\rm WS} - \lambda_i \left[\frac{2n_p}{1-I} \left(1 - \frac{n_{\rm gn}}{n_i} \right) + n_{\rm gn} \right], \tag{B.28}$$

$$\Omega = \varepsilon_e + \varepsilon_{\rm g}(1-u) + \frac{E_i}{V_{\rm WS}} - \lambda_i \left[\frac{2n_p}{1-I} \left(1 - \frac{n_{\rm gn}}{n_i} \right) + n_{\rm gn} \right], \tag{B.29}$$

$$\Omega = \varepsilon_e + \varepsilon_{\rm g} \left(1 - \frac{2n_p}{n_i(1-I)} \right) + \frac{2n_p}{(1-I)} \frac{E_i}{A} - \lambda_i \left[\frac{2n_p}{1-I} \left(1 - \frac{n_{\rm gn}}{n_i} \right) + n_{\rm gn} \right]. \tag{B.30}$$

Minimizing Ω with respect to r_N:

$$\left. \frac{\partial \Omega}{\partial r_N} \right|_{n_i, I, n_p, n_{\rm gn}} = 0, \tag{B.31}$$

$$\frac{\partial}{\partial r_N} \left(\frac{E_i}{A} \right) = 0, \tag{B.32}$$

which is the same as Eq. (B.5) for the outer crust.

Minimizing with respect to the neutron gas density $n_{\rm g}n$, one obtains:

$$\left. \frac{\partial \Omega}{\partial n_{\rm gn}} \right|_{r_N, n_i, I, n_p} = 0, \tag{B.33}$$

$$\left(1 - \frac{2n_p}{n_i(1-I)} \right) \frac{\partial \varepsilon_{\rm g}}{\partial n_{\rm gn}} - \lambda_i \left(1 - \frac{2n_p}{n_i(1-I)} \right) = 0. \tag{B.34}$$

Thus,

$$\lambda_i = \frac{\partial \varepsilon_{\rm g}}{\partial n_{\rm gn}} = \mu_{{\rm HM},n}, \tag{B.35}$$

which is the neutron chemical potential of nuclear matter including the nucleon rest mass (defined in Eq. (2.29)). Note that in the solid phase that we are considering, there is no dependence of the cluster energy per nucleon E_i/A on $n_{\rm gn}$. Therefore, $\partial(E_i/A)/(\partial n_{\rm gn}) = 0$.

The minimization with respect to cluster density n_i reads:

$$\left. \frac{\partial \Omega}{\partial n_i} \right|_{r_N, I, n_p, n_{\rm gn}} = 0, \tag{B.36}$$

$$\frac{2n_p}{(1-I)} \frac{\partial}{\partial n_i} \left(\frac{E_i}{A} \right) + \frac{2n_p}{n_i^2(1-I)} \varepsilon_{\rm g} - \frac{2n_p n_{\rm gn}}{n_i^2(1-I)} \mu_{{\rm HM},n} = 0 \tag{B.37}$$

$$n_i^2 \frac{\partial}{\partial n_i} \left(\frac{E_i}{A} \right) - n_{\rm gn} \mu_{{\rm HM},n} + \varepsilon_{\rm g} = 0, \tag{B.38}$$

$$n_i^2 \frac{\partial}{\partial n_i} \left(\frac{E_i}{A} \right) = P_{\rm gn}. \tag{B.39}$$

with

$$P_{\rm gn} = \mu_{{\rm HM},n} n_{\rm gn} - \varepsilon_{\rm g} \tag{B.40}$$

being the pressure of the neutron background.

Let us turn to the minimization with respect to the cluster isospin asymmetry I:

$$\left.\frac{\partial\Omega}{\partial I}\right|_{r_N,n_i,n_p,n_{gn}} = 0, \tag{B.41}$$

$$\frac{2n_p}{(1-I)^2}\left[\frac{E_i}{A} + (1-I)\frac{\partial}{\partial I}\left(\frac{E_i}{A}\right) - \frac{\varepsilon_g}{n_i} - \left(1-\frac{n_{gn}}{n_i}\right)\mu_{HM,n}\right] = 0, \tag{B.42}$$

$$\frac{E_i}{A} + (1-I)\frac{\partial}{\partial I}\left(\frac{E_i}{A}\right) - \frac{\varepsilon_g}{n_i} - \left(1-\frac{n_{gn}}{n_i}\right)\mu_{HM,n} = 0. \tag{B.43}$$

Therefore,

$$\frac{E_i}{A} + (1-I)\frac{\partial}{\partial I}\left(\frac{E_i}{A}\right) = \mu_{HM,n} - \frac{P_{gn}}{n_i}. \tag{B.44}$$

Finally, the minimization with respect to n_p results in:

$$\left.\frac{\partial\Omega}{\partial n_p}\right|_{r_N,I,n_i,n_{gn}} = 0, \tag{B.45}$$

$$\frac{E_i}{A} + n_p\frac{\partial}{\partial n_p}\left(\frac{E_i}{A}\right) + \frac{1-I}{2}\frac{\partial\varepsilon_e}{\partial n_p} - \frac{\varepsilon_g}{n_i} - \left(1-\frac{n_g}{n_i}\right)\mu_{HM,n} = 0. \tag{B.46}$$

From Eqs. (B.44) and (B.46), we obtain:

$$2\left[\frac{\partial}{\partial I}\left(\frac{E_i}{A}\right) - \frac{n_p}{1-I}\frac{\partial}{\partial n_p}\left(\frac{E_i}{A}\right)\right] = \mu_e. \tag{B.47}$$

To summarize, for the inner crust, we solve the following of equations for five variables: r_N, n_i, I, n_p, and n_{gn}:

$$\frac{2n_p}{1-I}\left(1-\frac{n_{gn}}{n_i}\right) + n_{gn} = n_B, \tag{B.48}$$

$$\frac{\partial}{\partial r_N}\left(\frac{E_i}{A}\right) = 0, \tag{B.49}$$

$$n_i^2\frac{\partial}{\partial n_i}\left(\frac{E_i}{A}\right) = P_{gn}, \tag{B.50}$$

$$\frac{E_i}{A} + (1-I)\frac{\partial}{\partial I}\left(\frac{E_i}{A}\right) = \mu_{HM,n} - \frac{P_{gn}}{n_i}, \tag{B.51}$$

$$2\left[\frac{\partial}{\partial I}\left(\frac{E_i}{A}\right) - \frac{n_p}{1-I}\frac{\partial}{\partial n_p}\left(\frac{E_i}{A}\right)\right] = \mu_e. \tag{B.52}$$

APPENDIX C

Equilibrium equations for proto-neutron-star inner crust

As discussed in Sect. 4.1.3, to obtain the equilibrium composition of the PNS inner crust, one needs to minimize the following equation:

$$\begin{aligned}\Omega = &\frac{2n_p}{1-I}\frac{F_i}{A} + \left[1 - \frac{2n_p}{(1-I)n_i}\right]\mathcal{F}_{\rm g} + \mathcal{F}_e \\ &+ \gamma_1\left[n_B - \frac{2n_p}{1-I}\left(1 - \frac{n_{gn}+n_{gp}}{n_i}\right) - n_{gn} - n_{gp}\right] \\ &+ \gamma_2\left[n_e - n_p - n_{gp}\left(1 - \frac{2n_p}{n_i(1-I)}\right)\right],\end{aligned} \tag{C.1}$$

with

$$\gamma_1 = \mu_n \tag{C.2}$$

$$\gamma_2 = -\mu_n + \mu_p, \tag{C.3}$$

in which μ_n and μ_p are respectively defined as in Eqs. (4.110) and (4.111), obtained from the minimization of Ω with respect to the neutron and proton gas densities, n_{gn} and n_{gp}.

C.1 Minimization with respect to electron density n_e

$$\left.\frac{\partial\Omega}{\partial n_e}\right|_{r_N,I,n_i,n_p,n_{gn},n_{gp}} = 0. \tag{C.4}$$

$$\frac{\partial\mathcal{F}_e}{\partial n_e} - \gamma_2 = 0. \tag{C.5}$$

Thus

$$\gamma_2 = \frac{\partial\mathcal{F}_e}{\partial n_e} = \mu_e. \tag{C.6}$$

From Eqs. (C.3) and (C.6), we get:

$$\mu_p + \mu_e = \mu_n, \tag{C.7}$$

which is the beta equilibrium equation for the gas components.

C.2 Minimization with respect to r_N

$$\left.\frac{\partial \Omega}{\partial r_N}\right|_{I,n_i,n_p,n_{\rm gn},n_{\rm gp},n_e} = 0, \tag{C.8}$$

$$\frac{\partial (F_i/A)}{\partial r_N} = 0. \tag{C.9}$$

If the crust is in the liquid phase, then Eq. (C.9) is equivalent to:

$$\frac{\partial (f_{\rm Coul} + f_{\rm surf} + f_{\rm curv} + f_{\rm trans})}{\partial r_N} = 0. \tag{C.10}$$

C.3 Minimization with respect to cluster density n_i

$$\begin{aligned}
\left.\frac{\partial \Omega}{\partial n_i}\right|_{r_N,I,n_p,n_{\rm gn},n_{\rm gp},n_e} &= 0 \\
\frac{\partial}{\partial n_i}\left(\frac{F_i}{A}\right) + \frac{1}{n_i^2}\mathcal{F}_{\rm g} - \mu_n(n_{\rm gn}+n_{\rm gp})\frac{1}{n_i^2} - (-\mu_n+\mu_p)\frac{n_{\rm gp}}{n_i^2} &= 0, \\
n_i^2 \frac{\partial}{\partial n_i}\left(\frac{F_i}{A}\right) &= \mu_p n_{\rm gp} + \mu_n n_{\rm gn} - \mathcal{F}_{\rm g}, \\
P_{\rm cl} &= P_{\rm g},
\end{aligned} \tag{C.11}$$

in which $P_{\rm cl} = n_i^2 \frac{\partial}{\partial n_i}\left(\frac{F_i}{A}\right)$ is the cluster pressure, and $P_g = \mu_p n_{\rm gp} + \mu_n n_{\rm gn} - \mathcal{F}_{\rm g}$ is the gas density. The latter includes the in-medium effect. Thus, Eq. (C.11) indicates the pressure equilibrium between the cluster and the surrounding nucleon gas.

C.4 Minimization with respect to the cluster asymmetry I

$$\begin{aligned}
\left.\frac{\partial \Omega}{\partial I}\right|_{r_N,n_i,n_p,n_{\rm gn},n_{\rm gp},n_e} &= 0 \\
\frac{2n_p}{(1-I)^2}\left[\frac{F_i}{A} + (1-I)\frac{\partial}{\partial I}\left(\frac{F_i}{A}\right) - \frac{\mathcal{F}_{\rm g}}{n_i} - \gamma_1\left(1 - \frac{n_{\rm gn}+n_{\rm gp}}{n_i}\right) - \gamma_2\frac{n_{\rm gp}}{n_i}\right] &= 0, \\
\frac{F_i}{A} + (1-I)\frac{\partial}{\partial I}\left(\frac{F_i}{A}\right) - \frac{\mathcal{F}_{\rm g}}{n_i} - \mu_n\left(1 - \frac{n_{\rm gn}+n_{\rm gp}}{n_i}\right) - (\mu_p-\mu_n)\frac{n_{\rm gp}}{n_i} &= 0, \\
\frac{F_i}{A} + (1-I)\frac{\partial}{\partial I}\left(\frac{F_i}{A}\right) &= \mu_n - \frac{P_{\rm g}}{n_i}.
\end{aligned} \tag{C.12}$$

C.5 Minimization with respect to n_p

$$\left.\frac{\partial \mathcal{L}}{\partial n_p}\right|_{r_N,I,n_i,n_{gn},n_{gp},n_e} = 0$$
$$\frac{F_i}{A} + n_p \frac{\partial}{\partial n_p}\left(\frac{F_i}{A}\right) - \frac{1}{n_i}\mathcal{F}_g - \gamma_1\left(1 - \frac{n_{gn}+n_{gp}}{n_i}\right) - \gamma_2\left(-\frac{1-I}{2} + \frac{n_{gp}}{n_i}\right) = 0. \tag{C.13}$$

We can identify similar terms in Eqs. (C.12) and (C.13), therefore, we have:

$$(1-I)\frac{\partial}{\partial I}\left(\frac{F_i}{A}\right) - n_p \frac{\partial}{\partial n_p}\left(\frac{F_i}{A}\right) - \gamma_2 \frac{1-I}{2} = 0. \tag{C.14}$$

Thus

$$2\left[\frac{\partial}{\partial I}\left(\frac{F_i}{A}\right) - \frac{n_p}{1-I}\frac{\partial}{\partial n_p}\left(\frac{F_i}{A}\right)\right] = \mu_n - \mu_p. \tag{C.15}$$

Bibliography

[1] P. Haensel, A. Y. Potekhin, and D. G. Yakovlev, *Neutron Stars 1 : Equation of State and Structure*. New York: Springer, 2007, vol. 326. [Online]. Available: https://link.springer.com/book/10.1007/978-0-387-47301-7

[2] W. Baade and F. Zwicky, "On Super-Novae," *Proceedings of the National Academy of Sciences*, vol. 20, no. 5, pp. 254–259, May 1934. [Online]. Available: https://pnas.org/doi/full/10.1073/pnas.20.5.254

[3] A. Hewish, S. J. Bell, J. D. H. Pilkington, P. F. Scott, and R. A. Collins, "Observation of a Rapidly Pulsating Radio Source," *Nature*, vol. 217, no. 5130, pp. 709–713, Feb 1968. [Online]. Available: https://www.nature.com/articles/217709a0

[4] J. M. Comella, H. D. Craft, R. V. E. Lovelace, J. M. Sutton, and G. L. Tyler, "Crab Nebula Pulsar NP 0532," *Nature*, vol. 221, no. 5179, pp. 453–454, Feb 1969. [Online]. Available: https://www.nature.com/articles/221453a0

[5] T. Gold, "Rotating Neutron Stars as the Origin of the Pulsating Radio Sources," *Nature*, vol. 218, no. 5143, pp. 731–732, May 1968. [Online]. Available: https://www.nature.com/articles/218731a0

[6] "ATNF Pulsar Catalogue," https://www.atnf.csiro.au/research/pulsar/psrcat/.

[7] M. Oertel, M. Hempel, T. Klähn, and S. Typel, "Equations of state for supernovae and compact stars," *Reviews of Modern Physics*, vol. 89, p. 015007, Mar 2017. [Online]. Available: https://doi.org/10.1103/RevModPhys.89.015007

[8] J. M. Lattimer and M. Prakash, "The Physics of Neutron Stars," *Science*, vol. 304, no. 5670, pp. 536–542, Apr 2004. [Online]. Available: https://www.science.org/doi/10.1126/science.1090720

[9] G. Baym, H. A. Bethe, and C. J. Pethick, "Neutron star matter," *Nuclear Physics A*, vol. 175, no. 2, pp. 225–271, 1971. [Online]. Available: https://doi.org/10.1016/0375-9474(71)90281-8

[10] G. Watanabe, K. Sato, K. Yasuoka, and T. Ebisuzaki, "Structure of cold nuclear matter at subnuclear densities by quantum molecular dynamics," *Physical Review C - Nuclear Physics*, vol. 68, no. 3, p. 20, 2003. [Online]. Available: https://doi.org/10.1103/PhysRevC.68.035806

[11] J. Lattimer, C. Pethick, D. Ravenhall, and D. Lamb, "Physical properties of hot, dense matter: The general case," *Nuclear Physics A*, vol. 432, no. 3, pp. 646–742, Jan 1985. [Online]. Available: https://doi.org/10.1016/0375-9474(85)90006-5

[12] D. G. Ravenhall, C. J. Pethick, and J. R. Wilson, "Structure of Matter below Nuclear Saturation Density," *Physical Review Letters*, vol. 50, no. 26, pp. 2066–2069, Jun 1983. [Online]. Available: https://doi.org/10.1103/PhysRevLett.50.2066

[13] G. Watanabe, K. Iida, and K. Sato, "Thermodynamic properties of nuclear "pasta" in neutron star crusts," *Nuclear Physics A*, vol. 676, no. 1-4, pp. 455–473, Aug 2000. [Online]. Available: https://doi.org/10.1016/S0375-9474(00)00197-4

[14] A. G. Cameron, "Neutron Star Models," *The Astrophysical Journal*, vol. 130, p. 884, Nov 1959. [Online]. Available: http://adsabs.harvard.edu/doi/10.1086/146780

[15] V. A. Ambartsumyan and S. G. Saakyan, "The Degenerate Superdense Gas of Elementary Particles," *Soviet Astronomy*, vol. 37, no. 2, pp. 193–368, 1960. [Online]. Available: https://adsabs.harvard.edu/full/1960SvA.....4..187A

[16] N. K. Glendenning, "The hyperon composition of neutron stars," *Physics Letters B*, vol. 114, no. 6, pp. 392–396, Aug 1982. [Online]. Available: https://linkinghub.elsevier.com/retrieve/pii/0370269382900788

[17] R. Knorren, M. Prakash, and P. J. Ellis, "Strangeness in hadronic stellar matter," *Physical Review C*, vol. 52, no. 6, pp. 3470–3482, Dec 1995. [Online]. Available: https://link.aps.org/doi/10.1103/PhysRevC.52.3470

[18] M. Baldo, G. F. Burgio, and H.-J. Schulze, "Hyperon stars in the Brueckner-Bethe-Goldstone theory," *Physical Review C*, vol. 61, no. 5, p. 055801, Apr 2000. [Online]. Available: https://link.aps.org/doi/10.1103/PhysRevC.61.055801

[19] H.-J. Schulze and T. Rijken, "Maximum mass of hyperon stars with the Nijmegen ESC08 model," *Physical Review C*, vol. 84, p. 035801, Sep 2011. [Online]. Available: https://link.aps.org/doi/10.1103/PhysRevC.84.035801

[20] T. Katayama and K. Saito, "Hyperons in neutron stars," *Physics Letters B*, vol. 747, pp. 43–47, 2015. [Online]. Available: https://www.sciencedirect.com/science/article/pii/S0370269315002026

[21] Y. Yamamoto, T. Furumoto, N. Yasutake, and T. A. Rijken, "Hyperon-mixed neutron star with universal many-body repulsion," *The European Physical Journal A*, vol. 52, no. 2, p. 19, Feb 2016. [Online]. Available: http://link.springer.com/10.1140/epja/i2016-16019-0

[22] A. Sedrakian and A. Harutyunyan, "Delta-resonances and hyperons in proto-neutron stars and merger remnants," *The European Physical Journal A*, vol. 58, no. 7, p. 137, Jul 2022. [Online]. Available: https://doi.org/10.1140/epja/s10050-022-00792-w

[23] C. Providência, M. Fortin, H. Pais, and A. Rabhi, "Hyperonic Stars and the Nuclear Symmetry Energy," *Frontiers in Astronomy and Space Sciences*, vol. 6, no. March, pp. 1–20, Mar 2019. [Online]. Available: https://www.frontiersin.org/article/10.3389/fspas.2019.00013/full

[24] T. Malik and C. Providência, "Bayesian inference of signatures of hyperons inside neutron stars," *Physical Review D*, vol. 106, no. 6, p. 063024, Sep 2022. [Online]. Available: https://link.aps.org/doi/10.1103/PhysRevD.106.063024

[25] G. Fiorella Burgio and A. F. Fantina, *Nuclear Equation of State for Compact Stars and Supernovae*. Cham: Springer International Publishing, 2018, pp. 255–335. [Online]. Available: https://doi.org/10.1007/978-3-319-97616-7_6

[26] D. Logoteta, "Hyperons in Neutron Stars," *Universe*, vol. 7, no. 11, p. 408, Oct 2021. [Online]. Available: https://www.mdpi.com/2218-1997/7/11/408

[27] I. Vidaña, "Neutron stars and the hyperon puzzle," *EPJ Web of Conferences*, vol. 271, p. 09001, 2022. [Online]. Available: https://doi.org/10.1051/epjconf/202227109001

[28] D. Blaschke and N. Chamel, *Phases of Dense Matter in Compact Stars*. Cham: Springer International Publishing, 2018, pp. 337–400. [Online]. Available: https://doi.org/10.1007/978-3-319-97616-7_7

[29] G. F. Burgio, H. J. Schulze, I. Vidaña, and J. B. Wei, "Neutron stars and the nuclear equation of state," *Progress in Particle and Nuclear Physics*, vol. 120, p. 103879, 2021. [Online]. Available: https://doi.org/10.1016/j.ppnp.2021.103879

[30] H. Đapo, B.-J. Schaefer, and J. Wambach, "Appearance of hyperons in neutron stars," *Physical Review C*, vol. 81, no. 3, p. 035803, Mar 2010. [Online]. Available: https://link.aps.org/doi/10.1103/PhysRevC.81.035803

[31] J. Antoniadis, P. C. C. Freire, N. Wex, T. M. Tauris, L. R. S. *et al.*, "A Massive Pulsar in a Compact Relativistic Binary," *Science*, vol. 340, 2013. [Online]. Available: https://www.science.org/doi/10.1126/science.1233232

[32] G. Baym, T. Hatsuda, T. Kojo, P. D. Powell, Y. Song, and T. Takatsuka, "From hadrons to quarks in neutron stars: A review," *Reports on Progress in Physics*, vol. 81, no. 5, 2018. [Online]. Available: https://iopscience.iop.org/article/10.1088/1361-6633/aaae14

[33] V. Dexheimer, M. Hempel, I. Iosilevskiy, and S. Schramm, "Phase transitions in dense matter," *Nuclear Physics A*, vol. 967, pp. 780–783, Nov 2017. [Online]. Available: https://linkinghub.elsevier.com/retrieve/pii/S0375947417301021

[34] A. Pfaff, H. Hansen, and F. Gulminelli, "Bayesian analysis of the properties of hybrid stars with the Nambu–Jona-Lasinio model," *Physical Review C*, vol. 105, no. 3, p. 035802, Mar 2022. [Online]. Available: https://link.aps.org/doi/10.1103/PhysRevC.105.035802

[35] T. E. Riley, A. L. Watts, S. Bogdanov, P. S. Ray *et al.*, "A NICER View of PSR J0030+0451: Millisecond Pulsar Parameter Estimation," *The Astrophysical Journal Letters*, vol. 887, no. 1, p. L21, Dec 2019. [Online]. Available: https://dx.doi.org/10.3847/2041-8213/ab481c

[36] M. C. Miller, F. K. Lamb, A. J. Dittmann, S. Bogdanov, Z. Arzoumanian *et al.*, "PSR J0030+0451 Mass and Radius from NICER Data and Implications for the Properties of Neutron Star Matter," *The Astrophysical Journal Letters*, vol. 887, no. 1, p. L24, Dec 2019. [Online]. Available: https://dx.doi.org/10.3847/2041-8213/ab50c5

[37] T. E. Riley, A. L. Watts, P. S. Ray, S. Bogdanov, S. Guillot *et al.*, "A NICER View of the Massive Pulsar PSR J0740+6620 Informed by Radio Timing and XMM-Newton Spectroscopy," *The Astrophysical Journal Letters*, vol. 918, no. 2, p. L27, Sep 2021. [Online]. Available: https://dx.doi.org/10.3847/2041-8213/ac0a81

[38] M. C. Miller, F. K. Lamb, A. J. Dittmann, S. Bogdanov, Z. Arzoumanian *et al.*, "The Radius of PSR J0740+6620 from NICER and XMM-Newton Data," *The Astrophysical Journal Letters*, vol. 918, no. 2, p. L28, Sep 2021. [Online]. Available: https://dx.doi.org/10.3847/2041-8213/ac089b

[39] B. P. Abbott, R. Abbott, T. D. Abbott, F. Acernese *et al.*, "GW170817: Observation of Gravitational Waves from a Binary Neutron Star Inspiral," *Physical Review Letters*, vol. 119, p. 161101, Oct 2017. [Online]. Available: https://doi.org/10.1103/PhysRevLett.119.161101

[40] B. Abbott, R. Abbott, T. D. Abbott, F. Acernese *et al.*, "GW170817: Measurements of Neutron Star Radii and Equation of State," *Physical Review Letters*, vol. 121, p. 161101, Oct 2018. [Online]. Available: https://doi.org/10.1103/PhysRevLett.119.161101

[41] B. P. Abbott, R. Abbott, T. D. Abbott, F. Acernese *et al.*, "Properties of the Binary Neutron Star Merger GW170817," *Physical Review X*, vol. 9, p. 011001, Jan 2019. [Online]. Available: https://doi.org/10.1103/PhysRevX.9.011001

[42] B. P. Abbott, R. Abbott, T. D. Abbott, F. Acernese, K. Ackley *et al.*, "Prospects for observing and localizing gravitational-wave transients with Advanced LIGO, Advanced Virgo and KAGRA," *Living Reviews in Relativity*, vol. 23, no. 3, 2020. [Online]. Available: https://doi.org/10.1007/lrr-2016-1

[43] L. McLerran and S. Reddy, "Quarkyonic Matter and Neutron Stars," *Physical Review Letters*, vol. 122, no. 12, p. 122701, Mar 2019. [Online]. Available: https://link.aps.org/doi/10.1103/PhysRevLett.122.122701

[44] R. Somasundaram and J. Margueron, "Impact of massive neutron star radii on the nature of phase transitions in dense matter," *Europhysics Letters*, vol. 138, no. 1, 2022. [Online]. Available: https://iopscience.iop.org/article/10.1209/0295-5075/ac63de

[45] A. Kumar, D. Dey, S. Haque, R. Mallick, and S. K. Patra, "Quarkyonic Model for Neutron Star Matter: A Relativistic Mean-Field Approach," no. April, Apr 2023. [Online]. Available: http://arxiv.org/abs/2304.08223

[46] J. M. Lattimer, "Neutron Star Mass and Radius Measurements," *Universe*, vol. 5, no. 7, p. 159, Jun 2019. [Online]. Available: https://www.mdpi.com/2218-1997/5/7/159

[47] L. Suleiman, M. Fortin, J. L. Zdunik, and P. Haensel, "Influence of the crust on the neutron star macrophysical quantities and universal relations," *Physical Review C*, vol. 104, no. 1, p. 015801, Jul 2021. [Online]. Available: https://link.aps.org/doi/10.1103/PhysRevC.104.015801

[48] I. H. Stairs, "Testing General Relativity with Pulsar Timing," *Living Reviews in Relativity*, vol. 6, no. 1, p. 5, Dec 2003. [Online]. Available: http://link.springer.com/10.12942/lrr-2003-5

[49] P. B. Demorest, T. Pennucci, S. M. Ransom, M. S. E. Roberts, and J. W. T. Hessels, "A two-solar-mass neutron star measured using Shapiro delay," *Nature*, vol. 467, no. 7319, pp. 1081–1083, Oct 2010. [Online]. Available: http://www.nature.com/articles/nature09466

[50] E. Fonseca, T. T. Pennucci, J. A. Ellis, I. H. Stairs *et al.*, "the Nanograv Nine-Year Data Set: Mass and Geometric Measurements of Binary Millisecond Pulsars," *The Astrophysical Journal*, vol. 832, no. 2, p. 167, 2016. [Online]. Available: http://dx.doi.org/10.3847/0004-637X/832/2/167

[51] Z. Arzoumanian, A. Brazier, S. Burke-Spolaor, S. Chamberlin *et al.*, "The NANOGrav 11-year Data Set: High-precision Timing of 45 Millisecond Pulsars," *The Astrophysical Journal Supplement Series*, vol. 235, no. 2, p. 37, Apr 2018. [Online]. Available: https://iopscience.iop.org/article/10.3847/1538-4365/aab5b0

[52] E. Fonseca, H. T. Cromartie, T. T. Pennucci, P. S. Ray *et al.*, "Refined Mass and Geometric Measurements of the High-mass PSR J0740+6620," *The Astrophysical Journal Letters*, vol. 915, no. 1, p. L12, Jul 2021. [Online]. Available: https://dx.doi.org/10.3847/2041-8213/ac03b8

[53] F. Özel and P. Freire, "Masses, Radii, and the Equation of State of Neutron Stars," *Annual Review of Astronomy and Astrophysics*, vol. 54, no. 1, pp. 401–440, Sep 2016. [Online]. Available: https://www.annualreviews.org/doi/10.1146/annurev-astro-081915-023322

[54] J. Lattimer, "Neutron Stars and the Nuclear Matter Equation of State," *Annual Review of Nuclear and Particle Science*, vol. 71, no. 1, pp. 433–464, Sep 2021. [Online]. Available: https://www.annualreviews.org/doi/10.1146/annurev-nucl-102419-124827

[55] D. Viganó, N. Rea, J. A. Pons, R. Perna, D. N. Aguilera, and J. A. Miralles, "Unifying the observational diversity of isolated neutron stars via magneto-thermal evolution models," *Monthly Notices of the Royal Astronomical Society*, vol. 434, no. 1, pp. 123–141, 2013. [Online]. Available: https://doi.org/10.1093/mnras/stt1008

[56] J. A. Pons, D. Viganò, and N. Rea, "A highly resistive layer withi. The crust of X-ray pulsars limits their spin periods," *Nature Physics*, vol. 9, no. 7, pp. 431–434, 2013. [Online]. Available: https://www.nature.com/articles/nphys2640

[57] C. M. Espinoza, A. G. Lyne, B. W. Stappers, and M. Kramer, "A study of 315 glitches in the rotation of 102 pulsars," *Monthly Notices of the Royal Astronomical Society*, vol. 414, no. 2, pp. 1679–1704, 06 2011. [Online]. Available: https://doi.org/10.1111/j.1365-2966.2011.18503.x

[58] N. Chamel and P. Haensel, "Physics of neutron star crusts," *Living Reviews in Relativity*, vol. 11, 2008. [Online]. Available: https://doi.org/10.12942/lrr-2008-10

[59] T. Carreau, F. Gulminelli, and J. Margueron, "General predictions for the neutron star crustal moment of inertia," *Physical Review C*, vol. 100, p. 055803, Nov 2019. [Online]. Available: https://link.aps.org/doi/10.1103/PhysRevC.100.055803

[60] J. Swank, "Quasi-Periodic Oscillations from Low-mass X-Ray Binaries with Neutron Stars," in *AIP Conference Proceedings*, vol. 714. AIP, 2004, pp. 357–364. [Online]. Available: https://pubs.aip.org/aip/acp/article/714/1/357-364/660573

[61] J. Wang, "A Brief Review for Quasi-Periodic Oscillations in Neutron-Star Low-Mass X-Ray Binaries," *International Journal of Astronomy and Astrophysics*, vol. 06, no. 01, pp. 82–98, 2016. [Online]. Available: http://www.scirp.org/journal/doi.aspx?DOI=10.4236/ijaa.2016.61006

[62] H.-M. Zhang, R.-Y. Liu, S.-Q. Zhong, and X.-Y. Wang, "Magnetar Giant Flare Origin for GRB 200415A Inferred from a New Scaling Relation," *The Astrophysical Journal*, vol. 903, no. 2, p. L32, Nov 2020. [Online]. Available: http://dx.doi.org/10.3847/2041-8213/abc2c9

[63] A. T. Deibel, A. W. Steiner, and E. F. Brown, "Magnetar giant flare oscillations and the nuclear symmetry energy," *Physical Review C - Nuclear Physics*, vol. 90, no. 2, Mar 2013. [Online]. Available: http://dx.doi.org/10.1103/PhysRevC.90.025802

[64] J. Margueron, R. Hoffmann Casali, and F. Gulminelli, "Equation of state for dense nucleonic matter from metamodeling. I. Foundational aspects," *Physical Review C*, vol. 97, no. 2, p. 025805, Feb 2018. [Online]. Available: https://doi.org/10.1103/PhysRevC.97.025805

[65] ——, "Equation of state for dense nucleonic matter from metamodeling. II. Predictions for neutron star properties," *Physical Review C*, vol. 97, no. 2, p. 025806, Feb 2018. [Online]. Available: https://doi.org/10.1103/PhysRevC.97.025806

[66] J. Negele and D. Vautherin, "Neutron star matter at sub-nuclear densities," *Nuclear Physics A*, vol. 207, no. 2, pp. 298–320, 1973. [Online]. Available: https://www.sciencedirect.com/science/article/pii/0375947473903497

[67] A. Pastore, S. Baroni, and C. Losa, "Superfluid properties of the inner crust of neutron stars," *Physical Review C - Nuclear Physics*, vol. 84, no. 6, p. 065807, 2011. [Online]. Available: https://journals.aps.org/prc/abstract/10.1103/PhysRevC.84.065807

[68] F. Grill, J. Margueron, and N. Sandulescu, "Cluster structure of the inner crust of neutron stars in the Hartree-Fock-Bogoliubov approach," *Physical Review C*, vol. 84, no. 6, p. 065801, Dec 2011. [Online]. Available: https://link.aps.org/doi/10.1103/PhysRevC.84.065801

[69] M. Shelley and A. Pastore, "Comparison between the Thomas–fermi and Hartree–Fock–Bogoliubov methods in the inner crust of a neutron star: The role of pairing correlations," *Universe*, vol. 6, no. 11, 2020. [Online]. Available: https://doi.org/10.3390/universe6110206

[70] M. Baldo, U. Lombardo, E. Saperstein, and S. Tolokonnikov, "The role of superfluidity in the structure of the neutron star inner crust," *Nuclear Physics A*, vol. 750, no. 2-4, pp. 409–424, Apr 2005. [Online]. Available: https://linkinghub.elsevier.com/retrieve/pii/S0375947405000072

[71] M. Baldo, E. E. Saperstein, and S. V. Tolokonnikov, "The role of the boundary conditions in the Wigner-Seitz approximation applied to the neutron star inner crust," *Nuclear Physics A*, vol. 775, no. 3-4, pp. 235–244, 2006. [Online]. Available: https://www.sciencedirect.com/science/article/abs/pii/S0375947406004143

[72] ——, "A realistic model of superfluidity in the neutron star inner crust," *The European Physical Journal A*, vol. 32, no. 1, pp. 97–108, Apr 2007. [Online]. Available: http://link.springer.com/10.1140/epja/i2006-10356-5

[73] F. Aymard, F. Gulminelli, and J. Margueron, "In-medium nuclear cluster energies within the extended thomas-fermi approach," *Physical Review C*, vol. 89, p. 065807, Jun 2014. [Online]. Available: https://link.aps.org/doi/10.1103/PhysRevC.89.065807

[74] N. Martin and M. Urban, "Liquid-gas coexistence versus energy minimization with respect to the density profile in the inhomogeneous inner crust of neutron stars," *Physical Review C*, vol. 92, p. 015803, Jul 2015. [Online]. Available: https://link.aps.org/doi/10.1103/PhysRevC.92.015803

[75] J. M. Pearson, N. Chamel, A. Y. Potekhin, A. F. Fantina, C. Ducoin, A. K. Dutta, and S. Goriely, "Unified equations of state for cold non-accreting neutron stars with Brussels-Montreal functionals - I. Role of symmetry energy," *Monthly Notices of the Royal Astronomical Society*, vol. 481, no. 3, pp. 2994–3026, 2018. [Online]. Available: https://doi.org/10.1093/mnras/sty2413

[76] J. M. Pearson, N. Chamel, and A. Y. Potekhin, "Unified equations of state for cold nonaccreting neutron stars with Brussels-Montreal functionals. II. Pasta phases

in semiclassical approximation," *Physical Review C*, vol. 101, p. 015802, Jan 2020. [Online]. Available: https://doi.org/10.1103/PhysRevC.101.015802

[77] M. Shelley and A. Pastore, "Systematic analysis of inner crust composition using the extended thomas-fermi approximation with pairing correlations," *Physical Review C*, vol. 103, p. 035807, Mar 2021. [Online]. Available: https://link.aps.org/doi/10.1103/PhysRevC.103.035807

[78] G. Grams, J. Margueron, R. Somasundaram, N. Chamel, and S. Goriely, "Neutron star crust properties: comparison between the compressible liquid-drop model and the extended thomas-fermi approach," *Journal of Physics: Conference Series*, vol. 2340, no. 1, p. 012030, Sep 2022. [Online]. Available: https://dx.doi.org/10.1088/1742-6596/2340/1/012030

[79] T. Carreau, F. Gulminelli, N. Chamel, A. F. Fantina, and J. M. Pearson, "Crystallization of the inner crust of a neutron star and the influence of shell effects," *Astronomy & Astrophysics*, vol. 635, p. A84, Mar 2020. [Online]. Available: https://doi.org/10.1051/0004-6361/201937236

[80] T. Carreau, A. F. Fantina, and F. Gulminelli, "Inner crust of a neutron star at the point of crystallization in a multicomponent approach," *Astronomy & Astrophysics*, vol. 640, p. A77, Aug 2020. [Online]. Available: https://doi.org/10.1051/0004-6361/202038347

[81] A. F. Fantina, S. De Ridder, N. Chamel, and F. Gulminelli, "Crystallization of the outer crust of a non-accreting neutron star," *Astronomy & Astrophysics*, vol. 633, p. A149, Jan 2020. [Online]. Available: https://doi.org/10.1051/0004-6361/201936359

[82] F. Gulminelli and A. R. Raduta, "Unified treatment of subsaturation stellar matter at zero and finite temperature," *Physical Review C*, vol. 92, no. 5, p. 055803, Nov 2015. [Online]. Available: https://doi.org/10.1103/PhysRevC.92.055803

[83] G. Grams, S. Giraud, A. F. Fantina, and F. Gulminelli, "Distribution of nuclei in equilibrium stellar matter from the free-energy density in a Wigner-Seitz cell," *Physical Review C*, vol. 97, no. 3, p. 035807, Mar 2018. [Online]. Available: https://link.aps.org/doi/10.1103/PhysRevC.97.035807

[84] A. Burrows and J. M. Lattimer, "On the accuracy of the single-nucleus approximation in the equation of state of hot, dense matter," *The Astrophysical Journal*, vol. 285, no. 9, p. 294, Oct 1984. [Online]. Available: http://adsabs.harvard.edu/doi/10.1086/162505

[85] S. R. Souza, A. W. Steiner, W. G. Lynch, R. Donangelo, and M. A. Famiano, "Comparison of statistical treatments for the equation of state for core-collapse supernovae," *The Astrophysical Journal*, vol. 707, no. 2, pp. 1495–1505, Dec 2009. [Online]. Available: https://iopscience.iop.org/article/10.1088/0004-637X/707/2/1495

[86] M. R. Pelicer, D. P. Menezes, C. C. Barros, and F. Gulminelli, "Fluctuations in the nuclear pasta phase," *Physical Review C*, vol. 104, p. L022801, Aug 2021. [Online]. Available: https://link.aps.org/doi/10.1103/PhysRevC.104.L022801

[87] M. Hempel and J. Schaffner-Bielich, "A statistical model for a complete supernova equation of state," *Nuclear Physics A*, vol. 837, no. 3-4, pp. 210–254, 2010. [Online]. Available: http://dx.doi.org/10.1016/j.nuclphysa.2010.02.010

[88] A. Botvina and I. Mishustin, "Statistical approach for supernova matter," *Nuclear Physics A*, vol. 843, no. 1-4, pp. 98–132, Oct 2010. [Online]. Available: https://linkinghub.elsevier.com/retrieve/pii/S0375947410005099

[89] C. C. Barros, D. P. Menezes, and F. Gulminelli, "Fluctuations in the composition of nuclear pasta in symmetric nuclear matter at finite temperature," *Physical Review C*, vol. 101, no. 3, p. 035211, Mar 2020. [Online]. Available: https://doi.org/10.1103/PhysRevC.101.035211

[90] J. M. Lattimer and F. Douglas Swesty, "A generalized equation of state for hot, dense matter," *Nuclear Physics A*, vol. 535, no. 2, pp. 331–376, Dec 1991. [Online]. Available: https://doi.org/10.1016/0375-9474(91)90452-C

[91] H. Shen, H. Toki, K. Oyamatsu, and K. Sumiyoshi, "Relativistic equation of state of nuclear matter for supernova and neutron star," *Nuclear Physics A*, vol. 637, no. 3, pp. 435–450, 1998. [Online]. Available: https://doi.org/10.1016/S0375-9474(98)00236-X

[92] S. S. Avancini, C. C. Barros, L. Brito, S. Chiacchiera, D. P. Menezes, and C. Providência, "Light clusters in nuclear matter and the "pasta" phase," *Physical Review C*, vol. 85, no. 3, p. 035806, Mar 2012. [Online]. Available: https://doi.org/10.1103/PhysRevC.85.035806

[93] S. S. Avancini, M. Ferreira, H. Pais, C. Providência, and G. Röpke, "Light clusters and pasta phases in warm and dense nuclear matter," *Physical Review C*, vol. 95, no. 4, p. 045804, Apr 2017. [Online]. Available: http://link.aps.org/doi/10.1103/PhysRevC.95.045804

[94] H. Pais, S. Chiacchiera, and C. Providência, "Light clusters, pasta phases, and phase transitions in core-collapse supernova matter," *Physical Review C*, vol. 91, no. 5, p. 055801, May 2015. [Online]. Available: https://doi.org/10.1103/PhysRevC.91.055801

[95] "McGill Online Magnetar Catalog," http://www.physics.mcgill.ca/~pulsar/magnetar/main.html.

[96] V. M. Kaspi and A. M. Beloborodov, "Magnetars," *Annual Review of Astronomy and Astrophysics*, vol. 55, pp. 261–301, 2017. [Online]. Available: https://www.annualreviews.org/doi/abs/10.1146/annurev-astro-081915-023329

[97] N. Chamel, R. L. Pavlov, L. M. Mihailov, C. J. Velchev, Z. K. Stoyanov, Y. D. Mutafchieva, M. D. Ivanovich, J. M. Pearson, and S. Goriely, "Properties of the outer crust of strongly magnetized neutron stars from Hartree-Fock-Bogoliubov atomic mass models," *Physical Review C*, vol. 86, no. 5, p. 055804, Nov 2012. [Online]. Available: https://link.aps.org/doi/10.1103/PhysRevC.86.055804

[98] D. Chatterjee, J. Novak, and M. Oertel, "Structure of ultra-magnetised neutron stars," *The European Physical Journal A*, vol. 57, no. 8, p. 249, Aug 2021. [Online]. Available: https://link.springer.com/10.1140/epja/s10050-021-00525-5

[99] N. Chamel, A. F. Fantina, L. Suleiman, J.-L. Zdunik, and P. Haensel, "Internal Heating in Magnetars: Role of Electron Captures," *Journal of Physics: Conference Series*, vol. 2340, no. 1, Oct 2022. [Online]. Available: http://arxiv.org/abs/2210.02790http://dx.doi.org/10.1088/1742-6596/2340/1/012029

[100] X. Wang, J. Li, J. Fang, H. Pais, and C. m. c. Providência, "Pasta phases in neutron stars under strong magnetic fields," *Physical Review D*, vol. 105, p. 063004, Mar 2022. [Online]. Available: https://link.aps.org/doi/10.1103/PhysRevD.105.063004

[101] A. Le Fèvre, Y. Leifels, W. Reisdorf, J. Aichelin, and C. Hartnack, "Constraining the nuclear matter equation of state around twice saturation density," *Nuclear Physics A*, vol. 945, pp. 112–133, 2016. [Online]. Available: https://doi.org/10.1016/j.nuclphysa.2015.09.015

[102] P. Russotto, S. Gannon, S. Kupny, P. Lasko, L. Acosta *et al.*, "Results of the ASY-EOS experiment at GSI: The symmetry energy at suprasaturation density," *Physical Review C*, vol. 94, p. 034608, Sep 2016. [Online]. Available: https://doi.org/10.1103/PhysRevC.94.034608

[103] S. Huth, P. T. H. Pang, I. Tews *et al.*, "Constraining neutron-star matter with microscopic and macroscopic collisions," *Nature*, vol. 606, pp. 276–280, Jun 2022. [Online]. Available: https://doi.org/10.1038/s41586-022-04750-w

[104] "NICER PSR J0030+0451 Illinois-Maryland MCMC Samples," https://zenodo.org/record/3473466#.Y9pxhVNKhH5.

[105] "NICER PSR J0740+6620 Illinois-Maryland MCMC Samples," https://zenodo.org/record/4670689#.Y9pxiVNKhH6.

[106] J. B. Hartle, "Slowly Rotating Relativistic Stars. 1. Equations of Structure," *Astrophysical Journal*, vol. 150, pp. 1005–1029, 1967. [Online]. Available: https://adsabs.harvard.edu/full/1967ApJ...150.1005H

[107] J. M. Pearson, N. Chamel, S. Goriely, and C. Ducoin, "Inner crust of neutron stars with mass-fitted Skyrme functionals," *Physical Review C*, vol. 85, p. 065803, Jun 2012. [Online]. Available: https://doi.org/10.1103/PhysRevC.85.065803

[108] T. Lesinski, K. Bennaceur, T. Duguet, and J. Meyer, "Isovector splitting of nucleon effective masses, ab initio benchmarks and extended stability criteria for Skyrme energy functionals," *Physical Review C*, vol. 74, p. 044315, Oct 2006. [Online]. Available: https://doi.org/10.1103/PhysRevC.74.044315

[109] R. Somasundaram, C. Drischler, I. Tews, and J. Margueron, "Constraints on the nuclear symmetry energy from asymmetric-matter calculations with chiral NN and 3N interactions," *Physical Review C*, vol. 103, no. 4, p. 45803, 2021. [Online]. Available: https://doi.org/10.1103/PhysRevC.103.045803

[110] C. Drischler, K. Hebeler, and A. Schwenk, "Asymmetric nuclear matter based on chiral two- and three-nucleon interactions," *Physical Review C*, vol. 93, no. 5, p. 054314, 2016. [Online]. Available: https://doi.org/10.1103/PhysRevC.93.054314

[111] P. Wen and J. W. Holt, "Constraining the nonanalytic terms in the isospin-asymmetry expansion of the nuclear equation of state," *Physical Review C*, vol. 103, no. 6, p. 064002, Jun 2021. [Online]. Available: https://link.aps.org/doi/10.1103/PhysRevC.103.064002

[112] S. Goriely, N. Chamel, and J. M. Pearson, "Further explorations of Skyrme-Hartree-Fock-Bogoliubov mass formulas. XIII. The 2012 atomic mass evaluation and the symmetry coefficient," *Physical Review C*, vol. 88, p. 024308, Aug 2013. [Online]. Available: https://link.aps.org/doi/10.1103/PhysRevC.88.024308

[113] E. Chabanat, P. Bonche, P. Haensel, J. Meyer, and R. Schaeffer, "A Skyrme parametrization from subnuclear to neutron star densities Part II. Nuclei far from stabilities," *Nuclear Physics A*, vol. 635, no. 1, pp. 231–256, 1998. [Online]. Available: https://doi.org/10.1016/S0375-9474(98)00180-8

[114] M. Rayet, M. Arnould, F. Tondeur, and G. Paulus, "Nuclear forces and the properties of matter at high temperature and density," *Astronomy and Astrophysics*, vol. 116, no. 1, pp. 183–187, 1982. [Online]. Available: https://ui.adsabs.harvard.edu/abs/1982A%26A...116..183R/abstract

[115] A. Steiner, M. Prakash, J. Lattimer, and P. Ellis, "Isospin asymmetry in nuclei and neutron stars," *Physics Reports*, vol. 411, no. 6, pp. 325–375, 2005. [Online]. Available: https://doi.org/10.1016/j.physrep.2005.02.004

[116] G. A. Lalazissis, T. Nikšić, D. Vretenar, and P. Ring, "New relativistic mean-field interaction with density-dependent meson-nucleon couplings," *Physical Review C*, vol. 71, p. 024312, Feb 2005. [Online]. Available: https://doi.org/10.1103/PhysRevC.71.024312

[117] X. Roca-Maza, X. Viñas, M. Centelles, P. Ring, and P. Schuck, "Relativistic mean-field interaction with density-dependent meson-nucleon vertices based on microscopical calculations," *Physical Review C*, vol. 84, p. 054309, Nov 2011. [Online]. Available: https://doi.org/10.1103/PhysRevC.84.054309

[118] B. G. Todd-Rutel and J. Piekarewicz, "Neutron-Rich Nuclei and Neutron Stars: A New Accurately Calibrated Interaction for the Study of Neutron-Rich Matter," *Physical Review Letters*, vol. 95, p. 122501, Sep 2005. [Online]. Available: https://doi.org/10.1103/PhysRevLett.95.122501

[119] G. A. Lalazissis, J. König, and P. Ring, "New parametrization for the lagrangian density of relativistic mean field theory," *Physical Review C*, vol. 55, pp. 540–543, Jan 1997. [Online]. Available: https://doi.org/10.1103/PhysRevC.55.540

[120] W. Long, J. Meng, N. V. Giai, and S.-G. Zhou, "New effective interactions in relativistic mean field theory with nonlinear terms and density-dependent

meson-nucleon coupling," *Physical Review C*, vol. 69, p. 034319, Mar 2004. [Online]. Available: https://doi.org/10.1103/PhysRevC.69.034319

[121] H. Dinh Thi, T. Carreau, A. F. Fantina, and F. Gulminelli, "Uncertainties in the pasta-phase properties of catalysed neutron stars," *Astronomy & Astrophysics*, vol. 654, p. A114, Oct 2021. [Online]. Available: https://doi.org/10.1051/0004-6361/202141192

[122] T. Carreau, "Modeling the (proto)neutron star crust : toward a controlled estimation of uncertainties," Theses, Normandie Université, Sep. 2020. [Online]. Available: https://theses.hal.science/tel-03019954

[123] M. A. Ruderman, "Crystallization and Torsional Oscillations of Superdense Stars," *Nature*, vol. 218, no. 5147, pp. 1128–1129, Jun 1968. [Online]. Available: https://www.nature.com/articles/2181128a0

[124] E. Wigner and F. Seitz, "On the Constitution of Metallic Sodium. II," *Physical Review*, vol. 46, pp. 509–524, Sep 1934. [Online]. Available: https://doi.org/10.1103/PhysRev.46.509

[125] F. Douchin and P. Haensel, "A unified equation of state of dense matter and neutron star structure," *Astronomy and Astrophysics*, vol. 380, no. 1, pp. 151–167, Dec 2001. [Online]. Available: https://doi.org/10.1051/0004-6361:20011402

[126] X. Viñas, C. Gonzalez-Boquera, B. Sharma, and M. Centelles, "Pasta-phase Transitions in the Inner Crust of Neutron Stars," *Acta Physica Polonica B Proceedings Supplement*, vol. 10, no. 1, p. 259, 2017. [Online]. Available: https://www.actaphys.uj.edu.pl/S/10/1/259/pdf

[127] T. Carreau, F. Gulminelli, and J. Margueron, "Bayesian analysis of the crust-core transition with a compressible liquid-drop model," *European Physical Journal A*, vol. 55, no. 10, 2019. [Online]. Available: https://link.springer.com/article/10.1140/epja/i2019-12884-1

[128] C. J. Pethick and D. G. Ravenhall, "Matter at Large Neutron Excess and the Physics of Neutron-Star Crusts," *Annual Review of Nuclear and Particle Science*, vol. 45, no. 1, pp. 429–484, Dec 1995. [Online]. Available: https://doi.org/10.1146/annurev.ns.45.120195.002241

[129] T. Maruyama, T. Tatsumi, D. N. Voskresensky, T. Tanigawa, and S. Chiba, "Nuclear "pasta" structures and the charge screening effect," *Physical Review C*, vol. 72, p. 015802, Jul 2005. [Online]. Available: https://doi.org/10.1103/PhysRevC.72.015802

[130] K. Kolehmainen, M. Prakash, J. M. Lattimer, and J. R. Treiner, "Surface and curvature properties of neutron-rich nuclei," *Nuclear Physics A*, vol. 439, no. 3, pp. 535–572, 1985. [Online]. Available: https://www.sciencedirect.com/science/article/pii/0375947485904257

[131] W. G. Newton, M. Gearheart, and B.-A. Li, "A survey of the parameter space of the compressible liquid drop model as applied to the neutron star inner crust," *The*

Astrophysical Journal Supplement Series, vol. 204, no. 1, p. 9, Dec 2012. [Online]. Available: https://dx.doi.org/10.1088/0067-0049/204/1/9

[132] U. J. Furtado and F. Gulminelli, "Parametrization of the surface energy in the ETF approximation," *Journal of Physics G: Nuclear and Particle Physics*, vol. 48, no. 1, p. 015102, Jan 2020. [Online]. Available: https://doi.org/10.1088/1361-6471/abb44b

[133] D. Ravenhall, C. Pethick, and J. Lattimer, "Nuclear interface energy at finite temperatures," *Nuclear Physics A*, vol. 407, no. 3, pp. 571–591, 1983. [Online]. Available: https://www.sciencedirect.com/science/article/pii/037594748390667X

[134] L. E. Balliet, W. G. Newton, S. Cantu, and S. Budimir, "Prior Probability Distributions of Neutron Star Crust Models," *The Astrophysical Journal*, vol. 918, no. 2, p. 79, Sep 2021. [Online]. Available: http://dx.doi.org/10.3847/1538-4357/ac06a4

[135] M. Wang, G. Audi, F. G. Kondev, W. Huang, S. Naimi, and X. Xu, "The AME2016 atomic mass evaluation (II). Tables, graphs and references," *Chinese Physics C*, vol. 41, no. 3, p. 030003, Mar 2017. [Online]. Available: https://dx.doi.org/10.1088/1674-1137/41/3/030003

[136] P. Papakonstantinou, J. Margueron, F. Gulminelli, and A. R. Raduta, "Densities and energies of nuclei in dilute matter at zero temperature," *Physical Review C*, vol. 88, p. 045805, Oct 2013. [Online]. Available: https://doi.org/10.1103/PhysRevC.88.045805

[137] C. P. Lorenz, D. G. Ravenhall, and C. J. Pethick, "Neutron star crusts," *Physical Review Letters*, vol. 70, pp. 379–382, Jan 1993. [Online]. Available: https://doi.org/10.1103/PhysRevLett.70.379

[138] Y. Lim and J. W. Holt, "Structure of neutron star crusts from new Skyrme effective interactions constrained by chiral effective field theory," *Physical Review C*, vol. 95, p. 065805, Jun 2017. [Online]. Available: https://link.aps.org/doi/10.1103/PhysRevC.95.065805

[139] Y. Lim, J. W. Holt, and R. J. Stahulak, "Predicting the moment of inertia of pulsar j0737-3039a from bayesian modeling of the nuclear equation of state," *Physical Review C*, vol. 100, p. 035802, Sep 2019. [Online]. Available: https://doi.org/10.1103/PhysRevC.100.035802

[140] C. Pethick, D. Ravenhall, and C. Lorenz, "The inner boundary of a neutron-star crust," *Nuclear Physics A*, vol. 584, no. 4, pp. 675–703, Mar 1995. [Online]. Available: https://linkinghub.elsevier.com/retrieve/pii/037594749400506I

[141] J. Dobaczewski, W. Nazarewicz, and P.-G. Reinhard, "Error estimates of theoretical models: a guide," *Journal of Physics G: Nuclear and Particle Physics*, vol. 41, no. 7, p. 074001, May 2014. [Online]. Available: https://dx.doi.org/10.1088/0954-3899/41/7/074001

[142] H. Dinh Thi, A. F. Fantina, and F. Gulminelli, "The effect of the energy functional on the pasta-phase properties of catalysed neutron stars," *The European*

Physical Journal A, vol. 57, no. 10, p. 296, Oct 2021. [Online]. Available: https://doi.org/10.1140/epja/s10050-021-00605-6

[143] C. Pethick, D. Ravenhall, and J. Lattimer, "Effect of nuclear curvature energy on the transition between nuclei and bubbles in dense matter," *Physics Letters B*, vol. 128, no. 3-4, pp. 137–140, Aug 1983. [Online]. Available: https://linkinghub.elsevier.com/retrieve/pii/0370269383903763

[144] G. Baym, C. Pethick, and P. Sutherland, "The Ground State of Matter at High Densities: Equation of State and Stellar Models," *The Astrophysical Journal*, vol. 170, p. 299, Dec 1971. [Online]. Available: http://adsabs.harvard.edu/doi/10.1086/151216

[145] W. D. Myers and W. J. Swiatecki, "Nuclear masses and deformations," *Nuclear Physics*, vol. 81, no. 1, pp. 1–60, Jun 1966. [Online]. Available: https://linkinghub.elsevier.com/retrieve/pii/0029558266906390

[146] S. Goriely, M. Samyn, J. Pearson, and M. Onsi, "Further explorations of Skyrme–Hartree–Fock–Bogoliubov mass formulas. IV: Neutron-matter constraint," *Nuclear Physics A*, vol. 750, no. 2, pp. 425–443, 2005. [Online]. Available: https://doi.org/10.1016/j.nuclphysa.2005.01.009

[147] C. Mondal, X. Viñas, M. Centelles, and J. N. De, "Structure and composition of the inner crust of neutron stars from gogny interactions," *Physical Review C*, vol. 102, p. 015802, Jul 2020. [Online]. Available: https://doi.org/10.1103/PhysRevC.102.015802

[148] J. Piekarewicz, F. J. Fattoyev, and C. J. Horowitz, "Pulsar glitches: The crust may be enough," *Physical Review C*, vol. 90, p. 015803, Jul 2014. [Online]. Available: https://link.aps.org/doi/10.1103/PhysRevC.90.015803

[149] F. Grill, C. Providência, and S. S. Avancini, "Neutron star inner crust and symmetry energy," *Physical Review C*, vol. 85, p. 055808, May 2012. [Online]. Available: https://doi.org/10.1103/PhysRevC.85.055808

[150] F. Douchin and P. Haensel, "Inner edge of neutron-star crust with SLy effective nucleon-nucleon interactions," *Physics Letters, Section B: Nuclear, Elementary Particle and High-Energy Physics*, vol. 485, no. 1-3, pp. 107–114, 2000. [Online]. Available: https://doi.org/10.1016/S0370-2693(00)00672-9

[151] K. Oyamatsu and K. Iida, "Symmetry energy at subnuclear densities and nuclei in neutron star crusts," *Physical Review C*, vol. 75, p. 015801, Jan 2007. [Online]. Available: https://doi.org/10.1103/PhysRevC.75.015801

[152] C. Ducoin, P. Chomaz, and F. Gulminelli, "Isospin-dependent clusterization of neutron-star matter," *Nuclear Physics A*, vol. 789, no. 1-4, pp. 403–425, 2007. [Online]. Available: https://doi.org/10.1016/j.nuclphysa.2007.03.006

[153] S. Kubis, "Nuclear symmetry energy and stability of matter in neutron stars," *Physical Review C*, vol. 76, p. 025801, Aug 2007. [Online]. Available: https://doi.org/10.1103/PhysRevC.76.025801

[154] J. M. Lattimer and M. Prakash, "Neutron star observations: Prognosis for equation of state constraints," *Physics Reports*, vol. 442, no. 1, pp. 109–165, 2007, the Hans Bethe Centennial Volume 1906-2006. [Online]. Available: https://doi.org/10.1016/j.physrep.2007.02.003

[155] C. J. Horowitz and J. Piekarewicz, "Neutron star structure and the neutron radius of 208Pb," *Physical Review Letters*, vol. 86, no. 25, pp. 5647–5650, 2001. [Online]. Available: https://doi.org/10.1103/PhysRevLett.86.5647

[156] J. Carriere, C. J. Horowitz, and J. Piekarewicz, "Low-Mass Neutron Stars and the Equation of State of Dense Matter," *The Astrophysical Journal*, vol. 593, no. 1, pp. 463–471, 2003. [Online]. Available: https://iopscience.iop.org/article/10.1086/376515

[157] J. Xu, L. W. Chen, B. A. Li, and H. R. Ma, "Nuclear constraints on properties of neutron star crusts," *Astrophysical Journal*, vol. 697, no. 2, pp. 1549–1568, 2009. [Online]. Available: https://dx.doi.org/10.1088/0004-637X/697/2/1549

[158] C. Ducoin, J. Margueron, C. Providência, and I. Vidaña, "Core-crust transition in neutron stars: Predictivity of density developments," *Physical Review C - Nuclear Physics*, vol. 83, no. 4, p. 045810, 2011. [Online]. Available: https://doi.org/10.1103/PhysRevC.83.045810

[159] C. Providência, S. S. Avancini, R. Cavagnoli, S. Chiacchiera, C. Ducoin, F. Grill, J. Margueron, D. P. Menezes, A. Rabhi, and I. Vidaña, "Imprint of the symmetry energy on the inner crust and strangeness content of neutron stars," *European Physical Journal A*, vol. 50, no. 2, p. 44, 2014. [Online]. Available: https://doi.org/10.1140/epja/i2014-14044-7

[160] G. Baym, S. Furusawa, T. Hatsuda, T. Kojo, and H. Togashi, "New Neutron Star Equation of State with Quark–Hadron Crossover," *The Astrophysical Journal*, vol. 885, no. 1, p. 42, Oct 2019. [Online]. Available: https://dx.doi.org/10.3847/1538-4357/ab441e

[161] M. Fortin, C. Providência, A. R. Raduta, F. Gulminelli, J. L. Zdunik, P. Haensel, and M. Bejger, "Neutron star radii and crusts: Uncertainties and unified equations of state," *Physical Review C*, vol. 94, no. 3, p. 035804, Sep 2016. [Online]. Available: https://doi.org/10.1103/PhysRevC.94.035804

[162] R. Gamba, J. S. Read, and L. E. Wade, "The impact of the crust equation of state on the analysis of GW170817," *Classical and Quantum Gravity*, vol. 37, no. 2, p. 025008, Jan 2020. [Online]. Available: https://dx.doi.org/10.1088/1361-6382/ab5ba4

[163] M. Branchesi, M. Maggiore *et al.*, "Science with the Einstein Telescope: a comparison of different designs," Mar 2023. [Online]. Available: http://arxiv.org/abs/2303.15923

[164] K. C. Gendreau, Z. Arzoumanian, and T. Okajima, "The Neutron star Interior Composition ExploreR (NICER): an Explorer mission of opportunity for soft X-ray timing spectroscopy," in *Space Telescopes and Instrumentation 2012:*

Ultraviolet to Gamma Ray, T. Takahashi, S. S. Murray, and J.-W. A. den Herder, Eds., vol. 8443, no. March, Sep 2012, p. 844313. [Online]. Available: http://proceedings.spiedigitallibrary.org/proceeding.aspx?doi=10.1117/12.926396

[165] M. Maggiore, C. V. D. Broeck, N. Bartolo, E. Belgacem *et al.*, "Science case for the Einstein telescope," *Journal of Cosmology and Astroparticle Physics*, vol. 2020, no. 03, pp. 050–050, Mar 2020. [Online]. Available: https://iopscience.iop.org/article/10.1088/1475-7516/2020/03/050

[166] R. C. Tolman, "Static Solutions of Einstein's Field Equations for Spheres of Fluid," *Physical Review*, vol. 55, pp. 364–373, Feb 1939. [Online]. Available: https://doi.org/10.1103/PhysRev.55.364

[167] J. R. Oppenheimer and G. M. Volkoff, "On massive neutron cores," *Physical Review*, vol. 55, pp. 374–381, Feb 1939. [Online]. Available: https://doi.org/10.1103/PhysRev.55.374

[168] K. S. Thorne, "Tidal stabilization of rigidly rotating, fully relativistic neutron stars," *Physical Review D*, vol. 58, p. 124031, Nov 1998. [Online]. Available: https://link.aps.org/doi/10.1103/PhysRevD.58.124031

[169] E. E. Flanagan and T. Hinderer, "Constraining neutron-star tidal Love numbers with gravitational-wave detectors," *Physical Review D*, vol. 77, p. 021502, Jan 2008. [Online]. Available: https://link.aps.org/doi/10.1103/PhysRevD.77.021502

[170] T. Hinderer, "Tidal Love Numbers of Neutron Stars," *The Astrophysical Journal*, vol. 677, no. 2, pp. 1216–1220, Apr 2008. [Online]. Available: https://dx.doi.org/10.1086/533487

[171] T. Hinderer, B. D. Lackey, R. N. Lang, and J. S. Read, "Tidal deformability of neutron stars with realistic equations of state and their gravitational wave signatures in binary inspiral," *Physical Review D*, vol. 81, p. 123016, Jun 2010. [Online]. Available: https://link.aps.org/doi/10.1103/PhysRevD.81.123016

[172] J. M. Lattimer and M. Prakash, "The equation of state of hot, dense matter and neutron stars," *Physics Reports*, vol. 621, pp. 127–164, 2016. [Online]. Available: http://dx.doi.org/10.1016/j.physrep.2015.12.005

[173] D. Pines and M. A. Alpar, "Superfluidity in neutron stars," *Nature*, vol. 316, no. 6023, pp. 27–32, Jul 1985. [Online]. Available: http://www.nature.com/articles/316027a0

[174] Anderson, P. W. and Itoh, N., "Pulsar glitches and restlessness as a hard superfluidity phenomenon," *Nature*, vol. 256, no. 5512, pp. 25–27, Jul 1975. [Online]. Available: http://www.nature.com/articles/256025a0

[175] T. Carreau, "NSEOS," https://github.com/thomascarreau/NSEoS, May 2020.

[176] A. Maselli, V. Cardoso, V. Ferrari, L. Gualtieri, and P. Pani, "Equation-of-state-independent relations in neutron stars," *Physical Review D*, vol. 88, p. 023007, Jul 2013. [Online]. Available: https://link.aps.org/doi/10.1103/PhysRevD.88.023007

[177] B. Link, R. I. Epstein, and J. M. Lattimer, "Pulsar Constraints on Neutron Star Structure and Equation of State," *Physical Review Letters*, vol. 83, pp. 3362–3365, Oct 1999. [Online]. Available: https://doi.org/10.1103/PhysRevLett.83.3362

[178] T. Delsate, N. Chamel, N. Gürlebeck, A. F. Fantina, J. M. Pearson, and C. Ducoin, "Giant pulsar glitches and the inertia of neutron star crusts," *Physical Review D*, vol. 94, no. 2, pp. 1–12, 2016. [Online]. Available: https://doi.org/10.1103/PhysRevD.94.023008

[179] N. Andersson, K. Glampedakis, W. C. Ho, and C. M. Espinoza, "Pulsar glitches: The crust is not enough," *Physical Review Letters*, vol. 109, no. 24, pp. 1–5, 2012. [Online]. Available: https://doi.org/10.1103/PhysRevLett.109.241103

[180] J. Aasi, B. P. Abbott, R. Abbott, T. Abbott, M. R. Abernathy, K. Ackley *et al.*, "Advanced LIGO," *Classical and Quantum Gravity*, vol. 32, no. 7, 2015. [Online]. Available: https://dx.doi.org/10.1088/0264-9381/32/7/074001

[181] F. Acernese, M. Agathos, K. Agatsuma, D. Aisa, N. Allemandou, A. Allocca *et al.*, "Advanced Virgo: A second-generation interferometric gravitational wave detector," *Classical and Quantum Gravity*, vol. 32, no. 2, 2015. [Online]. Available: https://doi.org/10.1088/0264-9381/32/2/024001

[182] C. J. Horowitz, "Neutron rich matter in the laboratory and in the heavens after GW170817," *Annals of Physics*, vol. 411, p. 167992, 2019. [Online]. Available: https://doi.org/10.1016/j.aop.2019.167992

[183] G. Fiorella Burgio and I. Vidaña, "The equation of state of nuclear matter: From finite nuclei to neutron stars," *Universe*, vol. 6, no. 8, p. 119, 2020. [Online]. Available: https://www.mdpi.com/2218-1997/6/8/119

[184] H. Dinh Thi, C. Mondal, and F. Gulminelli, "The nuclear matter density functional under the nucleonic hypothesis," *Universe*, vol. 7, no. 10, 2021. [Online]. Available: https://doi.org/10.3390/universe7100373

[185] P. T. H. Pang, I. Tews, M. W. Coughlin, M. Bulla, C. Van Den Broeck, and T. Dietrich, "Nuclear Physics Multimessenger Astrophysics Constraints on the Neutron Star Equation of State: Adding NICER's PSR J0740+6620 Measurement," *The Astrophysical Journal*, vol. 922, no. 1, p. 14, 2021. [Online]. Available: http://dx.doi.org/10.3847/1538-4357/ac19ab

[186] I. Legred, K. Chatziioannou, R. Essick, S. Han, and P. Landry, "Impact of the PSR J0740+6620 radius constraint on the properties of high-density matter," *Physical Review D*, vol. 104, no. 6, p. 63003, 2021. [Online]. Available: https://doi.org/10.1103/PhysRevD.104.063003

[187] A. W. Steiner, J. M. Lattimer, and E. F. Brown, "The neutron star mass-radius relation and the equation of state of dense matter," *The Astrophysical Journal*, vol. 765, no. 1, p. L5, Feb 2013. [Online]. Available: https://doi.org/10.1088/2041-8205/765/1/l5

[188] N.-B. Zhang, B.-A. Li, and J. Xu, "Combined Constraints on the Equation of State of Dense Neutron-rich Matter from Terrestrial Nuclear Experiments and Observations of Neutron Stars," *The Astrophysical Journal*, vol. 859, no. 2, p. 90, 2018. [Online]. Available: http://dx.doi.org/10.3847/1538-4357/aac027

[189] Y. Lim and J. W. Holt, "Bayesian modeling of the nuclear equation of state for neutron star tidal deformabilities and GW170817," *The European Physical Journal A*, vol. 55, no. 11, p. 209, Nov 2019. [Online]. Available: https://doi.org/10.1140/epja/i2019-12917-9

[190] C. Y. Tsang, M. B. Tsang, P. Danielewicz, W. G. Lynch, and F. J. Fattoyev, "Impact of the neutron-star deformability on equation of state parameters," *Physical Review C*, vol. 102, no. 4, p. 045808, Oct 2020. [Online]. Available: https://doi.org/10.1103/PhysRevC.102.045808

[191] D. Adhikari, H. Albataineh, D. Androic, K. Aniol, D. S. Armstrong, T. Averett *et al.*, "Accurate Determination of the Neutron Skin Thickness of Pb 208 through Parity-Violation in Electron Scattering," *Physical Review Letters*, vol. 126, no. 17, p. 172502, 2021. [Online]. Available: https://doi.org/10.1103/PhysRevLett.126.172502

[192] C. Mondal and F. Gulminelli, "Nucleonic metamodeling in light of multimessenger, PREX-II, and CREX data," *Physical Review C*, vol. 107, no. 1, pp. 1–13, 2023. [Online]. Available: https://doi.org/10.1103/PhysRevC.107.015801

[193] D. S. Sivia and J. Skilling, "Data Analysis: A Bayesian Tutorial," *Oxford University Press*, 2006.

[194] C. Mondal, M. Antonelli, F. Gulminelli, M. Mancini, J. Novak, and M. Oertel, "Detectability of a phase transition in neutron star matter with third-generation gravitational wave interferometers," May 2023. [Online]. Available: http://arxiv.org/abs/2305.05999

[195] "LIGO Document P1800370-v5: Parameter Estimation Sample Release for GWTC-1," https://doi.org/10.7935/KSX7-QQ51.

[196] B. Biswas, "Impact of PREX-II and Combined Radio/NICER/XMM-Newton's Mass–radius Measurement of PSR J0740+6620 on the Dense-matter Equation of State," *The Astrophysical Journal*, vol. 921, no. 1, p. 63, 2021. [Online]. Available: http://dx.doi.org/10.3847/1538-4357/ac1c72

[197] T. Malik, N. Alam, M. Fortin, C. Providência, B. K. Agrawal, T. K. Jha, B. Kumar, and S. K. Patra, "GW170817: Constraining the nuclear matter equation of state from the neutron star tidal deformability," *Physical Review C*, vol. 98, no. 3, p. 035804, Sep 2018. [Online]. Available: https://doi.org/10.1103/PhysRevC.98.035804

[198] F. J. Fattoyev, J. Piekarewicz, and C. J. Horowitz, "Neutron Skins and Neutron Stars in the Multimessenger Era," *Physical Review Letters*, vol. 120, no. 17, p. 172702, 2018. [Online]. Available: https://doi.org/10.1103/PhysRevLett.120.172702

[199] E. Annala, T. Gorda, A. Kurkela, and A. Vuorinen, "Gravitational-Wave Constraints on the Neutron-Star-Matter Equation of State," *Physical Review Letters*, vol. 120, no. 17, p. 172703, 2018. [Online]. Available: https://doi.org/10.1103/PhysRevLett.120.172703

[200] O. Lourenço, M. Dutra, C. H. Lenzi, C. V. Flores, and D. P. Menezes, "Consistent relativistic mean-field models constrained by GW170817," *Physical Review C*, vol. 99, no. 4, p. 045202, Apr 2019. [Online]. Available: https://doi.org/10.1103/PhysRevC.99.045202

[201] H. Dinh Thi, C. Mondal, and F. Gulminelli, "Confronting the nucleonic hypothesis with current neutron star observations from GW170817 and PSR J0740+6620 ," in *Proceedings of Journées de Rencontre des Jeunes Chercheurs 2021*, 2022, pp. 209–214. [Online]. Available: https://hal.science/hal-03832762/

[202] T. Klähn, D. Blaschke, S. Typel, E. N. E. van Dalen, A. Faessler, C. Fuchs, T. Gaitanos, H. Grigorian, A. Ho, E. E. Kolomeitsev, M. C. Miller, G. Röpke, J. Trümper, D. N. Voskresensky, F. Weber, and H. H. Wolter, "Constraints on the high-density nuclear equation of state from the phenomenology of compact stars and heavy-ion collisions," *Physical Review C*, vol. 74, no. 3, p. 035802, Sep 2006. [Online]. Available: https://doi.org/10.1103/PhysRevC.74.035802

[203] L. Lindblom, "Spectral representations of neutron-star equations of state," *Physical Review D*, vol. 82, no. 10, p. 103011, Nov 2010. [Online]. Available: https://doi.org/10.1103/PhysRevD.82.103011

[204] J. M. Lattimer and M. Prakash, "Neutron Star Structure and the Equation of State," *The Astrophysical Journal*, vol. 550, no. 1, pp. 426–442, Mar 2001. [Online]. Available: https://dx.doi.org/10.1086/319702

[205] P. Landry, R. Essick, and K. Chatziioannou, "Nonparametric constraints on neutron star matter with existing and upcoming gravitational wave and pulsar observations," *Physical Review D*, vol. 101, no. 12, p. 123007, 2020. [Online]. Available: https://doi.org/10.1103/PhysRevD.101.123007

[206] G. Raaijmakers, S. K. Greif, K. Hebeler, T. Hinderer, S. Nissanke, A. Schwenk, T. E. Riley, A. L. Watts, J. M. Lattimer, and W. C. G. Ho, "Constraints on the dense matter equation of state and neutron star properties from nicer's mass–radius estimate of psr j0740+6620 and multimessenger observations," *The Astrophysical Journal Letters*, vol. 918, no. 2, p. L29, Sep 2021. [Online]. Available: https://dx.doi.org/10.3847/2041-8213/ac089a

[207] C. Mondal and F. Gulminelli, "Can we decipher the composition of the core of a neutron star?" *Physical Review D*, vol. 105, no. 8, p. 083016, Apr 2022. [Online]. Available: https://doi.org/10.1103/PhysRevD.105.083016https://link.aps.org/doi/10.1103/PhysRevD.105.083016

[208] J. Margueron and F. Gulminelli, "Effect of high-order empirical parameters on the nuclear equation of state," *Physical Review C*, vol. 99, no. 2, p. 025806, Feb 2019. [Online]. Available: https://doi.org/10.1103/PhysRevC.99.025806

[209] P. Danielewicz and J. Lee, "Symmetry energy I: Semi-infinite matter," *Nuclear Physics A*, vol. 818, no. 1-2, pp. 36–96, Feb 2009. [Online]. Available: https://doi.org/10.1016/j.nuclphysa.2008.11.007

[210] L.-W. Chen, B.-J. Cai, C. M. Ko, B.-A. Li, C. Shen, and J. Xu, "Higher-order effects on the incompressibility of isospin asymmetric nuclear matter," *Physical Review C*, vol. 80, no. 1, p. 014322, Jul 2009. [Online]. Available: https://doi.org/10.1103/PhysRevC.80.014322

[211] I. Vidaña, C. m. c. Providência, A. Polls, and A. Rios, "Density dependence of the nuclear symmetry energy: A microscopic perspective," *Physical Review C*, vol. 80, p. 045806, Oct 2009. [Online]. Available: https://doi.org/10.1103/PhysRevC.80.045806

[212] C. Ducoin, J. Margueron, and C. Providência, "Nuclear symmetry energy and core-crust transition in neutron stars: A critical study," *EPL (Europhysics Letters)*, vol. 91, no. 3, p. 32001, Aug 2010. [Online]. Available: https://dx.doi.org/10.1209/0295-5075/91/32001

[213] B. M. Santos, M. Dutra, O. Lourenço, and A. Delfino, "Correlations between the nuclear matter symmetry energy, its slope, and curvature from a nonrelativistic solvable approach and beyond," *Physical Review C*, vol. 90, no. 3, p. 035203, Sep 2014. [Online]. Available: https://doi.org/10.1103/PhysRevC.90.035203

[214] C. Mondal, B. K. Agrawal, J. N. De, S. K. Samaddar, M. Centelles, and X. Viñas, "Interdependence of different symmetry energy elements," *Physical Review C*, vol. 96, p. 021302, Aug 2017. [Online]. Available: https://doi.org/10.1103/PhysRevC.96.021302

[215] J. Adamczewski-Musch, O. Arnold, C. Behnke, A. Belounnas, A. Belyaev, J. C. Berger-Chen, A. Blanco, C. Blume, M. Böhmer *et al.*, "Directed, Elliptic, and Higher Order Flow Harmonics of Protons, Deuterons, and Tritons in Au+Au Collisions at sNN =2.4 GeV," *Physical Review Letters*, vol. 125, no. 26, p. 262301, 2020. [Online]. Available: https://doi.org/10.1103/PhysRevLett.125.262301

[216] M. Hashimoto, H. Seki, and M. Yamada, "Shape of Nuclei in the Crust of Neutron Star," *Progress of Theoretical Physics*, vol. 71, no. 2, pp. 320–326, 1984. [Online]. Available: https://doi.org/10.1143/PTP.71.320

[217] H. Dinh Thi, A. F. Fantina, and F. Gulminelli, "Properties of pasta phases in catalyzed neutron stars," *Nuovo Cimento della Societa Italiana di Fisica C*, vol. 45, no. 3, pp. 1–7, 2022. [Online]. Available: https://www.sif.it/riviste/sif/ncc/econtents/2022/045/03/article/20

[218] M. E. Caplan and C. J. Horowitz, "Colloquium: Astromaterial science and nuclear pasta," *Reviews of Modern Physics*, vol. 89, no. 4, pp. 1–13, 2017. [Online]. Available: https://doi.org/10.1103/RevModPhys.89.041002

[219] W. G. Newton, S. Cantu, S. Wang, A. Stinson, M. A. Kaltenborn, and J. R. Stone, "Glassy quantum nuclear pasta in neutron star crusts," *Physical*

Review C, vol. 105, no. 2, pp. 1–29, 2022. [Online]. Available: https://doi.org/10.1103/PhysRevC.105.025806

[220] J. M. Pearson and N. Chamel, "Unified equations of state for cold nonaccreting neutron stars with Brussels-Montreal functionals. III. Inclusion of microscopic corrections to pasta phases," *Physical Review C*, vol. 105, no. 1, pp. 1–12, 2022. [Online]. Available: https://doi.org/10.1103/PhysRevC.105.015803

[221] G. Grams, A. M. Santos, P. K. Panda, C. Providência, and D. P. Menezes, "Pasta Phases Within the QMC Model," *Springer Proceedings in Physics*, vol. 238, pp. 649–652, 2020. [Online]. Available: https://doi.org/10.1007/978-3-030-32357-8_102

[222] Z. Lin, M. E. Caplan, C. J. Horowitz, and C. Lunardini, "Fast neutrino cooling of nuclear pasta in neutron stars: Molecular dynamics simulations," *Physical Review C*, vol. 102, no. 4, pp. 1–12, 2020. [Online]. Available: https://doi.org/10.1103/PhysRevC.102.045801

[223] K. Nakazato, K. Oyamatsu, and S. Yamada, "Gyroid Phase in Nuclear Pasta," *Physical Review Letters*, vol. 103, no. 13, pp. 1–4, 2009. [Online]. Available: https://doi.org/10.1103/PhysRevLett.103.132501

[224] S. S. Avancini, D. P. Menezes, M. D. Alloy, J. R. Marinelli, M. M. Moraes, and C. Providência, "Warm and cold pasta phase in relativistic mean field theory," *Physical Review C - Nuclear Physics*, vol. 78, no. 1, pp. 1–12, 2008. [Online]. Available: https://doi.org/10.1103/PhysRevC.78.015802

[225] L. Scurto, H. Pais, and F. Gulminelli, "Strong magnetic fields and pasta phases revisited," *arXiv*, pp. 1–11, Dec 2022. [Online]. Available: http://arxiv.org/abs/2212.09355

[226] R. Williams and S. Koonin, "Sub-saturation phases of nuclear matter," *Nuclear Physics A*, vol. 435, no. 3-4, pp. 844–858, Mar 1985. [Online]. Available: https://doi.org/10.1016/0375-9474(85)90191-5

[227] H. Pais, D. P. Menezes, and C. Providência, "Neutron stars: From the inner crust to the core with the (extended) Nambu-Jona-Lasinio model," *Physical Review C*, vol. 93, no. 6, pp. 1–12, 2016. [Online]. Available: https://doi.org/10.1103/PhysRevC.93.065805

[228] S. Kubis and W. Wójcik, "Geometric approach to nuclear pasta phases," *Physical Review C*, vol. 94, no. 6, pp. 1–8, 2016. [Online]. Available: https://doi.org/10.1103/PhysRevC.94.065805

[229] N. N. Shchechilin, N. A. Zemlyakov, A. I. Chugunov, and M. E. Gusakov, "Pasta Phases in Neutron Star Mantle: Extended Thomas–Fermi vs. Compressible Liquid Drop Approaches," *Universe*, vol. 8, no. 11, p. 582, 2022. [Online]. Available: https://doi.org/10.3390/universe8110582

[230] M. Lassaut, H. Flocard, P. Bonche, P. H. Heenen, and E. Suraud, "Equation of state of hot dense matter," *Astronomy & Astrophysics*, vol. 183, pp. L3–L6, 1987. [Online]. Available: https://ui.adsabs.harvard.edu/abs/1987A%26A...183L...3L/abstract

[231] B. K. Sharma, M. Centelles, X. Vinas, M. Baldo, and G. F. Burgio, "Unified equation of state for neutron stars on a microscopic basis," *Astronomy and Astrophysics*, vol. 584, pp. 1–22, 2015. [Online]. Available: https://doi.org/10.1051/0004-6361/201526642

[232] I. Sengo, H. Pais, B. Franzon, and C. Providência, "Neutron star inner crust: Effects of rotation and magnetic fields," *Physical Review D*, vol. 102, no. 6, p. 63013, 2020. [Online]. Available: https://doi.org/10.1103/PhysRevD.102.063013

[233] F. Ji, J. Hu, and H. Shen, "Nuclear pasta and symmetry energy in the relativistic point-coupling model," *Physical Review C*, vol. 103, no. 5, pp. 1–13, 2021. [Online]. Available: https://doi.org/10.1103/PhysRevC.103.055802

[234] B. Schuetrumpf and W. Nazarewicz, "Twist-averaged boundary conditions for nuclear pasta Hartree-Fock calculations," *Physical Review C - Nuclear Physics*, vol. 92, no. 4, pp. 1–6, 2015. [Online]. Available: https://doi.org/10.1103/PhysRevC.92.045806

[235] I. Sagert, G. I. Fann, F. J. Fattoyev, S. Postnikov, and C. J. Horowitz, "Quantum simulations of nuclei and nuclear pasta with the multiresolution adaptive numerical environment for scientific simulations," *Physical Review C*, vol. 93, no. 5, 2016. [Online]. Available: https://doi.org/10.1103/PhysRevC.93.055801

[236] F. J. Fattoyev, C. J. Horowitz, and B. Schuetrumpf, "Quantum nuclear pasta and nuclear symmetry energy," *Physical Review C*, vol. 95, no. 5, pp. 20–23, 2017. [Online]. Available: https://doi.org/10.1103/PhysRevC.95.055804

[237] C. J. Horowitz, D. K. Berry, C. M. Briggs, M. E. Caplan, A. Cumming, and A. S. Schneider, "Disordered Nuclear Pasta, Magnetic Field Decay, and Crust Cooling in Neutron Stars," *Physical Review Letters*, vol. 114, no. 3, p. 031102, Jan 2015. [Online]. Available: https://link.aps.org/doi/10.1103/PhysRevLett.114.031102

[238] A. S. Schneider, D. K. Berry, M. E. Caplan, C. J. Horowitz, and Z. Lin, "Effect of topological defects on "nuclear pasta" observables," *Physical Review C*, vol. 93, no. 6, p. 065806, Jun 2016. [Online]. Available: https://link.aps.org/doi/10.1103/PhysRevC.93.065806

[239] G. Watanabe, H. Sonoda, T. Maruyama, K. Sato, K. Yasuoka, and T. Ebisuzaki, "Formation of nuclear "pasta" in supernovae," *Physical Review Letters*, vol. 103, no. 12, pp. 1–4, 2009. [Online]. Available: https://doi.org/10.1103/PhysRevLett.103.121101

[240] W. G. Newton, "Modeling nuclear pasta and the transition to uniform nuclear matter with the 3D-Skyrme-Hartree-Fock method," *AIP Conference Proceedings*, vol. 1128, no. May, pp. 154–164, 2009. [Online]. Available: https://doi.org/10.1103/PhysRevC.79.055801

[241] H. Pais and J. R. Stone, "Exploring the Nuclear Pasta Phase in Core-Collapse Supernova Matter," *Physical Review Letters*, vol. 109, no. 15, p. 151101, Oct 2012. [Online]. Available: https://link.aps.org/doi/10.1103/PhysRevLett.109.151101

[242] G. Watanabe and T. Maruyama, "Nuclear pasta in supernovae and neutron stars," Sep 2011. [Online]. Available: http://arxiv.org/abs/1109.3511

[243] P. N. Alcain, P. A. Giménez Molinelli, and C. O. Dorso, "Beyond nuclear "pasta" : Phase transitions and neutrino opacity of new "pasta" phases," *Physical Review C*, vol. 90, no. 6, p. 065803, Dec 2014. [Online]. Available: https://link.aps.org/doi/10.1103/PhysRevC.90.065803

[244] A. S. Schneider, D. K. Berry, C. M. Briggs, M. E. Caplan, and C. J. Horowitz, "Nuclear "waffles"," *Physical Review C - Nuclear Physics*, vol. 90, no. 5, pp. 1–15, 2014. [Online]. Available: https://doi.org/10.1103/PhysRevC.90.055805

[245] D. K. Berry, M. E. Caplan, C. J. Horowitz, G. Huber, and A. S. Schneider, ""Parking-Garage" Structures in Nuclear Astrophysics and Cellular Biophysics," *Physical Review C*, vol. 94, no. 5, pp. 1–5, 2016. [Online]. Available: https://doi.org/10.1103/PhysRevC.94.055801

[246] C. J. Horowitz, M. A. Pérez-García, and J. Piekarewicz, "Neutrino-"pasta" scattering: The opacity of nonuniform neutron-rich matter," *Physical Review C - Nuclear Physics*, vol. 69, no. 4, pp. 1–9, 2004. [Online]. Available: https://doi.org/10.1103/PhysRevC.69.045804

[247] C. J. Horowitz, D. K. Berry, M. E. Caplan, T. Fischer, Z. Lin, W. G. Newton, E. O'Connor, and L. F. Roberts, "Nuclear pasta and supernova neutrinos at late times," *arXiv*, pp. 1–6, Nov 2016. [Online]. Available: http://arxiv.org/abs/1611.10226

[248] M. E. Gusakov, D. G. Yakovlev, P. Haensel, and O. Y. Gnedin, "Direct Urca process in a neutron star mantle," *Astronomy and Astrophysics*, vol. 421, no. 3, pp. 1143–1148, 2004. [Online]. Available: https://doi.org/10.1051/0004-6361:20040288

[249] W. G. Newton, K. Murphy, J. Hooker, and B. A. Li, "The cooling of the cassiopeia a neutron star as a probe of the nuclear symmetry energy and nuclear pasta," *Astrophysical Journal Letters*, vol. 779, no. 1, pp. 4–8, 2013. [Online]. Available: https://dx.doi.org/10.1088/2041-8205/779/1/L4

[250] D. G. Yakovlev, "Electron transport through nuclear pasta in magnetized neutron stars," *Monthly Notices of the Royal Astronomical Society*, vol. 453, no. 1, pp. 581–590, 2015. [Online]. Available: https://doi.org/10.1093/mnras/stv1642

[251] A. Schmitt and P. Shternin, "Reaction Rates and Transport in Neutron Stars," Nov 2018, pp. 455–574. [Online]. Available: http://arxiv.org/abs/1711.06520

[252] M. R. Pelicer, M. Antonelli, D. P. Menezes, and F. Gulminelli, "Anisotropic electron transport in the nuclear pasta phase," *Monthly Notices of the Royal Astronomical Society*, vol. 521, no. 1, pp. 743–759, 02 2023. [Online]. Available: https://doi.org/10.1093/mnras/stad562

[253] C. J. Pethick and A. Y. Potekhin, "Liquid crystals in the mantles of neutron stars," *Physics Letters, Section B: Nuclear, Elementary Particle and*

High-Energy Physics, vol. 427, no. 1-2, pp. 7–12, 1998. [Online]. Available: https://doi.org/10.1016/S0370-2693(98)00341-4

[254] H. Sotani, "Constraints on pasta structure of neutron stars from oscillations in giant flares," *Monthly Notices of the Royal Astronomical Society: Letters*, vol. 417, no. 1, pp. 70–73, 2011. [Online]. Available: https://doi.org/10.1111/j.1745-3933.2011.01122.x

[255] M. Gearheart, W. G. Newton, J. Hooker, and B. A. Li, "Upper limits on the observational effects of nuclear pasta in neutron stars," *Monthly Notices of the Royal Astronomical Society*, vol. 418, no. 4, pp. 2343–2349, 2011. [Online]. Available: https://doi.org/10.1111/j.1365-2966.2011.19628.x

[256] M. Antonelli and B. Haskell, "Superfluid vortex-mediated mutual friction in non-homogeneous neutron star interiors," *Monthly Notices of the Royal Astronomical Society*, vol. 499, no. 3, pp. 3690–3705, Oct 2020. [Online]. Available: https://doi.org/10.1093/mnras/staa3097

[257] M. Antonelli, A. Montoli, and P. M. Pizzochero, "Insights Into the Physics of Neutron Star Interiors from Pulsar Glitches," in *Astrophysics in the XXI Century with Compact Stars*. WORLD SCIENTIFIC, Nov 2022, no. August 2021, pp. 219–281. [Online]. Available: http://dx.doi.org/10.1142/9789811220944_0007

[258] F. Douchin, P. Haensel, and J. Meyer, "Nuclear surface and curvature properties for SLy Skyrme forces and nuclei in the inner neutron-star crust," *Nuclear Physics A*, vol. 665, no. 3-4, pp. 419–446, Feb 2000. [Online]. Available: https://doi.org/10.1016/S0375-9474(99)00397-8

[259] C. Pethick, D. Ravenhall, and J. Lattimer, "Effect of nuclear curvature energy on the transition between nuclei and bubbles in dense matter," *Physics Letters B*, vol. 128, no. 3, pp. 137–140, 1983. [Online]. Available: https://www.sciencedirect.com/science/article/pii/0370269383903763

[260] K. Nakazato, K. Iida, and K. Oyamatsu, "Curvature effect on nuclear "pasta": Is it helpful for gyroid appearance?" *Physical Review C*, vol. 83, p. 065811, Jun 2011. [Online]. Available: https://link.aps.org/doi/10.1103/PhysRevC.83.065811

[261] I. Tews, J. Margueron, and S. Reddy, "Confronting gravitational-wave observations with modern nuclear physics constraints," *European Physical Journal A*, vol. 55, no. 6, 2019. [Online]. Available: https://doi.org/10.1140/epja/i2019-12774-6

[262] R. Essick, I. Tews, P. Landry, S. Reddy, and D. E. Holz, "Direct astrophysical tests of chiral effective field theory at supranuclear densities," *Physical Review C*, vol. 102, no. 5, pp. 1–18, 2020. [Online]. Available: https://doi.org/10.1103/PhysRevC.102.055803

[263] C. J. Yang, M. Grasso, and D. Lacroix, "From dilute matter to the equilibrium point in the energy-density-functional theory," *Physical Review C*, vol. 94, no. 3, pp. 1–5, 2016. [Online]. Available: https://doi.org/10.1103/PhysRevC.94.031301

[264] M. Grasso, D. Lacroix, and C. J. Yang, "Lee-Yang-inspired functional with a density-dependent neutron-neutron scattering length," *Physical Review C*, vol. 95, no. 5, pp. 3–6, 2017. [Online]. Available: https://doi.org/10.1103/PhysRevC.95.054327

[265] S. Goriely, N. Chamel, and J. M. Pearson, "The decompression of the outer neutron star crust and r-process nucleosynthesis," *A & A*, vol. 531, p. A78, Jun 2011. [Online]. Available: https://doi.org/10.1051/0004-6361/201116897

[266] M. Prakash, J. M. Lattimer, J. A. Pons, A. W. Steiner, and S. Reddy, *Evolution of a Neutron Star from Its Birth to Old Age*. Berlin, Heidelberg: Springer Berlin Heidelberg, 2001, pp. 364–423. [Online]. Available: https://doi.org/10.1007/3-540-44578-1_14

[267] J. A. Pons, S. Reddy, M. Prakash, J. M. Lattimer, and J. A. Miralles, "Evolution of Proto–Neutron Stars," *The Astrophysical Journal*, vol. 513, no. 2, pp. 780–804, Mar 1999. [Online]. Available: https://iopscience.iop.org/article/10.1086/306889

[268] M. V. Beznogov, D. Page, and E. Ramirez-Ruiz, "Thermal Evolution of Neo-neutron Stars. I. Envelopes, Eddington Luminosity Phase, and Implications for GW170817," *The Astrophysical Journal*, vol. 888, no. 2, p. 97, 2020. [Online]. Available: http://dx.doi.org/10.3847/1538-4357/ab5fd6

[269] H. Dinh Thi, A. F. Fantina, and F. Gulminelli, "The proto-neutron star inner crust in a multi-component plasma approach," *Astronomy & Astrophysics*, 2023. [Online]. Available: https://doi.org/10.1051/0004-6361/202346606

[270] ——, "The proto-neutron star inner crust in the liquid phase," *Astronomy & Astrophysics*, vol. 672, p. A160, Apr 2023. [Online]. Available: https://www.aanda.org/10.1051/0004-6361/202245061

[271] R. I. Epstein, "Acoustic properties of neutron stars," *The Astrophysical Journal*, vol. 333, p. 880, Oct 1988. [Online]. Available: http://adsabs.harvard.edu/doi/10.1086/166797

[272] A. D. Sedrakian, "Neutron-phonon interaction in neutron stars: Phonon spectrum of Coulomb lattice," *Astrophysics and Space Science*, vol. 236, no. 2, pp. 267–276, 1996. [Online]. Available: http://link.springer.com/10.1007/BF00645148

[273] P. Magierski and A. Bulgac, "Nuclear structure and dynamics in the inner crust of neutron stars," *Nuclear Physics A*, vol. 738, no. 1-4 SUPPL., pp. 143–149, 2004. [Online]. Available: https://doi.org/10.1016/j.nuclphysa.2004.04.023

[274] ——, "Nuclear hydrodynamics in the inner crust of neutron stars," *Acta Physica Polonica B*, vol. 35, no. 4, pp. 1203–1213, 2004. [Online]. Available: https://www.actaphys.uj.edu.pl/R/35/3/1203

[275] N. Martin and M. Urban, "Superfluid hydrodynamics in the inner crust of neutron stars," *Physical Review C*, vol. 94, no. 6, p. 065801, Dec 2016. [Online]. Available: https://doi.org/10.1103/PhysRevC.94.065801

[276] N. Chamel, "Entrainment in Superfluid Neutron-Star Crusts: Hydrodynamic Description and Microscopic Origin," *Journal of Low Temperature Physics*, vol. 189, no. 5-6, pp. 328–360, Dec 2017. [Online]. Available: http://link.springer.com/10.1007/s10909-017-1815-x

[277] A. Weiss, J. P. Cox, and R. T. Giuli, *Cox & Giuli's Principles of Stellar Structure*. Cambridge Scientific Publishers, 2004, vol. 8.

[278] B. Carter, N. Chamel, and P. Haensel, "Entrainment coefficient and effective mass for conduction neutrons in neutron star crust: simple microscopic models," *Nuclear Physics A*, vol. 748, no. 3-4, pp. 675–697, Feb 2005. [Online]. Available: https://doi.org/10.1016/j.nuclphysa.2004.11.006

[279] N. Chamel, "Effective mass of free neutrons in neutron star crust," *Nuclear Physics A*, vol. 773, no. 3-4, pp. 263–278, Jul 2006. [Online]. Available: https://linkinghub.elsevier.com/retrieve/pii/S0375947406001771

[280] ——, "Neutron conduction in the inner crust of a neutron star in the framework of the band theory of solids," *Physical Review C*, vol. 85, no. 3, p. 035801, Mar 2012. [Online]. Available: https://link.aps.org/doi/10.1103/PhysRevC.85.035801

[281] Y. Kashiwaba and T. Nakatsukasa, "Self-consistent band calculation of the slab phase in the neutron-star crust," *Physical Review C*, vol. 100, no. 3, p. 035804, Sep 2019. [Online]. Available: https://link.aps.org/doi/10.1103/PhysRevC.100.035804

[282] K. Sekizawa, S. Kobayashi, and M. Matsuo, "Time-dependent extension of the self-consistent band theory for neutron star matter: Anti-entrainment effects in the slab phase," *Physical Review C*, vol. 105, no. 4, p. 045807, Apr 2022. [Online]. Available: https://link.aps.org/doi/10.1103/PhysRevC.105.045807

[283] J. A. Sauls, N. Chamel, and M. A. Alpar, "Superfluidity in Disordered Neutron Stars Crusts," pp. 1–6, Jan 2020. [Online]. Available: http://arxiv.org/abs/2001.09959

[284] S. Typel, M. Oertel, and T. & Klähn, "CompOSE CompStar online supernova equations of state harmonising the concert of nuclear physics and astrophysics compose.obspm.fr," *Physics of Particles and nuclei*, vol. 46, p. 633–664, 2015. [Online]. Available: https://compose.obspm.fr

[285] A. R. Raduta and F. Gulminelli, "Nuclear Statistical Equilibrium equation of state for core collapse," *Nuclear Physics A*, vol. 983, pp. 252–275, 2019. [Online]. Available: https://doi.org/10.1016/j.nuclphysa.2018.11.003

[286] S. Mallik and F. Gulminelli, "Statistical treatment of nuclear clusters in the continuum," *Physical Review C*, vol. 103, no. 1, p. 015803, Jan 2021. [Online]. Available: https://link.aps.org/doi/10.1103/PhysRevC.103.015803

[287] S. Typel, "Variations on the excluded-volume mechanism," *The European Physical Journal A*, vol. 52, no. 1, p. 16, Jan 2016. [Online]. Available: http://link.springer.com/10.1140/epja/i2016-16016-3

[288] H. Shen, H. Toki, K. Oyamatsu, and K. Sumiyoshi, "Relativistic equation of state for core-collapse supernova simulations," *The Astrophysical Journal Supplement Series*, vol. 197, no. 2, p. 20, Dec 2011. [Online]. Available: https://iopscience.iop.org/article/10.1088/0067-0049/197/2/20

[289] K. Sato, "Supernova Explosion and Neutral Currents of Weak Interaction," *Progress of Theoretical Physics*, vol. 54, no. 5, pp. 1325–1338, Nov 1975. [Online]. Available: https://doi.org/10.1143/PTP.54.1325

[290] S. W. Bruenn, "Stellar core collapse - Numerical model and infall epoch," *The Astrophysical Journal Supplement Series*, vol. 58, p. 771, Aug 1985. [Online]. Available: http://adsabs.harvard.edu/doi/10.1086/191056

[291] M. Liebendorfer, M. Rampp, H. Janka, and A. Mezzacappa, "Supernova Simulations with Boltzmann Neutrino Transport: A Comparison of Methods," *The Astrophysical Journal*, vol. 620, no. 2, pp. 840–860, Feb 2005. [Online]. Available: https://iopscience.iop.org/article/10.1086/427203

[292] G. Shen, C. J. Horowitz, and S. Teige, "New equation of state for astrophysical simulations," *Physical Review C*, vol. 83, no. 3, p. 035802, Mar 2011. [Online]. Available: https://link.aps.org/doi/10.1103/PhysRevC.83.035802

[293] A. S. Schneider, L. F. Roberts, and C. D. Ott, "Open-source nuclear equation of state framework based on the liquid-drop model with Skyrme interaction," *Physical Review C*, vol. 96, no. 6, p. 065802, Dec 2017. [Online]. Available: https://link.aps.org/doi/10.1103/PhysRevC.96.065802

[294] S. S. Avancini, L. Brito, J. R. Marinelli, D. P. Menezes, M. M. W. de Moraes, C. Providência, and A. M. Santos, "Nuclear "pasta" phase within density dependent hadronic models," *Physical Review C*, vol. 79, no. 3, p. 035804, Mar 2009. [Online]. Available: https://link.aps.org/doi/10.1103/PhysRevC.79.035804

[295] H. Pais, W. G. Newton, and J. R. Stone, "Phase transitions in core-collapse supernova matter at sub-saturation densities," *Physical Review C*, vol. 90, no. 6, p. 065802, Dec 2014. [Online]. Available: https://link.aps.org/doi/10.1103/PhysRevC.90.065802

[296] F. Ji, J. Hu, S. Bao, and H. Shen, "Nuclear pasta in hot and dense matter and its influence on the equation of state for astrophysical simulations," *Physical Review C*, vol. 102, no. 1, p. 015806, Jul 2020. [Online]. Available: https://doi.org/10.1103/PhysRevC.102.015806

[297] Z. Medin and A. Cumming, "Crystallization of classical multicomponent plasmas," *Physical Review E*, vol. 81, no. 3, p. 036107, Mar 2010. [Online]. Available: https://link.aps.org/doi/10.1103/PhysRevE.81.036107

[298] H. Dinh Thi, A. F. Fantina, and F. Gulminelli, "Light clusters in the liquid proto-neutron star inner crust," *The European Physical Journal A*, 2023.

[299] E. Flowers and M. A. Ruderman, "Evolution of pulsar magnetic fields," *The Astrophysical Journal*, vol. 215, no. 2, p. 302, Jul 1977. [Online]. Available: http://adsabs.harvard.edu/doi/10.1086/155359

[300] D. Bhattacharya and B. Datta, "Ohmic decay of magnetic flux expelled from neutron star interiors," *Monthly Notices of the Royal Astronomical Society*, vol. 282, no. 3, pp. 1059–1063, Oct 1996. [Online]. Available: https://academic.oup.com/mnras/article-lookup/doi/10.1093/mnras/282.3.1059

[301] J. Daligault and S. Gupta, "Electronion scattering in dense multi-component plasmas: application to the outer crust of an accreting neutron star," *Astrophysical Journal*, vol. 703, no. 1, pp. 994–1011, 2009. [Online]. Available: https://iopscience.iop.org/article/10.1088/0004-637X/703/1/994

[302] A. Roggero and S. Reddy, "Thermal conductivity and impurity scattering in the accreting neutron star crust," *Physical Review C*, vol. 94, p. 015803, Jul 2016. [Online]. Available: https://link.aps.org/doi/10.1103/PhysRevC.94.015803

[303] F. V. de Blasio, "Crustal impurities and the internal temperature of a neutron star crust," *Monthly Notices of the Royal Astronomical Society*, vol. 299, no. 1, pp. 118–122, Aug 1998. [Online]. Available: https://academic.oup.com/mnras/article/299/1/118/1015146

[304] F. V. de Blasio and G. Lazzari, "Is the Crust of a Neutron Star an Impurity-free Crystal?" *The Astrophysical Journal*, vol. 468, p. 346, Sep 1996. [Online]. Available: http://adsabs.harvard.edu/doi/10.1086/177695

[305] E. Flowers and N. Itoh, "Transport properties of dense matter," *The Astrophysical Journal*, vol. 206, no. 1969, p. 218, May 1976. [Online]. Available: http://adsabs.harvard.edu/doi/10.1086/154375

[306] A. S. Schneider, M. E. Caplan, D. K. Berry, and C. J. Horowitz, "Domains and defects in nuclear pasta," *Physical Review C*, vol. 98, p. 055801, Nov 2018. [Online]. Available: https://link.aps.org/doi/10.1103/PhysRevC.98.055801

[307] M. E. Caplan, C. R. Forsman, and A. S. Schneider, "Thermal fluctuations in nuclear pasta," *Physical Review C*, vol. 103, no. 5, p. 055810, May 2021. [Online]. Available: https://link.aps.org/doi/10.1103/PhysRevC.103.055810

[308] H. Pais, F. Gulminelli, C. Providência, and G. Röpke, "Light clusters in warm stellar matter: Explicit mass shifts and universal cluster-meson couplings," *Physical Review C*, vol. 97, no. 4, p. 045805, Apr 2018. [Online]. Available: https://link.aps.org/doi/10.1103/PhysRevC.97.045805

[309] G. Röpke, "Light p-shell nuclei with cluster structures ($4 \leq A \leq 16$) in nuclear matter," *Physical Review C*, vol. 101, no. 6, p. 064310, Jun 2020. [Online]. Available: https://link.aps.org/doi/10.1103/PhysRevC.101.064310

[310] C. Y. Tsang, M. B. Tsang, P. Danielewicz, W. G. Lynch, and F. J. Fattoyev, "Constraining neutron-star equation of state using heavy-ion collisions," *arXiv:1807.06571 [nucl-ex, physics:nucl-th]*, Jul 2018. [Online]. Available: http://arxiv.org/abs/1807.06571

[311] H. Dinh Thi, "NS-PNS modeling," https://gitlab.in2p3.fr/lpc-caen/ns-pns-modeling.git, November 2021.

A unified equation of state for neutron stars and core-collapse supernovae

This thesis aims to study the interior properties of isolated, non-accreting, and non-rotating (proto-)neutron stars. For this purpose, the meta-modeling technique was employed to compute the properties of nuclear matter, while the inhomogeneities in the crust were characterized using a compressible liquid drop model. Furthermore, the equation of state was consistently calculated in a unified manner under the nucleonic hypothesis. Within a Bayesian study, we investigated the impact of different constraints from nuclear physics and astrophysical data on the equation of state of cold neutron stars. Notably, the results of our Bayesian analysis suggest that the nucleonic hypothesis remains compatible with all current data from neutron-star observations provided by the NICER and LIGO-Virgo collaborations. The non-spherical structures of nuclei in the innermost region of the crust, known as pasta phases, and the uncertainties associated with their properties were thoroughly investigated. Particularly, we demonstrated that both the bulk and surface terms have a significant impact on the prediction of the pasta-phase properties. Finally, we studied the inner crust of proto-neutron stars in the liquid phase. In particular, we demonstrated that the translational free energy has important effects on the crust composition. At high densities and temperatures, the one-component plasma approximation becomes less reliable, and the coexistence of different nuclear species in a multi-component plasma approach has been considered, thus allowing us to consistently calculate the so-called impurity parameter, needed for neutron-star cooling simulations. The formalism and numerical tools developed in this thesis could be further extended for future studies, such as investigating phase transitions in the core and calculating transport properties of the crust.
Keywords: neutron star, dense matter, equation of state, Bayesian analysis, pasta phases, plasma

---

Une équation d'état unifiée pour les étoiles à neutrons et les supernovae à effondrement de cœur

Cette thèse vise à étudier les propriétés à l'intérieur des (proto-)étoiles à neutrons isolées, non accrétantes et statiques. À cette fin, un meta-modèle a été utilisée pour décrire les propriétés de la matière nucléaire, tandis que les inhomogénéités dans la croûte ont été caractérisées en employant un modèle de goutte liquide compressible. De plus, l'équation d'état a été calculée de manière unifiée sous l'hypothèse nucléonique. Avec une étude bayésienne, nous avons examiné l'impact de différentes contraintes issues de la physique nucléaire et des données astrophysiques sur l'équation d'état des étoiles à neutrons froides. Les résultats de notre analyse bayésienne suggèrent notamment que l'hypothèse nucléonique reste compatible avec toutes les données actuelles provenant des observations d'étoiles à neutrons fournies par les collaborations NICER et LIGO-Virgo. Les structures non sphériques des noyaux dans la région la plus interne de la croûte, connues sous le nom de phases de pâtes, ainsi que les incertitudes associées à leurs propriétés ont été exhaustivement étudiées. En particulier, nous avons démontré que les termes de volume et de surface de l'énergie nucléaire ont un impact significatif sur la prédiction des propriétés des phases de pâtes. Enfin, nous avons étudié la croûte interne des proto-étoiles à neutrons en phase liquide. En particulier, nous avons démontré que l'énergie libre de translation a des effets importants sur la composition de la croûte. À des densités et des températures élevées, l'approximation du plasma à une composante devient moins fiable, et la coexistence de différentes espèces nucléaires a été prise en compte dans une approche de plasma à plusieurs composantes, qui a permis d'ailleurs de calculer de façon conhérente le paramètre d'impureté, donnée nécessaire dans les calculs de refroidissement des étoiles à neutrons. Le formalisme et les outils numériques développés dans cette thèse pourraient être étendus pour des études futures, telles que l'investigation des transitions de phase dans le cœur et des propriétés de transport de la croûte.

Mots clés : étoile à neutrons, matière dense, équation d'état, analyse bayésienne, phases de pâtes, plasma